

1980

Design of turbine cascades with transitional profile boundary layers

Gabriel Acacio Alarcon
Iowa State University

Follow this and additional works at: <https://lib.dr.iastate.edu/rtd>

 Part of the [Mechanical Engineering Commons](#), and the [Oil, Gas, and Energy Commons](#)

Recommended Citation

Alarcon, Gabriel Acacio, "Design of turbine cascades with transitional profile boundary layers " (1980). *Retrospective Theses and Dissertations*. 6680.
<https://lib.dr.iastate.edu/rtd/6680>

This Dissertation is brought to you for free and open access by the Iowa State University Capstones, Theses and Dissertations at Iowa State University Digital Repository. It has been accepted for inclusion in Retrospective Theses and Dissertations by an authorized administrator of Iowa State University Digital Repository. For more information, please contact digirep@iastate.edu.

INFORMATION TO USERS

This was produced from a copy of a document sent to us for microfilming. While the most advanced technological means to photograph and reproduce this document have been used, the quality is heavily dependent upon the quality of the material submitted.

The following explanation of techniques is provided to help you understand markings or notations which may appear on this reproduction.

1. The sign or "target" for pages apparently lacking from the document photographed is "Missing Page(s)". If it was possible to obtain the missing page(s) or section, they are spliced into the film along with adjacent pages. This may have necessitated cutting through an image and duplicating adjacent pages to assure you of complete continuity.
2. When an image on the film is obliterated with a round black mark it is an indication that the film inspector noticed either blurred copy because of movement during exposure, or duplicate copy. Unless we meant to delete copyrighted materials that should not have been filmed, you will find a good image of the page in the adjacent frame.
3. When a map, drawing or chart, etc., is part of the material being photographed the photographer has followed a definite method in "sectioning" the material. It is customary to begin filming at the upper left hand corner of a large sheet and to continue from left to right in equal sections with small overlaps. If necessary, sectioning is continued again—beginning below the first row and continuing on until complete.
4. For any illustrations that cannot be reproduced satisfactorily by xerography, photographic prints can be purchased at additional cost and tipped into your xerographic copy. Requests can be made to our Dissertations Customer Services Department.
5. Some pages in any document may have indistinct print. In all cases we have filmed the best available copy.

University
Microfilms
International

300 N. ZEEB ROAD, ANN ARBOR, MI 48106
18 BEDFORD ROW, LONDON WC1R 4EJ, ENGLAND

ALARCON, GABRIEL ACACIO

DESIGN OF TURBINE CASCADES WITH TRANSITIONAL PROFILE
BOUNDARY LAYERS

Iowa State University

PH.D.

1980

University
Microfilms
International 300 N. Zeeb Road, Ann Arbor, MI 48106

Design of turbine cascades with
transitional profile boundary layers

by

Gabriel Acacio Alarcon

A Dissertation Submitted to the
Graduate Faculty in Partial Fulfillment of the
Requirements for the Degree of
DOCTOR OF PHILOSOPHY

Major: Mechanical Engineering

Approved:

Signature was redacted for privacy.

In Charge of Major Work

Signature was redacted for privacy.

For the Major Department

Signature was redacted for privacy.

For the Graduate College

Iowa State University
Ames, Iowa

1980

TABLE OF CONTENTS

	page
LIST OF SYMBOLS	vi
1. INTRODUCTION	1
1.1. The Turbine Design Problem Considered	1
1.2. Practical Importance of a Turbine Cascade Design System	4
1.3. Objective and Scope of Present Work	6
2. TURBINE CASCADE DESIGN	10
2.1. Introduction	10
2.2. Selection Methods for Two-Dimensional Turbine Cascades	10
2.3. Design Methods for Two-Dimensional Airfoils in Cascade	14
2.4. The Two-Dimensional Turbine Cascade Geometry Design	17
2.4.1. Description of input for geometry design programs GDPLS, GDPNLS	18
2.4.2. Airfoil profile solution	20
2.4.3. Determination of input for geometry design programs GDPLS, GDPNLS	23
2.4.4. Operation of geometry design programs, GDPLS, GDPNLS	26
2.4.5. Examples of turbine cascade designs	27
3. GLOBAL INVISCID ANALYSIS	35
3.1. Introduction	35
3.2. Review of Recent Blade-to-Blade Flow Calculation Methods	36
3.2.1. Hodograph methods	36
3.2.2. Matrix methods	37
3.2.3. Time-marching methods	38

	page
3.2.4. Space-marching methods	39
3.2.5. Streamline curvature methods	40
3.3. The Present Streamline Curvature Method (SCA)	42
3.3.1. Governing equations	42
3.3.2. Computational flow field	47
3.3.3. General description of calculation	49
3.3.4. Continuity equation solution	54
3.3.5. Stability and convergence	56
3.3.6. Stagnation streamline shifts	63
3.3.7. Numerical differentiation	71
3.3.8. Validation of streamline curvature method (SCA)	81
4. INVISCID REANALYSIS OF LEADING EDGE	100
4.1. Introduction	100
4.2. Review of Previous Reanalysis Techniques	100
4.3. The Present Finite Area Reanalysis Method (REA)	103
4.3.1. Governing equations	103
4.3.2. Computational flow field	106
4.3.3. Numerical approximation	109
4.3.4. General description of calculation	112
4.3.5. Interpolation of boundary values	115
4.3.6. Approximation of stream function gradient	119
4.3.7. Validation of reanalysis method (REA)	120
5. INTEGRAL BOUNDARY LAYER ANALYSIS	126
5.1. Introduction	126

	page
5.2. The Dissipation-Integral Boundary Layer Calculation Method	127
5.2.1. Brief outline of the theory	127
5.2.2. Numerical approximation of boundary layer equations	138
5.2.3. General description of boundary layer calculation method	139
5.2.4. Test case results for auxiliary relations	142
5.3. Laminar Starting Procedure	146
5.4. Natural Transition Model	148
5.5. Laminar Separation Bubble Model	155
5.6. Inclusion of Wall Curvature Effects on Development of Turbulent Boundary Layer	157
5.7. Inclusion of Free Stream Turbulence Effects on Development of Turbulent Boundary Layer	161
5.8. Empirical Model for Proceeding After Turbulent Separation	168
5.9. Wake Mixing Loss Calculations	171
6. VALIDATION OF THE INVISCID-VISCOUS BLADE-TO-BLADE FLOW ANALYSIS	172
6.1. Introduction	172
6.2. Experimental Cascade Data as Test Cases	172
6.3. Test Cases and Results	175
7. CONCLUSIONS	192
8. SUGGESTIONS FOR FURTHER RESEARCH	194
9. REFERENCES	196
10. ACKNOWLEDGMENTS	205

	page
11. APPENDIX A. CALCULATION OF FLOW PASSAGE CROSS SECTIONAL AREA	206
12. APPENDIX B. PRESSURE-MOMENTUM BALANCE IN TANGENTIAL DIRECTION	208
13. APPENDIX C. SYSTEMS OF EQUATIONS FOR PERIODICITY CONDITIONS IN STREAMLINE CURVATURE ANALYSIS	211
14. APPENDIX D. DERIVATION OF K IN REANALYSIS EQUATIONS	215
15. APPENDIX E. LEAST SQUARES QUADRATIC POLYNOMIAL	218
16. APPENDIX F. VISCOSITY-TEMPERATURE RELATIONSHIPS	220
17. APPENDIX G. SPEIDEL WAKE MIXING CALCULATION	222
18. APPENDIX H. DESCRIPTION OF INPUT TO CASCADE FLOW ANALYSIS PROGRAM	227

LIST OF SYMBOLS

a	constant
$a_{i,j}$	numerical differentiation coefficient
a, b, c	coefficients
A	aspect ratio of streamline curvature grid element, or banded coefficient matrix
AVDR	axial velocity density ratio, $\frac{\rho_2 V_2 \sin\beta_2}{\rho_1 V_1 \sin\beta_1}$
$b_{i,j}$	numerical differentiation coefficient
\bar{b}	vector of zeros or boundary information
B_x	axial chord
c	chord length, or speed of sound
c_f	local skin friction coefficient
c_D	dissipation integral
C_{d_1}	drag coefficient as in Dunavant and Erwin (1956)
f	damping factor to correct initial error to zero
f'	optimum damping factor
f_c	critical damping factor
F_1, F_2, F_3, F_4	functions
G	Clauser's velocity parameter
h	enthalpy, or q-o spacing
H/L	height-to-length ratio
H_{12}, H_{32}, H_{43}	shape factors
k	numerical differentiation function, as in Wilkinson (1970)

K	constant
l	length along streamline, or distance between points conforming a finite area element
l_1, l_2	lengths within the laminar separation bubble
\dot{m}	mass flow rate
\bar{m}	mass velocity
M	Mach number, or number of q-os
M*	critical Mach number, V/V_{CRIT}
ML	number of q-o just in front of leading edge
MT	number of q-o through trailing edge
n	number of iterations, or normal direction, or exponent in boundary layer calculation
N	number of streamlines
p	pressure
q	tangential distance measured from suction side
r	recovery factor
RLE	radius of leading edge circle
RTE	radius of trailing edge circle
R_c	chord Reynolds number based on exit conditions
R_{δ}	Reynolds number based on boundary layer thickness and local edge velocity
R_{δ_2}	Reynolds number based on momentum loss thickness and local edge velocity
s	entropy, or side of finite area element, or coordinate along flow boundary
S	pressure coefficient, $\frac{P_{01} - P}{\frac{1}{2} \rho V_1^2}$

t	maximum profile thickness
T	temperature
T_e	recovery temperature
Tu	turbulence intensity
u, v, w	velocities in the x, y, and z directions, respectively
$(\bar{u}_\delta)_{re}$	reattachment velocity ratio, $(u_\delta)_{re}/(u_\delta)_{sep}$
V	flow velocity
V_{CRIT}	critical velocity
x	Cartesian coordinate
y	Cartesian, or normal to the flow boundary coordinate
Y_p	Ainley's pressure loss coefficient
Z	length parameter
α	gas angle measured with respect to the axial direction, or a function in the boundary layer calculation
β	gas angle measured with respect to the tangential direction except as noted in text
β_λ	gaging angle
β^*	metal angle
γ	ratio of specific heats
Γ	uncovered turning
δ	deviation angle, or stagnation streamline shift, or boundary layer thickness
δ_1	displacement thickness
δ_2	momentum loss thickness

δ_3	energy loss thickness
δ_4	density loss thickness
Δz	stream sheet thickness
$\Delta\beta^*$	wedge angle
$\Delta\theta_{ind}$	induced flow angle
θ	heat transfer parameter, or turning angle
θ_c	design camber angle
λ	throat length, or wave length, or pressure gradient parameter
Λ	von Karman pressure gradient parameter
μ	dynamic viscosity
ν	kinematic viscosity
ξ	Speidel total pressure loss coefficient
Π	pressure gradient parameter, or Coles wake parameter
ρ	density
σ	density ratio
τ	cascade spacing in tangential direction or shear stress
ϕ	a function of Mach number
ψ	stream function
ψ_T	loading coefficient
ψ_1	a function of Mach number and heat transfer parameter
$\bar{\omega}_2$	total pressure loss coefficient based on exit conditions as in Stewart (1955)

Subscripts

f	fluctuating
i	q-o index, or incompressible
j	streamline index, or q-o index for stagnation streamline shifts calculation
M	last q-o
num	numerical
N	suction surface
NM	mid-streamline
re	turbulent reattachment
req	required
sep	separation
TE	trailing edge
tr	natural transition
tur	fully turbulent
u	quantities depending only on velocity distribution in the boundary layer
w	wall value
x	axial direction
y	tangential direction
δ	edge of boundary layer
λ	throat value
0	total or stagnation conditions
1	upstream or pressure surface
2	downstream

Superscripts

i	inviscid
*	compressible
-	average quantities
~	half of the more common values
'	turbulent fluctuation

1. INTRODUCTION

1.1. The Turbine Design Problem Considered

The aerothermodynamic design of cooled or uncooled axial flow turbines, and in general of any modern axial flow turbomachine, involves fairly well-established step-by-step procedures which have been described (with some variations) by many authors in the literature. Upon selected review of the design methods of Talbert and Smith (1948), Duncombe (1964), Horlock (1973), Whitney and Stewart (1973), Stewart and Glassman (1973), Wright (1974), Webster (1976), and Dring and Heiser (1978), the four major steps noted and discussed below may be regarded as a satisfactory procedure leading to successful axial flow turbine designs. The iterative character of the design procedure should be emphasized since the order of execution might be interrupted at any intermediate step and the procedure restarted after readjustment of one or more of the specified design parameters.

Step 1 involves the determination of the overall turbine performance requirements and the preliminary design of the flow path and meanline velocity triangles. Parameters such as inlet and exit pressures and temperatures (and therefore overall efficiency), mass flow, maximum diameter and allowable speed range must be established in this step. Also, the number of stages and stage work splits are decided on consistent with required stage efficiencies. Past design experience and related information from the open literature are important in making these decisions. Webster (1976), for example, performs a parametric

meanline analysis in which the influence of exit annulus area and stage work splits on turbine efficiency is determined. Design experience and incorporation of other design information reflects directly in the accuracy of the empirical loss system needed in connection with the meanline analysis to estimate the magnitude of the various stage losses (profile, endwall, parasitic, and cooling).

The objective of the preliminary meanline analysis is to point out the best performance configuration (flow path and velocity triangles) that will satisfy overall design requirements. The main difficulties with this procedure are in the proper estimation of the different stage losses based upon the little geometric data available at this step. The profile loss, for instance, must be estimated without having detailed airfoil profile information, knowing only the velocity triangles, chord, solidity, and trailing edge radius. As stated by Dring and Heiser (1978), the loss system is the most crucial feature of a meanline analysis. Baljé (1968) has presented an excellent review of current axial cascade technology and its application to flow path design.

Step 2 of the procedure is the determination of spanwise distributions of work extraction and losses per stage. Use has been made in the past of constant work distribution along the blade from hub to tip, mainly for the sake of mathematical simplicity; however, with the availability of sophisticated "through-flow" analysis computer codes, and with the need for increased stage loadings, the constant work

assumption is being dropped in favor of the controlled vortex flow principle of Dorman et al. (1968). The controlled vortex principle enhances the design by application of nonconstant spanwise work distributions which increase reaction at the blade hub while decreasing it at the tip. The loss levels estimated at this point are distributed along the blade span to account for endwall, tip leakage, and parasitic losses. Design experience and empirical correlations are used in this task. Dunham and Came (1970), for instance, have correlated endwall losses against gas angles, cascade geometric parameters, displacement thickness of inlet boundary layer and profile loss coefficient. Many authors have reported empirical correlations of tip leakage losses; the two most widely used are due to Schlichting and Das (1966) and Dunham and Came (1970). Baljé and Binsley (1968) have reviewed available correlations for all the different losses present in a turbine blade row.

Step 3 consists of solving the radial component of the equations of motion to determine the spanwise variation of velocity diagrams at the blade inlet and outlet for each stage. The assumption of axially symmetric flow is invariably made for this "through-flow" analysis in the meridional plane. The simplicity of the solution depends on the spanwise distribution of work and losses assumed in Step 2. With constant work and loss distributions simple theoretical solutions (free vortex design) are obtained as compared to complicated numerical solutions when the controlled vortex principle is used. Two main

"through-flow" analysis methods are presently used in connection with the controlled vortex principle: the matrix inversion technique (see, for instance, Marsh (1968)), and the streamline curvature technique (see, for instance, Frost (1970)).

Step 4, the final step, is the selection or design of the two-dimensional airfoil sections that will produce at each radial location the flow angles and velocities required by the velocity triangles previously determined.

The research work reported on here has been devoted in its entirety to Step 4, with the specific objective of developing a rapid (and robust) numerical procedure for the design of two-dimensional turbine cascades. In this procedure, the profile of the airfoils in cascade can be arbitrarily designed from velocity triangle information and the subsequent aerodynamic and profile boundary layer performance determined. What has evolved is an automated and interactive "direct" design system by which cascades approaching optimum performance under high subsonic to transonic flow conditions and transitional boundary layer behavior can be designed.

1.2. Practical Importance of a Turbine Cascade Design System

The relevance of a reliable and accurate design system for high performance two-dimensional airfoil cascades should be obvious from the discussion of the previous section. Two-dimensional cascade flow is obviously simpler than the flow in an axial flow turbine blade row

in which important spanwise (three-dimensional) flow gradients are present due to annulus boundary layers, tip clearance flows, and secondary flows. However, spanwise comparisons with blade-to-blade analysis show that, under restrictions to cascades with large or moderately large blade aspect ratios, experimental cascade performance is essentially two-dimensional. Under such conditions, the penetration of three-dimensional flow effects from the endwalls into the main flow is small; consequently, airfoils in cascades may be successfully designed over a range of inlet flow angles using two-dimensional cascade flow calculations in conjunction with conventional boundary layer analysis.

Plane cascade flow analysis yields a complete definition of the flow field between airfoils; however, the following information is of primary importance to the designer:

- (i) pressure distribution over the airfoil, and
- (ii) flow outlet direction from the cascade.

Pressure distributions as produced by the design and which result in separation-free performance of the cascade are essential. Also, determination of pressure distributions is required in the design of airfoil cooling systems in cooled turbine applications. Accurate determination of the flow outlet direction is required for the proper design of the next row of vanes or blades in the machine.

In conclusion, well designed airfoil contours are demanded in the design of high performance turbines. As can be shown, for example, in

cycle analysis of a gas turbine engine performing at typical conditions of aircraft applications, a 1% increase in turbine efficiency through improved aerodynamic design increases cycle thermal efficiency by approximately 2.5%; equivalently, a 1.7% increase in compressor efficiency is required for the same improvement in cycle thermal efficiency. This emphasizes the importance of high turbine efficiency in overall engine performance.

1.3. Objective and Scope of Present Work

The objective of the present investigation has been the development and testing of a programmed numerical procedure which would be useful in the context of a "direct" design system for axial flow turbine cascades. The design system would enable the user to design turbine cascades satisfying design specifications of velocity triangle and loading requirements while incorporating transitional boundary layers on the airfoils. A flow diagram of the complete "direct" design system is shown in Fig. 1.1 in which the sequence of the main calculations and the techniques employed with each of them are pointed out. The interaction stations are noted where the user can branch back to the beginning of the procedure if the design is found to be unsatisfactory.

During the development of the procedure, the requirements of a good design system have been kept in mind; i.e., that the system be economical and relatively easy to use, and that analysis techniques used be accurate and widely applicable. As a result, complicated methods involving

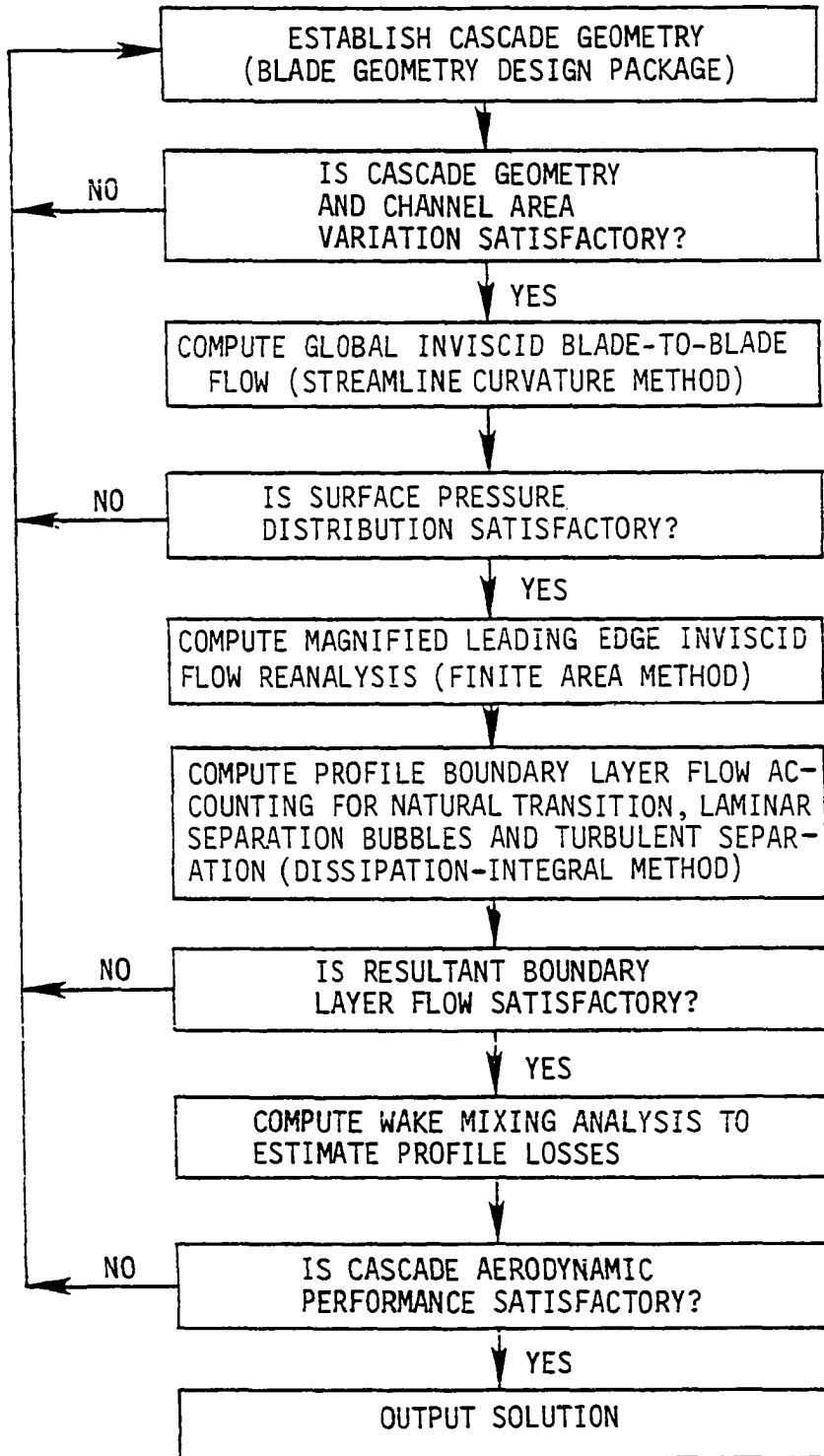


Figure 1.1. Turbine cascade design system flow diagram

excessive computing times, such as boundary layer analyses involving inviscid-viscous matching techniques, as developed by Hansen (1978), have been precluded.

The scope of the work which has been carried out can be divided into the following four categories:

(i) Development of airfoil geometry design procedure The geometry design procedure has been developed to accomplish the design of the airfoils in cascade in an interactive fashion. Rapid graphing capabilities are essential to the method.

The procedure, presented in Chapter 2, is applicable to axial turbine inlet guide vanes, stators, and rotors. It can be easily extended to the design of exit guide vanes as well.

(ii) Development of blade-to-blade calculation procedure The two-dimensional global blade-to-blade numerical procedure has been developed from streamline curvature concepts. The primary emphasis has been to account for compressibility effects up to slightly (shock free) transonic pockets in the flow, and for change in stream sheet thickness from cascade inlet to outlet. The cascade exit inviscid flow angle is predicted from periodicity conditions or from given empirical correlations.

A detailed reanalysis of the leading edge flow region uses finite area techniques and a body fitted mesh. Stream sheet thickness change is also accounted for in the reanalysis.

The details of the blade-to-blade global and reanalysis methods are presented in Chapters 3 and 4, respectively.

(iii) Development of profile boundary layer calculation Chapter 5 describes the two-dimensional, transitional, dissipation-integral boundary layer calculation method. The procedure has been developed to account for the important effects of compressibility, longitudinal wall curvature and free stream turbulence. Turbulent separation has also been considered and a wake mixing calculation included to determine cascade profile losses.

(iv) Validation of the prediction procedure In order to test the capabilities of the inviscid-viscous prediction procedure, two turbine cascades have been computed as test cases. The numerical results for these test cases, including incompressible as well as compressible conditions, are compared with experimental data in Chapter 6.

2. TURBINE CASCADE DESIGN

2.1. Introduction

This chapter presents a detailed discussion of the selection and design methods for two-dimensional cascades of airfoils for axial flow turbine applications.

First, selection methods for turbine cascades and associated turbomachine cascade design approaches used in the past are reviewed. Following this, the description of two interactive computer programs (GDPLS and GDPNLS) developed during the course of this investigation for the design of turbine airfoils in cascade is given. The manner in which the geometric parameters required by the design programs are related to aerodynamic and structural constraints is also treated.

Finally, four cascade design examples are presented, and guidelines are drawn for using the programs in general design applications.

2.2. Selection Methods for Two-Dimensional Turbine Cascades

The selection of a two-dimensional turbine cascade of airfoils consists of choosing a particular cascade from previously tested families of cascades to satisfy required velocity diagrams. The selection methods preclude any profile optimization procedure since the airfoil profile cannot be altered from the original tested configuration. The published methods of Ainley and Mathieson (1955) and Dumavant and Erwin (1956) for the selection of turbine cascades are reviewed below:

a) Ainley and Mathieson (1955) correlated the profile losses of a variety of turbine airfoils in cascades tested at Mach numbers up to 0.6, Reynolds numbers in the neighborhood of 2×10^5 , and at small incidence angles. The tested cascades comprised RAF 27 and C.7 airfoil sections with thicknesses of 10 and 20 per cent of chord, on circular-arc (C.50) and parabolic-arc (P.40) camber-lines. "Conventional" sections having thicknesses of 10 and 20 per cent were also tested. The term "conventional" refers to profiles composed of a number of circular arcs and straight lines approximating a T.6 section (see Ainley (1948)) on a parabolic camber-line, the point of maximum camber being at 40 to 43 per cent of chord from the leading edge.

Figure 2.1 shows Ainley's profile loss coefficient, Y_p , for nozzle and impulse cascades. As can be observed, the dependence of losses on pitch to chord ratio (τ/c) for given exit gas angle is stronger for impulse cascades than for nozzle cascades. Nevertheless, a minimum loss can be observed to occur at an optimum value of τ/c in both types of cascades. As τ/c decreases, the frictional surface area per unit flow increases. On the other hand, as τ/c increases, the loss per unit surface area increases due to increased surface diffusion on the suction side of the airfoil. These two effects combine to give a point of minimum loss.

For cascades intermediate to the nozzle and impulse cases, the correlation of pressure loss coefficient is

$$Y_{P(i=0)} = Y_{P(\alpha_1=0)} + \left(\frac{\alpha_1}{\alpha_2}\right)^2 (Y_{P(\alpha_1=\alpha_2)} - Y_{P(\alpha_1=0)}) \left(\frac{\tau/c}{0.2}\right)^{\alpha_1/\alpha_2} \quad (2.1)$$

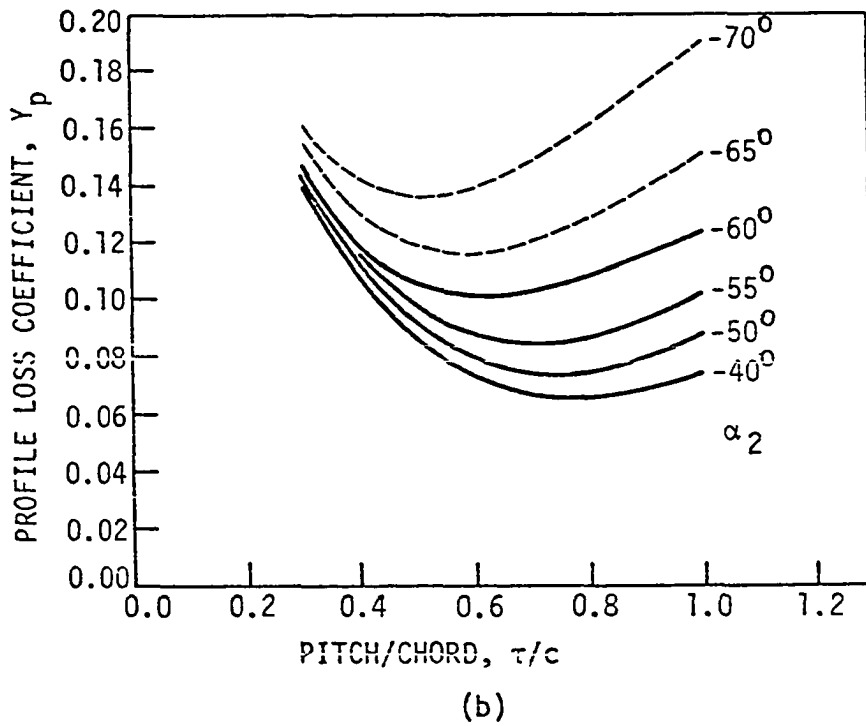
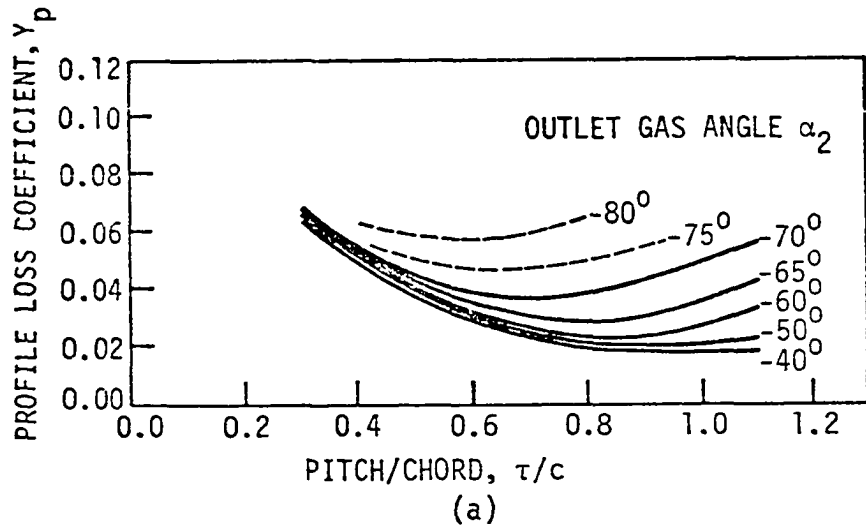


Figure 2.1. Profile-loss coefficients for conventional turbine airfoils in cascade at zero incidence. $t/c = 20$ percent; $R_c = 2 \times 10^5$; $M < 0.6$.
 (a) nozzle cascades $\alpha_1 = 0$
 (b) impulse cascades $\alpha_1 = \alpha_2$
 (From Ainley and Mathieson (1955))

where all the Y_p 's are taken at constant τ/c and exit gas angle (α_2). If the gas angles are given by the velocity triangles and a value of thickness/chord (t/c) is assumed, Eqn. 2.1 may be used in conjunction with Fig. 2.1 to construct a curve of Y_p against τ/c . From this, the τ/c value for minimum losses can be determined. For off-design purposes Ainley and Mathieson also give a procedure to estimate the stalling incidence and the profile loss coefficients over a wide range of incidence. Attention is called to the fact that the correlations were developed from data with low inlet turbulence, whereas the real machine may see turbulence levels of 5 to 20 per cent. The correlations probably indicate losses which are too low for small turning (extensive laminar flow) and too high for large turning (premature laminar separation).

b) Dunavant and Erwin (1956) undertook a systematic testing of two-dimensional turbine cascades which were designed by applying the NACA airfoil design methods. Four of the primary (reaction) airfoils (design cambers 65, 80, 95, and 110 deg.) and one of the secondary (impulse) airfoils (camber 120 deg.) were tested in cascade at low speeds with τ/c values of 0.667 and 0.556. Some of the testing was done at high speed also.

The induced flow angle ($\Delta\theta_{ind}$), which is defined as the change in flow direction of the stagnation streamline from far upstream to the leading edge, and the deviation angle (δ) were determined for optimum design condition (minimum losses) as functions of inlet gas angle (α_1)

and camber angle (θ_c) for fixed values of τ/c . The results for $\Delta\theta_{ind}$ and δ are shown in Fig. 2.2 for a τ/c of 0.667.

In the selection process, the cascade is found by determining the design camber angle θ_c for given values of gas deflection ($\alpha_1 - \alpha_2$), α_1 , and τ/c . The process is an iterative one in which the camber angle is first guessed and a better estimate obtained from

$$\theta_c = \Delta\theta_{ind} + \delta + (\alpha_1 - \alpha_2). \quad (2.2)$$

To obtain design airfoil cambers for τ/c values different from those tested, an interpolation between α_1 , θ_c , and τ/c can be made.

The comments made regarding inlet turbulence level in the correlations of Ainley and Mathieson also apply in this case. Furthermore, Farn and Whirlow (1975) (among others) have found that the high speed tests of Dunavant and Erwin were not strictly two-dimensional.

2.3. Design Methods for Two-Dimensional Airfoils in Cascade

There appears to be unanimous consensus among turbomachinery designers to classify two-dimensional cascade design methods as either "indirect" or "direct" methods. There is also a tendency among designers to think of cascade selection methods not as simply selection procedures, but as design approaches as well. However, selection methods are not design methods in the full sense of the word since they do not involve airfoil profile shaping.

The "indirect" design approach consists of selecting the kind of boundary layers to be produced on the airfoil surfaces and deriving from

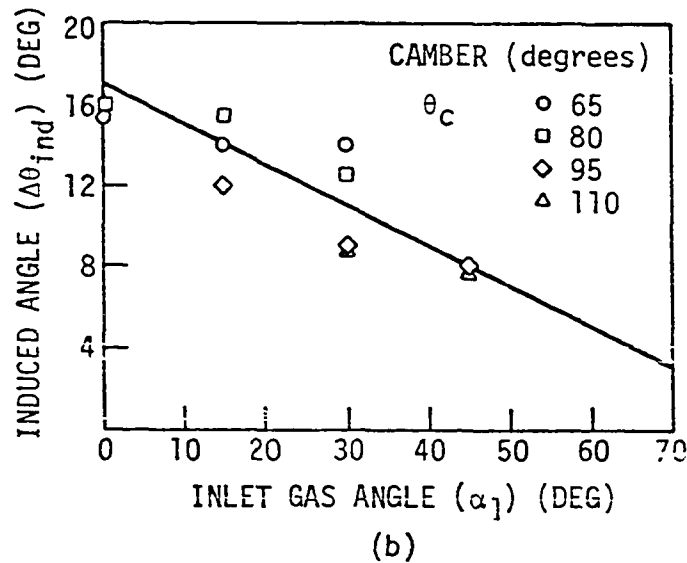
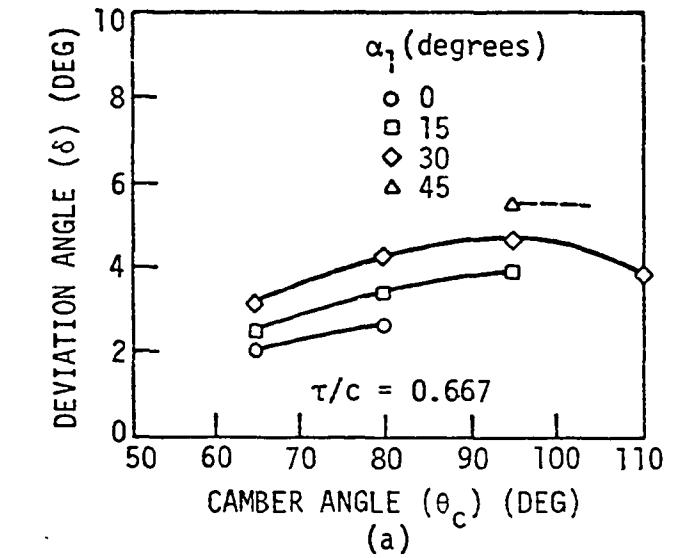


Figure 2.2. Turbine cascade performance
 (a) Deviation angle as function of inlet flow angle, camber angle and space to chord ratio for primary series.
 (b) Induced angle as function of inlet flow angle, camber angle and space to chord ratio for primary series.
 (From Dunavant and Erwin (1956)).

them the velocity distribution which will generate these boundary layers. The airfoil profile is then determined by solving the inverse inviscid potential flow problem. Cascades designed with the "indirect" method are usually called prescribed velocity distribution (PVD) cascades. Extensive work on this approach has been carried out at the von Karman Institute by Le Foll (1965), who developed an "indirect" method using a dissipation-integral boundary layer calculation procedure. This method is applicable to cascades for incompressible flow. Huo (1972) later extended Le Foll's method to compressible flow. Papailiou (1970) successfully applied Le Foll's method to the design of high turning axial flow compressor blades. More recently, Henderson (1978) has reported on an "indirect" design technique developed in the United States, and Boiko and Kozhevnikov (1978) have presented some of the Russian work on "indirect" design procedures as applied to turbine cascades. Schmidt (1980) reported an "indirect" method developed in Germany applicable to supercritical compressor and turbine cascades.

The "direct" design approach, on the other hand, involves a sequence of calculations in which the airfoil profile in cascade is arbitrarily designed from velocity diagram requirements, followed by an inviscid flow calculation of the velocity distribution. A transitional boundary layer analysis is then carried out followed by a wake mixing analysis to estimate the profile losses. The initial profile design can be rapidly iterated on through adjustment of a number of profile geometry parameters and the flow analysis repeated until a profile design

is found yielding the lowest profile losses. The "direct" method is gaining in popularity with the appearance of fast computer codes to perform the different calculations required. Examples of "direct" design systems have been reported by Monello et al. (1979) and by Thomas and Piendel (1974).

A rapid interactive design procedure to generate the geometry of turbine cascades from velocity triangles is described in the following paragraphs. The procedure represents the basis for the efficient implementation of an overall "direct" design system.

2.4. The Two-Dimensional Turbine Cascade Geometry Design

Two computer programs were developed during the course of this investigation to actually design the two-dimensional geometry for turbine cascades in an interactive fashion. The first of these programs, GDPLS, sets up and solves a linear system of equations for the cascade geometry; the second program, GDPNLS, obtains the solution by setting and solving a nonlinear system of equations. The design of the geometry is concluded with an analysis of the flow passage cross-sectional area through the cascade (see Appendix A).

Continuity in curvature of the profile for the designed airfoil is highly important. This is, in general, difficult to attain. Engeli et al. (1978), however, describe a method for turbomachinery airfoil design in which continuity in curvature is satisfied everywhere by using Bernstein polynomials. The computer codes described herein use third

and fourth order polynomials to fit segments of the profile to a given set of geometric conditions describing the cascade. Continuity in curvature is achieved everywhere except at the tangency points on the leading and trailing edge circles. The defining functions for the upper and lower sides of the airfoil should be single valued between tangency points.

2.4.1. Description of input for geometry design programs GDPLS, GDPNLS

Thirteen geometric parameters are required as input by the profile design programs GDPLS and GDPNLS. These parameters are described below in connection with Fig. 2.3.

An x-y coordinate system is used; the y axis passes through the cascade leading edge and the x axis through the center of the trailing edge circle. All distances in the input are normalized, for ease of graphing on axial chord.

The input geometric parameters are:

- RLE Radius of leading edge circle
- RTE Radius of trailing edge circle
- B_x Axial chord
- H/L Height-to-length ratio (a measure of stagger)
- β_1^* Metal angle at leading edge (measured from downward pointing vertical)
- $\Delta\beta_1^*$ Wedge angle between tangents drawn to the leading edge circle
- β_2^* Metal angle at trailing edge
- $\Delta\beta_2^*$ Wedge angle between tangents drawn to the trailing edge circle

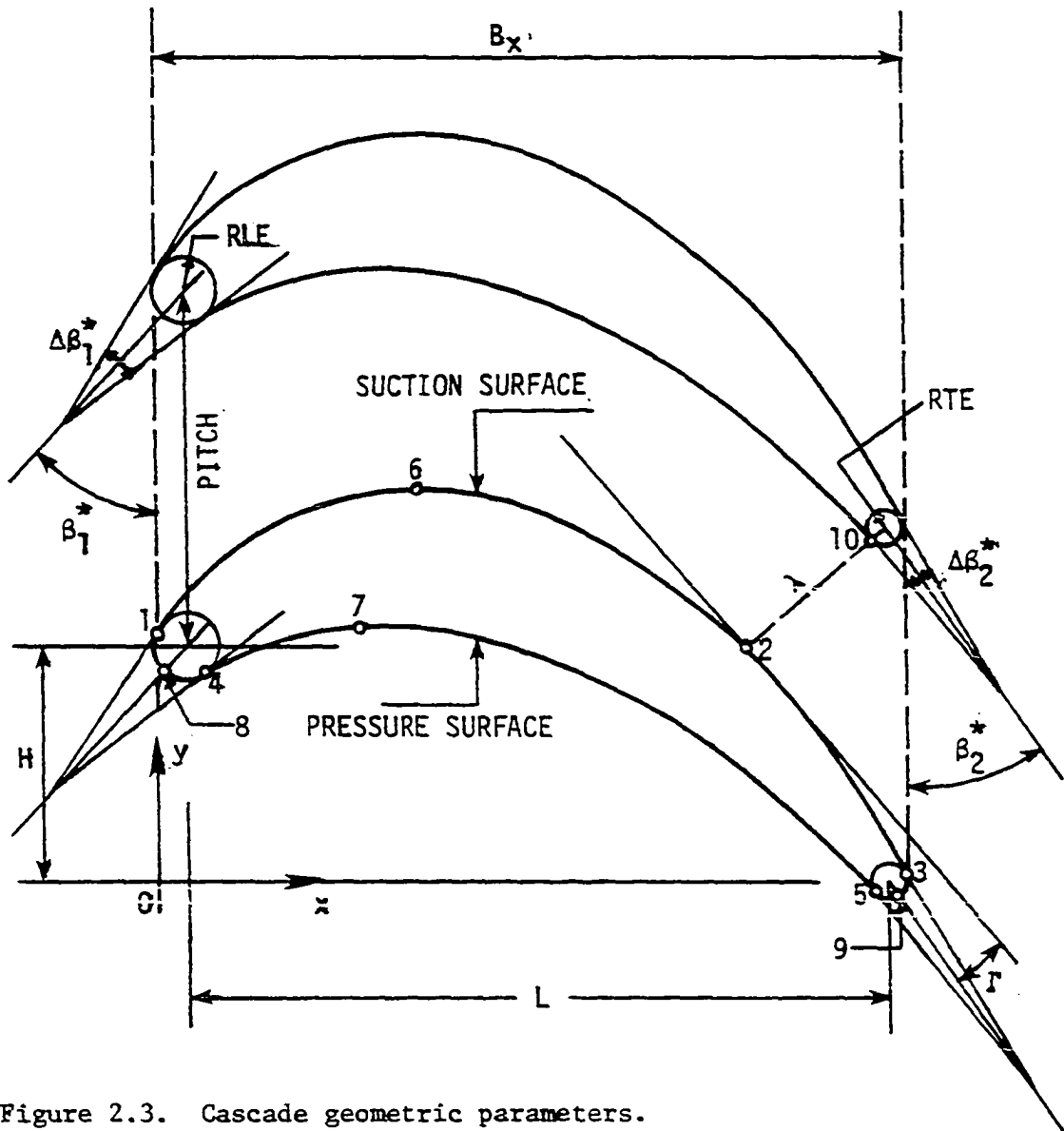


Figure 2.3. Cascade geometric parameters.

- (6) Upper surface defining point (optional)
- (7) Lower surface defining point (optional)
- τ Pitch
- β_λ Gaging angle ($\sin^{-1} \lambda/\tau$)
- Γ Uncovered turning; the difference between the profile angle at point (2) and the leaving metal angle β_2^* (required by GDPLS only)
- $(d^2y/dx^2)_6$ Second derivative at point (6) (required by GDPNLS only)

2.4.2. Airfoil profile solution

As already stated, either program GDPLS or GDPNLS can be used for cascade airfoil design.

Experience with program GDPLS (utilizing a fast linear solution) has shown that almost any turbine cascade can be easily and rapidly designed. Program GDPNLS (a slower nonlinear solution) may be resorted to whenever imposed geometric constraints are such that GDPLS yields unsatisfactory solutions. Also, fine profile adjustments can be achieved with GDPNLS.

GDPLS uses Gaussian elimination to solve a 13 x 13 linear system of equations for the upper surface and an 8 x 8 linear system for the lower surface of the profile. The solution must be carried out in double precision to avoid numerical errors inherent to the Gaussian elimination procedure. The order of the polynomials used between indicated profile points are:

(1) to (6)	4th order	}	upper surface
(6) to (2)	3rd order		
(2) to (3)	3rd order		
(4) to (7)	3rd order	}	lower surface
(7) to (5)	3rd order		

The 13 needed conditions to set up the system of equations for the upper surface are:

- y_1, s_1 (slope) are known
- y_6, s_6 , and second derivative match at (6), y_6 is known
- y_2, s_2 , and second derivative match at (2), y_2 and s_2 are known
- y_3, s_3 are known.

The eight conditions for the lower surface are:

- y_4, s_4 (slope) are known
- y_7, s_7 , and second derivative match at (7), y_7 is known
- y_5, s_5 are known.

If the auxiliary point (6) is not used (entered in the input as zero), GDPLS sets up a 9×9 linear system of equations for the upper surface.

The polynomials with this option are

(1) to (2)	4th order	}	upper surface
(2) to (3)	3rd order		

and the nine conditions are

y_1, s_1 (slope) are known

y_2, s_2 , and second derivative match at (2), y_2 and s_2 are known

y_3, s_3 are known.

Similarly, if the defining point (7) on the lower surface is not used (entered in the input as zero), a 4 x 4 linear system of equations is solved for the lower surface. The order of the polynomial is

(4) to (5) 3rd order } lower surface

and the four conditions are

y_4, s_4 are known

y_5, s_5 are known.

GDPNLS solves a 15 x 15 nonlinear system of equations for the upper surface by means of the Newton-Rhapson method. The lower surface is calculated in the same manner as in the linear solution, and the defining point (7) option is also available. The polynomials used between indicated profiles are:

(1) to (6) 4th order }
 (6) to (2) 4th order } upper surface
 (2) to (3) 3rd order }

The 15 conditions for the upper surface are:

y_1, s_1 (slope) are known

y_6 , s_6 , and second derivative match at (6),
 y_6 , s_6 , and $(d^2y/dx^2)_6$ are known at (6)
 y_2 , s_2 , and second derivative match at (2)
 point (2) is on the throat tangency circle
 s_2 equals s_2 calculated from the throat tangency circle
 y_3 and s_3 are known.

The 15 unknowns in this case are the 14 coefficients of the polynomials plus the y coordinate at the throat point (y_2). As can be observed, the system becomes nonlinear because the coefficients of the polynomials depend on y_2 which is also unknown.

2.4.3. Determination of input for geometry design programs GDPLS, GDPNLS

The design of an airfoil in cascade from given velocity triangle requirements involves, to begin with, tentative selection of geometrical parameters to set up the profile for the design analysis process. It is likely in practical design applications that other aerodynamic, cooling or structural constraints supplied from design requirements or preliminary analyses will have to be observed in arriving at a final design. The airfoil and cascade parameters to be selected along with guidelines or recommendations for values are discussed below. These, of course, are general comments only. In particular applications, the selection procedure and parameter ranges may be substantially altered, the final decisions resting with the inviscid blade-to-blade and profile boundary

layer analyses of the proposed design as outlined in Fig. 1.1. Also, Fig. 2.3 should be referred to for the airfoil and cascade geometrical parameters. It may be helpful in getting started to make a proposed layout, by hand, of the airfoil in its cascade arrangement.

The cascade can be designed normalized with respect to axial chord, B_x , since the actual size of the airfoil is only needed for the analysis of the boundary layer. Therefore, the decision on the actual value of B_x , which bears directly on the amount of frictional losses, is postponed until later in the procedure. The design can be initiated by selecting a pitch to axial chord ratio, τ/B_x , from loading considerations. In the expression for loading coefficient ψ_T given below, the gas angles are given and a value of ψ_T is selected from design experience:

$$\psi_T = 2 \frac{\tau}{B_x} \sin^2 \beta_2 (\cot \beta_1 + \cot \beta_2). \quad (2.3)$$

Therefore, τ/B_x can be solved for from Eqn. 2.3. Typical values for ψ_T can range from 0.6 to 1.2 with the final choice being determined by the satisfactory performance of the cascade. Zweifel (1945) suggested 0.8 as an optimum loading coefficient for the turbine cascades of that time.

A value of H/L can now be selected which determines the camber distribution and stagger of the airfoil. This parameter plays a role, along with wedge angle $\Delta\beta_1^*$, in determining the channel area variation with chord and has, therefore, an effect on loading distribution.

The cascade gaging angle, β_λ , is determined from given exit gas angle and Mach number (β_2, M_2) using experimental correlations

accounting for flow deviation, such as presented later in Chapter 3. The cascade throat or gaging length λ is calculated from

$$\lambda = \tau \sin\beta_\lambda. \quad (2.4)$$

Next, the cascade metal angles can be selected. The inlet metal angle, β_1^* , coincides with the inlet gas angle given by the velocity triangles if the flow incidence is not taken into account. Usually, however, β_1^* is assigned so that the flow is accepted with negative incidence (or over-camber) of about 5° to establish a margin from leading edge overspeeding on the airfoil suction side. The exit metal angle, β_2^* , is determined by applying a gas angle deviation criterion derived from design experience, or from published correlations, as influenced by exit Mach number and gaging angle.

The leading and trailing edge radii selection may now be undertaken. The trailing edge radius, RTE, is dictated by manufacturing or airfoil cooling requirements, and by trailing edge blockage considerations. In general, the following relation should be observed:

$$0.03 < \frac{2 \text{ RTE}}{2 \text{ RTE} + \lambda} < 0.08. \quad (2.5)$$

The leading edge radius, RLE, generally tends to increase with blade loading and turning, with the following restrictions observed in its selection:

$$\text{RTE} < \text{RLE} < 0.1 B_x \quad (2.6)$$

and

$$\frac{\text{RLE}}{\tau \sin\beta_1} < 0.1. \quad (2.7)$$

The wedge angles, $\Delta\beta_1^*$, $\Delta\beta_2^*$, and the auxiliary points (x_6, y_6) , (x_7, y_7) on the suction and pressure sides are determined in a trial and error procedure to give an acceptable airfoil shape. These variables strongly influence the cross channel area variation and therefore the airfoil pressure distribution. Design experience shows, for example, that $\Delta\beta_2^*$ should be kept in the range 0 to 10 degrees.

The uncovered turning, Γ , directly controls the diffusion between the throat and trailing edge on the suction surface. For exit Mach numbers less than 0.8, the effect of uncovered turning on losses is small. However, for exit Mach numbers higher than 0.8 the effect is severe. In general, Γ is in the neighborhood of 2 to 10 degrees. Experience with the design programs has shown that uncovered turning strongly influences the profile shape and can be used to tune the suction side of the airfoil and the pressure distribution for a given set of geometrical parameters.

2.4.4. Operation of geometry design programs, GDPLS, GDNLS

The geometry design programs are operated in an interactive mode by which the input geometric parameters are adjusted according to intermediate results put out by the programs upon the request of the user.

The acceptability of the design of the airfoil profile for a given set of input geometric parameters is first determined by analyzing a graphical display of the cascade. Profile smoothness is sought in this first test. Turn-around-time of the graphical display should be a

minimum for efficient operation. A subsequent test is made on the sign and value of the second derivatives along the airfoil profile to establish the final acceptability of the design. The upper (suction) side should be convex, i.e., d^2y/dx^2 should be negative along the entire suction side. The lower (pressure) side should be convex around the leading edge, then concave, and then convex again around the trailing edge, i.e., d^2y/dx^2 should be positive, then negative, and then positive again along the pressure side. Smooth variation of the derivative values should also be sought. A final test is made on the variation of channel area ratio, A/A_λ , with axial chord. This variation should be reasonably smooth and monotone for an acceptable pressure distribution to exist on the airfoil.

More details on the operation of the program can be found in Alarcon (1980) which is a guide to the user on the operation of the geometry design package and the complete analysis program.

2.4.5. Examples of turbine cascade designs

Four turbine cascade designs obtained with program GDPLS are presented below. The first two of these examples involved the design and redesign of a gas turbine blade cascade. The last two examples constitute the design of an inlet guide vane and an impulse blade cascade for steam turbine applications.

Figure 2.4 is the computer generated graph of the resultant design of a gas turbine blade cascade, designated as GAI-ISU. This cascade,

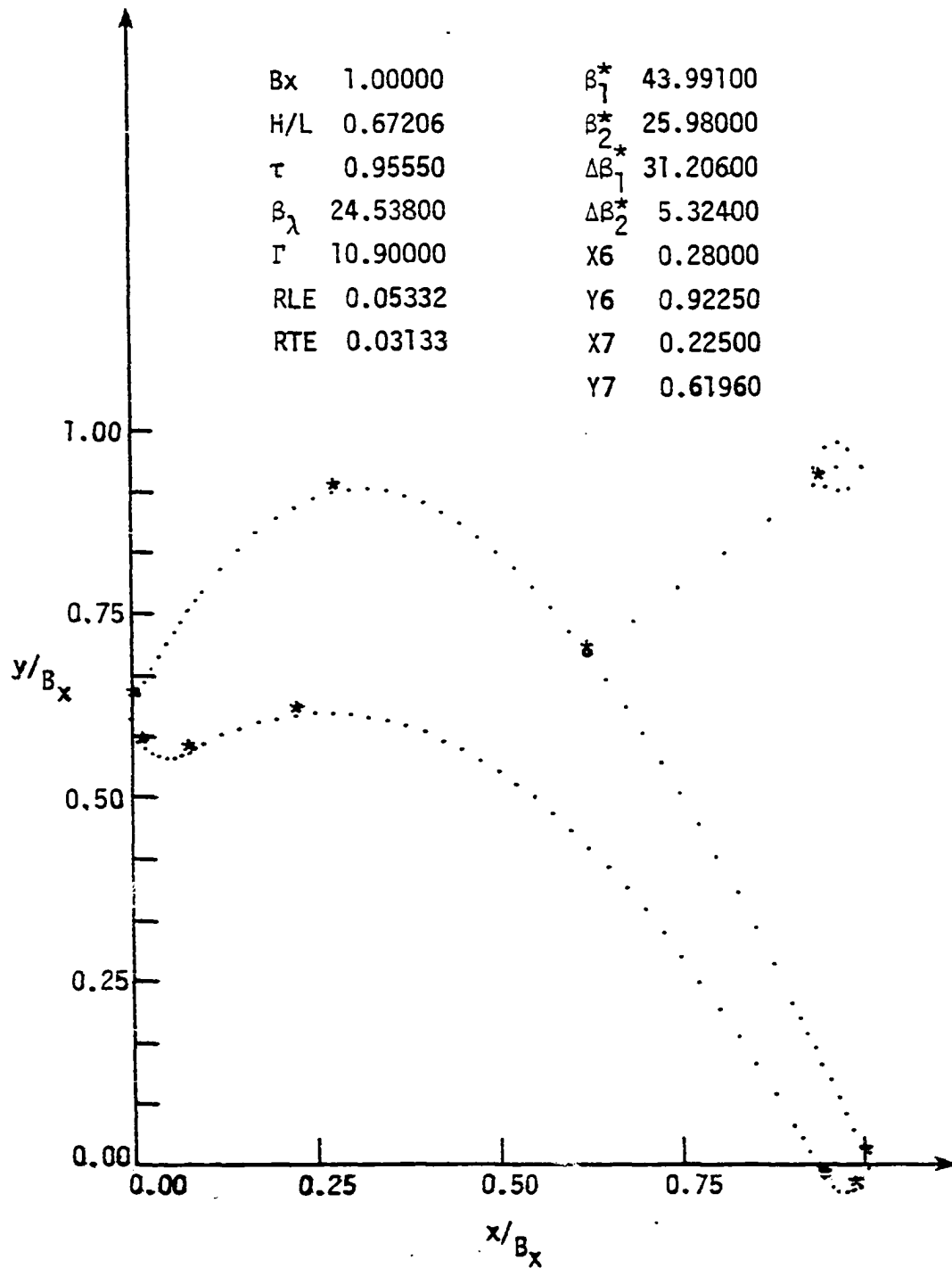


Figure 2.4. Gas turbine blade cascade design GA1-ISU.

which was designed for loading coefficient $\psi_T = 1.12$ and 0° degrees incidence, is typical of a first-blade cascade for a high-pressure cooled turbine. The design data used with program GDPLS are also listed in Fig. 2.4.

A redesign of cascade GA1-ISU to adjust the loading distribution, with same loading coefficient and incidence, to obtain a rearward-loaded airfoil (designated GA2-ISU) is shown in Fig. 2.5. The revised loading distribution was achieved by adjusting the coordinates of the suction side auxiliary point (x_6, y_6) . Slight adjustments were also made on the gaging angle β_λ and the uncovered turning Γ . The results of incompressible inviscid flow calculations for the two designs are presented in Fig. 2.6, along with the channel area variation for both designs. As can be observed, the rearward loading was indeed accomplished for GA2-ISU. Also, the pressure distribution was improved in GA2-ISU where the recompression after the velocity peak on the suction side has been decreased, therefore reducing the possibility of boundary layer separation. The channel area variation is seen to be smoother and more monotonic in GA2-ISU than in GA1-ISU.

The inviscid calculations were performed with the global and leading-edge reanalysis programs developed during the present investigation and reported on in Chapters 3 and 4.

Figures 2.7 and 2.8 display the computer generated graphs and the GDPLS program input data for the inlet guide vane cascade GA3-ISU (designed for $\psi_T = 0.62$ and zero incidence) and the impulse blade cascade

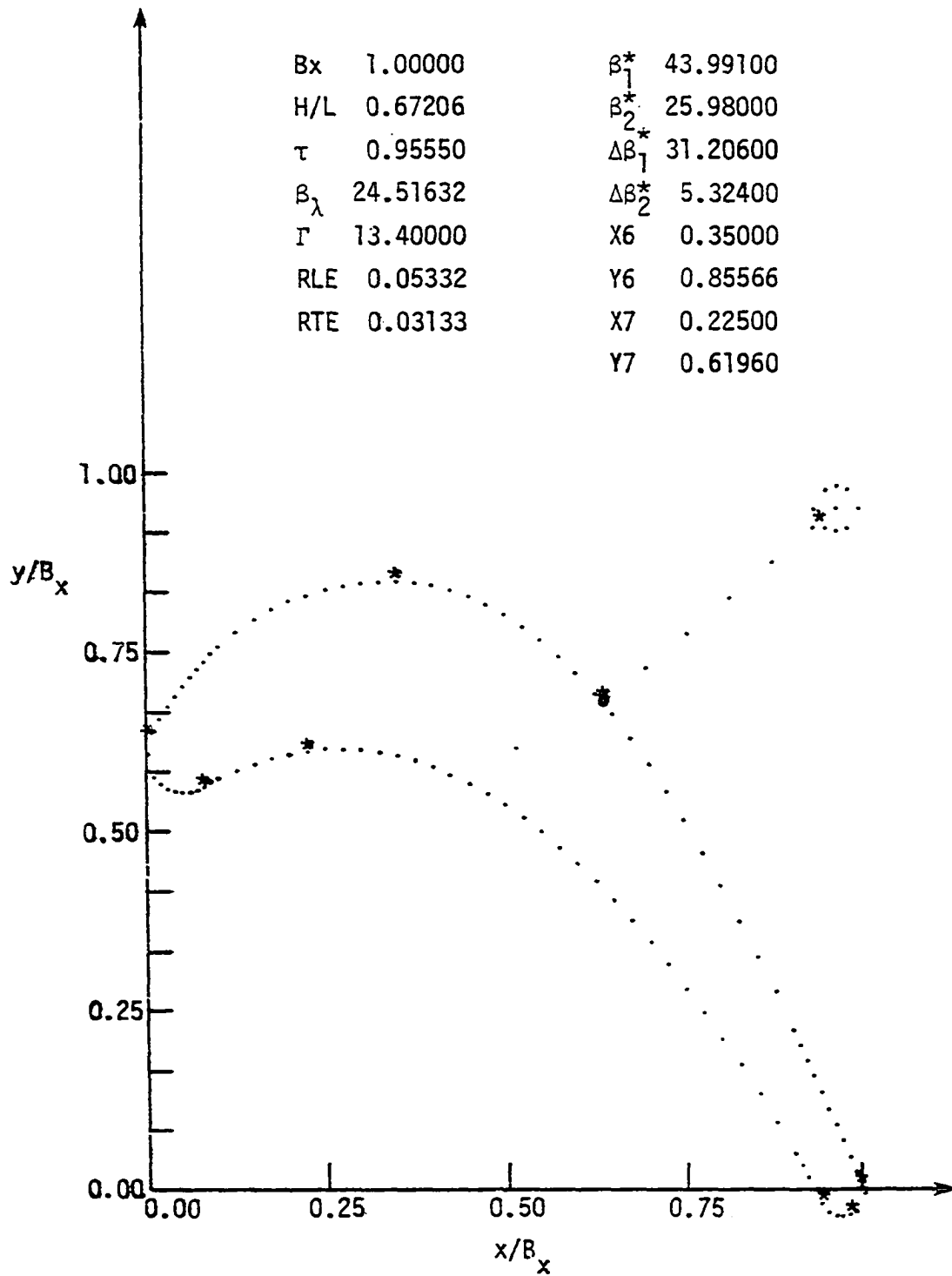


Figure 2.5. -Gas turbine blade cascade redesign GA2-ISU.

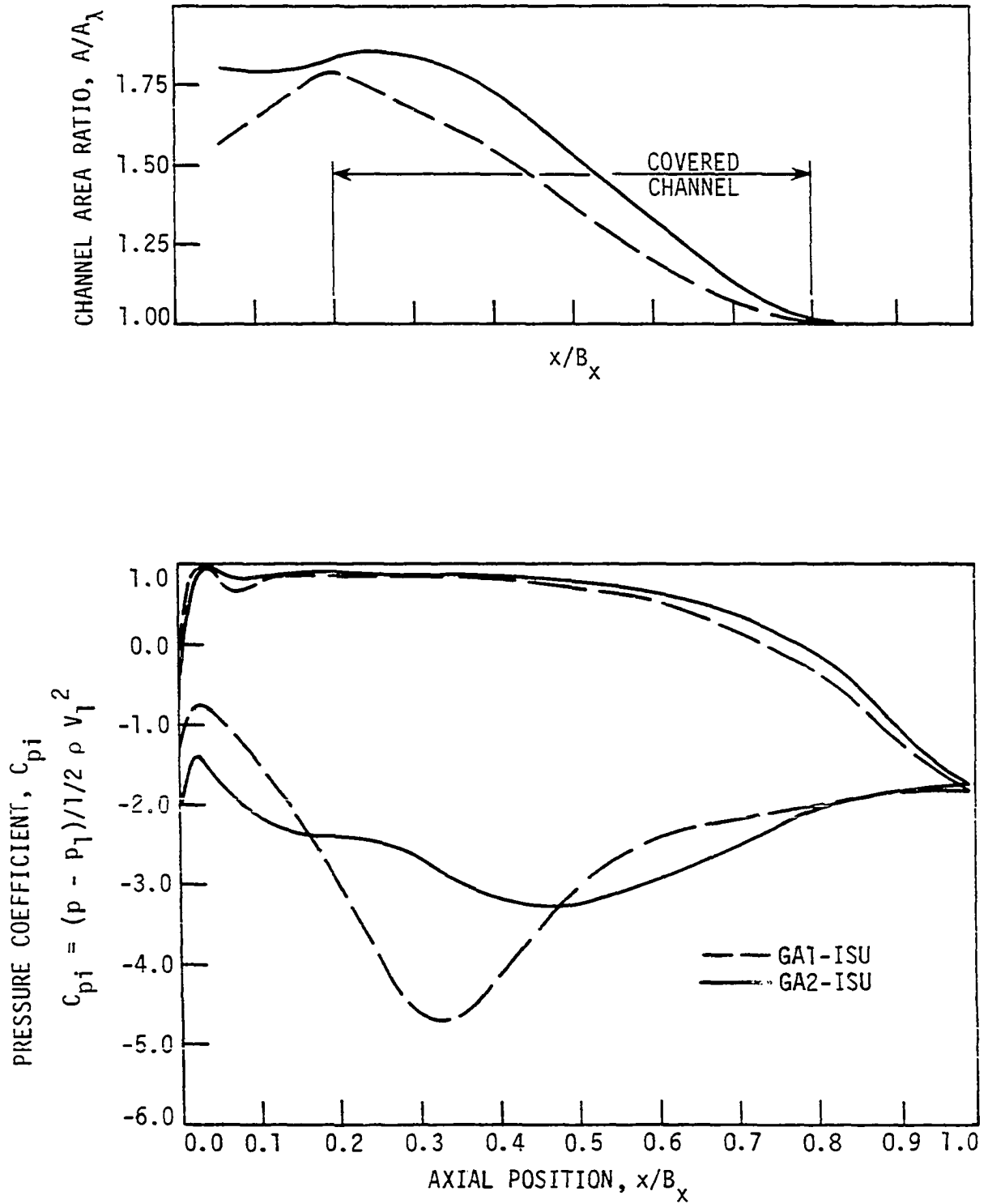


Figure 2.6. Comparison of calculated airfoil pressure distribution and channel area variation for cascade designs GA1-ISU and GA2-ISU.

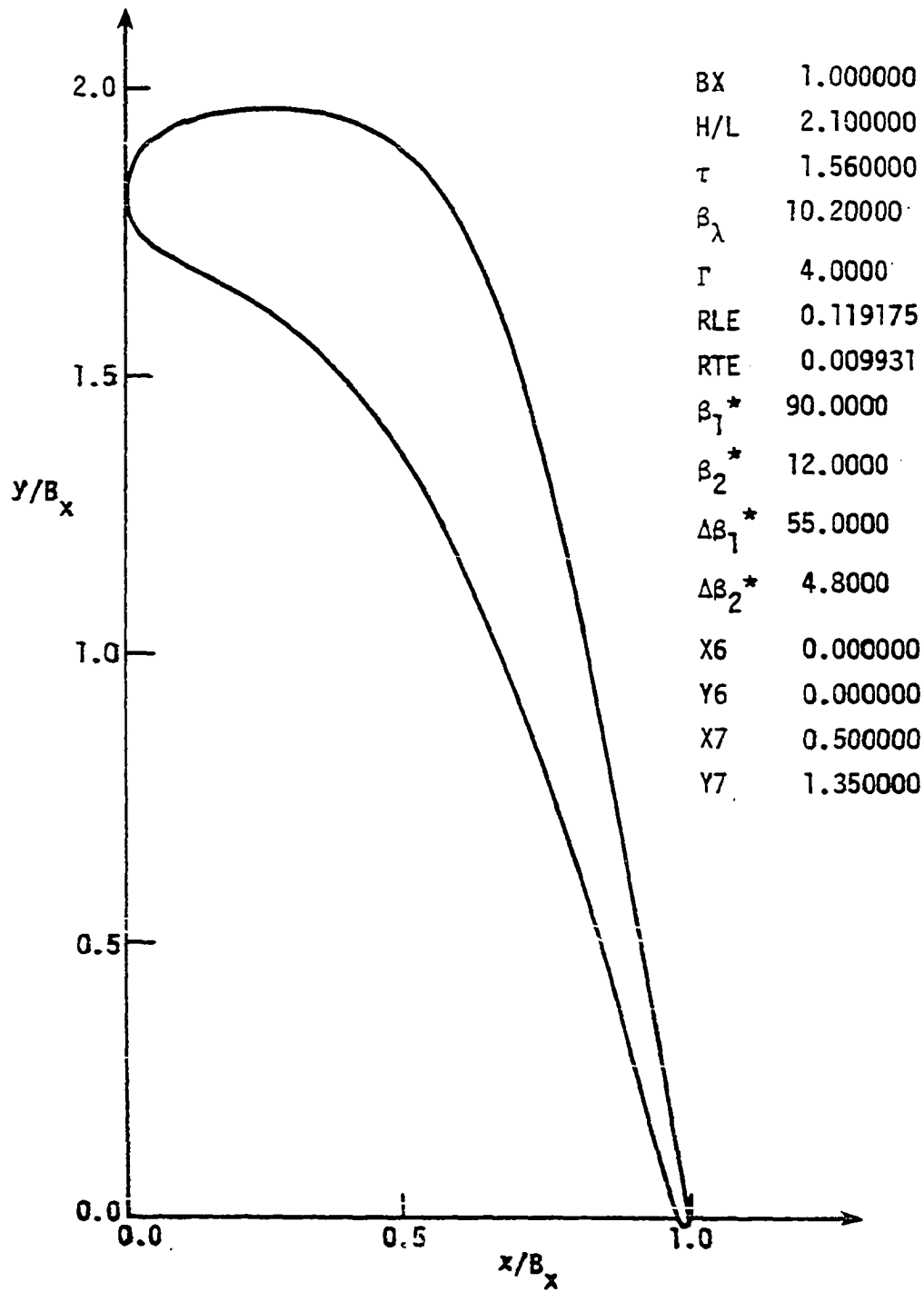


Figure 2.7. Inlet guide vane cascade design GA3-ISU.

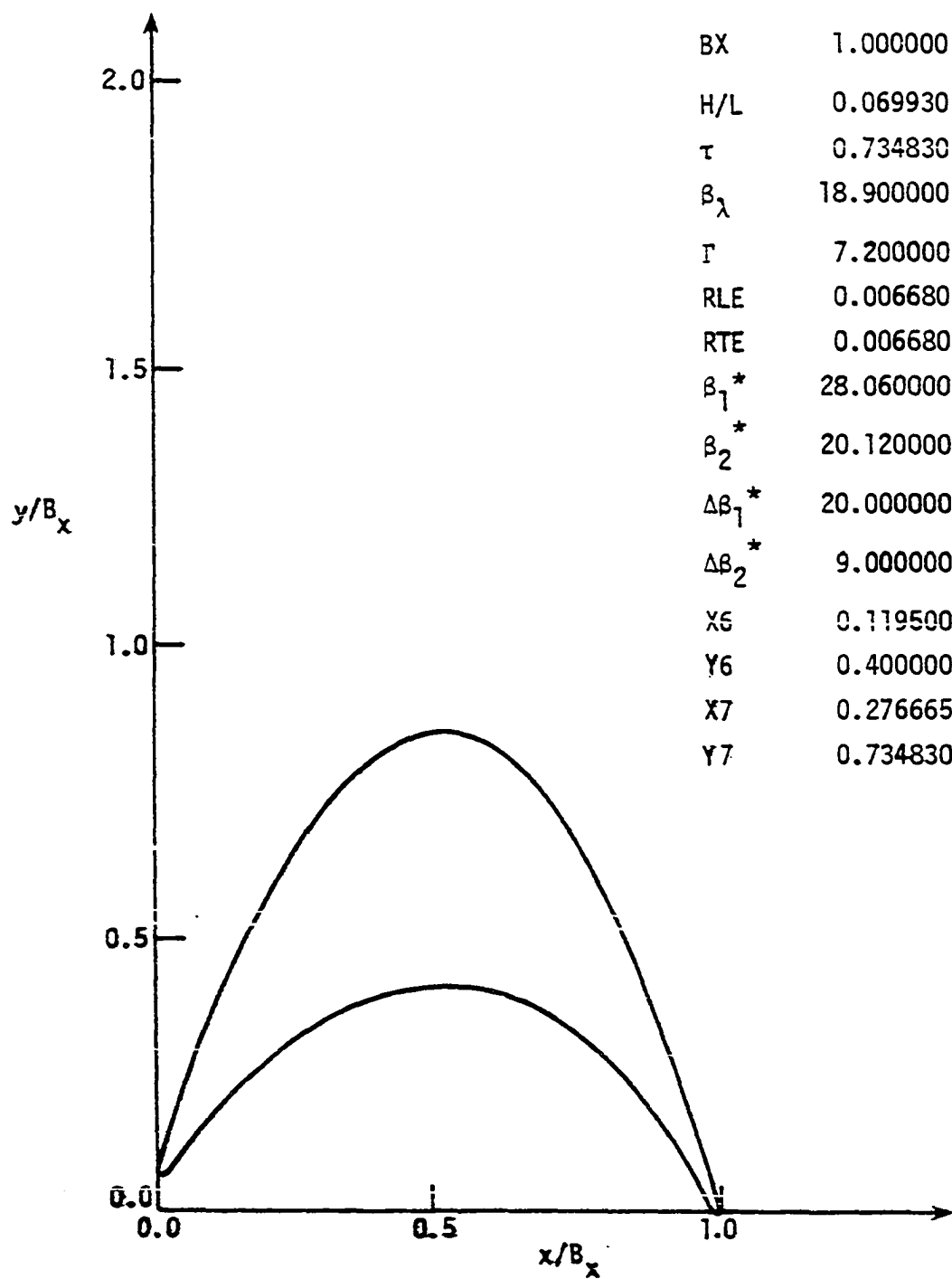


Figure 2.8. Impulse blade cascade design GA4-ISU.

GA4-ISU (designed for $\psi_T = 0.80$ and zero incidence) for a steam turbine first stage.

3. GLOBAL INVISCID ANALYSIS

3.1. Introduction

The streamline curvature prediction procedure developed in this investigation for steady, two-dimensional compressible and adiabatic cascade flow is described. Results obtained with this method for several example cascade flows are compared with theoretical solutions and experimental data to illustrate the development and general applicability of the method.

The objective of the streamline curvature analysis was to provide a global inviscid (preliminary) analysis of blade-to-blade flows used in conjunction with cascade geometry design procedures. A detailed reanalysis of the flow around the airfoil leading edge followed by a profile boundary layer analysis then completed the overall cascade design scheme.

The streamline curvature method was selected because of its general applicability to cascade analysis for high subsonic to transonic flow situations. It is essential for cascade design applications that such a global analysis provide rapid and accurate solutions over a range of Mach number for arbitrary flow conditions and cascade geometries. These capabilities have been met in the programmed streamline curvature analysis (SCA). Convergence acceleration and highly accurate numerical approximation techniques have been used for the iterative solutions involved. To begin the chapter, a review of recent inviscid flow analysis methods for high subsonic and transonic cascade flows is made.

3.2. Review of Recent Blade-to-Blade Flow Calculation Methods

Solutions to the "direct" problem of subsonic and transonic inviscid flow calculations in a blade-to-blade plane or in a cascade are reviewed in this section. Gostelow (1973) and Hansen (1976) have already surveyed these methods emphasizing incompressible and high subsonic solutions. The attempt here is to complement this previous work by extending the review to transonic solutions reported in the last several years.

Many transonic calculation methods have been presented in the literature for both external and internal flows; however, only those procedures developed for the particular problem in hand are surveyed, i.e., hodograph, matrix, time-marching, space-marching, and streamline curvature methods for blade-to-blade flow analysis.

3.2.1. Hodograph methods

The hodograph technique solves the steady state inviscid equations of motion by mapping the cascade region into a hodograph plane and solving the transformed equations there. The flow velocity components are used as independent variables, and the stream function as the main dependent variable. This choice of variables makes the hodograph techniques especially suitable for solving the "indirect" design problem.

Several hodograph methods have been developed in the past. Some of the recent ones are those of Garabedian and Korn (1971), Hobson (1974),

and Ives and Liutermoza (1977). Also Collyer (1977) has extended the method of Garabedian and Korn to include the effects of a boundary layer and wake.

The hodograph method usually allows high accuracy in the range from low speed to flows with embedded supersonic regions; however, difficulties often arise in transforming the solution back to the physical plane. Decreased pitch chord ratio, for example, makes cascades increasingly difficult to map. Another problem arises when two points in the physical plane have different values of stream function but the same velocity and flow direction. This is called a "double mapping" problem, in which case representation cannot be made by a single hodograph plane.

3.2.2. Matrix methods

The matrix technique involves an early algebraic combination of the inviscid steady state equations of continuity and momentum. The result is a second order differential equation in which the dependent variable is either the stream function or the velocity potential. The flow region of interest is covered by a computational grid and an algebraic equation obtained for every central grid point by using finite-difference or finite-area approximations. The resulting system of nonlinear equations is written in matrix form and solved by iterative matrix inversion techniques.

Matrix methods based on stream function have been successful in solving incompressible and subsonic flow problems; however, these methods

are not successful for general transonic flow problems due to the ambiguity of the density-stream function relationship at transonic conditions. The stream function differential equation has both a subsonic and a supersonic solution for given derivatives of the stream function. The inability of the method to choose for itself the appropriate root limits applicability to subsonic flow. Some of the recent applications of stream function matrix techniques to cascades have been reported by Katsanis (1969), Miller (1973), Smith and Frost (1970), Davis (1971), Silvester and Fitch (1974), who presented an "indirect" design matrix method, and Calvert and Smith (1976).

The difficulties with the stream function formulation in transonic flow are overcome by using the velocity potential instead. The solution of the velocity potential differential equation is single valued in both subsonic and supersonic flow; therefore, the density-velocity potential relationship is unique in the transonic regimes. Dodge (1976), and later Caspar et al. (1979), have presented velocity potential matrix techniques which have been successful in calculating transonic flows.

3.2.3. Time-marching methods

The unsteady inviscid flow equations (Euler equations) are solved in the time-marching approach to reach a steady state solution as the asymptotic limit of transient flow calculations.

The first time-marching methods successfully applied to transonic cascade flows were those of Gopalakrishnan and Bozzola (1971) and McDonald (1971). The former made use of MacCormack's finite difference

technique, whereas McDonald employed an integral representation of the equation over each computational element and named it a "finite area" technique. More recently, Denton (1975) has simplified and improved the finite area method of McDonald.

Kurzrock and Novick (1975) solved the time dependent Navier-Stokes equations in a time-marching fashion by using the MacCormack finite difference scheme. This method allows the presence of viscous shock waves in the flow field since the Navier-Stokes equations are treated.

Delaney and Kavanagh (1976) were the first in applying a time-dependent method of characteristics to calculate transonic cascade flows.

Time-marching methods are not limited to potential flows; however, great difficulty exists in imposing simultaneously all cascade boundary conditions. Also, a great many time steps are usually required before a steady state solution is reached with extensive computing time needed.

3.2.4. Space-marching methods

Space-marching methods solve the steady state inviscid equations by a finite difference, iterative, forward-marching integration scheme which assumes the flow situation to be "partially parabolic" (see Pratap and Spalding (1976)).

The space-marching denomination derives from the solution procedure which moves from one cross section computational line to the next in the downstream direction. Several sweeps of the flow domain are made from upstream to downstream to reach a converged solution.

Singhal and Spalding (1976) developed and applied this method to the calculation of subsonic or transonic flow in axial-flow turbomachinery cascades. The method is more economical in computer time and storage than are time-marching procedures.

3.2.5. Streamline curvature methods

Streamline curvature methods are characterized by the solution of the inviscid equations of motion and continuity in separate iterative steps. The equations are not algebraically combined in the process and are independently applied and satisfied in successive iterations. A floating computational grid is formed by the streamlines and by either lines normal to the flow or by pitchwise lines, i.e., the so-called "quasi-orthogonals."

Bindon and Carmichel (1971) chose to work with normals to the flow. This approach simplifies the form of the equations and also allows the calculation of isentropic supersonic flow. The computation is made difficult, however, since the location of the normals is not known beforehand, resulting in long computing times.

The use of "quasi-orthogonals," on the other hand, complicates the form of the equations but greatly facilitates the computing process. This approach appears to offer advantages over the streamline curvature method using normals due to the short running times made possible by applying convergence acceleration techniques. One of the first operational procedures using "quasi-orthogonals" was reported by Katsanis (1965).

However, two main problems were encountered: first, no theoretical basis was presented to estimate an optimum damping factor for convergence, and second, the locations of the stagnation streamlines were not calculated from periodicity conditions but were estimated from constancy of angular momentum considerations. The method of Smith and Frost (1970), using "quasi-orthogonals" was also subject to convergence problems in the same sense as was the method of Katsanis, but the locations of the stagnation streamlines were calculated, although convergence obtained on periodicity conditions was poor.

Wilkinson (1972) improved on the "quasi-orthogonal" methods by presenting theoretical means of calculating an optimum damping factor and by calculating the location of the stagnation streamlines with excellent convergence on periodicity conditions. Novak (1978) closely followed Wilkinson's approach, the only difference being that in his method the exit gas angle is not calculated but must be given as input.

A combined computational procedure developed by Katsanis (1969) uses the matrix solution for subsonic flows with the streamline curvature method taking over for transonic flows. This procedure has been extensively used in the United States for hub-to-tip solutions as well as for blade-to-blade flow solutions.

In general, the objectives of the streamline curvature method appear to be the efficiency of operation and the capability to handle transonic flow. The success of the method in transonic calculations can be attributed to the separate stepwise solution procedure for the

momentum and continuity equations, and to the use of a density relationship in terms of enthalpy and velocity instead of in terms of stream function derivatives.

3.3. The Present Streamline Curvature Method (SCA)

The present streamline curvature method for plane cascade adiabatic flow solution is an implementation of techniques using "quasi-orthogonals" (q -os) recommended by Wilkinson (1972). The primary emphasis has been to account for compressibility effects up to slightly (shock free) transonic pockets in the flow, and for stream sheet thickness change from cascade inlet to outlet. The cascade inviscid exit gas angle is predicted from periodicity conditions by requiring equal velocities at the trailing edge. Alternatively, the exit gas angle may be an input condition to the calculation, in which case the determined surface velocities at the trailing edge will not generally be equal. This latter option is probably more useful in calculating transonic trailing edge flows where, as shown by Forster (1964), the presence of shock waves often destroys flow periodicity in this region.

3.3.1. Governing equations

The governing equations to be solved are the velocity gradient equation and the continuity equation. The velocity gradient relationship along a q -o, which for this application coincides with the y -axis (see Fig. 3.1.), is obtained by combining the equations of momentum, energy and entropy in the following way:

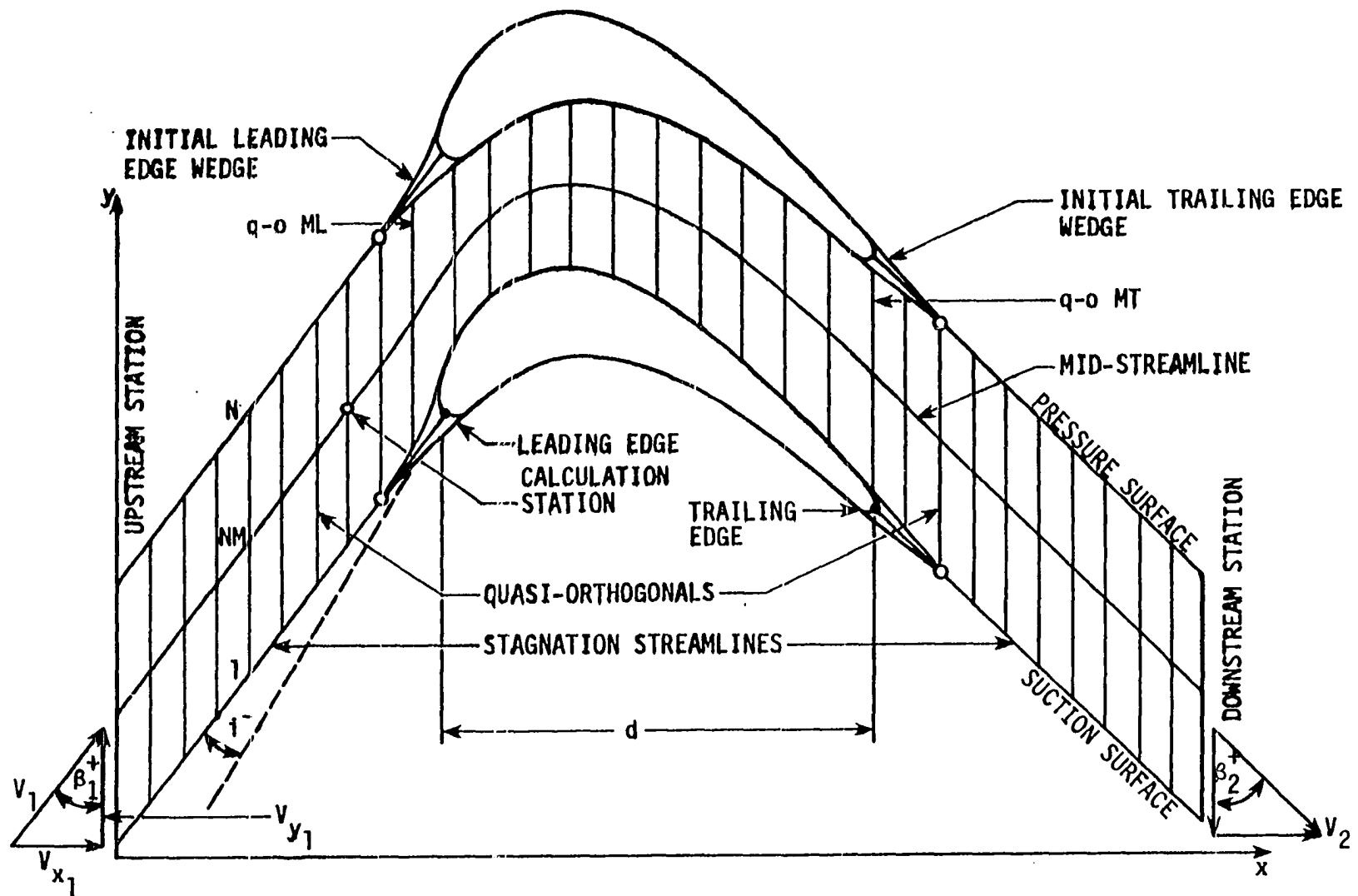


Figure 3.1. Cascade flow field for streamline curvature calculation.

The momentum equation along a q-o is

$$v_x \frac{\partial v_y}{\partial x} + v_y \frac{\partial v_y}{\partial y} = - \frac{1}{\rho} \frac{\partial p}{\partial y} . \quad (3.1)$$

The energy and entropy equations are, respectively

$$h_0 = h + \frac{v^2}{2} \quad (3.2)$$

$$T \frac{\partial s}{\partial y} = \frac{\partial h}{\partial y} - \frac{1}{\rho} \frac{\partial p}{\partial y} . \quad (3.3)$$

Elimination of the static enthalpy gradient, $\frac{\partial h}{\partial y}$, between Eqns. 3.2 and 3.3 gives the expression

$$- \frac{1}{\rho} \frac{\partial p}{\partial y} = T \frac{\partial s}{\partial y} - \frac{\partial h_0}{\partial y} + v \frac{\partial v}{\partial y} . \quad (3.4)$$

Equations 3.1 and 3.4 are now used to eliminate the pressure gradient, resulting in the velocity gradient relationship

$$v \frac{\partial v}{\partial y} = v_x \frac{\partial v_y}{\partial x} + v_y \frac{\partial v_y}{\partial y} + \frac{\partial h_0}{\partial y} - T \frac{\partial s}{\partial y} . \quad (3.5)$$

Since the total derivative along a streamline of the y component of velocity can be written as

$$v \frac{dv_y}{d\ell} = v_x \frac{\partial v_y}{\partial x} + v_y \frac{\partial v_y}{\partial y} \quad (3.6)$$

then Eqn. 3.5 for the velocity gradient becomes

$$v \frac{\partial v}{\partial y} = v \frac{dv_y}{d\ell} + \frac{\partial h_0}{\partial y} - T \frac{\partial s}{\partial y} . \quad (3.7)$$

The following assumptions are now made regarding the total enthalpy and entropy gradients in Eqn. 3.7:

- (i) The gas angle and total and static conditions are uniform at the upstream station (see Fig. 3.1). Therefore, $\frac{\partial h_0}{\partial y} = 0$. The total enthalpy gradient, therefore, is zero throughout the flow field since the flow is isoenergetic.
- (ii) Entropy gradients due to losses within the airfoil boundary layers are neglected, i.e., $\frac{\partial s}{\partial y} = 0$. This assumption, however, does not preclude entropy gradients in the x direction which can be modeled via a total pressure loss distribution in this direction.

With these assumptions, Eqn. 3.7 becomes simply

$$\frac{\partial V}{\partial y} = \frac{dV}{dl} \cdot y \quad (3.8)$$

With definition of the angle β of the streamline as shown in Fig. 3.2, the velocity gradient equation (Eqn. 3.8) is written in its final form as

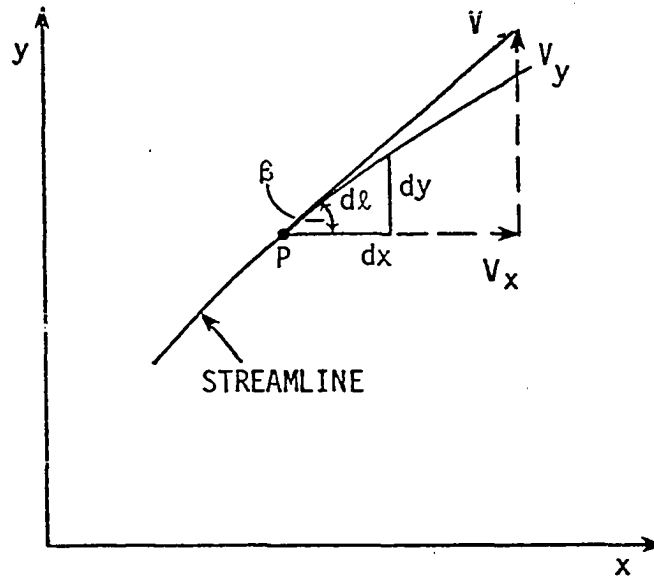
$$\frac{\partial V}{\partial y} = \cos\beta \left(\frac{dV}{dx} \frac{dy}{dx} + V \frac{d^2 y}{dx^2} \right) \quad (3.9)$$

The continuity equation to be solved in conjunction with Eqn. 3.9 is developed by considering the plane stream surface to have a thickness Δz . The mass flow rate crossing any q-o is then

$$\dot{m} = \int_{y_1}^{y_N} \rho V \cos\beta \Delta z dy \quad (3.10)$$

Equation 3.10 is more useful written in mass velocity form as

$$\bar{m} = \frac{\dot{m}}{\Delta z(y_N - y_1)} \quad (3.11)$$



$$\cos \beta = \frac{dx}{d\ell} = \frac{V_x}{V} \quad \tan \beta = \frac{V_y}{V_x} = \frac{dy}{dx}$$

Figure 3.2. Geometric relations used in derivation of the velocity gradient equation.

The term Δz takes into account any variation in the stream sheet thickness in the x direction.

The local total pressure for a q-o is given by

$$P_0 = P_{01} - \Delta p_0 \quad (3.12)$$

where Δp_0 is the assigned total pressure loss from inlet to the q-o as estimated from experimental cascade data. The local total and static densities are calculated then, assuming the fluid to be a perfect gas, by the relations

$$\rho_0 = \frac{\gamma}{(\gamma - 1)} \frac{P_0}{h_0} \quad (3.13)$$

$$\rho = \rho_0 \left(1 - \frac{v^2}{2h_0} \right)^{\frac{1}{\gamma-1}} \quad (3.14)$$

Equation 3.14 enables the static density to be found in Eqn. 3.11 to obtain the mass velocity.

3.3.2. Computational flow field

The computational flow field for the global streamline curvature calculation is shown in Fig. 3.1. The field is extended a distance d upstream and approximately a distance d downstream of the cascade to satisfy flow uniformity conditions at the upstream and downstream stations. The distance d is the axial distance between the defined leading and trailing edges of the airfoil.

The floating computational grid is formed by streamlines and uniformly spaced q-os which extend in the y (pitchwise) direction.

The grid obtains its floating character from the fact that the streamline positions in the x-y plane are not known in advance. The streamlines are determined by the computation, changing position from one iteration to the next. The main advantages of this computation grid are:

- (i) Arbitrarily shaped or irregular boundaries, such as those for airfoil surfaces, can be handled in a convenient and accurate way.
- (ii) The q-os are particularly suited for imposing the periodic boundary conditions outside the cascade passage.

The total number of q-os (M) is divided evenly between the upstream, cascade passage, and downstream regions. The q-o just ahead of the leading edge is q-o number ML ; the q-o passing through the trailing edge is q-o number MT . The spacing is arranged so that the leading edge lies midway between q-o ML and q-o $ML+1$. The total number of streamlines (N) must be an odd number. The mid-streamline is streamline number NM .

The positions of the upstream stagnation streamlines are approximated at the beginning of the calculation by extending them as straight lines from the airfoil leading edge at an angle equal to the inlet gas angle. Similarly, the downstream stagnation streamlines are extended from the airfoil trailing edge at an angle equal to the exit metal angle. The stagnation streamlines are subsequently "shaped" in the calculation to satisfy flow periodicity in the pitchwise direction.

The leading edge and trailing edge wedges shown in Fig. 3.1 for the computational field are used to speed up convergence of the streamline curvature solution, especially at the leading edge. These wedges extend over q -os ML and ML-1 at the leading edge, and over q -os MT+1 and MT+2 at the trailing edge. The wedges follow along with the stagnation streamline shaping.

The initial wedges are determined by fairing in pressure and suction side stagnation streamlines with the airfoil profile. Smoothing procedures described later are used for the fairing process. It was found that eight smoothing passes produced no further changes in the formed wedges.

The periodicity condition for the q -os involved with the wedges is handled by requiring equal velocities on the intersection of the q -os with the initial wedges.

For the programmed streamline curvature analysis (SCA), the trailing edge wedge was finally abandoned because it tended to move the location of the cascade throat in the downstream direction.

In the program, 39 q -os and 9 streamlines are used for solutions.

3.3.3. General description of calculation

A general discussion of the streamline curvature solution procedure framing the details of the calculation is presented. An accompanying flow diagram of the procedure is given in Fig. 3.3. Complete description of the details of the calculation procedure is given later in this chapter.

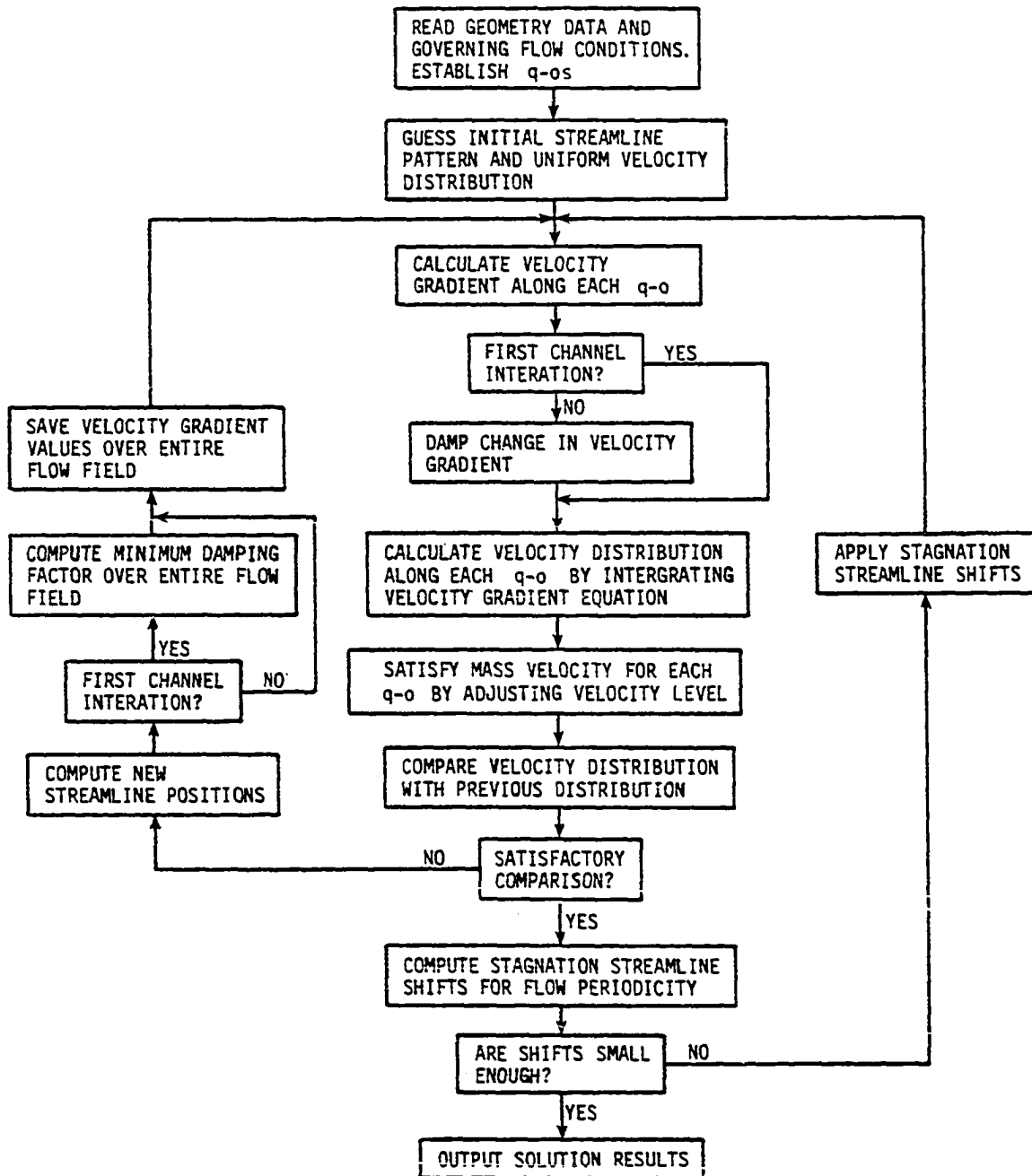


Figure 3.3. Overall computing flow diagram for the global streamline curvature analysis (SCA).

The streamline curvature method for cascade flow analysis consists of two main iteration loops. The first, or inner loop, called herein the "channel" solution, solves the velocity gradient and continuity equations inside the channel formed by given stagnation streamlines and the cascade passage. The second or outer loop corrects the stagnation streamline shapes in order for flow periodicity to be achieved at the end of the next "channel" solution. The steps in the two iteration loops are the following:

1. Airfoil geometry and governing upstream and downstream flow conditions are supplied. Also, total pressure loss and stream sheet thickness distribution are given. The initial stagnation streamlines and the $q-o$ locations are calculated.

2. An initial guess of the streamline pattern is made based on uniform spacing along the $q-os$ and a constant V along the streamlines is assumed throughout.

3. The right hand side of the velocity gradient equation (Eqn. 3.9) is evaluated and a matrix of velocity gradient values determined and stored.

4. Equation 3.9 is then integrated by starting with the mid-streamline velocity $V_{i,NM}$ from the previous iteration (initial guess in the first iteration) and using the trapezoidal rule to proceed in both directions along a $q-o$ finding the new velocity distribution from suction to pressure surface. The integration is carried out for each $q-o$. It is not necessary to recalculate $\partial V/\partial y$ until the

iteration on continuity is complete and a new set of streamlines found. The new velocities allow the static density to be calculated along the q-os and the mass velocity computed with Eqn. 3.11.

5. In general, the calculated mass velocity at a particular q-o will not satisfy the specified mass velocity. The level of the velocity distribution along the q-o must then be increased or decreased as required, and the process of calculating the static densities and mass velocity repeated until continuity is satisfied. The iteration on continuity then moves to the next q-o downstream and so on, until q-o number M is reached. The new velocity distribution is now compared with the old. If these distributions are very similar the "channel" solution is assumed converged and the calculation proceeds with the outer loop.

6. If the "channel" solution failed to converge, the streamline pattern is recalculated from the new velocity distribution found along the q-os and based on a constant percentage of the mass flow between adjacent streamlines.

7. With the new velocity distribution and streamline pattern, a matrix of predicted velocity gradients is obtained. A damping factor is calculated (in the first iteration of the channel solution) to damp the change in velocity gradients from iteration to iteration. The objective of this damping is to reduce the initial errors (made with the first velocity distribution and streamline pattern) to zero in the least number of iterations. A new matrix of velocity gradient values is determined based on the damped differences between the predicted and old values before integrating Eqn. 3.9 again in step 4.

8. If the "channel" solution converged in step 5, the shifts in stagnation streamlines are calculated in order to achieve flow periodicity at the end of the next "channel" solution. The calculation is then continued in step 3 if the magnitude of the shifts are larger than a prescribed tolerance. Otherwise, the streamline curvature calculation is considered converged.

9. With SCA converged, a momentum-pressure balance is performed in the tangential direction. This procedure, described in Appendix B, checks the computed pressure distribution against velocity triangles.

In the programmed method (SCA) the following limits were placed on the number of iterations for each iterative procedure:

- (i) Continuity (for a ζ -o); 50 iterations
- (ii) Channel solution; 50 iterations
- (iii) Outer loop; 20 iterations.

Also, the following tolerances were used:

- (i) Continuity; $\Delta V \leq 0.001$ ft/s
- (ii) Channel solution; $\left[\frac{V_{i,j}^{\text{new}} - V_{i,j}^{\text{old}}}{\bar{V}_i} \right] \leq 0.0008$

The channel solution is not required to converge to 0.0008 in the first few outer loops since the initial stagnation streamline shapes are incorrect. The tolerance was programmed as a function of the number of outer loop iterations, reducing from 0.004 for the first outer loop to 0.0008 after about 10 outer loops.

- (iii) Outer loop; $\delta_j \leq 0.005 B_x$.

3.3.4. Continuity equation solution

The convergence of the continuity calculations at each particular q-o was found to be a key factor in the overall computing time required for a given problem. To improve the convergence rate, the techniques presented by Novak (1978) were, therefore, implemented in this investigation. As a result, the computing time requirements were cut by about half.

As already stated in the general description, a given velocity distribution obtained from the integration of the velocity gradient equation will not immediately satisfy the specified mass velocity; an increment ΔV must be added or subtracted, as required, at all points along the q-o. Wilkinson (1972) found the variation of calculated mass velocity \bar{m} with respect to V in the form

$$\frac{d\bar{m}}{dV} = \cos\beta_{NM} \frac{d(\rho V)_{NM}}{dV} \quad (3.15)$$

where the subscript NM means "on the mid-streamline." Equations 3.14 and 3.15 then yield

$$\frac{d\bar{m}}{dV} = \left\{ \cos\beta \rho_0 \left[1 - \frac{\gamma+1}{\gamma-1} \frac{V^2}{2h_0} \right] \left[1 - \frac{V^2}{2h_0} \right]^{(2-\gamma)/(\gamma-1)} \right\}_{NM} \quad (3.16)$$

and ΔV can be calculated from

$$\frac{d\bar{m}}{dV} = \frac{\bar{m}_{\text{specified}} - \bar{m}_{\text{calculated}}}{\Delta V} \quad (3.17)$$

For q-os on which the Mach number may reach or exceed 1.0, Wilkinson suggested the evaluation of $d\bar{m}/dV$ at all points on the q-o to find

$$\frac{d\bar{m}}{dV} = \frac{1}{(y_N - y_1)} \int_{y_1}^{y_N} \cos\beta \frac{d(\rho V)}{dV} dy. \quad (3.18)$$

Wilkinson's reasoning in proposing Eqn. 3.18 was that if the q-o intersects a supersonic patch at a high inclination with the streamlines, the velocity could be subsonic at both ends and supersonic in the middle and still not be choked. Thus, the $d\bar{m}/dV$ calculated on the mid-streamline may not be a good indicator of choking for the q-o.

Equations 3.15 and 3.18 have worked satisfactorily in reducing ΔV to a small value in the problems treated in this investigation; however, in some cases it was found that the predicted ΔV tended to oscillate about zero as smaller and smaller values of ΔV were approached. As a result, the procedure, although close to convergence, usually exceeded the allowed number of iterations without converging to the required tolerance. Novak's (1978) scheme wherein ΔV is bracketed and further refined was implemented to solve this problem. The procedure is explained below in connection with high subsonic solutions for mass velocity. The argument is completely analogous for the case of supersonic solutions.

1. If $d\bar{m}/dV < 0$, the initially chosen V_{NM} is on the supersonic branch of the function $\bar{m}(V)$. Since a subsonic solution is being considered, it is necessary to move toward the subsonic branch.

This is accomplished by letting

$$\Delta V = -0.1 V_{NM} \quad (3.19)$$

2. If $d\bar{m}/dV > 0$, then ΔV is given by Eqn. 3.17.

3. The extreme values of V_{NM} (high and low) encountered on the subsonic branch by applying ΔV are retained as bracketing values and revised as further calculations of ΔV are made. In addition, if a new V_{NM} is calculated outside the range defined by the current bracketing values, it is discarded and taken at the midpoint of the range. The plausible range is in this way continually refined. The decision on a V_{NM} value as an upper or lower bracket value is made by comparing the calculated \bar{m} with the required value.

A special comment is in order here concerning the prediction of choking in high Mach number solutions. The Mach number is so sensitive to area variation near $M=1$ that choking was always predicted with the first guessed streamline pattern. This problem was eliminated by not allowing the q -os to choke during the first four outer loop iterations. This approach worked well for the transonic and high Mach number cases treated in this investigation.

3.3.5. Stability and convergence

The usual approach in streamline curvature calculations is to damp the change in streamline position from one iteration to the next to prevent divergence of the calculation process. Wilkinson (1972), however, recommended that the change in velocity gradient be damped instead of the change in streamline position when calculating blade-to-blade flows. This approach was followed in the present investigation.

The details of the optimum damping factor derivation for plane

cascade flow are reported in Alarcon and Kavanagh (1980). The relevant aspects of the derivation and the main results are presented here.

An optimum damping factor is formulated in the context of the following formula:

$$\left. \frac{\partial v}{\partial y} \right|_n = \left. \frac{\partial v}{\partial y} \right|_o + f' \left[\left. \frac{\partial v}{\partial y} \right|_p - \left. \frac{\partial v}{\partial y} \right|_o \right] \quad (3.20)$$

where

$\left. \frac{\partial v}{\partial y} \right|_n$ = the damped "new" value of velocity gradient to be used
in a succeeding iteration

$\left. \frac{\partial v}{\partial y} \right|_o$ = the "old" value of velocity gradient used in the previous
iteration

$\left. \frac{\partial v}{\partial y} \right|_p$ = the "predicted" value of velocity gradient resulting as
an undamped value from the previous iteration

f' = optimum damping factor.

Wilkinson's important contribution to streamline curvature calculations was the development of an analytical formulation for the optimum damping factor, i.e., a damping factor which reduces the initial errors (made with the first velocity field and streamline pattern) to zero in a least number of iterations. The flow model for the stability analysis is shown in Fig. 3.4 where the exact solution is a uniform inclined flow in the x-y plane and the exact values of $\partial v / \partial y$ are zero. A theoretical perturbation of the flow is introduced by collectively displacing the streamlines in such a way that the change introduced in the velocity gradient is of the form

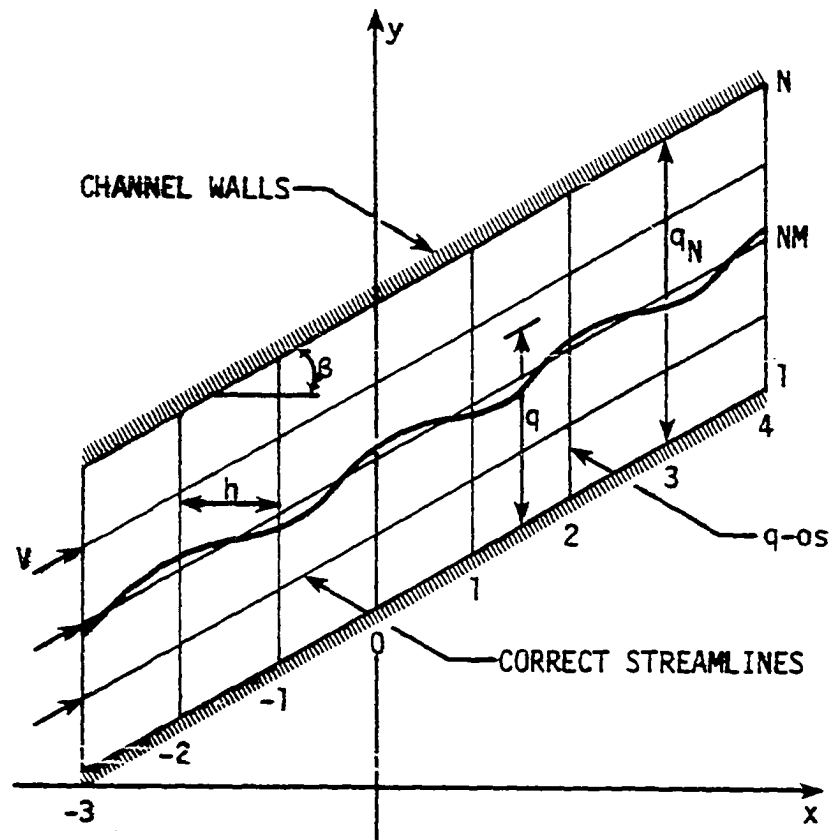


Figure 3.4. Flow model for stability analysis.

$$\Delta \frac{\partial V}{\partial y} = K \frac{4}{2} (q \ q_N - q^2) \cos \frac{2\pi}{\lambda} (x). \quad (3.21)$$

Attention is focused on the mid-streamline and on $q=0$ zero.

Equation 3.21 is integrated to yield the perturbed velocity distribution, and the continuity equation is used to calculate the new position of the mid-streamline. The velocity gradient equation (Eqn. 3.9) then provides the calculated perturbed value of $\partial V/\partial y$ where the inaccuracies of the numerical approximation are taken into account. This is the numerical $\partial V/\partial y$ on the mid-streamline and $q=0$ zero which can be compared with the value K from Eqn. 3.21. The change in $\partial V/\partial y$ due to the numerical calculation is therefore

$$\Delta \frac{\partial V}{\partial y} = \left[\frac{\partial V}{\partial y} \right]_{\text{num}} - K \quad (3.22)$$

or

$$\Delta \frac{\partial V}{\partial y} = -K \left[1 - \frac{\frac{\partial V}{\partial y}}{K} \right]_{\text{num}}. \quad (3.23)$$

The zero velocity gradient can be retrieved at the end of the numerical calculation if the calculated change in $\partial V/\partial y$ is equal and opposite in sign to that introduced by Eqn. 3.21, i.e., $-K$. The initial error can then be reduced to zero by factoring the calculated change in velocity gradient by

$$f = \frac{1}{\left[1 - \frac{\frac{\partial V}{\partial y}}{K} \right]_{\text{num}}}. \quad (3.24)$$

The following result is obtained when the algebra is carried out for the flow model in Fig. 3.4:

$$f = \frac{1}{1 - \frac{5}{48} k (1-M^2) \cos^2 \beta A^2} \quad (3.25)$$

The factor "k" in Eqn. 3.25 takes into account the accuracy with which the second derivative d^2y/dx^2 can be numerically calculated and is considered in detail later. "A" is the grid aspect ratio, i.e., q_N/h . It should be noted that k is negative, so $f \leq 1$ in subsonic flow.

Wilkinson (1970) argued that a general displacement from the correct velocity gradient could be represented as a Fourier series of all wavelengths. Since k depends on the ratio of wavelength to q-o spacing, as will be shown later, the different harmonics would be corrected by different amounts depending on k, the most unstable being the one with the largest negative k (k_{\min}). Therefore,

$$f = \frac{1}{1 - \frac{5}{48} k_{\min} (1-M^2) \cos^2 \beta A^2} \quad (3.26)$$

The calculation diverges when f is such that it causes the k_{\min} harmonic to overshoot to an error in velocity gradient of equal magnitude but opposite sign. This f is just twice that value required to reduce the error to zero; therefore, the critical damping factor for convergence, f_c , is

$$f_c = 2f. \quad (3.27)$$

Wilkinson (1970) further calculated the optimum damping factor, f' , by which in one iteration the errors for the k_{\min} and $k=0$ harmonics are

reduced by factors $(f'/f-1)$ and $(1-f')$ respectively. For equal reduction of errors for these two harmonics

$$1 - f' = \frac{f'}{f} - 1 \quad (3.28)$$

or

$$f' = \frac{2f}{1+f} \quad (3.29)$$

Therefore,

$$f' = \frac{1}{1 - \frac{5}{96} k_{\min} (1-M^2) \cos^2 \beta A^2} \quad (3.30)$$

The initial error in the velocity gradient is obviously reduced by the factor $(1-f')^n$ after n iterations. Therefore, for a ratio of final to initial error of 0.01, the number of iterations required is

$$n = \frac{-4.61}{\ln(1-f')} \quad (3.31)$$

In the programmed method, f' is determined at each calculation station (the intersection of a streamline with a $q=0$) using the local Mach number and gas angle β . The smallest value is subsequently used to damp the whole flow field. Use of the smallest f' causes the more stable stations to be overdamped and therefore convergence is ensured.

Figure 3.5 portrays the behavior of the optimum damping factor, f' , critical damping factor, f_c , and number of iterations, n , when f' is used. The k_{\min} in Fig. 3.5 is normalized by $k_{\min} = -1.88$ for a differentiation method using a quartic through five points with double

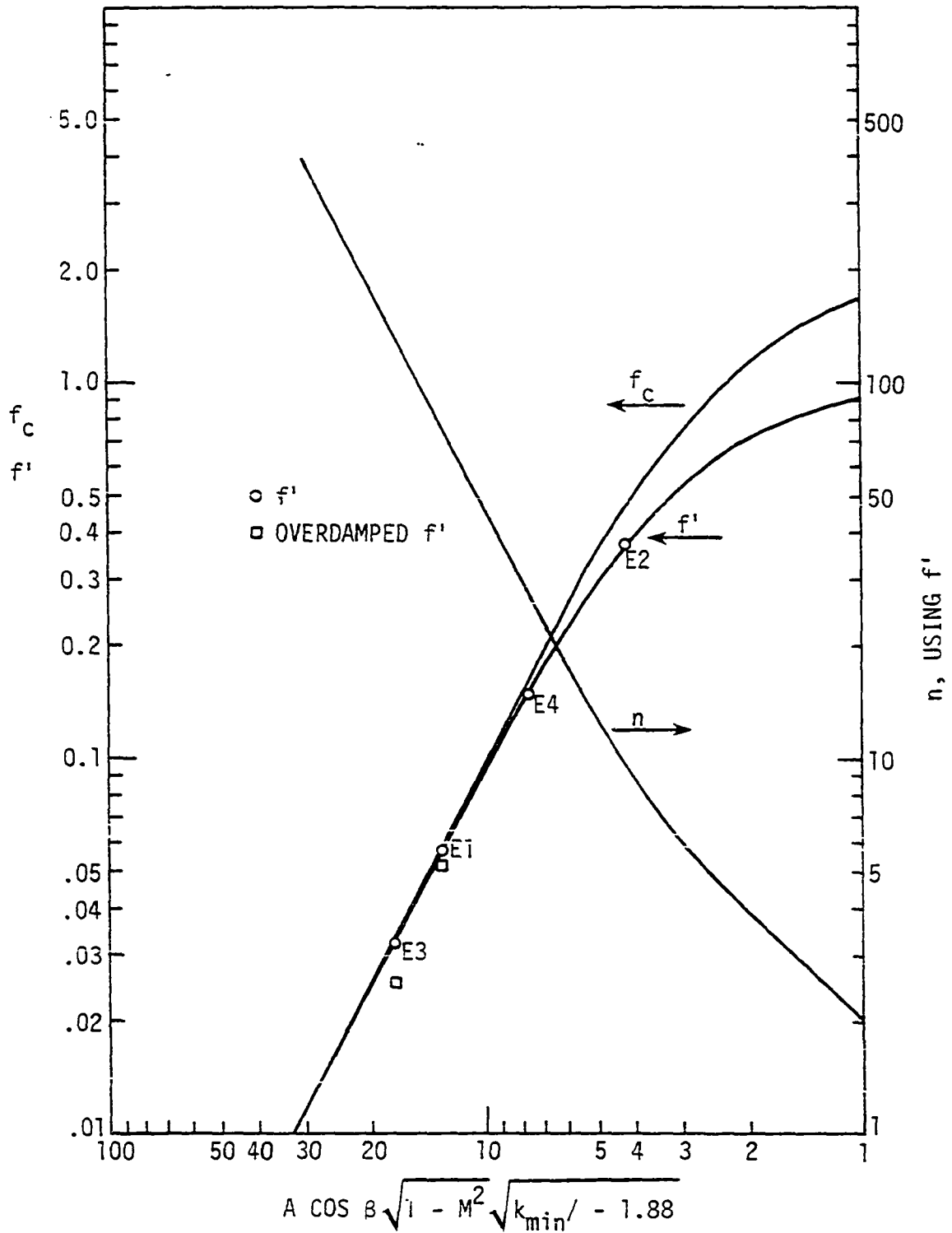


Figure 3.5. Optimum damping factor f' , critical damping factor, f_c , and number of iterations, n , for subsonic flow. Damping factors for example cascade cases E1-E4 are indicated.

differentiation to calculate d^2y/dx^2 (this method was one of the best among those tested by Wilkinson (1970)). An important characteristic of f' and f_c can be observed in Fig. 3.5 at high values of the parameter $A \cos\beta \sqrt{1-M^2} \sqrt{k_{\min}} / -1.88$ where the difference between both damping factors tends to zero. This behavior makes the calculation in this region difficult with divergence usually occurring when f' is used. Cases in this region are often encountered in turbomachinery cascades with high values of grid aspect ratio.

Figure 3.5 also shows the damping factor used in the final channel solution for four cascade flow examples computed as test cases and presented later in this chapter. The f' for the two cases in the difficult convergence region were overdamped by an additional arbitrary factor in order to achieve convergence. This approach was successfully used to overcome the difficulties in this region.

A last comment regarding Wilkinson's optimum damping factor is that the term dV_x/dx in the velocity gradient equation was neglected in the derivation of f' . This is only significant for high Mach numbers and high flow inclinations; Wilkinson empirically recommended damping the change in slope dy/dx between iterations by a factor less than unity whenever convergence is not achieved with f' .

3.3.6. Stagnation streamline shifts

The converged "channel" solution provides answers for the velocities in the channel defined by the airfoils and the stagnation streamlines.

If the velocities at either end of the q-os (at the stagnation streamlines) of the cascade are not equal, the calculation stations in these regions must be shifted by increments δ_j along the q-os so that the next "channel" solution will result in equality of velocities along the stagnation streamline locii. The increment δ_j is constant along a q-o changing from one q-o to the next.

At the end of the current "channel" solution, a linearized cross-channel velocity gradient in the upstream and downstream regions can be expressed for the i^{th} q-o as

$$\left. \frac{\partial V}{\partial y} \right)_{i, \text{NM}} = \frac{(V_{i, \text{N}} - V_{i, \text{L}})}{(y_{i, \text{N}} - y_{i, \text{L}})} \quad (3.32)$$

It is desired that the similar cross-channel velocity derivative (or velocity difference) be zero at the end of the next "channel" solution. Therefore, the velocity gradient $\partial V / \partial y$ on the mid-streamline should be changed by

$$\frac{\Delta \partial V}{\partial y} \Big|_{i, \text{NM}} = - \frac{(V_{i, \text{N}} - V_{i, \text{L}})}{(y_{i, \text{N}} - y_{i, \text{L}})} \quad (3.33)$$

The velocity gradient equation (Eqn. 3.9) can now be differentiated on the mid-streamline with respect to δ_j to find the effect of a change δ_j in the y coordinates at the i^{th} q-o, resulting in (see Alarcon and Kavanagh (1980) for details)

$$\frac{\partial}{\partial \delta_j} \left(\frac{\partial V}{\partial y} \right)_{i, \text{NM}} = \left\{ \cos \beta \left[\left(-\sin \beta \frac{\partial V}{\partial y} + \frac{dV_x}{dx} \right) \frac{\partial}{\partial \delta_j} \left(\frac{dy}{dx} \right) + V_x \frac{\partial}{\partial \delta_j} \left(\frac{d^2 y}{dx^2} \right) \right] \right\}_{i, \text{NM}} \quad (3.34)$$

From the numerical differentiation formulae presented later in this chapter, the general forms for dy/dx and d^2y/dx^2 are

$$\left. \frac{dy}{dx} \right|_i = \frac{1}{h} \sum_j a_{i,j} y_j ; \quad \left. \frac{d^2y}{dx^2} \right|_i = \frac{1}{h^2} \sum_j b_{i,j} y_j . \quad (3.35)$$

Therefore,

$$\frac{\partial}{\partial \delta_j} \left(\left. \frac{dy}{dx} \right|_i \right) = \frac{a_{i,j}}{h} \quad (3.36)$$

and

$$\frac{\partial}{\partial \delta_j} \left(\left. \frac{d^2y}{dx^2} \right|_i \right) = \frac{b_{i,j}}{h^2} . \quad (3.37)$$

Equation 3.33 then becomes

$$\sum_j \delta_j \frac{\partial}{\partial \delta_j} \left(\left. \frac{\partial V}{\partial y} \right|_{i,NM} \right) = \frac{(V_{i,1} - V_{i,N})}{(y_{i,N} - y_{i,1})} . \quad (3.38)$$

Combination of Eqns. 3.34, 3.36, 3.37 and 3.38 yields

$$\sum_j (A_i a_{i,j} + b_{i,j}) \delta_j = B_i \quad (3.39)$$

where

$$A_i = \frac{h}{V_{x_{i,NM}}} \left(-\sin\beta \frac{\partial V}{\partial y} + \frac{dV}{dx} \right)_{i,NM} \quad (3.40)$$

$$B_i = \frac{h^2}{(y_{i,N} - y_{i,1})} \frac{(V_{i,1} - V_{i,N})}{(V_x \cos\beta)_{i,NM}} . \quad (3.41)$$

The index j in the equations above is the "running" variable, its upper limit depending upon the number of points used in the numerical approximation of the first and second derivatives.

3.3.6.1. The upstream region The unknowns in the upstream region of the cascade are δ_1 through δ_{ML} for a total of ML unknowns. Equation 3.39 must be satisfied for q-os 2 through ML, taking into account the various differentiation procedures used in this region. For q-o 5 through q-o M-4, the differentiation procedure uses a total of nine points with four points either side of the central point. For q-os 3 and 4, a simplified version of the procedure is used wherein two points are used either side of the central point. For q-o 2, a non-symmetric version of the five point procedure is employed. For q-o 1, it is necessary to satisfy the condition of given inlet flow angle β_1 . Assuming that the current slope is dy/dx and that the required slope is $\tan(90^\circ - \beta_1)$, a parabola through three points is used, giving

$$\frac{1}{h} (-1.5\delta_1 + 2\delta_2 - 0.5\delta_3) = \tan(90^\circ - \beta_1)_{NM} - \left(\frac{dy}{dx}\right)_{1,NM}. \quad (3.42)$$

The resultant ML x ML system of equations in the upstream region to be solved by Gaussian elimination is shown in Appendix C.

3.3.6.2. The downstream region The downstream region system of equations leading to δ_j s can be written in two different ways depending on the trailing edge condition used. The velocities at the ends of the q-o passing through the airfoil trailing edge are required to be equal in Wilkinson's trailing edge condition, allowing in turn the calculation of the exit gas angle β_2 . On the other hand, the angle β_2 can be specified from experimental correlations, in which case, the calculation is very similar to that in the upstream region. As a result, the velocities might not be equal at the ends of q-o MT at the trailing edge.

When Wilkinson's trailing edge condition (called the calculated β_2 option) is used the unknown δ_j 's are δ_{MT+1} through δ_M : The q-o MT (at the trailing edge) cannot move, i.e., $\delta_{MT} = 0$. Equation 3.39 must be satisfied for q-os MT through M-1. Equation 3.39 is not written for the last q-o; however, δ_M appears in the equations written for q-os M-1, M-2, and M-4. Therefore, there is one more unknown than equations. The additional needed equation is obtained from the condition $\delta_{MT} = 0$. The system can now be solved for δ_{MT+1} through δ_M .

For q-os M-3 and M-2, a simplified five point symmetric version of the differentiation procedure is again used, and for q-o M-1, a non-symmetric version of the five point procedure is used.

The periodicity condition could be applied in a more general sense at the trailing edge by requiring equal velocities to occur on a line making a specified angle ϕ to the pitchwise direction (i.e., on points A and B in Fig. 3.6). Experience with cascade examples using this method showed that changing the ϕ angle had some effect on the pressure distribution towards the trailing edge, but the calculated exit gas angle did not appreciably differ from that calculated by requiring equal velocities at points 1 and N in Fig. 3.6. In this investigation, ϕ was kept at zero.

The system of equations to be solved by Gaussian elimination with the calculated β_2 option for the trailing edge condition is shown in Appendix C.

If the β_2 angle is specified (called the input β_2 option), the unknowns are δ_{MT+1} through δ_M . Equation 3.39 must be satisfied for

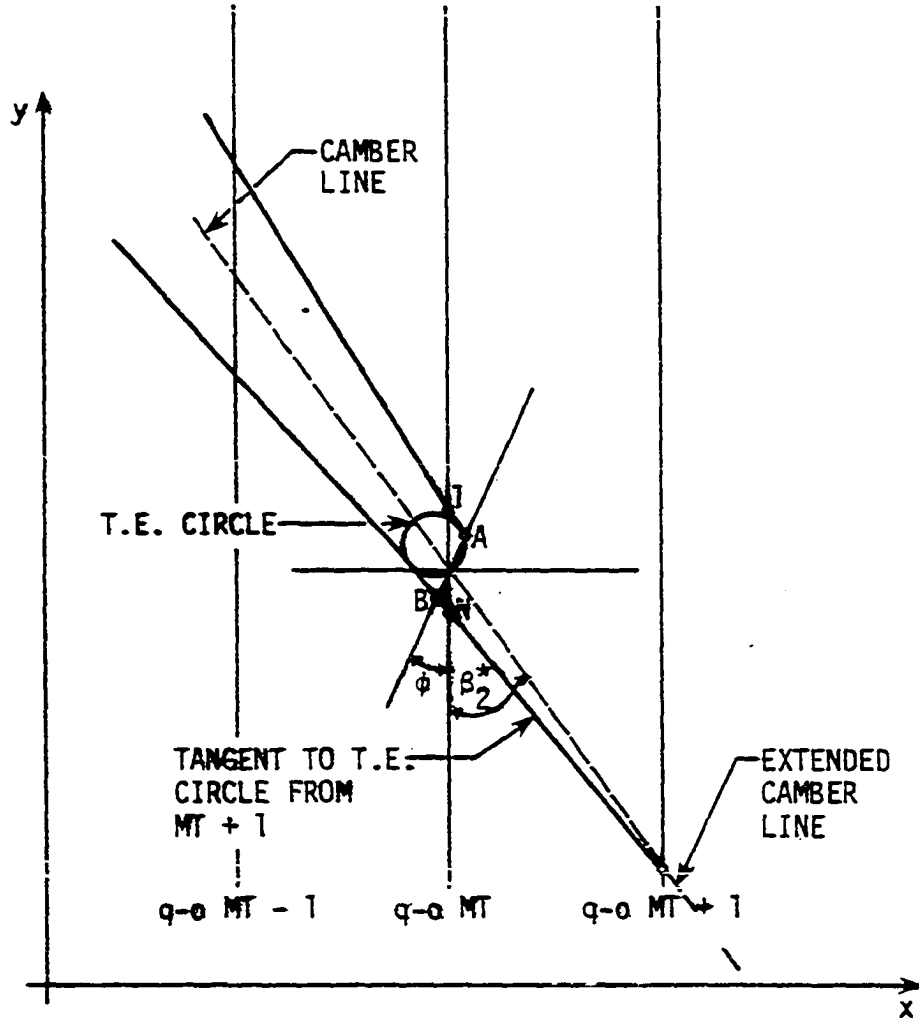


Figure 3.6. The airfoil trailing edge region.

q-os MT+1 through M-1, again taking into account the various differentiation procedures. For q-o M, it is necessary to satisfy the given exit gas angle β_2 . If the current slope is dy/dx and the required slope is $\tan(\beta_2 - 90^\circ)$, a parabola through three points gives the relationship (for q-o M)

$$\frac{1}{h}(0.5\delta_{M-2} - 2\delta_{M-1} + 1.5\delta_M) = \tan(\beta_2 - 90^\circ)_{NM} - \left(\frac{dy}{dx}\right)_{M,NM}. \quad (3.43)$$

The systems of equations for the input β_2 option to be also solved by Gaussian elimination is shown in Appendix C.

One further comment is in order here regarding Wilkinson's findings on stagnation streamline convergence improvement. He found that at low Mach numbers, convergence to final shape of the stagnation streamlines was speeded up by multiplying the determined δ_j s by about 1.5. For high subsonic Mach numbers, on the other hand, the movement of the stagnation streamlines should be damped by multiplying the δ_j s by

$$1.5\sqrt{1 - M_{i,NM}^2} \quad (3.44)$$

and

$$1.5\sqrt{1 - M_{M,NM}^2} \quad (3.45)$$

for upstream and downstream regions, respectively. Experience with the method has shown that faster convergence is obtained by changing the factor from 1.5 to 0.5 in high subsonic Mach number cases when using superheated steam as the working fluid.

3.3.6.3. Continuity mechanics for exit gas angle β_2 The exit gas angle β_2 was assumed known in the input β_2 option for the trailing edge condition. Here, some ways of determining β_2 from continuity considerations and empirical relations are considered.

For compressible flow through the cascade, a relationship between β_1 , β_2 , M_1 , M_2 , and $\Delta p_0/p_{01}$ can be obtained by applying continuity between upstream and downstream in the form

$$\frac{p_{02} A_2 M_2}{\sqrt{T_{02}} \left(1 + \frac{\gamma-1}{2} M_2^2\right)^{(\gamma+1)/2(\gamma-1)}} = \frac{p_{01} A_1 M_1}{\sqrt{T_{01}} \left(1 + \frac{\gamma-1}{2} M_1^2\right)^{(\gamma+1)/2(\gamma-1)}} \quad (3.46)$$

where

$$\begin{aligned} A_1 &= \Delta z_1 \tau \sin \beta_1, \\ A_2 &= \Delta z_2 \tau \sin \beta_2, \text{ and} \\ p_{02} &= (1 - \Delta p_0/p_{01}) p_{01}. \end{aligned} \quad (3.47)$$

If the total temperature remains constant, Eqn. 3.46 becomes

$$\frac{(1 - \Delta p_0/p_{01}) \frac{\Delta z_2}{\Delta z_1} M_2 \sin \beta_2}{\left(1 + \frac{\gamma-1}{2} M_2^2\right)^{(\gamma+1)/2(\gamma-1)}} = \frac{M_1 \sin \beta_1}{\left(1 + \frac{\gamma-1}{2} M_1^2\right)^{(\gamma+1)/2(\gamma-1)}} \quad (3.48)$$

which can be used to obtain β_2 if the remaining four quantities are known.

If M_2 and β_2 are both unspecified, the exit gas angle β_2 can be obtained by applying continuity between the cascade throat and the

downstream stations as described by Martelli (1979),

$$\sin\beta_2 = \frac{\lambda}{\tau} \frac{\Delta z_\lambda}{\Delta z_2} \frac{P_{0\lambda}}{P_{02}} F_1(M_2) F_2(\tau/R) \quad (3.49)$$

where, Δz_λ is the average streamsheet thickness at the throat, and $P_{0\lambda}/P_{02}$ is a measure of the mixing losses as estimated from Cox's (1976) loss correlation

$$\frac{P_{0\lambda}}{P_{02}} = 0.833 \frac{(P_{01} - P_{02})}{P_{02}} + 1. \quad (3.50)$$

The functions $F_1(M_2)$ and $F_2(\tau/R)$ in Eqn. 3.49 are

$$\left. \begin{aligned} F_1 &= 1.09 & , & \quad M_2 \leq 0.5 \\ F_1 &= 0.6333 + 2.16M_2 - 3.24M_2^2 + 1.44M_2^3 & , & \quad 0.5 < M_2 < 1 \\ F_1 &= A/A^* & , & \quad 1.0 < M_2 \\ F_2 &= 1.01 - 0.04(\tau/R) \end{aligned} \right\} \quad (3.51)$$

where R is the mean radius of curvature of the airfoil suction surface between the throat and the trailing edge. The solution of Eqn. 3.49 involves an iterative procedure wherein M_2 is guessed and the angle β_2 is calculated from Eqns. 3.48 and 3.49. The iteration converges when the two β_2 values obtained agree.

3.3.7. Numerical differentiation

The integration of the velocity gradient equation requires the numerical evaluation of dV_x/dx , dy/dx and d^2y/dx^2 from data at equally spaced points along the streamlines. This was done by fitting a curve

through a point and eight of its neighbors (four either side) on the same streamline followed by one or two differentiations.

Wilkinson (1970) compared several differentiation methods by applying them to a sinusoidal function and then comparing the numerical value of d^2y/dx^2 with the theoretical one. The function used was of the form

$$y = e \cos \left(\frac{2\pi x}{\lambda/h} \right) \quad (3.52)$$

and a parameter k defined as

$$k = \frac{h^2}{e} \left(\frac{d^2y}{dx^2} \right)_{(x=0)} = \frac{-4\pi^2}{(\lambda/h)^2} \quad (3.53)$$

where λ is the wavelength and h the point spacing.¹

For an ordinate y given at equal intervals of the argument $x = 0, \pm h, \pm 2h, \dots$, the numerical differentiation method described above gives a formula of the type

$$\left(\frac{d^2y}{dx^2} \right)_0 = \frac{1}{h^2} \sum_{n=-N}^N f_n y_n \quad (3.54)$$

with k as given below when applied to Eqn. 3.53

$$k = \sum_{n=-N}^N f_n \frac{y_n}{e} . \quad (3.55)$$

¹Wilkinson further argued that a given curve may be represented by a Fourier series, but that the second derivative of the series is in general not the second derivative of the given curve. However, by using proper weighting functions of the coefficients of the differentiated series, convergence to the derivative of the given curve can be obtained. The accuracy of a numerical method in determining the derivatives of a sinusoidal function is, therefore, a valid test of its accuracy for an arbitrary curve.

In these relations, N and the coefficients f_n depend on the number of neighbor points used either side of the central point.

Curves of "numerical" and "exact" k constructed as function of λ/h to compare the differentiation method used by Wilkinson (1972) (five point formula) with the present method (nine point formula) are shown in Fig. 3.7.

Several important conclusions can be immediately drawn from Fig. 3.7. First, k_{\min} is less negative for the present differentiation method than for Wilkinson's method. Thus, the present method produces a greater optimum damping factor (see Eqn. 3.26) which in turn implies that the "channel" solution converges in fewer iterations. Second, Wilkinson's method is observed to overpredict the second derivative for $\lambda/h > 10$ which are values typically encountered in turbomachinery cascades. For $\lambda/h < 10$, (needed to accurately represent fast changes in curvature) both methods are observed to perform with about the same degree of inaccuracy. The over prediction of the second derivative was checked by applying both Wilkinson's and the present method to a cascade typical of modern gas turbine applications and for which exact second derivatives for the airfoil were available. The results displayed in Fig. 3.8 confirmed that Wilkinson's method actually overpredicted the second derivatives on the suction surface. The same trend was observed on the pressure surface. The effect of such overprediction on the suction side is to make the surface appear more convex than it actually is; therefore, the streamline curvature method will predict higher

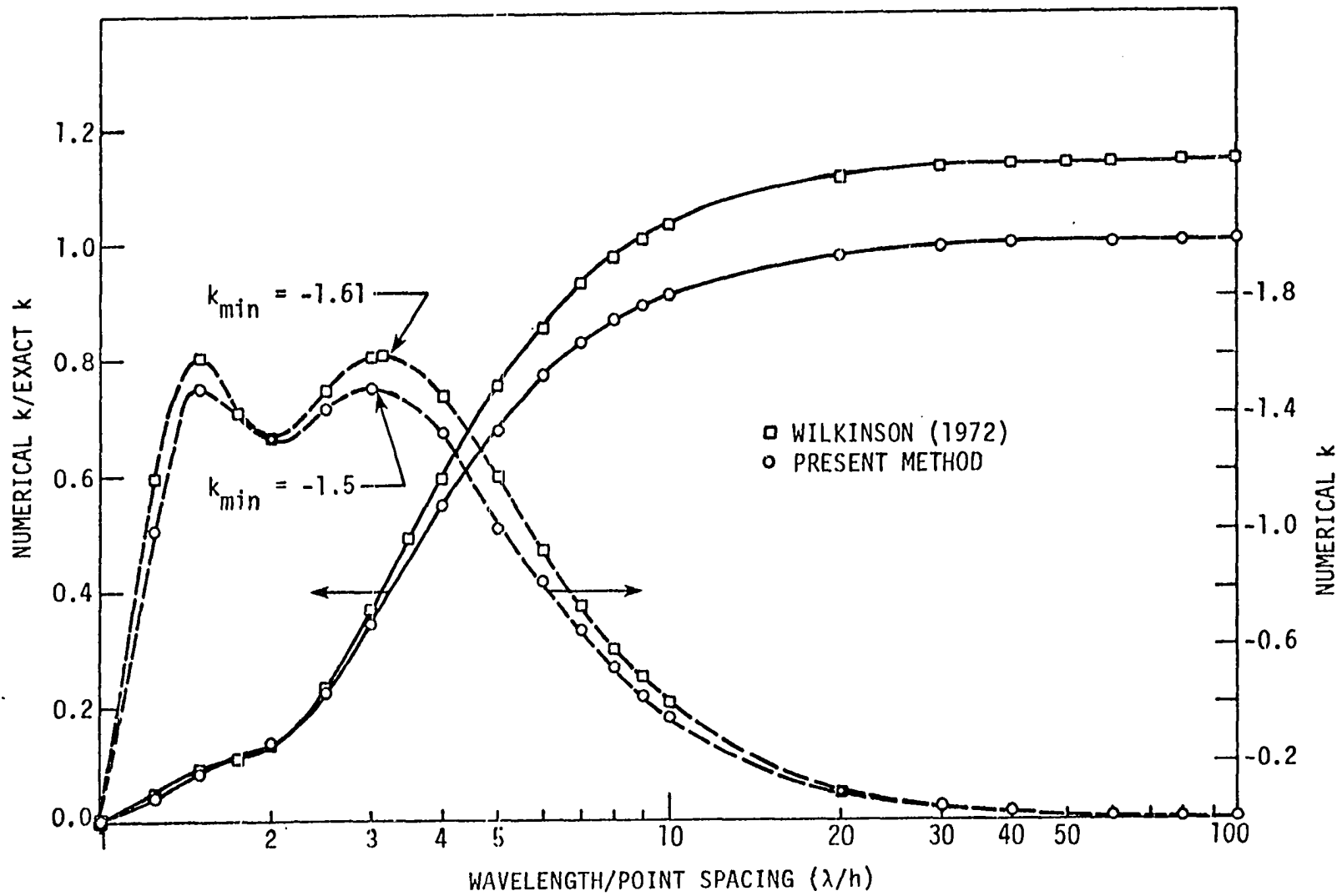


Figure 3.7. Frequency response of numerical second derivative formulae.

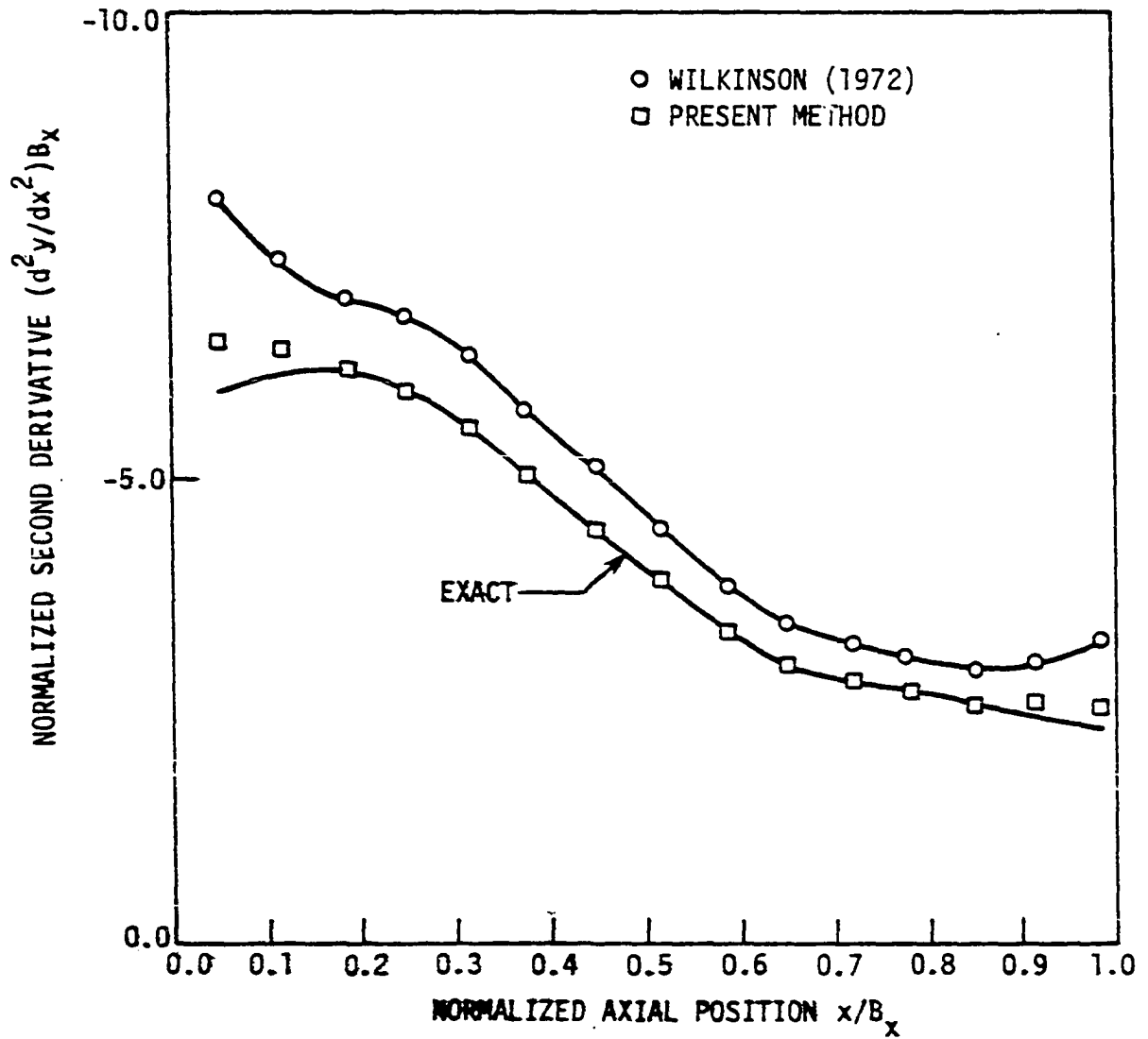


Figure 3.8. Comparison of calculated and exact airfoil suction surface second derivatives.

velocities on this surface. The pressure side, on the other hand, appears less concave to the streamline curvature method and the predicted velocities are therefore lower. This trend is observed in Fig. 3.9 where a theoretical solution for a compressor cascade is compared with SCA results. The theoretical solution shown is an incompressible conformal mapping solution due to Gostelow (1965). The same velocity anomalies were found for several other cascade results when compared with solutions obtained with a distributed singularities method.

The present numerical differentiation procedure was obtained from guidelines given by Wilkinson (1972). Wilkinson's procedure is to fit a quartic through five points and subsequently differentiate at the central point to calculate $(dy/dx)_0$ and $(d^2y/dx^2)_0$. Wilkinson then smoothed the derivatives by using the general smoothing formula

$$y_0 := ay_{-2} + by_{-1} + cy_0 + by_1 + ay_2 \quad (3.56)$$

where $:=$ means "is replaced by," and the y 's are dy/dx , d^2y/dx^2 or any other quantity to be smoothed. The three coefficients involved are determined from the following three conditions:

- (i) for $\lambda/h = \infty$, the curve to be smoothed is left unchanged,
- (ii) for $\lambda/h = 2$, $y_0 := py_0$, and
- (iii) for $\lambda/h = 3$, $y_0 := qy_0$.

Therefore,

$$a = \frac{1-q}{3} - \frac{1-p}{4}, \quad b = \frac{1-p}{4}, \quad c = \frac{1+2q}{3}. \quad (3.57)$$

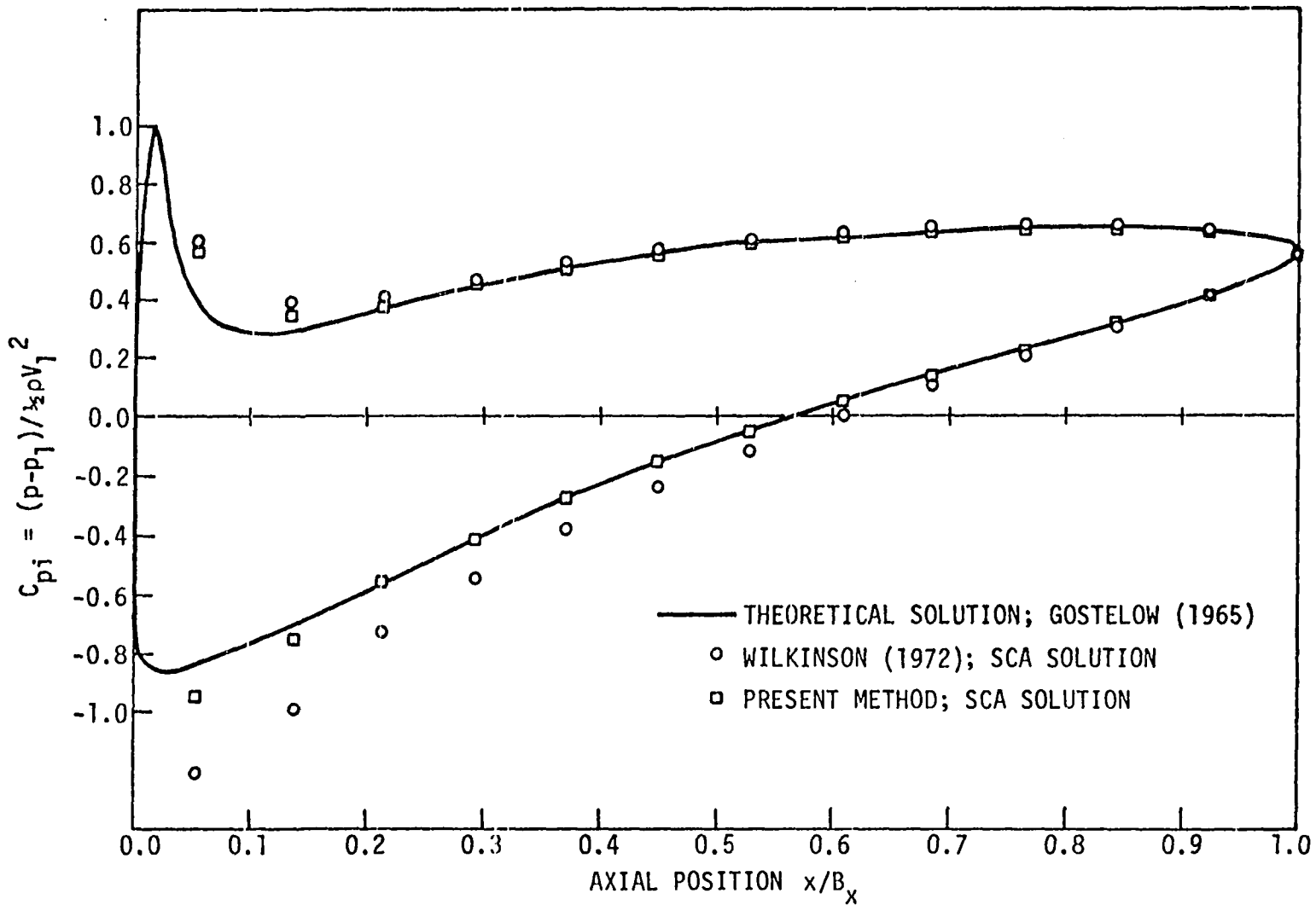


Figure 3.9. Comparison of airfoil surface pressure coefficients.

The expressions for $(dy/dx)_0$ and $(d^2y/dx^2)_0$ can then be written in the form

$$\begin{aligned} \left. \frac{dy}{dx} \right)_0 &= \frac{1}{12h} [ay_{-4} + (-8a + b)y_{-3} + (-8b + c)y_{-2} \\ &\quad + (8a + b - 8c)y_{-1} + (-8a - b + 8c)y_1 \\ &\quad + (8b - c)y_2 + (8a - b)y_3 - ay_4] \end{aligned} \quad (3.58)$$

$$\begin{aligned} \left. \frac{d^2y}{dx^2} \right)_0 &= \frac{1}{12h^2} [-ay_{-4} + (16a - b)y_{-3} + (-30a + 16b - c)y_{-2} \\ &\quad + (16a - 31b + 16c)y_{-1} + (-2a + 32b - 30c)y_0 \\ &\quad + (16a - 31b + 16c)y_1 + (-30a + 16b - c)y_2 \\ &\quad + (16a - b)y_3 - ay_4]. \end{aligned} \quad (3.59)$$

Equations 3.58 and 3.59 constitute the present numerical differentiation procedure. Wilkinson, on the other hand, further simplified these expressions to reduce them to five point formulae. The number of points either side of the central point were reduced from four to two by changing the coefficients in Eqn. 3.59 so that the numerical k at $\lambda/h = 2$ remained the same. Also, the coefficients in Eqn. 3.58 were changed so that the slope of a straight line remained constant. The simplified expressions obtained for the first and second derivatives were, therefore,

$$\begin{aligned} \left. \frac{dy}{dx} \right)_0 &= \frac{1}{12h} [-(0.25 + 0.50(8a + b - 8c))y_{-2} \\ &\quad + (8a + b - 8c)y_{-1} - (8a + b - 8c)y_1 \\ &\quad + (0.25 + 0.50(8a + b - 8c))y_2] \end{aligned} \quad (3.60)$$

and

$$\begin{aligned} \left. \frac{d^2y}{dx^2} \right|_0 = \frac{1}{12h^2} [& (-31a + 16b - c)y_{-2} + (32a - 32b + 16c)y_{-1} \\ & + (-2a + 32b - 30c)y_0 + (32a - 32b + 16c)y_1 \\ & + (-31a + 16b - c)y_2]. \end{aligned} \quad (3.61)$$

Equations 3.60 and 3.61 were also used in the present numerical method for q-os 3 and 4 in the upstream region and for q-os M-3 and M-2 in the downstream region but with different p and q values than those used by Wilkinson.

Several combinations of the parameters p and q were tried and the resultant differentiation procedures analyzed with respect to convergence and accuracy. The best choices of p and q were found to be 0.25 and 0.40, respectively. It should be pointed out that Wilkinson's five point formulae used p = 0.25 and q = 0.443.

The q-os 1, 2, M-1, and M also had to be treated as special cases. For q-os 2 and M-1, dy/dx was calculated with

$$\left. \frac{dy}{dx} \right|_2 = \frac{1}{2h} (-y_1 + y_3) \quad (3.62)$$

and

$$\left. \frac{dy}{dx} \right|_{M-1} = \frac{1}{2h} (-y_{M-2} + y_M) \quad (3.63)$$

followed with a smoothing of the form

$$y_0 := 0.25y_{-1} + 0.5y_0 + 0.25y_1 \quad (3.64)$$

giving the expressions for dy/dx

$$\left. \frac{dy}{dx} \right|_2 = \frac{1}{h} (-0.60417y_1 + 0.33333y_2 + 0.125y_3 + 0.16667y_4 - 0.02083y_5) \quad (3.65)$$

$$\left. \frac{dy}{dx} \right|_{M-1} = \frac{1}{h} (0.02083y_{M-4} - 0.16667y_{M-3} - 0.125y_{M-2} - 0.33333y_{M-1} + 0.60417y_M). \quad (3.66)$$

The second derivative was calculated with

$$\left. \frac{d^2y}{dx^2} \right|_2 = \frac{1}{h^2} (y_1 - 2.0y_2 + y_3) \quad (3.67)$$

and

$$\left. \frac{d^2y}{dx^2} \right|_{M-1} = \frac{1}{h^2} (y_{M-2} - 2.0y_{M-1} + y_M) \quad (3.68)$$

followed with the smoothing in Eqn. 3.64 to give

$$\left. \frac{d^2y}{dx^2} \right|_2 = \frac{1}{h^2} (0.72917y_1 - 1.16667y_2 + 0.125y_3 + 0.33333y_4 - 0.02083y_5) \quad (3.69)$$

$$\left. \frac{d^2y}{dx^2} \right|_{M-1} = \frac{1}{h^2} (-0.02083y_{M-4} + 0.33333y_{M-3} + 0.125y_{M-2} - 1.16667y_{M-1} + 0.72917y_M). \quad (3.70)$$

For q-os 1 and M, dy/dx was calculated by differentiating a parabola through three points, i.e.,

$$\left. \frac{dy}{dx} \right|_1 = \frac{1}{h} (-1.5y_1 + 2y_2 - 0.5y_3) \quad (3.71)$$

$$\left. \frac{dy}{dx} \right|_M = \frac{1}{h} (1.5y_M - 2y_{M-1} + 0.5y_{M-2}). \quad (3.72)$$

The second derivatives for q-os 1 and M were assumed to be the same as those at q-os 2 and M-2, respectively.

3.3.8. Validation of the streamline curvature method (SCA)

The capabilities of the global streamline curvature prediction procedure (SCA) were tested by comparing computed cascade results with available analytical, numerical, and experimental data. Four cascade examples of inviscid, adiabatic flows were considered (some of these examples are treated in greater detail again later after reanalysis and boundary layer procedures have been considered). In each example, uniform grid spacing, h , with a total of 39 q -os and 9 streamlines were used. These values were found from numerical experimentation with the method to give the best accuracy and convergence characteristics.

The first example (E1) considered two-dimensional, incompressible flow in a compressor cascade for which an analytical solution based on conformal mapping was obtained by Gostelow (1965). The cascade geometry and calculation region are shown in Fig. 3.10.

This example presented a difficult convergence problem due to the high grid aspect ratio involved (see Fig. 3.5). The predicted and theoretical distributions of surface pressure coefficient are shown in Fig. 3.11. The SCA results agree very well with the conformal mapping solution except in the leading edge region where the accurate calculation of derivatives becomes difficult due to the rapid change in curvature around the leading edge. The calculated β_2 also agrees well with the theoretical value. Figure 3.12 shows further comparisons of the SCA results obtained with the two trailing-edge options. The β_2 angle was matched with the theoretical value for the input β_2 option.

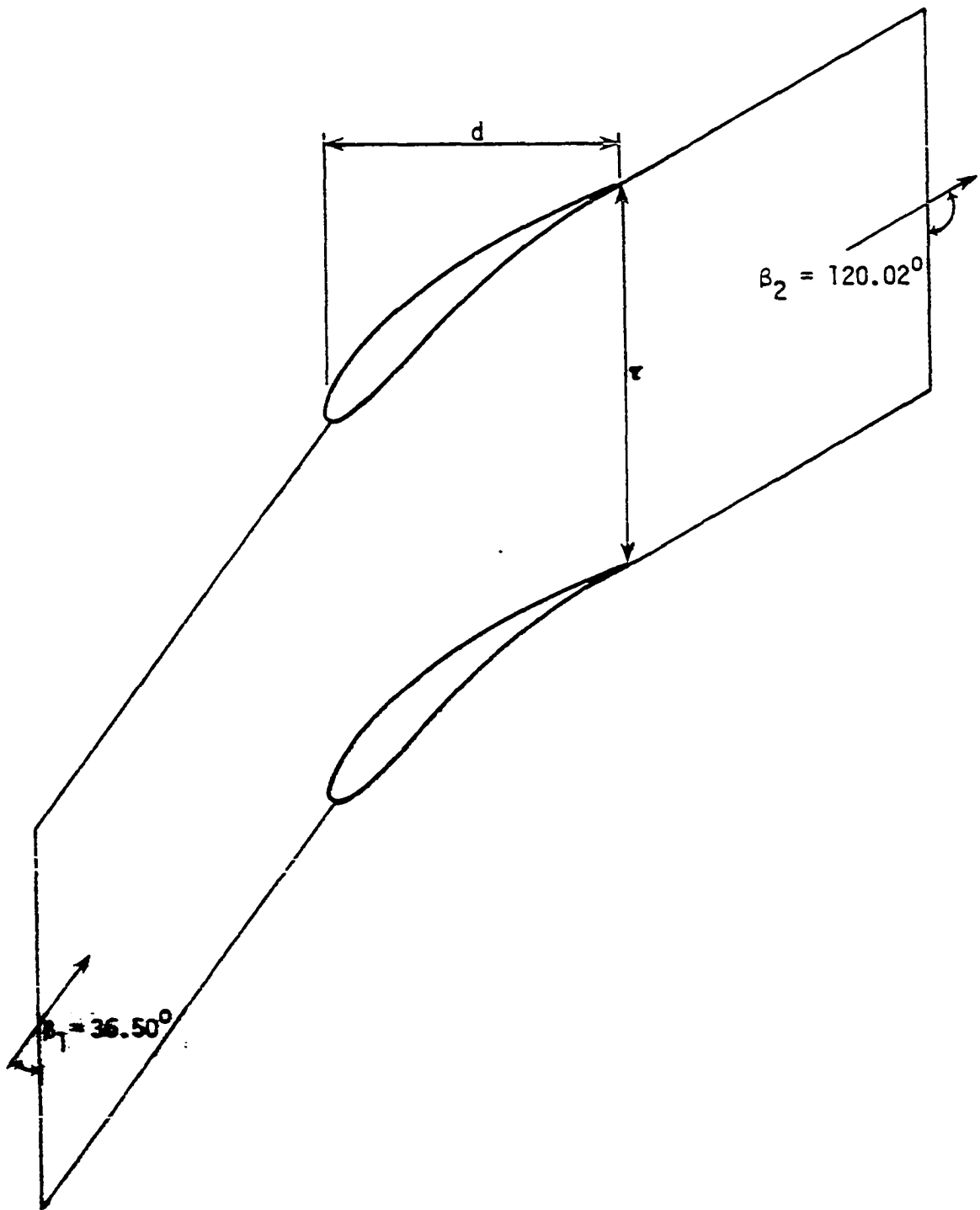


Figure 3.10. Geometry and calculation region for Gostelow (1965) cascade. $\tau/B_x = 1.239$, $d/B_x = 0.985$. β_1 and β_2 are theoretical values.

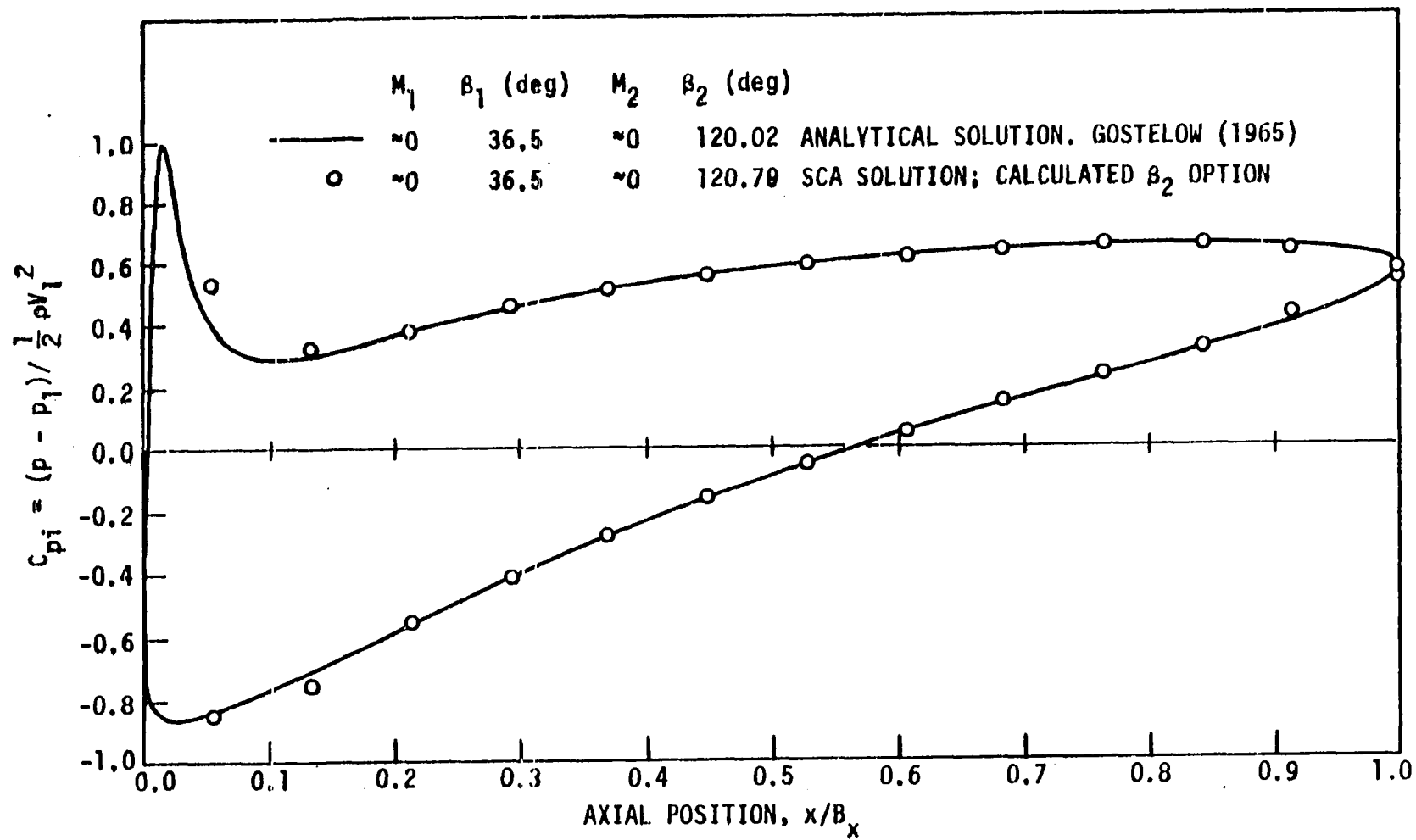


Figure 3.11. Comparison of predicted profile pressure distribution with analytical solution for Gostelow (1965) cascade.

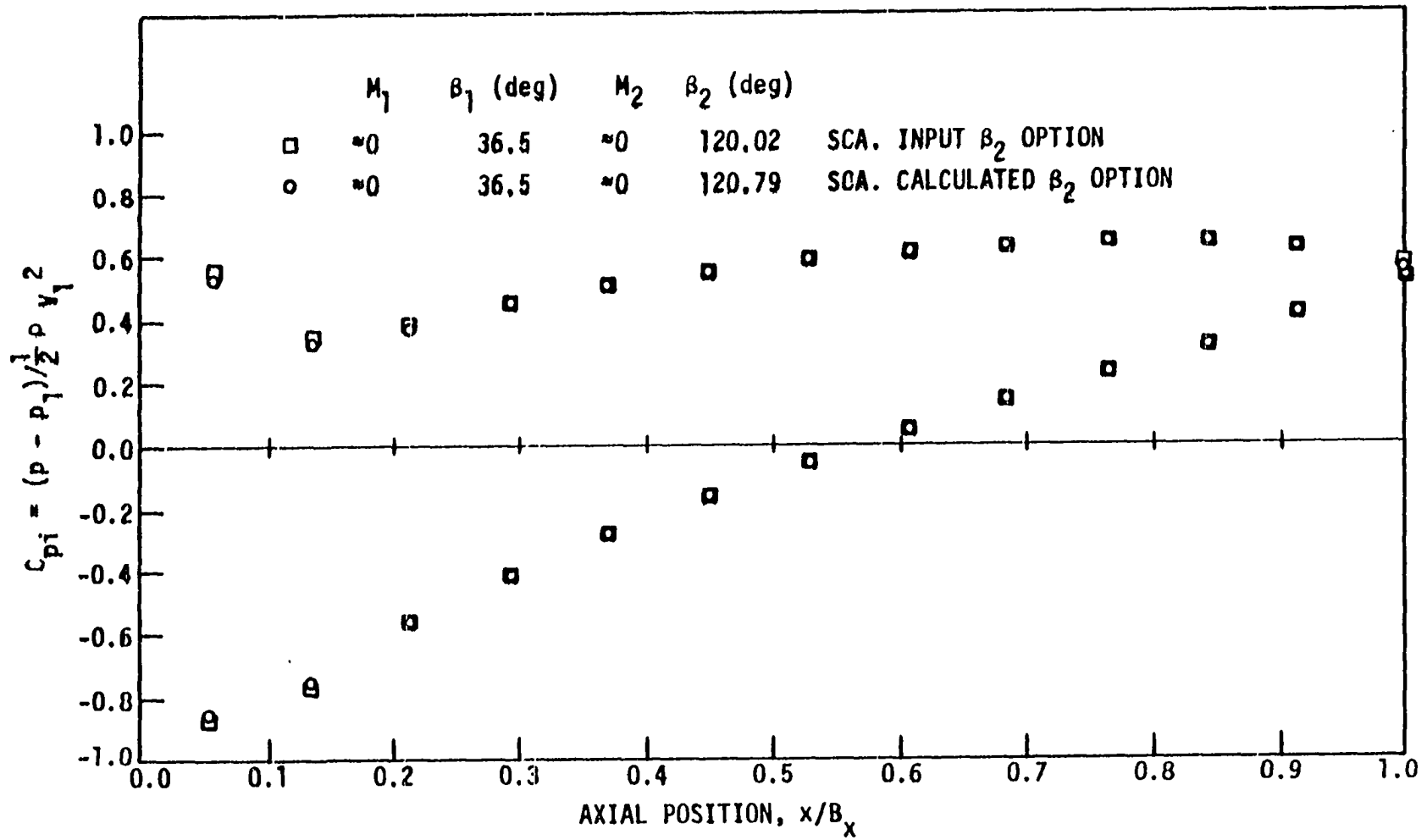


Figure 3.12. Comparison of SCA predicted profile pressure distributions. Different trailing-edge options.

As can be seen, the results are nearly the same except for very small differences in pressure coefficient in the leading- and trailing-edge regions. The solution with the calculated β_2 option was found to converge faster than that in the input β_2 option.

Example E2 involved calculation of Hobson's second impulse cascade which was designed with the "indirect" hodograph method reported by Hobson (1974). The flow was subsonic at both upstream and downstream stations with a supersonic pocket at about 50% of axial chord on the suction side. The airfoils in cascade and the calculation regions are shown in Fig. 3.13. The sharp leading and trailing edges were modified by introducing very small fictitious circles to allow spline fitting of the profile for geometry input to the SCA analysis.

The low grid aspect ratio in this case yielded quick convergence of the solution in spite of the high Mach number involved; therefore, grid aspect ratio proved to be a stronger constraint on convergence than Mach number. In Fig. 3.14 the computed distribution of the ratio of surface local velocity to critical velocity is compared with the hodograph design data, and also with results of the time-marching method reported by Denton (1975). The agreement with the theoretical data is excellent throughout. As Fig. 3.14 shows, the SCA method performed better in this problem than did Denton's. The SCA results obtained using the different trailing edge options are compared in Fig. 3.15 with β_2 matching the theoretical value for the input β_2 option. Again, nearly identical results were obtained with small discrepancies towards the trailing edge. The solution with the calculated β_2 option converged more

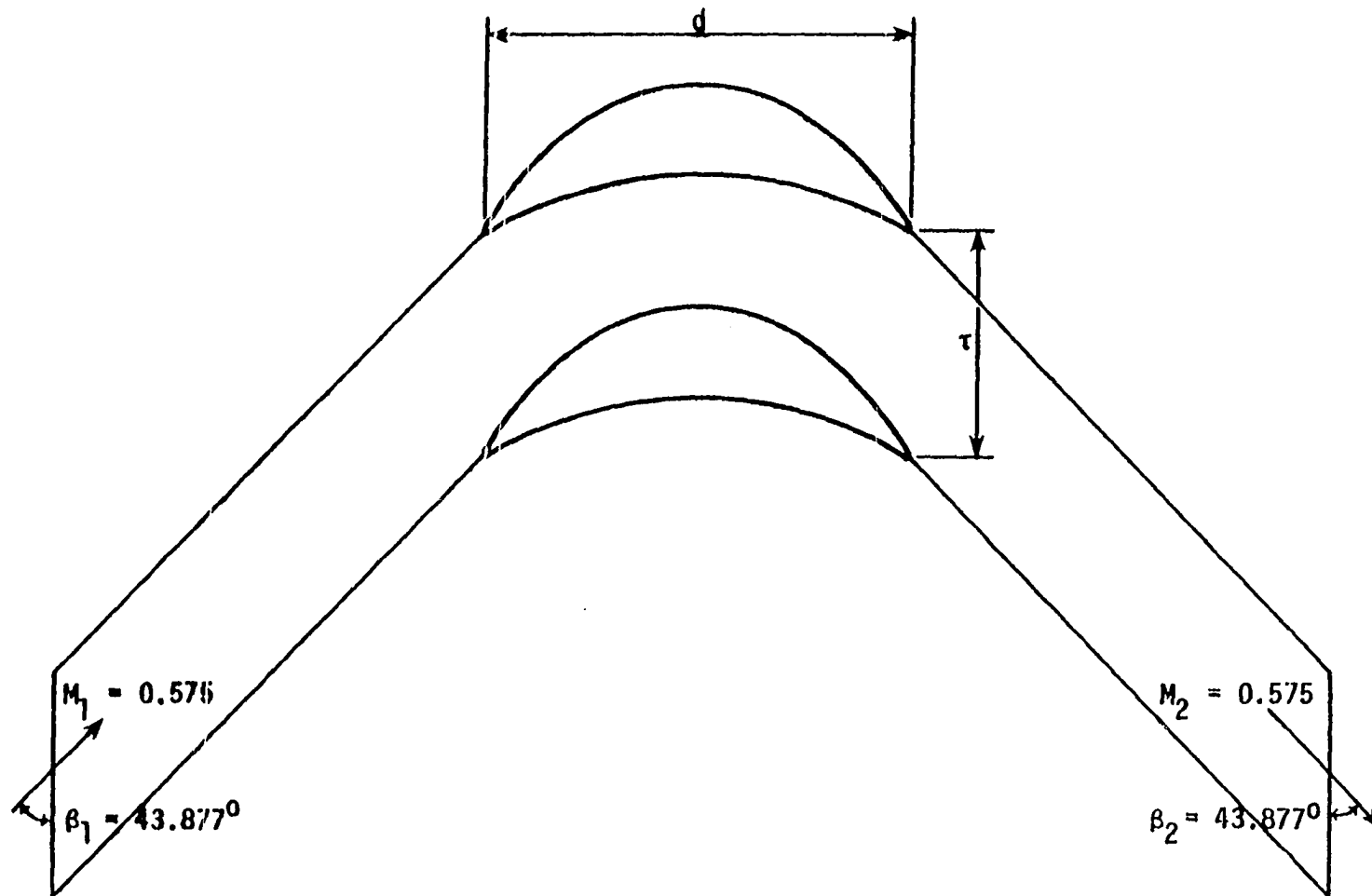


Figure 3.13. Geometry and calculation region for Hobson's second impulse cascade. Hobson (1974). $\tau/B_x = 0.5259$, $d/B_x = 0.999$. M_1 , β_1 , M_2 and β_2 are theoretical values.

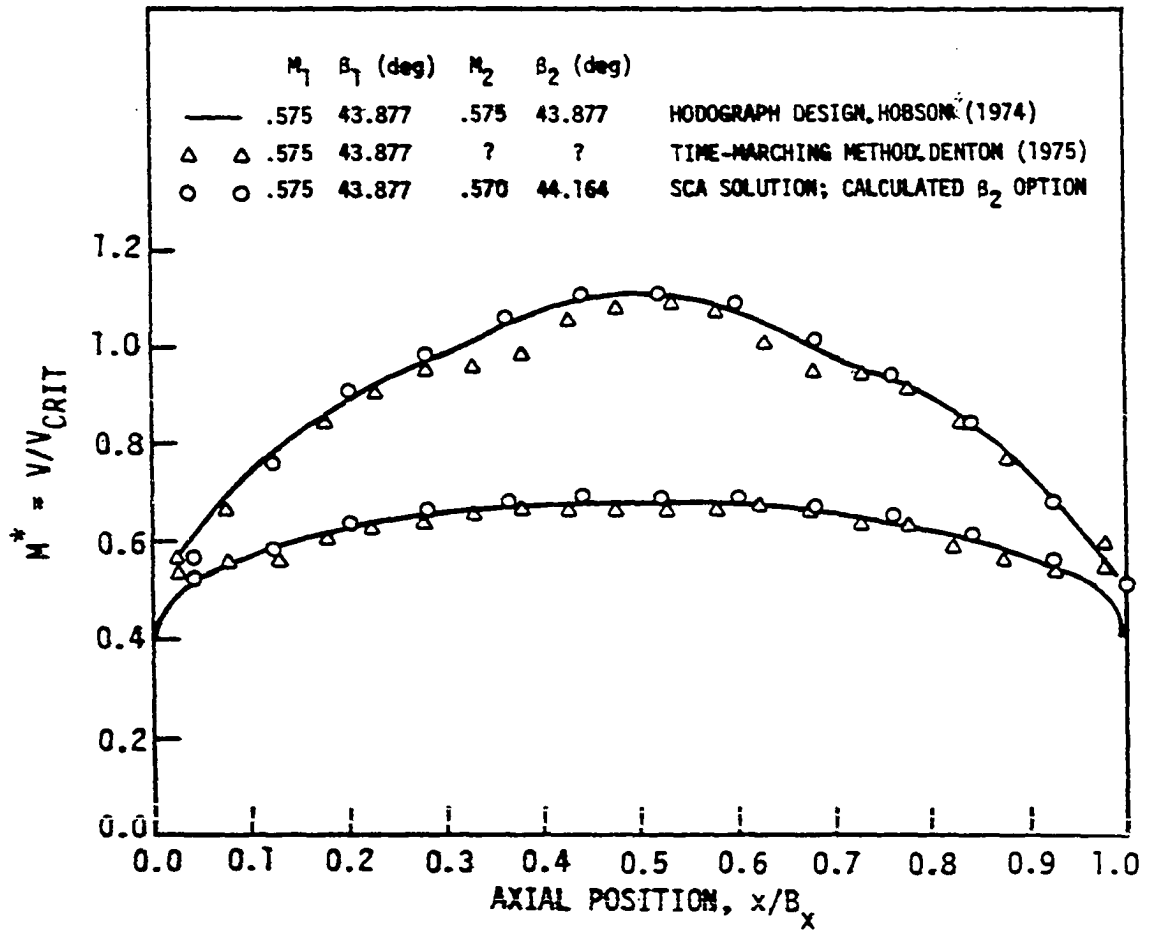


Figure 3.14. Comparison of predicted profile velocity distribution with Hobson (1974) theoretical (design) solution.

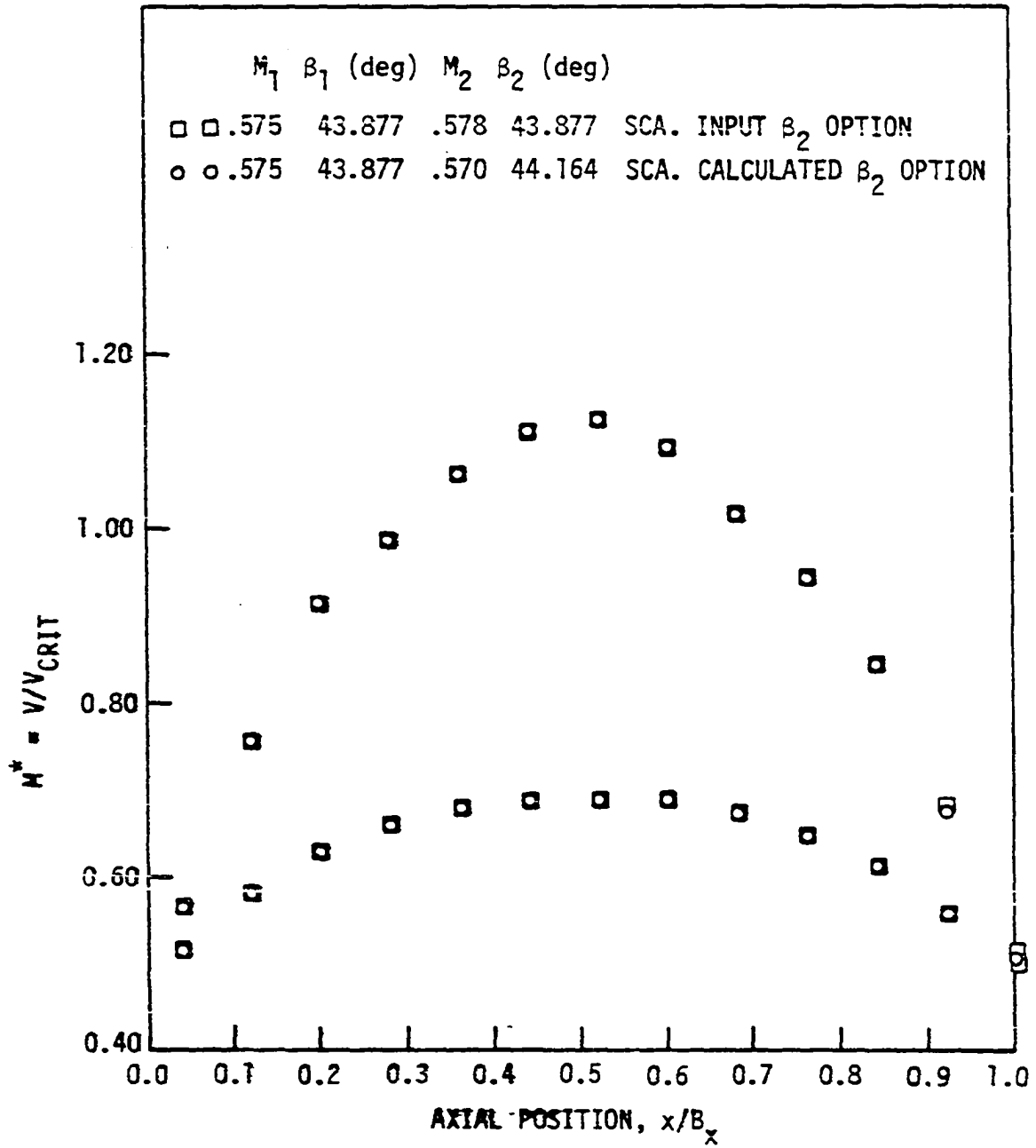


Figure 3.15. Comparison of SCA predicted profile velocity distributions. Different trailing-edge options.

slowly than the input β_2 option in this case. The sharp trailing edge geometry in both examples E1 and E2 helped in providing good agreement between the theoretical and the SCA solutions for the two trailing edge options. Such good agreement should not be expected in general for cascades with rounded trailing edges.

Example E3 dealt with compressible flow through a turbine cascade with a small supersonic region on the suction side close to the throat. The airfoils and cascade geometry are shown in Fig. 3.16. This cascade is representative of turbine nozzle cascades for current aircraft gas turbine applications.

The combination of high grid aspect ratio, high Mach number, and change in stream sheet thickness through the cascade made convergence of the solution for this case difficult. The predicted distribution of the ratio of surface local velocity to critical velocity is compared in Fig. 3.17 with experimental data reported by Huffman et al. (1971). The exit gas angle, β_2 , in Fig. 3.17 was calculated to satisfy continuity from Eqn. 3.48 with the measured values of $\Delta z_2/\Delta z_1$, ΔP_0 , P_{01} , M_1 , β_1 , and M_2 . The agreement between experimental and calculated surface velocities obtained after modification of the Δz distribution inside the cascade is reasonable in the front part of the cascade and deteriorates somewhat towards the rear part. The distribution of upstream stream sheet thickness to local value (as shown in the top graph) was obtained after several tries in which Δz was adjusted so that calculated and experimental surface velocity distributions matched reasonably well.

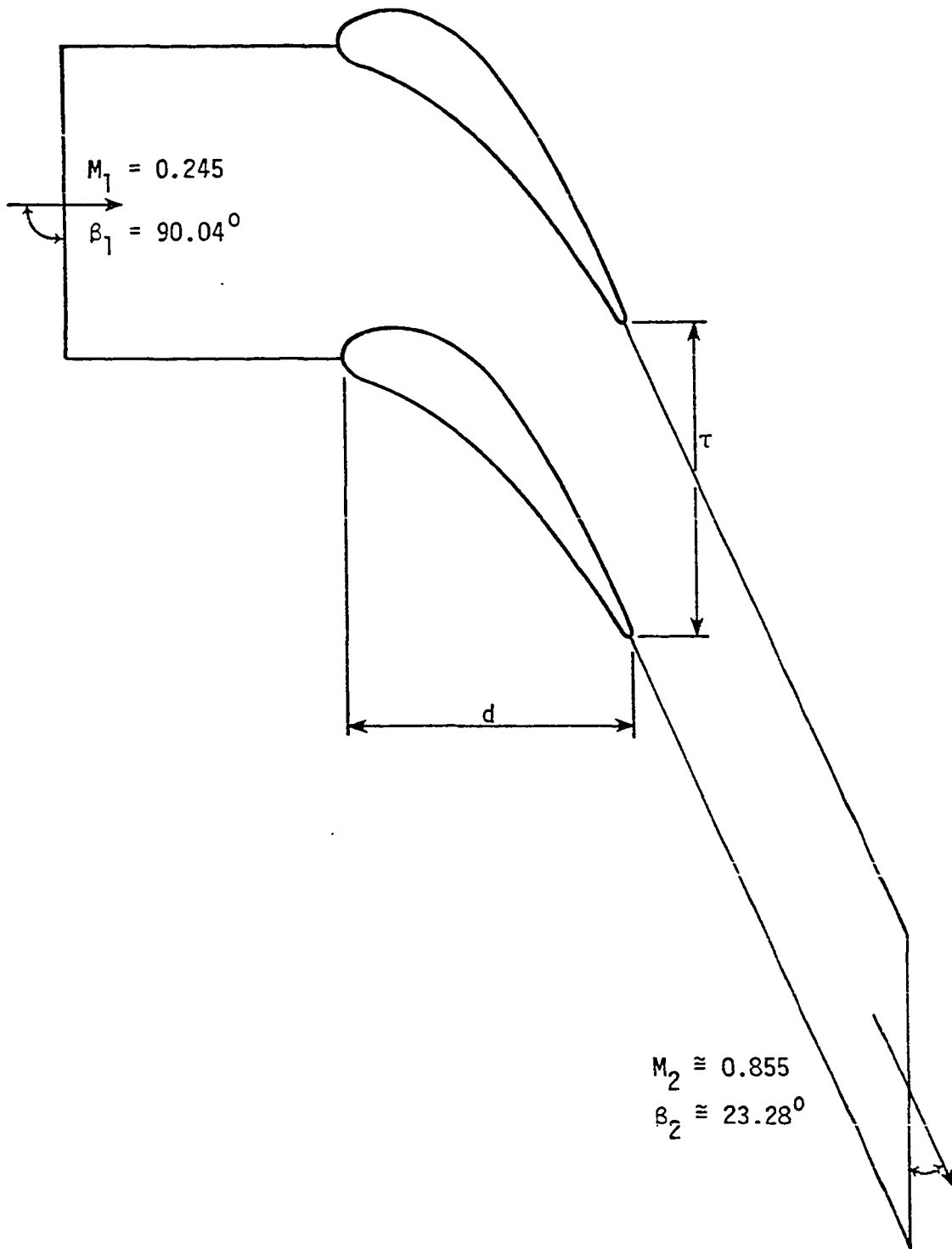


Figure 3.16. Geometry and calculation region for Huffman et al. (1971) turbine nozzle cascade. $\tau/B_x = 1.13$, $d/B_x = 0.992$, M_1 , β_1 , M_2 , and β_2 are experimental values.

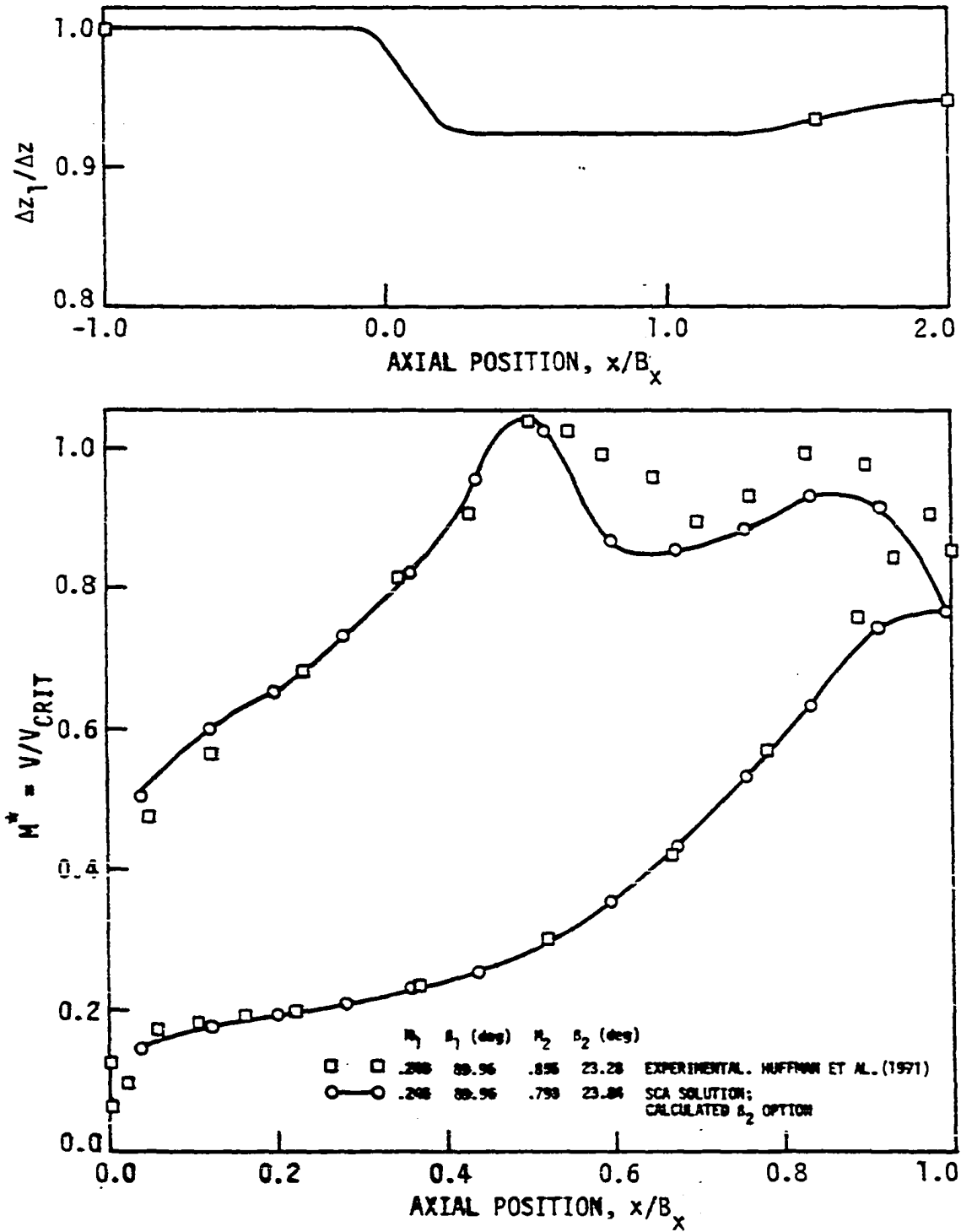


Figure 3.17. Comparison of predicted profile velocities and stream sheet thickness distribution with Huffman et al. (1971) data.

The determined distribution also matched the two experimental $\Delta z_1/\Delta z$ points given downstream of the trailing edge. Upstream of the leading edge, the endwall boundary layer was assumed to be negligible, giving, therefore, $\Delta z_1/\Delta z = 1.0$ in this region. Inside the cascade and downstream, $\Delta z_1/\Delta z < 1.0$ was required, indicating an increase in stream sheet thickness. This seemingly unusual behavior may be explained in terms of three-dimensional endwall flow effects and penetration of secondary flows which are known to affect the midspan two-dimensionality in cascades having moderate to low aspect ratios (the aspect ratio for this cascade was not reported).

In an experimental investigation of three-dimensional flow in a large-scale turbine cascade, Langston et al. (1977) found that the flow is predominated by three-dimensional separation of the endwall boundary layer just ahead of the leading edge of the airfoil. The entering boundary layer rolls up to form a strong passage vortex which interacts with the airfoil boundary layer on the suction side of the cascade passage. A new endwall boundary layer is formed downstream of the three-dimensional separation. This boundary layer is extremely thin, having a strong cross flow component from pressure to suction side within the passage. As a consequence, the pressure distribution on the airfoils is modified from a potential distribution through the three-dimensional effects due to the endwalls, with a pronounced "unloading" of the distributions as the endwall is approached. This effect may be evident along the entire span of the airfoil for low aspect ratio cases.

Lines of constant Mach number in the flow field for Example E3 are shown in Fig. 3.18. A strong acceleration around the airfoil leading edge on the suction side and relatively uniform flow on the pressure side are indicated by the contours. Also, an approximately uniform distribution of Mach number is shown downstream of the throat. The final leading- and trailing-edge wedge positions, achieved after periodicity of the flow was satisfied for the SCA solutions, are also shown in Fig. 3.18. Different trailing edge option surface velocity distributions calculated by SCA are presented in Fig. 3.19. Both distributions are very much the same except close to the trailing edge where the input β_2 results show a stronger reacceleration on the suction side with a second transonic region indicated. Also, it is noted that the velocities are not equal at the trailing edge $q=0$ in the case of the input β_2 option.

The fourth and final example E4 considered an impulse cascade typical of steam turbine rotors. The cascade, presented in Fig. 3.20, was designed with the geometry design program, GDPLS, described in Chapter 2. The purpose of this example was to compare numerical solutions from SCA with those from the blade-to-blade program (TSONIC) reported by Katsanis (1969). The TSONIC results, using steam properties, were reported by Hamm (1980).

Convergence of the SCA solution was easily obtained in this example by using the normal calculated damping factor. For SCA computations, the steam was assumed to be a perfect gas with a specific heat ratio of 1.308.

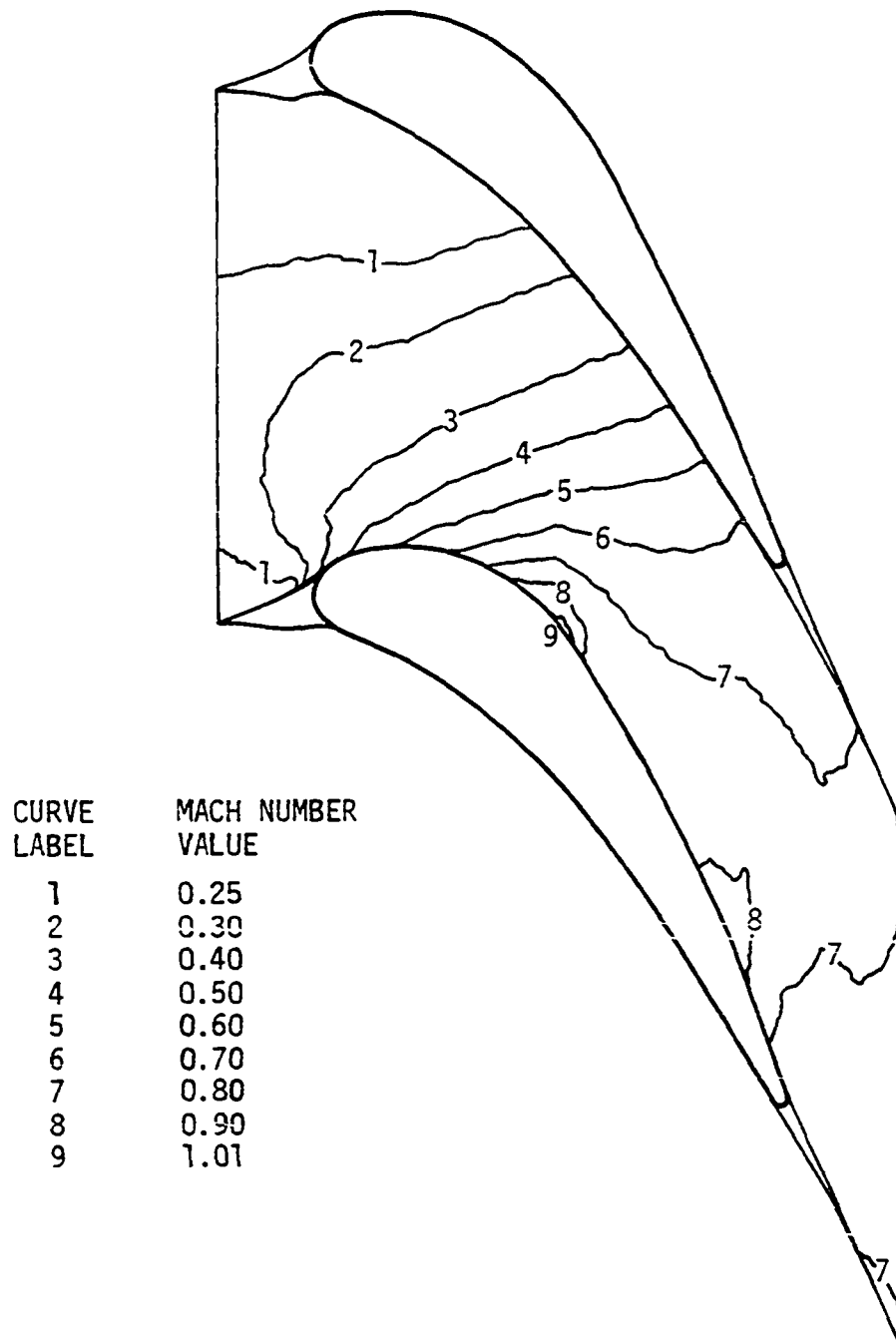


Figure 3.18. Contours of computed Mach number. Huffman et al. (1971) turbine nozzle cascade.

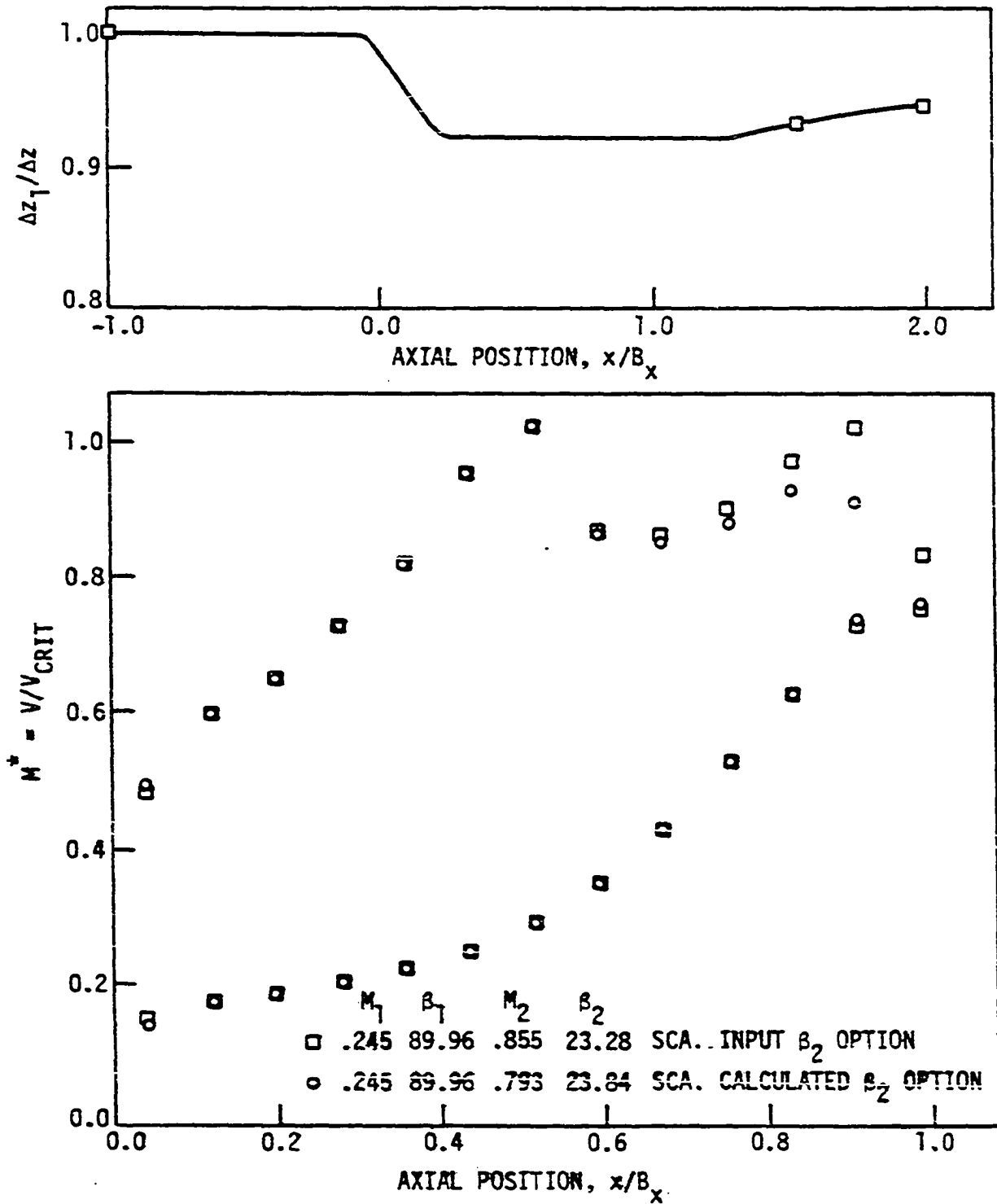


Figure 3.19. Comparison of SCA predicted profile velocity distributions. Different trailing edge options.

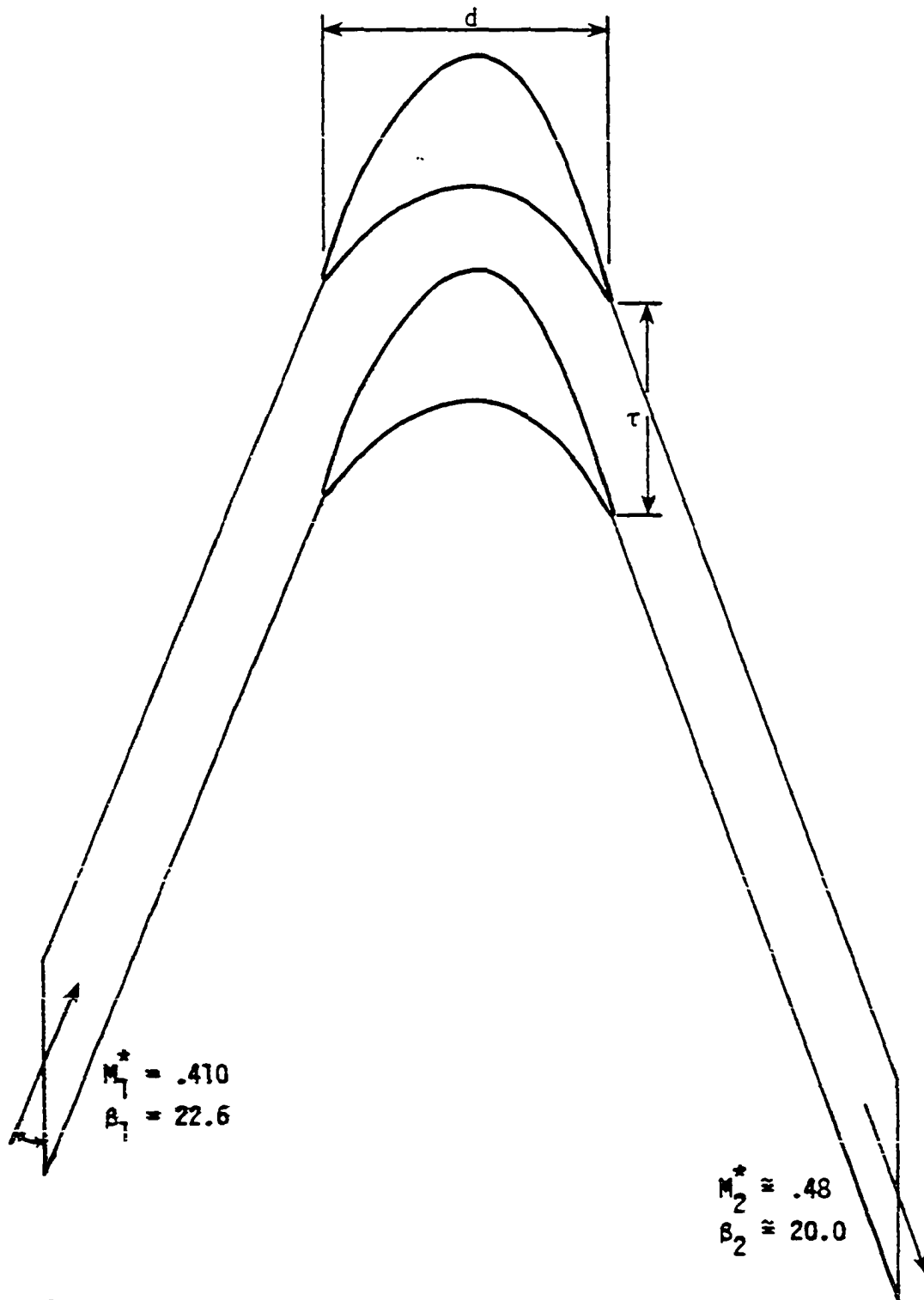


Figure 3.20. Geometry and calculation region for impulse turbine rotor cascade. $\tau/B_x = 0.7348$, $d/B_x = 0.992$, M_1^* , β_1 , M_2^* , and β_2 are design values.

The distributions of the ratio of surface local velocity to critical velocity at two different incidence angles are shown in Figs. 3.21 and 3.22. The comparisons with TSONIC are very encouraging as can be seen in these figures. A trailing edge problem with TSONIC can also be observed which consists of erratic prediction of velocities in this region if the input β_2 is not close to the value satisfying trailing edge periodicity. It is interesting to note that, for the specified total inlet conditions ($T_{01} = 466.8$ K and $P_{01} = 413.69$ kPa abs (60 psia)), the use of steam (real gas) properties in TSONIC did not appreciably alter the solution flow field from that calculated by SCA using perfect gas relationships.

The computations were carried out on the VAX PDP-11 and on the ITEL-AS6 computers of Iowa State University. Computational details are presented in Table 3.1 below.

Table 3.1. SCA Computational Details

Example	β_2	No. of outer iterations	Avg. No. of inner iterations	CPU seconds	
				VAX PDP-11	ITEL-AS6
E1	cal.	4	30	77	---
E1	in.	6	27	100	---
E2	cal.	6	6	33	---
E2	in.	4	7	29	---
E3	cal.	10	26	230	---
E3	in.	6	50	252	---
E4, $i=5.46^\circ$	cal.	10	6	46	10.83
E4, $i=0.00^\circ$	cal.	10	6	50	12.83

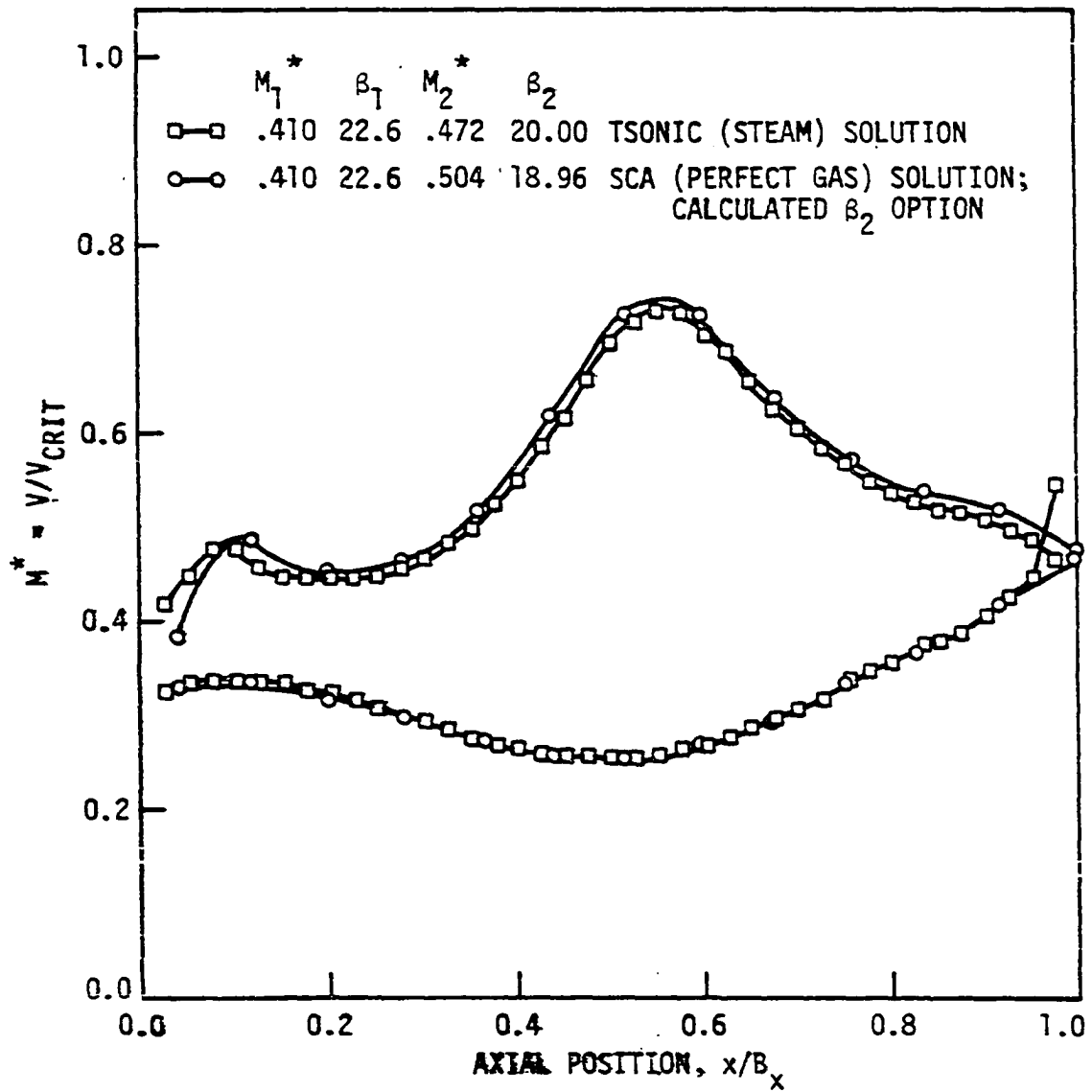


Figure 3.21. Comparison of predicted profile velocities with TSONIC results. Incidence of 5.46° .

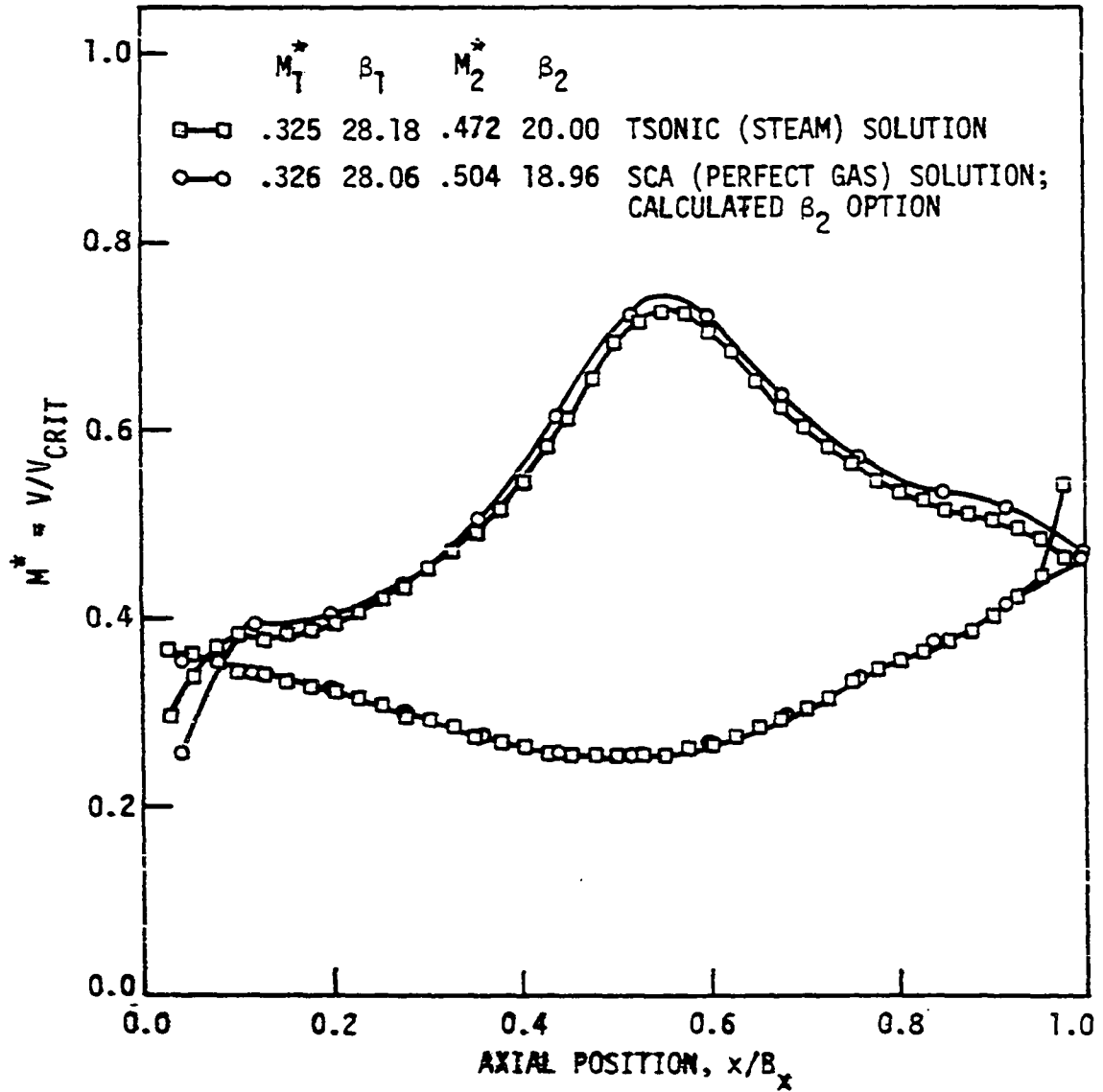


Figure 3.22. Comparison of predicted profile velocities with TSONIC results. Incidence of 0.0° .

4. INVISCID REANALYSIS OF LEADING EDGE

4.1. Introduction

The importance of accurate and detailed calculation of leading edge inviscid flow has long been recognized by workers engaged in the prediction of blade-to-blade flows. Hansen (1978), for instance, points out that to model laminar separation the inviscid leading edge velocity distribution must be accurately calculated, particularly the magnitude of the peak velocity.

This chapter presents the details of the reanalysis procedure developed in this investigation and checks its validity by comparing the numerical results with theoretical data. Also, a brief review is made of numerical techniques previously used, or that can be used, in this kind of magnified flow analysis around the airfoil leading edge.

4.2. Review of Previous Reanalysis Techniques

Katsanis and McNally (1969) were the first to produce a computer program to calculate velocities in a magnified region in a blade-to-blade plane. The analysis used a finite difference technique in terms of the stream function with an orthogonal grid (Grid A in Fig. 4.1). Two problems can be envisioned with Grid A. First, the grid spacing is refined in the x and y directions; however, the distance along the airfoil between grid lines is not refined to the same degree, especially in regions of high surface inclination such as at the leading edge.

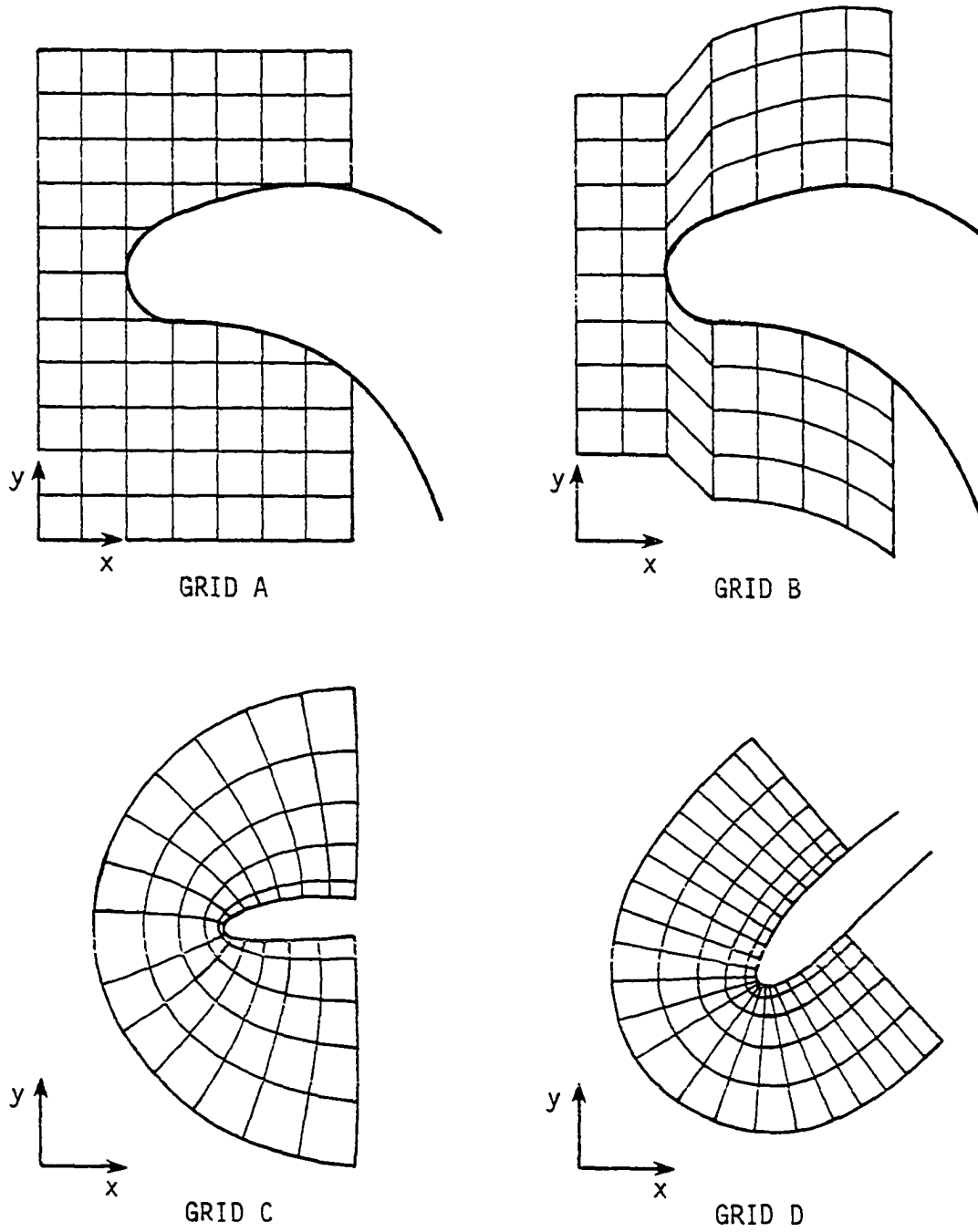


Figure 4.1. Reanalysis meshes.

As a result, the velocity peak might still be missed even though the mesh has been refined. Second, the surface velocities must be calculated from information at adjacent grid points. The results obtained are likely to be inaccurate, particularly in regions of high velocity gradient such as at the leading edge. Marsh (1968) has reported a finite difference scheme in terms of stream function which partially alleviated this latter problem by locating grid points on the airfoil. The grid is made up by pitchwise lines and lines following the airfoil profile as shown for Grid B in Fig. 4.1. This nonorthogonal mesh has not been used for reanalysis purposes as yet, but its application should not present difficulties.

The body-fitted Grid C in Fig. 4.1 was reported by Thompson et al. (1974). This nonorthogonal mesh is generated by taking the coordinate system to be the solution of an elliptic partial differential system in the physical plane with Dirichlet boundary conditions on all boundaries. The grid in the physical plane is then transformed into a rectangular mesh and the transformed stream function equation solved there by finite difference technique. This procedure solves the problems inherent to Grids A and B; however, the solution is rather involved due to the attendant transformations.

Caspar et al. (1979) solved the magnified or reanalysis problem using the body-fitted orthogonal mesh Grid D shown in Figure 4.1. The solution is carried out in the physical plane by means of a finite area technique in terms of the velocity potential. This procedure has

the advantages of the body-fitted mesh without incurring complicated transformations and is perhaps the best choice among the techniques reviewed here.

4.3. The Present Finite Area Reanalysis Method (REA)

The reanalysis procedure developed in this investigation for two-dimensional adiabatic flows is based on the finite area techniques presented by Caspar et al. (1979) and by McDonald (1971). The Grid D in Fig. 4.1 is used and the solution obtained in terms of the stream function, directly using the information provided by the global SCA. High subsonic flow can be handled, allowing also for changes in stream sheet thickness.

Results obtained in the global SCA are used to interpolate for values of stream function on the boundaries of the assigned computational region. In the interpolation procedure, advantage is taken of the fact that smoothed quartics used in the global SCA approximate the streamlines.

4.3.1. Governing equations

The equations to be solved must be valid not only around the leading edge, but for any small region within the cascade flow field. The two-dimensional continuity equation and the irrotationality condition are combined to obtain the equation to be approximated with the finite area technique.

The two-dimensional continuity equation, as modified by Wu (1952)

to include stream sheet thickness, Δz , is

$$\frac{\partial}{\partial x} (u\rho\Delta z) + \frac{\partial}{\partial y} (v\rho\Delta z) = 0. \quad (4.1)$$

A stream function, ψ , can be defined by

$$u = K \frac{\rho_{01}}{\rho} \frac{\Delta z_1}{\Delta z} \frac{\partial \psi}{\partial y}, \quad v = -K \frac{\rho_{01}}{\rho} \frac{\Delta z_1}{\Delta z} \frac{\partial \psi}{\partial x} \quad (4.2)$$

where K is a normalizing constant to be determined from the periodicity conditions imposed on u , v , $\frac{\rho_{01}}{\rho}$ and $\frac{\Delta z_1}{\Delta z}$. Thus,

$$\frac{\partial \psi}{\partial x} (x, y+\tau) = \frac{\partial \psi}{\partial x} (x, y) \quad (4.3)$$

$$\frac{\partial \psi}{\partial y} (x, y+\tau) = \frac{\partial \psi}{\partial y} (x, y). \quad (4.4)$$

Therefore,

$$\psi(x, y+\tau) - \psi(x, y) = \text{constant}. \quad (4.5)$$

K is now chosen so that the constant in Eqn. 4.5 is unity, i.e.,

$$K = u_1 \rho_1 \tau / \rho_{01} \quad (\text{see Appendix D}).$$

For two-dimensional irrotational flow

$$\frac{\partial v}{\partial x} = \frac{\partial u}{\partial y}. \quad (4.6)$$

If the following density ratio is defined

$$\sigma = \frac{\rho_{01}}{\rho} \frac{\Delta z_1}{\Delta z}. \quad (4.7)$$

then, from Eqns. 4.2, 4.6, and 4.7, we obtain

$$\frac{\partial}{\partial y} \left(\sigma \frac{\partial \psi}{\partial y} \right) + \frac{\partial}{\partial x} \left(\sigma \frac{\partial \psi}{\partial x} \right) = 0 \quad (4.8)$$

or,

$$\nabla \cdot (\sigma \nabla \psi) = 0. \quad (4.9)$$

The isentropic relationship between density ratio and Mach number can now be written as

$$\frac{\rho_0}{\rho} = \left(1 - \frac{\gamma-1}{2c_0^2} K^2 |\nabla \psi|^2 \sigma^2\right)^{\frac{-1}{\gamma-1}} \quad (4.10)$$

where c_0 is the speed of sound at the stagnation temperature.

From the perfect gas law and for constant stagnation temperature, a total pressure ratio, η , can be defined as

$$\eta = \frac{\rho_0}{\rho_{01}} = \frac{p_0}{p_{01}}. \quad (4.11)$$

Therefore, Eqn. 4.10 becomes

$$q \sigma^{\gamma-1} - q a \sigma^{\gamma+1} |\nabla \psi|^2 - 1 = 0 \quad (4.12)$$

where

$$q = \left(\eta \frac{\Delta z}{\Delta z_1}\right)^{\gamma-1} \quad (4.13)$$

and

$$a = \frac{\gamma-1}{2c_0^2} K^2. \quad (4.14)$$

The constant "a" can also be written after some manipulation as

$$a = \tau^2 \sin^2 \beta_1 (\sigma_1^{\gamma-1} - 1) / \sigma_1^{\gamma+1} \quad (4.15)$$

Equation 4.9, which is a combination of the continuity equation and the irrotationality condition, and Eqn. 4.12, which is a form of the energy equation, are used to perform the reanalysis with the constant "a" given by Eqn. 4.15. It should be noted that the constant "a" links the reanalysis with the global solution via the upstream boundary conditions. The elliptic boundary value problem to be solved is illustrated in Fig. 4.2.

4.3.2. Computational flow field

The reanalysis computational flow field with two computational elements noted is shown in Fig. 4.3. The extension d_1 of the mesh in the axial direction, which can be varied, is required to be large enough so that the normal boundaries of the mesh are far enough removed from the leading edge so that they have negligible effect on the flow close to the leading edge. Similarly, the extension d_2 normal to the airfoil (also variable) should be large enough so that the leading edge wedge from the global solution lies inside the computational region. Also, d_2 must be controlled to avoid running the mesh into the next airfoil.

The mesh is made up of 45 lines normal to the airfoil and 9 transverse curves (including the airfoil contour) around the profile. The point spacing along the normals is exponential, increasing from the airfoil towards the outer boundary. The spacing along the airfoil is uniform around the leading edge circle and then exponential from the

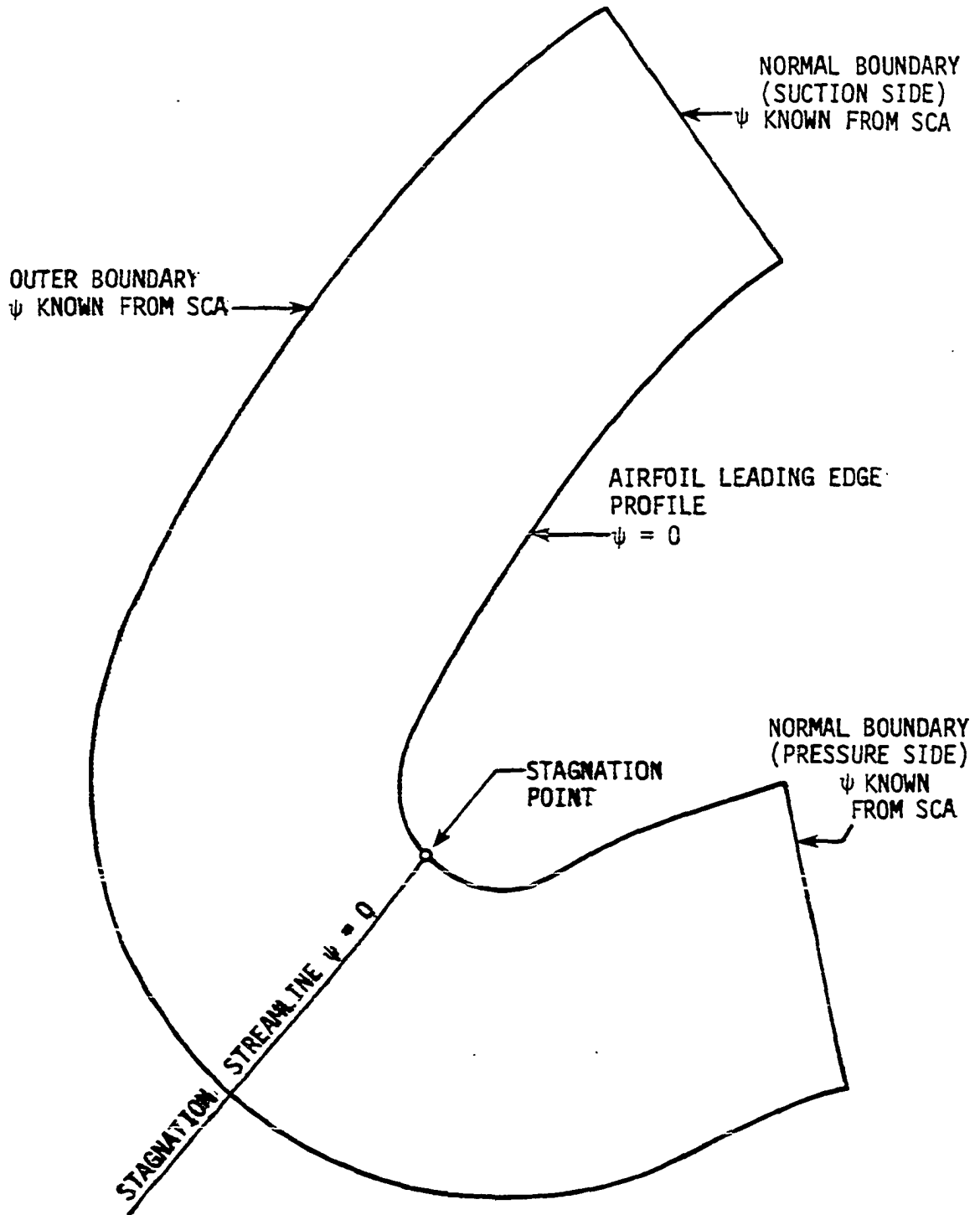


Figure 4.2. Solution domain for the reanalysis boundary value problem. Equations 4.9 and 4.12 are solved for stream function ψ and density ratio σ at interior points.

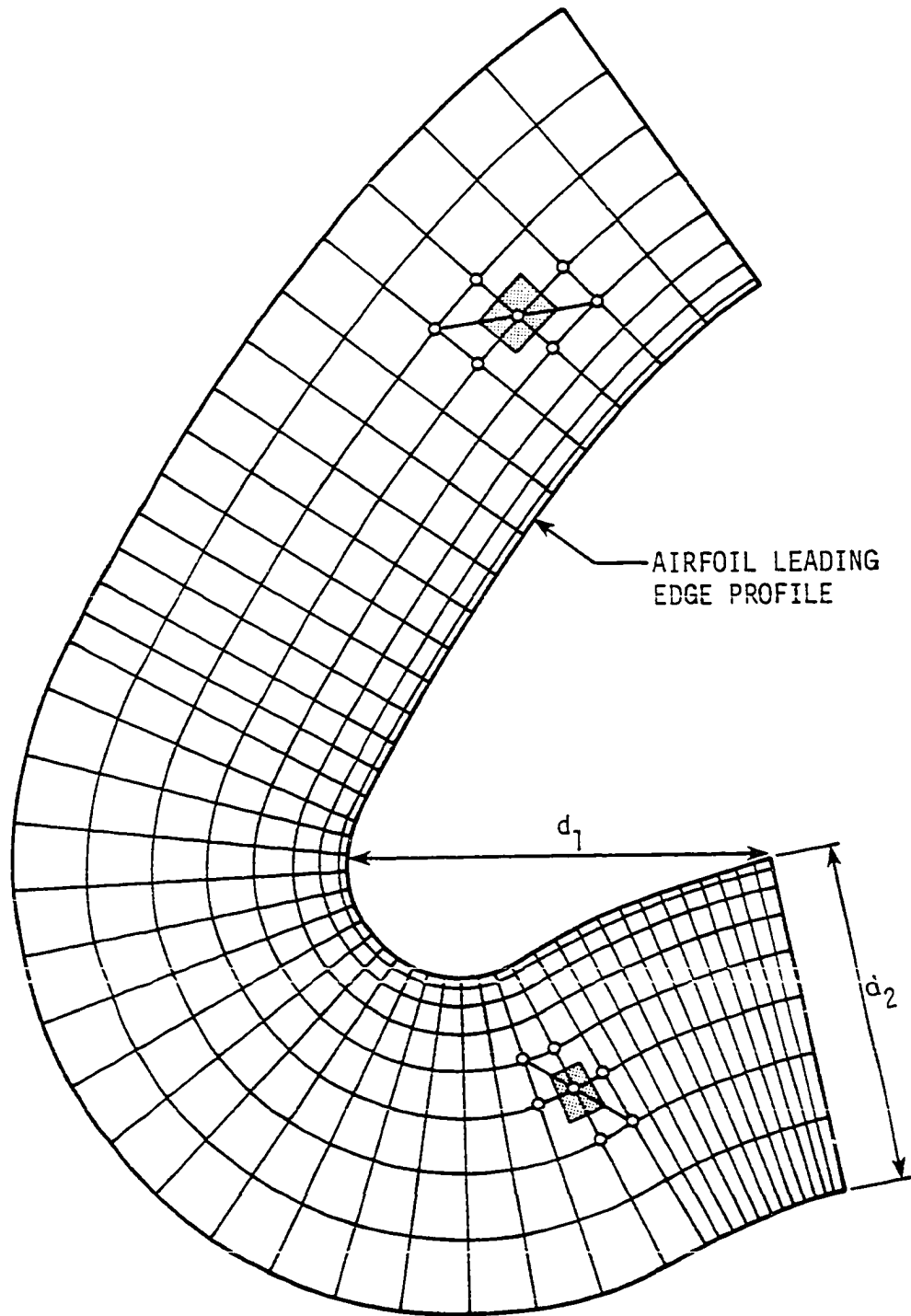


Figure 4.3. Reanalysis computational mesh. Two example computational elements are shown.

circle tangency points to the normal mesh boundaries.

The main advantages of this grid are:

- (i) The spacing of the normal lines along the airfoil surface allows high resolution in determining the velocity peak and the stagnation point.
- (ii) The location of grid points on the airfoil expedites the accurate calculation of surface velocities.

Initially, a certain number of normals are assigned to the leading edge circle. Half of the remaining normals are then assigned to the suction and pressure sides, respectively. A graphical display should be obtained to check the resultant mesh; in particular, any cross over of normals must be avoided.

4.3.3. Numerical approximation

The transverse curves of the mesh are constructed by joining the mesh points established on the normals with straight lines. The mesh thus formed is nonorthogonal; however, deviation from orthogonality is small, decreasing as the spacing of the normals is refined. Finite area equations are written at each mesh point in terms of quantities at the mesh point and at six neighboring points such as shown in Fig. 4.4.

Around each mesh point, Q_0 , with neighbors, Q_1, \dots, Q_6 , a six-sided polygon, D_Q , is constructed whose sides are the perpendicular bisectors of the neighbor lines defined in Fig. 4.4. Equation 4.9 is integrated over D_Q after first converting it to a line integral around

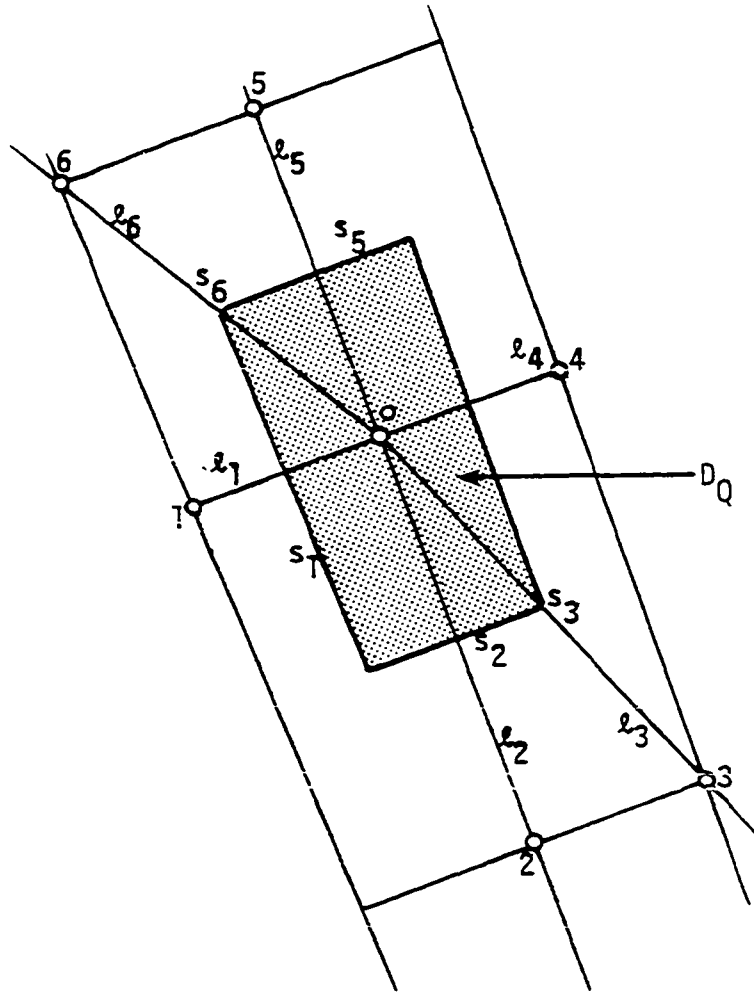


Figure 4.4. Geometry of the computational element. Lines and sides of the element are denoted l and s , respectively.

the boundary of D_Q using Gauss' integral theorem, and then approximating the result as follows:

$$\int_{D_Q} \nabla \cdot (\sigma \nabla \psi) \, dA = 0 \quad (4.16)$$

or

$$\int_{D_Q} \nabla \cdot (\sigma \nabla \psi) \, dA = \oint_{D_Q} \sigma \frac{\partial \psi}{\partial n} \, ds \quad (4.17)$$

and

$$\oint_{D_Q} \sigma \frac{\partial \psi}{\partial n} \, ds \approx \sum_{m=1}^6 \bar{\sigma}_m \frac{\psi_m - \psi_0}{\ell_m} s_m = 0. \quad (4.18)$$

Here, $(\psi_m - \psi_0)/\ell_m$ is a first order approximation of the derivative of ψ in the direction of the outward normal and $\bar{\sigma}_m$ is the average, $\frac{1}{2}(\sigma_m + \sigma_0)$.

If Eqn. 4.18 is satisfied at each mesh point, mass continuity is locally preserved. Moreover, since the mesh polygons cover the reanalysis region, mass continuity is globally preserved. On a uniform rectangular mesh, approximation 4.18 reduces to the well known second order accurate five point finite difference approximation. The polygon D_Q deviates very little from a rectangle due to the "quasi-orthogonality" of the mesh. Therefore, the approximation is expected to remain second order accurate; this is shown in Caspar et al. (1979). The sides s_3 and s_6 are typically several orders of magnitude smaller than the remaining sides. This fact considerably alleviates the problem of negative areas which might arise with re-entrant closure of the polygon D_Q in some cases, or if the neighboring mesh points are not properly chosen.

An important advantage of Eqn. 4.18 is that the approximation of only first derivatives is required.

4.3.4. General description of calculation

A general discussion of the reanalysis procedure is given below. A flow diagram of the programmed reanalysis method (REA) is shown in Fig. 4.5.

1. The body-fitted mesh is constructed from the known airfoil geometry, the mesh extensions in the axial direction and normal to the profile, and the number of normals assigned around the leading edge circle. Values of stream function ψ and density ratio σ are then interpolated on the boundaries of the computational mesh from the global SCA results. The stream function is set to zero on the airfoil.

2. The mesh points at which ψ is to be found are ordered, P_1, P_2, \dots, P_L ($L = 301$) outward along the normal lines starting on the normal next to the boundary on the pressure side and ending on the normal next to the boundary on the suction side. This way of numbering the mesh points ensures a densely packed banded coefficient matrix. Equation 4.18 and the appropriate boundary conditions are then applied at each mesh point to set the system

$$A \bar{\psi} = \bar{b}. \quad (4.19)$$

Here, $\bar{\psi}$ is the vector of ψ values, \bar{b} the vector of zeros or boundary information, and A is an $L \times L$ block tridiagonal coefficient matrix.

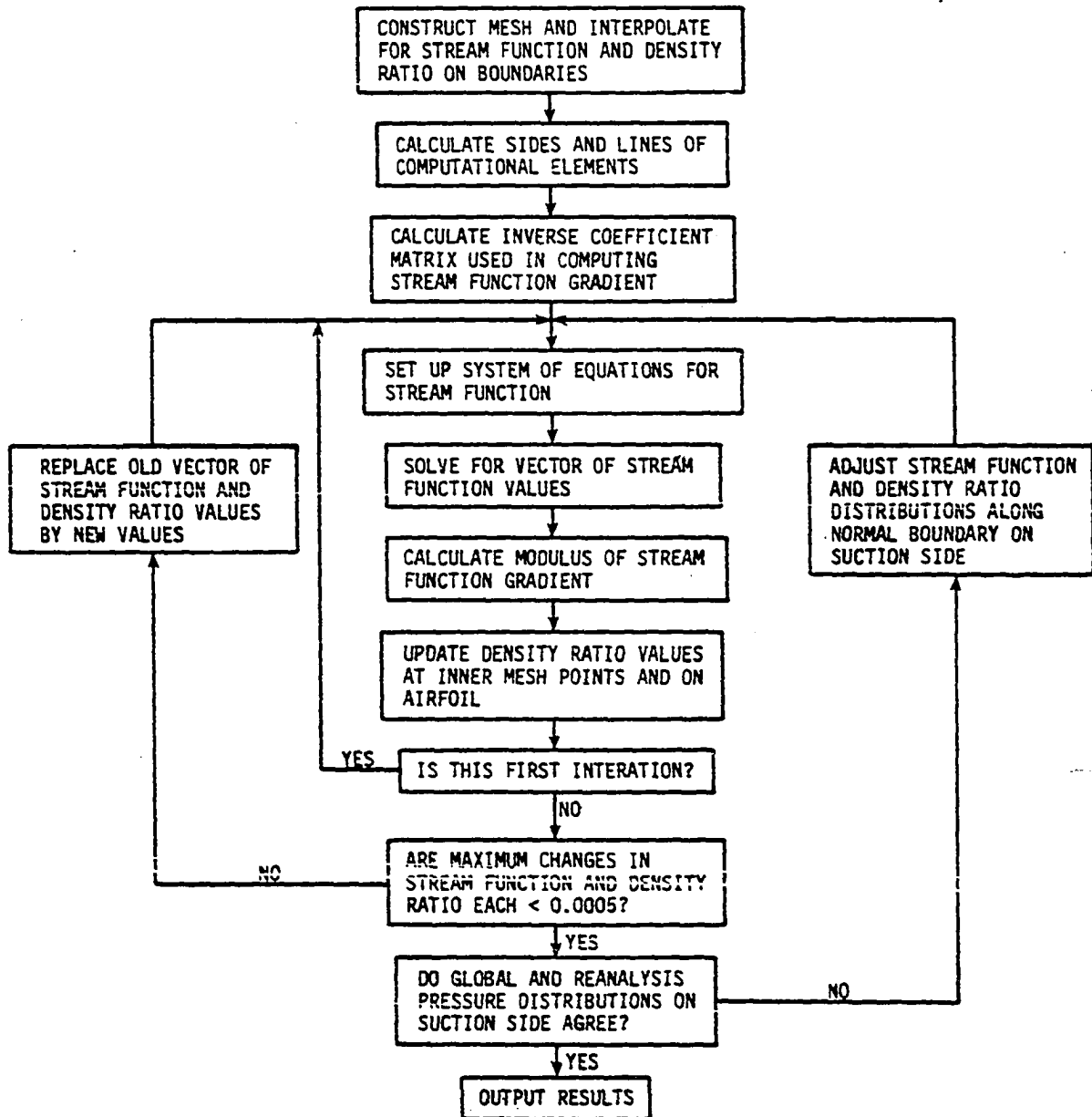


Figure 4.5. General computing flow diagram for reanalysis program (REA).

3. Writing Eqn. 4.18 on mesh points next to the boundaries involves σ values on the boundaries. These values are obtained by interpolation from the global SCA results using the same procedure as used for the stream function. As an alternative, σ values could be assumed on the boundaries and updated as the calculation proceeds. However, as will be seen later, this procedure involves the calculation of $|\nabla\psi|$ on the boundaries which is difficult. This problem does not arise for points on the airfoil where $|\nabla\psi|$ can be accurately calculated due to the close point spacing and the fact that $\nabla\psi$ acts normal to the airfoil. The smallest σ value on the mesh boundaries is then assumed to exist throughout the inner mesh points and on the airfoil to start the calculations.

4. The coefficient matrix A , which depends upon mesh geometry and σ , and the vector \bar{b} containing the boundary information are now computed. The block tridiagonal system 4.19 is then solved using an algorithm for a banded system of linear equations presented by Dongarra et al. (1979). The solution of the system 4.19 provides a new vector $\bar{\psi}$.

5. The new vector $\bar{\psi}$ is used to calculate $|\nabla\psi|$ at every inner mesh point and on the airfoil. Also σ can now be updated through Eqn. 4.12 using Newton's method to solve for the new σ 's starting from the old values. This is done at every mesh points where a new $|\nabla\psi|$ is obtained.

6. Convergence of the iteration procedure is checked at this point and the calculation continued with Step 4 if necessary. The convergence criteria are that the maximum changes in ψ and σ from one iteration to the next be both less than 0.0005. Thus, a minimum of two iterative steps is indicated even for the linear incompressible case.

4.3.5. Interpolation of boundary values

The interpolation procedure used to obtain the stream function, ψ , and density ratio, σ , on the mesh boundaries is described below in connection with Fig. 4.6. The procedure takes advantage of the fact that the smoothed quartics used in the global solution approximate the streamlines.

The interpolation is initiated by locating the first q-o upstream of the point (P) at which ψ is to be found together with the streamline immediately below the point. On this streamline, it is necessary to interpolate the y coordinate, y_b , at x_p (measured from the first q-o upstream of point P). This is done by fitting a quartic of the form

$$y = ax^4 + bx^3 + cx^2 + dx + y_0 \quad (4.20)$$

through the equally spaced points of coordinates y_{-2} , y_{-1} , y_0 , y_1 and y_2 giving the following relationship for the coefficients:

$$a = \frac{0.5y_{-2} - 2y_{-1} + 3y_0 - 2y_1 + 0.5y_2}{12h^4} \quad (4.21)$$

$$b = \frac{-y_{-2} + 2y_{-1} - 2y_1 + y_2}{12h^3} \quad (4.22)$$

$$c = \frac{-0.5y_{-2} + 8y_{-1} - 15y_0 + 8y_1 - 0.5y_2}{12h^2} \quad (4.23)$$

$$d = \frac{y_{-2} - 8y_{-1} + 8y_1 - y_2}{12h} \quad (4.24)$$

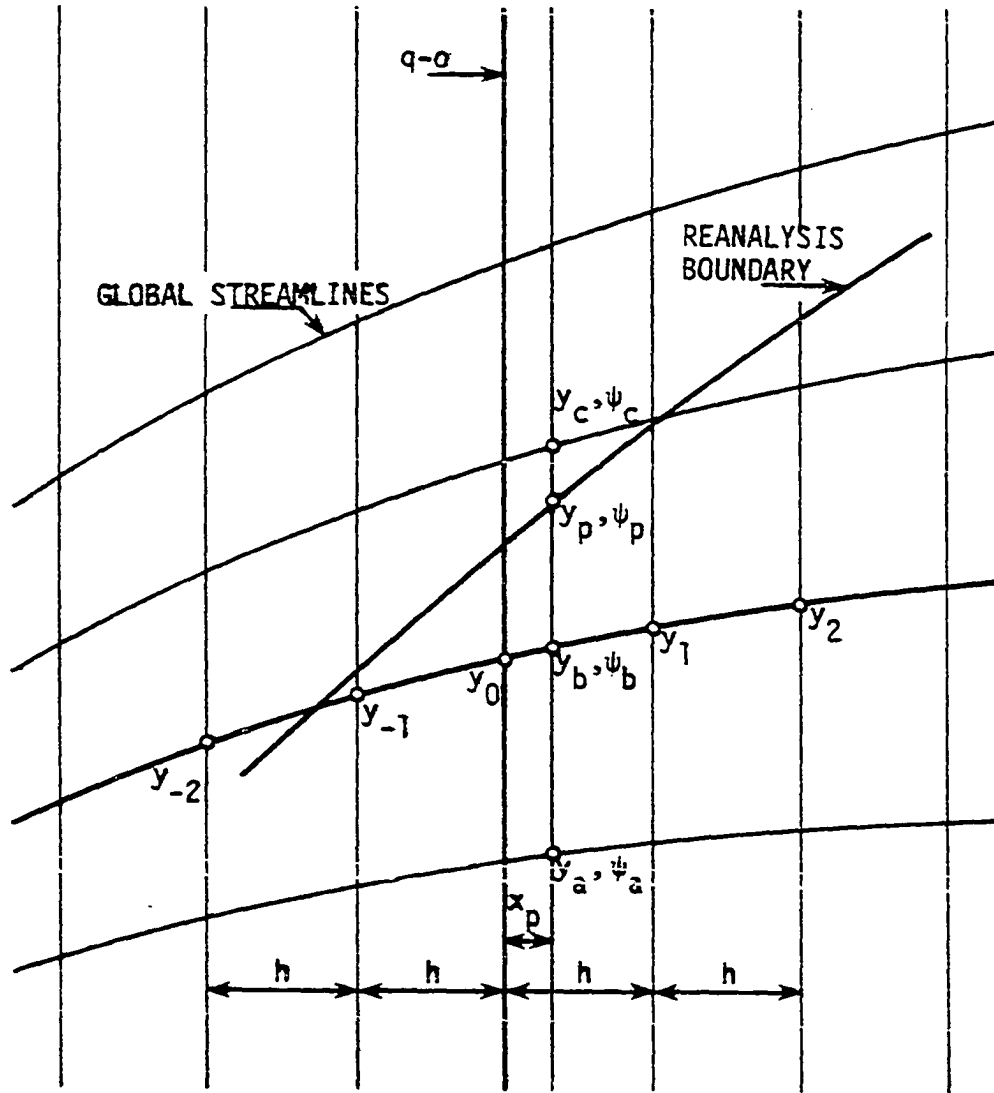


Figure 4.6. Basic reanalysis interpolation scheme.

The coordinate y_b interpolated with Eqn. 4.20 is subsequently smoothed with the general smoothing formula of Eqn. 3.56. The same procedure is followed to obtain the coordinate y_c of point c on the streamline immediately above point P, and the coordinate y_a of point a below point b. The points a, b, and c of coordinate (y_a, ψ_a) , (y_b, ψ_b) , and (y_c, ψ_c) then provide the necessary information to set up a three-point Lagrangian interpolation polynomial to solve for ψ_p knowing y_p .

This procedure worked well for the outer mesh boundary; however, erratic values were interpolated on the normal boundaries, particularly at points next to the airfoil.

A practical solution to the normal boundary interpolation problem was found when the reanalysis results for two assumed distributions of ψ on these boundaries were compared. First, the distribution of ψ was calculated by fitting a second order polynomial through the point on the airfoil and the two outermost points on the normal boundary. Second, a linear distribution of ψ between the airfoil point and the next outermost point was assumed. Figure 4.7 compares the reanalysis results for airfoil pressure distribution obtained with the two assumed ψ distributions on the boundary normal to the suction side. As can be observed, the effects of different ψ distributions do not propagate far into the upstream region, i.e., the solution is dominated by the outer boundary. Also, the correct distribution of ψ is seen to lie between the linear and the quadratic distributions assumed above.

An iterative procedure was then devised wherein the differences

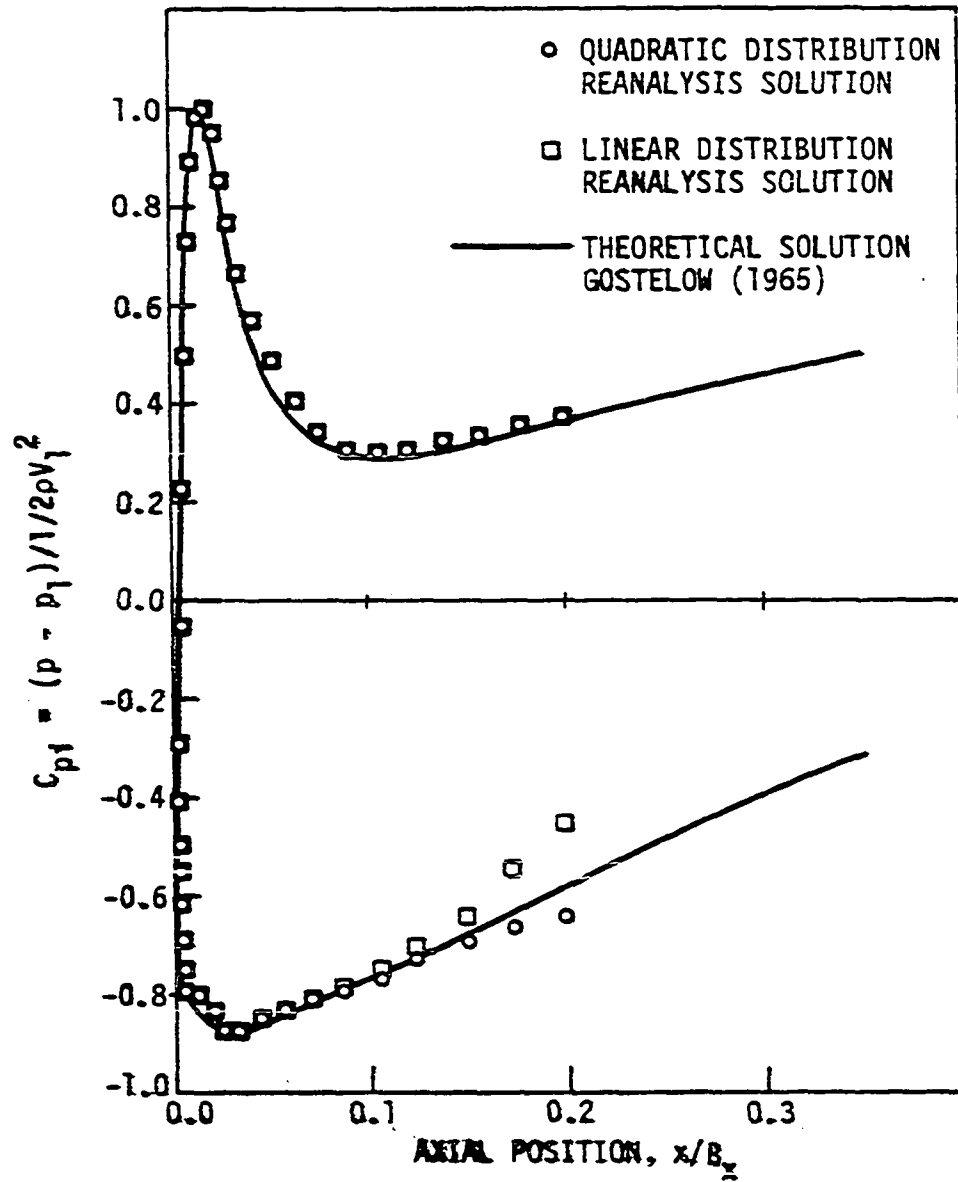


Figure 4.7. Effects of ψ distribution along boundary normal to suction side on computed airfoil pressure distribution.

between the linear and the quadratic ψ values were decreased by a constant factor and the reanalysis performed with this "in between" distribution. The obtained reanalysis pressure coefficient was compared with the global pressure coefficient on the airfoil. The iteration stopped when both pressure coefficients were very similar or when the allowed number of iterations was exceeded. This iteration was set for the suction side only, which was the side most susceptible to the ψ distribution along the normal boundary. The quadratic distribution was used for the pressure side even though a similar iteration could be used.

A similar procedure was used to adjust the σ distribution along the normal boundaries in the compressible case with the airfoil σ value obtained by interpolation from the global solution.

Finally, the reanalysis results on the last three normals to the suction side and on the first two normals to the pressure side were neglected. Therefore, the valid reanalysis results go from normal number 3 through normal number 42.

4.3.6. Approximation of stream function gradient

The derivatives $\partial\psi/\partial x$ and $\partial\psi/\partial y$ are needed to calculate the modulus of the gradient of the stream function, $|\nabla\psi|$, which in turn is used to update σ with Eqn. 4.12.

The approach followed in this investigation was to approximate ψ in the neighborhood of a mesh point by a quadratic polynomial of the form

$$\psi = a_1 + a_2x + a_3y + a_4xy + a_5x^2 + a_6y^2 \quad (4.25)$$

The coefficients in Eqn. 4.25 are obtained by a least squares fit through the data at the mesh point and its eight natural neighbors. The derivatives of ψ are then approximated by the derivatives of this quadratic.

The 6 x 6 system of equations formed at each mesh point when the least squares theory is applied (see Appendix E) can be written in the form

$$S \bar{a} = \bar{f} \quad (4.26)$$

S in Eqn. 4.26 is the coefficient matrix and depends only on the x, y coordinates of the eight natural neighbors; therefore, its inverse can be calculated at the beginning of the calculation and stored for subsequent use. The vector \bar{a} contains the unknowns a_1 through a_6 . The vector \bar{f} depends on the values of ψ at the eight natural neighbors and is updated from one iteration to the next.

On the airfoil boundary, the eight nearest neighbor points to the boundary point were used in Eqn. 4.26. The derivatives $\partial\psi/\partial x$, $\partial\psi/\partial y$ were evaluated at the inner mesh points and at the points on the airfoil boundary.

4.3.7. Validation of reanalysis method (REA)

The capabilities of the reanalysis finite area method (REA) were explored by comparing the computed results with available analytical data. Two test cases were considered, one involving the temperature

distribution in a two-dimensional slab, and the other an incompressible adiabatic leading edge flow reanalysis. The main features of the examples are presented below.

In the first test case, the steady state temperature distribution in a two-dimensional slab with constant conductivity was computed. The governing equation for this problem is Laplace's equation

$$\nabla \cdot \nabla T = 0 \quad (4.27)$$

which can be solved theoretically by separation of variables. The purpose of this example was the validation of the different algorithms used in setting up the block tridiagonal system 4.19 to approximate Laplace's equation. Also, the LINPACK banded system solver (see Dongarra et al. (1979)) was tested with respect to accuracy and speed. The geometry of the problem simulates a stretched leading edge reanalysis mesh. Figure 4.8 shows the geometry, computational mesh, and boundary conditions as well as the computed and theoretical temperature distributions along the midline of the slab. As can be observed, the accuracy of the finite area solution is excellent. The banded system solver proved to be extremely quick and accurate, which was the prime requirement of this algorithm in the REA program.

The second test case considered the leading edge reanalysis of the Gostelow (1965) compressor cascade calculated as example E1 with the global streamline curvature analysis. As already mentioned, the analytical solution for this cascade was obtained by conformal mapping.

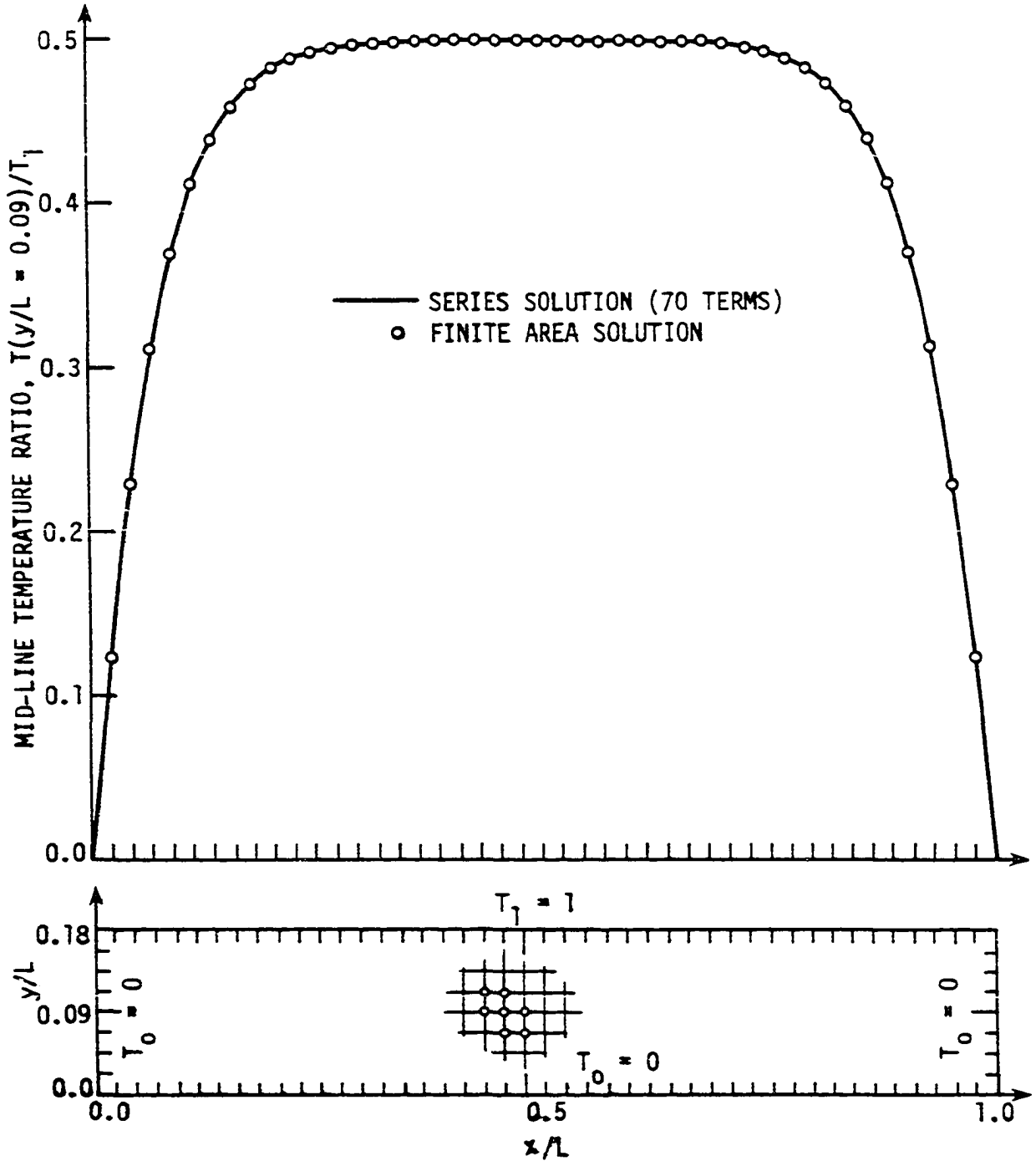


Figure 4.8. Comparison of computed and theoretical solutions for steady state temperature distribution in a two-dimensional slab. The isothermal boundary conditions, computing mesh, and a six-point element used are indicated.

The cascade geometry and the reanalysis computational mesh are shown in Fig. 4.9. The mesh was extended 20% of axial chord in the axial direction and 25% of axial chord in the direction normal to the airfoil.

The predicted reanalysis and global distributions of surface pressure coefficient are compared with theoretical values in Fig. 4.10. As can be seen, essentially perfect agreement in the leading edge region was obtained with the reanalysis. The small oscillation in pressure coefficient values observed around the leading edge suction surface was caused by the spline fit of the airfoil geometry. A smooth spline fit around the leading edge of an airfoil is difficult to achieve, and usually a small ripple in the profile is introduced by the fitting process. A remarkably good resolution of the leading stagnation point can also be observed in Fig. 4.10.

Further REA results in compressible flow situations are compared with experimental data in a later chapter to validate the complete blade-to-blade flow and boundary layer prediction procedure.

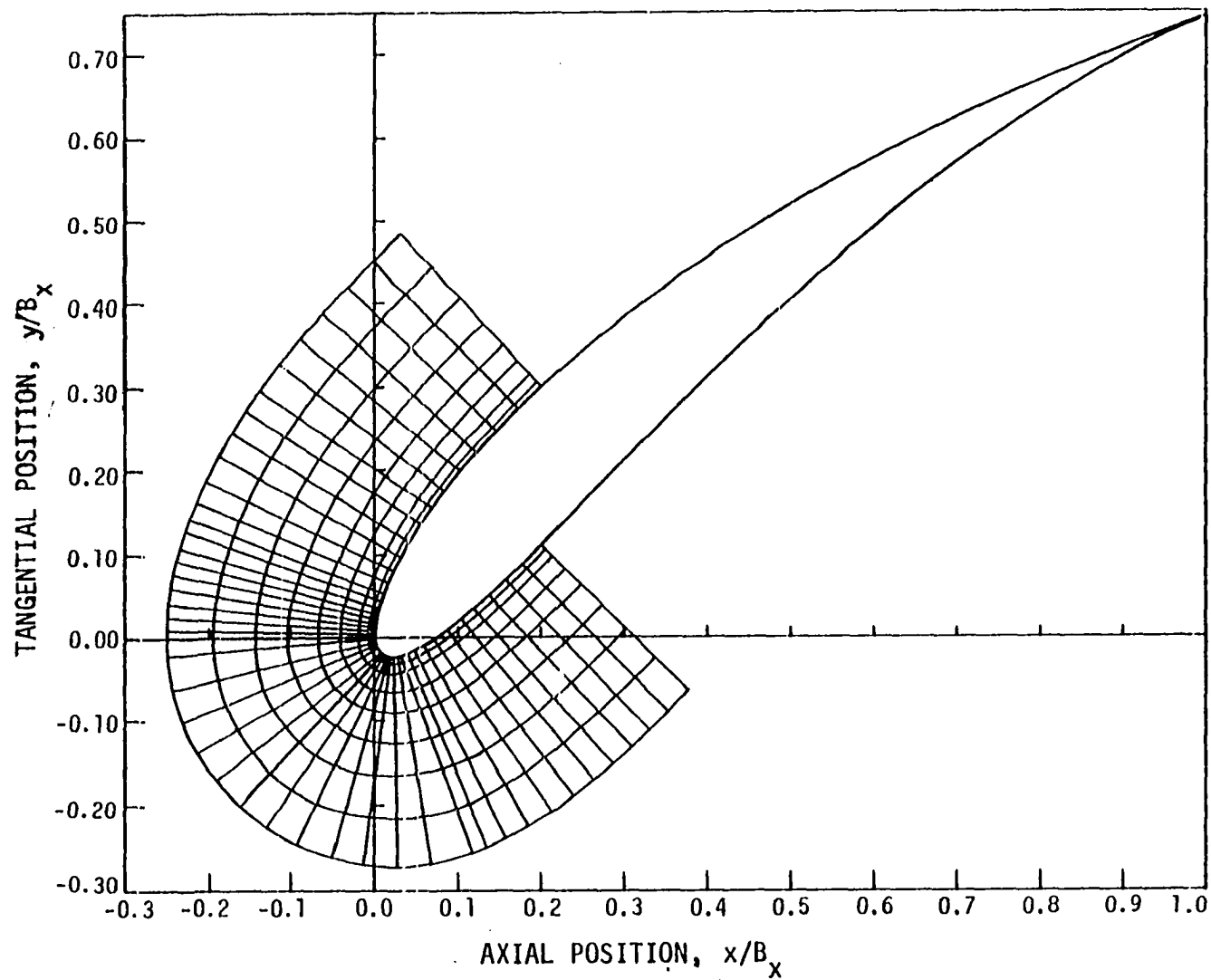


Figure 4:9. Cascade geometry and reanalysis computational mesh for Gostelov (1965) cascade.

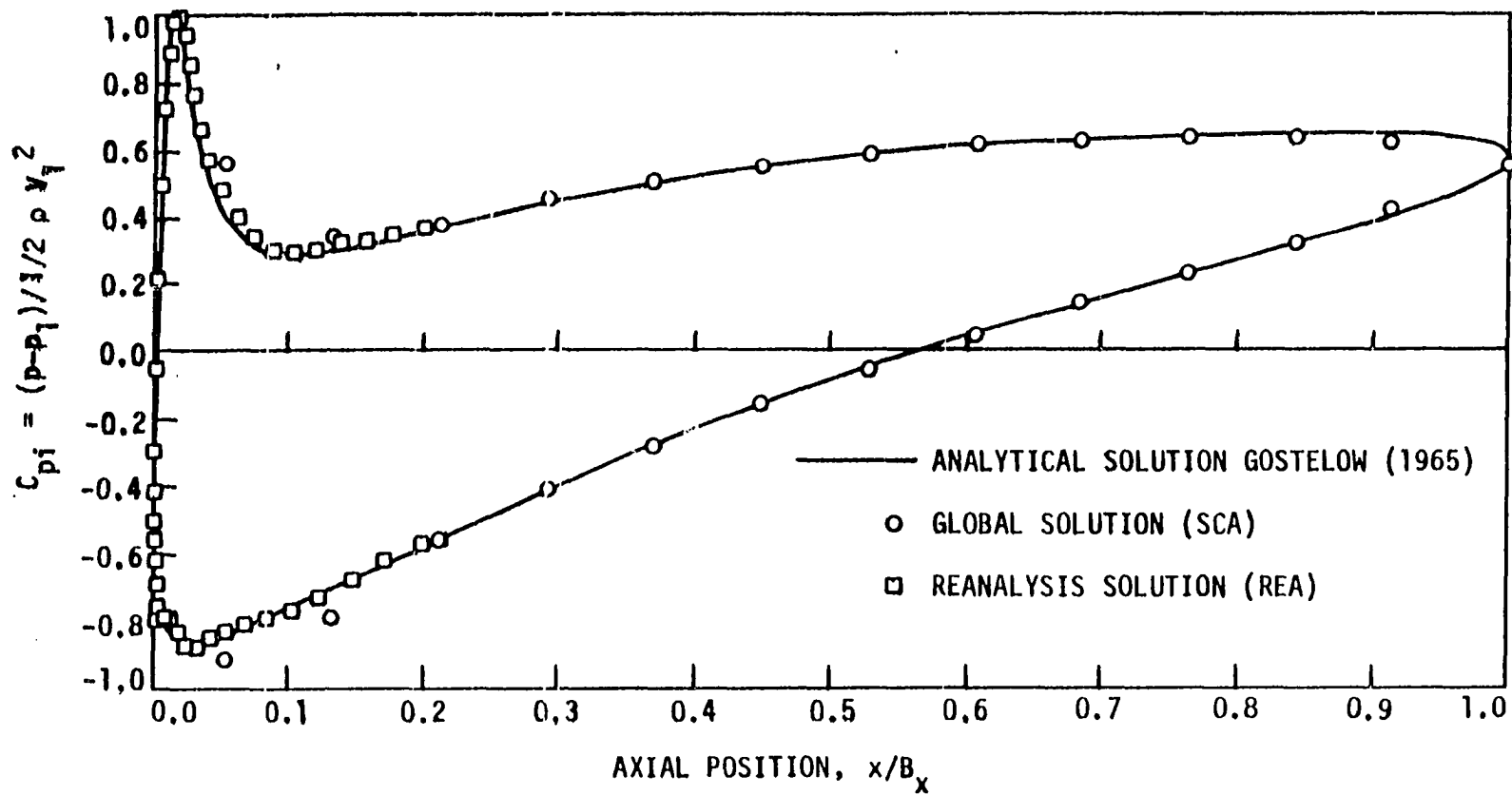


Figure 4.10. Comparison of predicted SCA and REA profile pressure distribution with analytical solution.

5. INTEGRAL BOUNDARY LAYER ANALYSIS

5.1. Introduction

The dissipation-integral boundary layer calculation procedure used in this investigation for two-dimensional compressible boundary layers is described. Results obtained with this method are compared with experimental boundary layer flows to document the development of the scheme.

A prime requirement placed on the procedure was that it should provide rapid calculation of the profile boundary layer development on an airfoil in order that design and analysis iterations could be quickly performed as demanded by the turbine cascade design system. An integral method, therefore, was preferred over more sophisticated and time-consuming field methods for boundary layer analysis. The implication was to give up some generality of approach in favor of speed of calculation.

In this application, the dissipation-integral method of Walz (1969) has been extensively modified to include improved empirical auxiliary relations in turbulent boundary layer calculations. Also, since the profile boundary layer is highly transitional in turbine cascades, the laminar and turbulent calculations have been linked through appropriate transition models. In addition, the important effects of wall curvature and free stream turbulence level on the development of the turbulent boundary layer have been included. Wake mixing calculation methods are used to determine the losses due to profile boundary layers and wake mixing.

5.2. The Dissipation-Integral Boundary Layer Calculation Method

The dissipation-integral method presented by Walz (1969) was programmed in this investigation to perform the profile boundary layer calculation. The method and solution procedure applies to both laminar and turbulent boundary layers, with or without heat transfer. Different sets of auxiliary relations are needed in the laminar and turbulent cases for closure of the system of equations to be solved.

5.2.1. Brief outline of the theory

The basic ordinary differential equations for the boundary layer are the mean momentum and energy integral equations

$$\frac{d\delta_2}{ds} + \delta_2 \frac{du_\delta/ds}{u_\delta} \left(2 + \frac{\delta_1}{\delta_2} - M_\delta^2\right) = \frac{\tau_w}{\rho_\delta u_\delta^2} \quad (5.1)$$

$$\frac{d\delta_3}{ds} + \delta_3 \frac{du_\delta/ds}{u_\delta} \left(3 + 2 \frac{\delta_4}{\delta_3} - M_\delta^2\right) = \frac{2}{\rho_\delta u_\delta^3} \int_0^{u_\delta} \tau \, du \quad (5.2)$$

which are written for the coordinate "s" along the boundary of the flow.

The following remarks and assumptions pertain to Eqns. 5.1 and 5.2:

- (i) The flow boundary is a smooth, two-dimensional impermeable wall.
- (ii) Incompressible ($M_\delta = 0$) or shock free compressible flows ($M_\delta < 5$) can be treated.
- (iii) The shear stress τ_δ at the edge of the boundary layer is assumed negligible. This assumption is acceptable for turbulent boundary layers with low free stream turbulence level.

- (iv) The Reynolds normal stress terms are neglected in comparison with $\tau_w/\rho_\delta u_\delta^2$. This is a reasonable assumption for turbulent layers with low free stream turbulence level and removed from the separation point.
- (v) Wall curvature effects on the development of the turbulent boundary layer are neglected.

The boundary layer integral parameters entering Eqns. 5.1 and 5.2 are defined below (with subscript "u" referring to quantities depending only on the velocity distribution in the boundary layer):

displacement thickness

$$\delta_1 = \int_0^\delta \left(1 - \frac{\rho u}{\rho_\delta u_\delta}\right) dy \quad (\delta_1)_u = \int_0^\delta \left(1 - \frac{u}{u_\delta}\right) dy \quad (5.3)$$

momentum loss thickness

$$\delta_2 = \int_0^\delta \frac{\rho u}{\rho_\delta u_\delta} \left(1 - \frac{u}{u_\delta}\right) dy \quad (\delta_2)_u = \int_0^\delta \frac{u}{u_\delta} \left(1 - \frac{u}{u_\delta}\right) dy \quad (5.4)$$

energy loss thickness

$$\delta_3 = \int_0^\delta \frac{\rho u}{\rho_\delta u_\delta} \left(1 - \frac{u^2}{u_\delta^2}\right) dy \quad (\delta_3)_u = \int_0^\delta \frac{u}{u_\delta} \left(1 - \frac{u^2}{u_\delta^2}\right) dy \quad (5.5)$$

density loss thickness

$$\delta_4 = \int_0^\delta \frac{\rho u}{\rho_\delta u_\delta} \left(\frac{\rho}{\rho_\delta} - 1\right) dy. \quad (5.6)$$

In these definitions, y is the coordinate normal to the boundary of the flow, u_δ is the velocity at the edge of the boundary layer and δ is the physical thickness of the boundary layer which extends normally from the

flow boundary to the point where $u = 0.99 u_\infty$.

The shape factors H_{12} , H_{12}^* , H_{32} , H_{32}^* , and H_{43}^* are defined as

$$H_{12} = (\delta_1)_u / (\delta_2)_u \quad H_{12}^* = \delta_1 / \delta_2 \quad (5.7)$$

$$H_{32} = (\delta_3)_u / (\delta_2)_u \quad H_{32}^* = \delta_3 / \delta_2 \quad (5.8)$$

$$H_{43}^* = \delta_4 / \delta_3 \quad (5.9)$$

The local skin friction coefficient \tilde{c}_f and the shear work (or "dissipation") integral \tilde{c}_D , which represents the rate of energy transfer from the mean velocity field into turbulence in an infinitesimal slice of the boundary layer, are introduced:

$$\tilde{c}_f = \frac{\tau_w}{\rho_\delta u_\delta^2} \quad (5.10)$$

$$\tilde{c}_D = \frac{1}{\rho_\delta u_\delta^3} \int_0^\delta \tau(y) \frac{\partial u}{\partial y} dy. \quad (5.11)$$

The tilde emphasizes that these definitions are half the more conventional forms. Also, a length parameter is defined for mathematical convenience as

$$Z = \delta_2 R_{\delta_2}^n \quad (5.12)$$

in which $n = 1$ for laminar and $n = 0.268$ for turbulent boundary layers.

R_{δ_2} is the local Reynolds number $\rho_\delta u_\delta \delta_2 / \mu_w$. Substitution of the definitions from Eqns. 5.7 through 5.12 into Eqns. 5.1 and 5.2 gives the governing relations

$$\frac{dZ}{ds} + Z \frac{du_\delta/ds}{u_\delta} (F_1 + n \frac{d\mu_w/ds}{du_\delta/ds} \frac{u_\delta}{\mu_w}) - F_2 = 0 \quad (5.13)$$

$$\frac{dH_{32}^*}{ds} + H_{32}^* \frac{du_\delta/ds}{u_\delta} F_3 - \frac{F_4}{Z} = 0 \quad (5.14)$$

in which

$$F_1 = (2 + n) + (1 + n) H_{12}^* - M_\delta^2 \quad (5.15)$$

$$F_2 = (1 + n) \tilde{c}_f R_{\delta_2}^n \quad (5.16)$$

$$F_3 = 1 - H_{12}^* + 2 H_{43}^* \quad (5.17)$$

$$F_4 = R_{\delta_2}^n (2 \tilde{c}_D - \tilde{c}_f H_{32}^*). \quad (5.18)$$

With the compressible local skin friction coefficient from Eqn. 5.10 rewritten in the form (see Walz (1969))

$$\tilde{c}_f = \frac{\alpha(H_{32})}{R_{\delta_2}^n} \frac{\delta_2}{(\delta_2)_u} \quad (5.19)$$

the functions F_2 and F_4 in Eqns. 5.16 and 5.17 become

$$F_2 = (1 + n) \alpha(H_{32}) \frac{\delta_2}{(\delta_2)_u} \quad (5.20)$$

$$F_4 = (2 \tilde{c}_D R_{\delta_2}^n - \alpha(H_{32}) \frac{\delta_2}{(\delta_2)_u} H_{32}^*). \quad (5.21)$$

Therefore, Eqns. 5.13 and 5.14 together with the F functions in Eqns.

5.15, 5.17, 5.20, and 5.21 constitute a simultaneous system of equations

for the two parameters $Z(s)$ and $H_{32}(s)$. The choice of shape factor H_{32} as dependent variable along with Z is largely a matter of convenience; H_{12} , for instance, could just as well have been chosen. The F functions and the parameter H_{32}^* in Eqn. 5.14 must, therefore, be expressed as functions of H_{32} for the system to be determinate.

The following relationships between shape parameters can be derived (see Walz (1969))

$$H_{12}^* = \frac{H_{12}}{\frac{(\delta_2)_u}{\delta_2}} + r \frac{\gamma - 1}{2} M_\delta^2 (H_{32}^* - \theta) \quad (5.22)$$

$$H_{43}^* = r \frac{\gamma - 1}{2} M_\delta^2 \left(1 - \frac{\theta}{H_{32}^*}\right) \quad (5.23)$$

where the usual Prandtl's assumption, i.e., $\partial p / \partial y = 0$ across the boundary layer was made along with the perfect gas assumption. Use was also made of Van Driest's coupling law between temperature and velocity profiles which reads

$$\frac{T}{T_\delta} = 1 + \frac{T_e - T_w}{T_\delta} \left(\frac{u}{u_\delta} - 1\right) + r \frac{\gamma - 1}{2} M_\delta^2 \left[1 - \left(\frac{u}{u_\delta}\right)^2\right] \quad (5.24)$$

where T_e is the "recovery temperature" and r is the "recovery factor."

The parameter θ is a heat transfer parameter defined as

$$\theta = \frac{T_e - T_w}{T_e - T_\delta} \quad (5.25)$$

Up to this point, the development has involved no empirical approximations; however, the F functions and H_{32}^* can be expressed as

functions of H_{32} only through the assumption of an empirical one-parameter trial solution for the velocity profile, or, equivalently, by using experimental data to obtain the functional relations. Therefore, the system 5.13 and 5.14 can be solved if the following auxiliary relations are provided:

$$\frac{\delta_2}{(\delta_2)_u} = \frac{\delta_2}{(\delta_2)_u} (H_{32}^*, M_\delta, \theta) \quad (5.26)$$

$$\alpha = \alpha (H_{32}) \quad (5.27)$$

$$\tilde{c}_D = \tilde{c}_D (H_{32}) \quad (5.28)$$

$$H_{32}^* = H_{32}^* (H_{32}) \quad (5.29)$$

$$H_{12} = H_{12} (H_{32}). \quad (5.30)$$

The sets of auxiliary relations for the laminar and turbulent boundary layer cases are discussed in the following two paragraphs.

5.2.1.1. Laminar boundary layer auxiliary relations For laminar

boundary layers, the auxiliary relations needed are found by assuming that the velocity profile in any laminar boundary layer can be well approximated by Hartree's similar profiles. These profiles are solutions to accelerating or decelerating flows of the type $u_\delta(s) = s^m$ (see Walz (1969)). The advantage of using Hartree's profiles is that velocities $u > u_\delta$ inside the boundary layer are avoided. This mathematical deficiency arises in other families of trial velocity profiles

(such as Pohlhausen's) in the case of very strongly accelerated flows as occur around the leading edge of an airfoil.

The auxiliary relation 5.26 can be derived by using Van Driest's coupling law in Eqn. 5.24, and by assuming that a suitable average for the density in the form $\bar{\rho}/\rho_\delta = T_\delta/\bar{T}$ can be taken outside the integral definition of δ_2 . The following expression is then obtained:

$$\frac{\delta_2}{(\delta_2)_u} = \frac{1}{1 + r \frac{\gamma - 1}{2} M_\delta^2 (H_{32}^* - \theta)(2 - H_{32}) \phi(M_\delta)} \quad (5.31)$$

where,

$$\phi(M_\delta) = 0.936 - 0.0572 M_\delta. \quad (5.32)^*$$

The auxiliary relation 5.29 is to a first approximation $H_{32}^* = H_{32}$. It is therefore suggested that

$$H_{32}^* = H_{32} \psi(H_{32}, M_\delta, \theta) \quad (5.33)$$

or

$$H_{32}^* = H_{32} (1 + (2 - H_{32}) \psi_1(M_\delta, \theta)) \quad (5.34)$$

with ψ_1 given by

$$\psi_1(M_\delta, \theta) = 0.0114 M_\delta (2 - \theta)^{0.8}. \quad (5.35)^*$$

The compressible laminar dissipation integral for the auxiliary relation 5.28 is given by Walz (1969) as

$$\tilde{c}_D = \frac{\beta_L}{R_{\delta_2}} \frac{\delta_2}{(\delta_2)_u} \quad (5.36)$$

* Equations denoted by an asterisk are experimentally obtained.

in which

$$\beta_L = \beta_{uL}(H_{32}) \chi(M_\delta, \theta, H_{32}) \quad (5.37)$$

and in which β_{uL} is obtained by integration of Hartree's velocity profiles, to give

$$\beta_{uL}(H_{32}) = 0.1573 + 1.691 (H_{32} - 1.515)^{1.637}. \quad (5.38)$$

Also, in Eqn. 5.37

$$\begin{aligned} & \chi(M_\delta, \theta, H_{32}) \\ &= \left\{ 1 + r \frac{\gamma - 1}{2} M_\delta^2 [(1.160H_{32} - 1.072) - \theta(2H_{32} - 2.581)] \right\}^\omega \\ & \quad \times \left\{ 1 + r \frac{\gamma - 1}{2} M_\delta^2 (1 - \theta) \right\}^{-\omega} \end{aligned} \quad (5.39)$$

in the development of which the Van Driest coupling law was again used, and a functional relation between average viscosity and average temperature was assumed in the form

$$\frac{\bar{\mu}}{\mu_w} = \left(\frac{\bar{T}}{T_w} \right)^\omega \quad (5.40)$$

with $\omega = 0.7$ for a wide range of temperatures.

Finally, the auxiliary relations 5.28 and 5.31 are obtained by straight-forward use of the analytical expressions for Hartree's profiles, giving

$$\alpha = 1.441 (H_{32} - 1.515)^{0.660} \quad (5.41)$$

and

$$H_{12} = 4.030 - 4.183 (H_{32} - 1.515)^{0.3945}. \quad (5.42)$$

5.2.1.2. Turbulent boundary layer auxiliary relations For purposes of determining the integral parameters of the boundary layer analysis method, Coles' formulation of the turbulent velocity profiles can be used in the form

$$\frac{u}{u_\tau} = \frac{1}{0.41} \ln \frac{y u_\tau}{\nu} + \frac{2\Pi}{0.41} \sin^2 \left(\frac{\Pi}{2} \frac{y}{\delta} \right) + 5.0 \quad (5.43)$$

in which Π is Coles' profile parameter (see Coles (1968)). The shortcoming of this approach, however, is that the skin friction relationship involves a transcendental formulation. Therefore, more explicit experimental correlations are usually relied upon instead.

The auxiliary relation 5.26 in the case of turbulent boundary layers is given by Eqn. 5.31 as in the laminar case but with $\phi(M_\delta)$ given by

$$\phi(M_\delta) = 1 - 0.0719 M_\delta + 0.00419 M_\delta^2. \quad (5.44)^*$$

Also, the auxiliary relation 5.29 for either turbulent or laminar boundary layers is given by Eqns. 5.34 and 5.35.

For the remaining auxiliary relations in Eqns. 5.27, 5.28, and 5.30, use is made of experimental results even though $H_{12}(H_{32})$, for instance, can be obtained by integrating Coles' formulation for different values of the parameter Π . However, experimental correlations are preferred

*Equations denoted by an asterisk are experimentally obtained.

because they provide more direct representation of the available data. Two different sets of experimental auxiliary relations were therefore proposed, and each set was tested with the developed boundary layer solution procedure. The results of the tests are described later in section 5.2.4.

The first set of auxiliary relations (referred to as AR-EN) involve correlations presented by Escudier and Nicoll (1968) as given below.

The auxiliary relation 5.27 is

$$\alpha = f(\xi) \left(R_{\delta_2} \right)_u^n / \ell^2 \quad (5.45)^*$$

where

$$\xi = \frac{2}{3} H_{32} - 1 + \sqrt{\frac{2}{3} H_{32} \left(\frac{2}{3} H_{32} - 1 \right)} \quad (5.46)^*$$

$$f(\xi) = 0.243\xi^2 + 0.0376\xi - 0.00106 + 0.0914\xi^2 / (1+65/\xi) \quad (5.47)^*$$

and

$$\ell = \ln \left[3.39 \left(R_{\delta_2} \right)_u \xi / (1 - \xi)(1 + 2\xi) \right]. \quad (5.48)^*$$

The auxiliary relation 5.28 was given by Walz (1969) as

$$\tilde{c}_D = \tilde{c}_{Di} \frac{\delta_2}{(\delta_2)_u} \quad (5.49)$$

with the incompressible dissipation integral given by Escudier and Nicoll (1968) in the form

$$\tilde{c}_{Di} = \frac{1}{3} (2\xi + 1) \frac{\alpha}{\left(R_{\delta_2} \right)_u^n} + 0.00565(1 - \xi)^{2.715} \quad (5.50)^*$$

* Equations denoted by an asterisk are experimentally obtained.

for $\xi < 1$, or

$$\tilde{c}_{Di} = \frac{1}{3} (2\xi + 1) \frac{\alpha}{(R_{\delta_2})_u} + 0.01 (\xi - 1)^3 \quad (5.51)^*$$

for $\xi > 1$. The auxiliary relation 5.30 for the range $(R_{\delta_2})_u > 0$ and $1.5 < H_{32} < 1.85$ is

$$H_{12} = 1.55 / (0.09714 \sqrt{(0.009428 - 3.1(1.431 - H_{32}))}) \quad (5.52)^*$$

The second set of auxiliary relations (referred to as AR-FWLNNE) involved a combination of experimental correlations presented by different authors in the literature. The auxiliary relation 5.27 was taken from Felsh et al. (1968)

$$\alpha = 0.029 [0.93 - 1.95 \log_{10} H_{12}]^{1.705}. \quad (5.53)^*$$

The incompressible dissipation integral in Eqn. 5.49 is according to LeFoll's formulation (see, for instance, Assasa and Papaliou (1979))

$$\tilde{c}_{Di} = \left(1 + \Pi \frac{H_{12} - 1}{H_{12}}\right) H_{32} \frac{\tilde{c}_{fi}}{2} \quad (5.54)^*$$

where Π is the pressure gradient parameter $(\delta_1 dp/ds)/\tau_w$. The dissipation integral is calibrated in equilibrium flow where the parameter Π is constant and a correspondence exists between the pressure gradient parameter Π (characterizing the outer flow) and Clauser's velocity parameter G (characterizing the velocity profile of the boundary layer). Such a correspondence is given by Nash (1965) as

* Equations denoted by an asterisk are experimentally obtained.

$$\Pi = 0.026874 (G^2 + 2.8G - 64.47)$$

where

$$G = \frac{H_{12} - 1}{H_{12} \sqrt{c_{fi}^*}} \quad (5.55)$$

and

$$c_{fi}^* = \frac{\alpha}{(R_{\delta_2})_u^n} \quad (5.56)$$

according to Walz (1969). The auxiliary relation 5.30 was taken from Nicoll and Escudier (1966) as

$$H_{12} = \frac{1}{H_{32} - 1.431} [0.775 H_{32} - 1.10667]^{\frac{1}{2}}. \quad (5.57)$$

5.2.2. Numerical approximation of boundary layer equations

Mean values of the universal functions F_j ($j = 1, 4$) in the boundary layer Eqns. 5.13 and 5.14 may be defined over a small increment

$$\Delta s = s_i - s_{i-1} \text{ as}$$

$$\bar{F}_j = \bar{F}_j(\bar{M}_{\delta}, \bar{\theta}, \bar{H}_{32}) \quad (5.58)$$

The system 5.13 and 5.14 may then be rewritten in finite difference form as:

momentum equation (Eqn. 5.13)

$$\frac{Z_i}{Z_{i-1}} = A_Z + B_Z \bar{F}_2 \frac{\Delta s}{Z_{i-1}} \quad (5.59)$$

energy equation (Eqn. 5.14)

$$H_{32_i}^* = H_{32_{i-1}}^* \left(A_H + B_H \bar{F}_4 \frac{2}{Z_i + Z_{i-1}} \frac{\Delta s}{H_{32_{i-1}}^*} \right) \quad (5.60)$$

where

$$A_Z = \left(\frac{u_{\delta_{i-1}}}{u_{\delta_i}} \right)^{\bar{F}_1} ; \quad B_Z = \frac{1 - A_Z \frac{u_{\delta_{i-1}}}{u_{\delta_i}}}{(1 + \bar{F}_1) \left(1 - \frac{u_{\delta_{i-1}}}{u_{\delta_i}} \right)} \quad (5.61)$$

$$A_H = \left(\frac{u_{\delta_{i-1}}}{u_{\delta_i}} \right)^{\bar{F}_3} ; \quad B_H = \frac{1 - A_H \frac{u_{\delta_{i-1}}}{u_{\delta_i}}}{(1 + \bar{F}_3) \left(1 - \frac{u_{\delta_{i-1}}}{u_{\delta_i}} \right)} \quad (5.62)$$

The linearization of F_j in the above approximations might cause convergence failure very near separation; however, integral methods neglecting Reynolds normal stresses are already questionable in this situation.

5.2.3. General description of boundary layer calculation method

The iterative solution procedure used to integrate Eqns. 5.59 and 5.60 is outlined below. The procedure is for either case of laminar or

turbulent boundary layers and as such forms the basis of the analysis of profile boundary layer on the airfoil. Additional models for laminar starting, natural transition, separation bubble, etc. as incorporated in the overall boundary layer analysis program are discussed in later sections of this chapter. The main steps in the procedure are:

1. The values of s , u_δ , $(\delta_2)_u$, and $(\delta_3)_u$ must be entered at the first calculation station, $i = 1$, along with static pressure and total temperature. The velocity at the edge of the boundary layer u_δ must be given in the form of a table of $u_\delta(s)$. In the case of heat transfer, a table $T_w(s)$ should be entered. For the adiabatic case the heat transfer parameter θ is set equal to zero. Additional input data concerning the type of fluid are the ratio of specific heats, recovery factor, gas constant, and the specific heat at constant pressure.

2. A new table $u_\delta(s)$ is calculated by interpolation such that

$$0.97 \leq \frac{u_{\delta_i}}{u_{\delta_{i-1}}} \leq 1.03. \quad (5.63)$$

This condition was found by Walz (1969) to give the optimum convergence characteristics. The given table is left unchanged if it already satisfies condition 5.63. Also, two tables of average values of $M_\delta(s)$ and $\theta(s)$ are calculated by using $\bar{M}_\delta = 0.5 [(M_\delta)_i + (M_\delta)_{i-1}]$ and $\bar{\theta} = 0.5 [\theta_i + \theta_{i-1}]$.

3. H_{32}^* at $i = 1$ is calculated from the initial data and from auxiliary relation 5.29.

4. H_{32}^* at the second calculation station, $i = 2$, is estimated as

$(H_{32}^*)_{i=2} = (H_{32}^*)_{i=1} - 0.001$ or, in general, as $(H_{32}^*)_i = (H_{32}^*)_{i-1} + 0.5 [(H_{32}^*)_{i-1} - (H_{32}^*)_{i-2}]$.

5. The estimated $(H_{32}^*)_{i=2}$ allows calculation of an estimated $(H_{32})_{i=2}$ and an average H_{32} obtained as $\bar{H}_{32} = 0.5 [(H_{32})_i + (H_{32})_{i-1}]$.

6. The coefficients of Eqns. 5.59 and 5.60 are calculated as follows:

$\bar{F}_1 (\bar{M}_\delta, \bar{\theta}, \bar{H}_{32})$ from Eqns. 5.15, 5.22, 5.26, 5.29, and 5.30.

$\bar{F}_2 (\bar{M}_\delta, \bar{\theta}, \bar{H}_{32})$ from Eqns. 5.20, 5.26 and 5.27.

$\bar{F}_3 (\bar{M}_\delta, \bar{\theta}, \bar{H}_{32})$ from Eqns. 5.17, 5.22, 5.23, 5.26, 5.29, and 5.30.

$\bar{F}_4 (\bar{M}_\delta, \bar{\theta}, \bar{H}_{32})$ from Eqns. 5.21, 5.26, 5.27, 5.28, and 5.29.

A_Z and B_Z from Eqn. 5.61, A_H and B_H from Eqn. 5.62.

The appropriate expressions for the auxiliary relations 5.26, 5.27, 5.28, 5.29, and 5.30 should be used in the laminar and turbulent case as given in sections 5.2.1.1. and 5.2.1.2.

7. A first estimate of Z at $i = 2$ is obtained from Eqn. 5.59. The estimated $(H_{32}^*)_{i=2}$ and $(Z)_{i=2}$ are substituted into the right hand side of Eqn. 5.60 to obtain a revised estimate of $(H_{32}^*)_{i=2}$.

8. The last and next to last estimates of $(H_{32}^*)_{i=2}$ are compared. If the difference exceeds a predetermined tolerance, the calculation returns to step 5 with the latest estimate of $(H_{32}^*)_{i=2}$.

9. After convergence of $(H_{32}^*)_{i=2}$, the calculation is stepped to the next station and steps 4 through 8 repeated, with iteration as required, to find $(H_{32}^*)_{i=3}$, and so forth.

In the program, the convergence criterion was that the absolute value of the difference between successive values of $(H_{32}^*)_i$ be less or equal to 0.0001 with a limit of 30 iterations set on H_{32}^* improvement. Convergence usually requires about four iterations except close to a separation point.

Viscosity is calculated wherever needed in the boundary layer procedure by using the relations presented in Appendix F.

5.2.4. Test case results for auxiliary relations

Calculations of H_{12} , $(\delta_2)_u$, and $c_f = 2 \tilde{c}_f$ were performed using the two different sets of experimental auxiliary relations proposed in section 5.2.1.2. together with the boundary layer calculation procedure just described. These calculations served the double purpose of testing the numerical solution procedure and of determining the accuracy of boundary layer predictions derived from using different auxiliary relations. Three turbulent boundary layer flows presented at the Stanford Conference (see Kline et al. (1969)) were chosen as the test cases for calculation. These flows were incompressible, with very little deviation from two-dimensionality, and involving low free stream turbulence level.

The first test case was that of an equilibrium turbulent boundary layer in a moderate positive pressure gradient reported by Clauser (1954). This flow was named Clauser Flow No. 2 at the Stanford Conference. The momentum thickness was matched at the second

experimental profile and the calculation initiated there with the experimental $u_\delta(s)$. The calculated and experimental results in Fig. 5.1 show that auxiliary relation set AR-EN gave better results in this flow than did set AR-FWLNNE. Some starting effects on the initially calculated c_f and H_{12} are noted with the latter set. The experimental flow in this case was known to be slightly three-dimensional, possibly explaining the discrepancies between calculated and experimental $(\delta_2)_u$ towards the final stages of the flow.

The second test case considered airfoil turbulent boundary layer flow proceeding towards separation originally reported by Newman (1951). As was done in the first test case, the calculation was started at the second experimental profile by matching the momentum thickness and using the experimental $u_\delta(s)$. The comparisons of predicted and experimental results are shown in Fig. 5.2. The auxiliary relation set AR-EN again performed better in this flow, with set AR-FWLNNE showing the same starting effects as in the first test case. The discrepancies shown between calculated and experimental H_{12} are due in large part to wall curvature effects which tend to drive the boundary layer closer to separation. The boundary layer analysis method is modified later in this chapter to include these important effects.

The third and last test case was that of a turbulent boundary layer developing in a straight cylindrical annulus with measurements taken along the inner cylinder. The flow was axially symmetric, with initial moderate diffusion followed by relaxation at constant pressure. This flow, originally reported by Moses (1964), was named Moses Flow No. 6

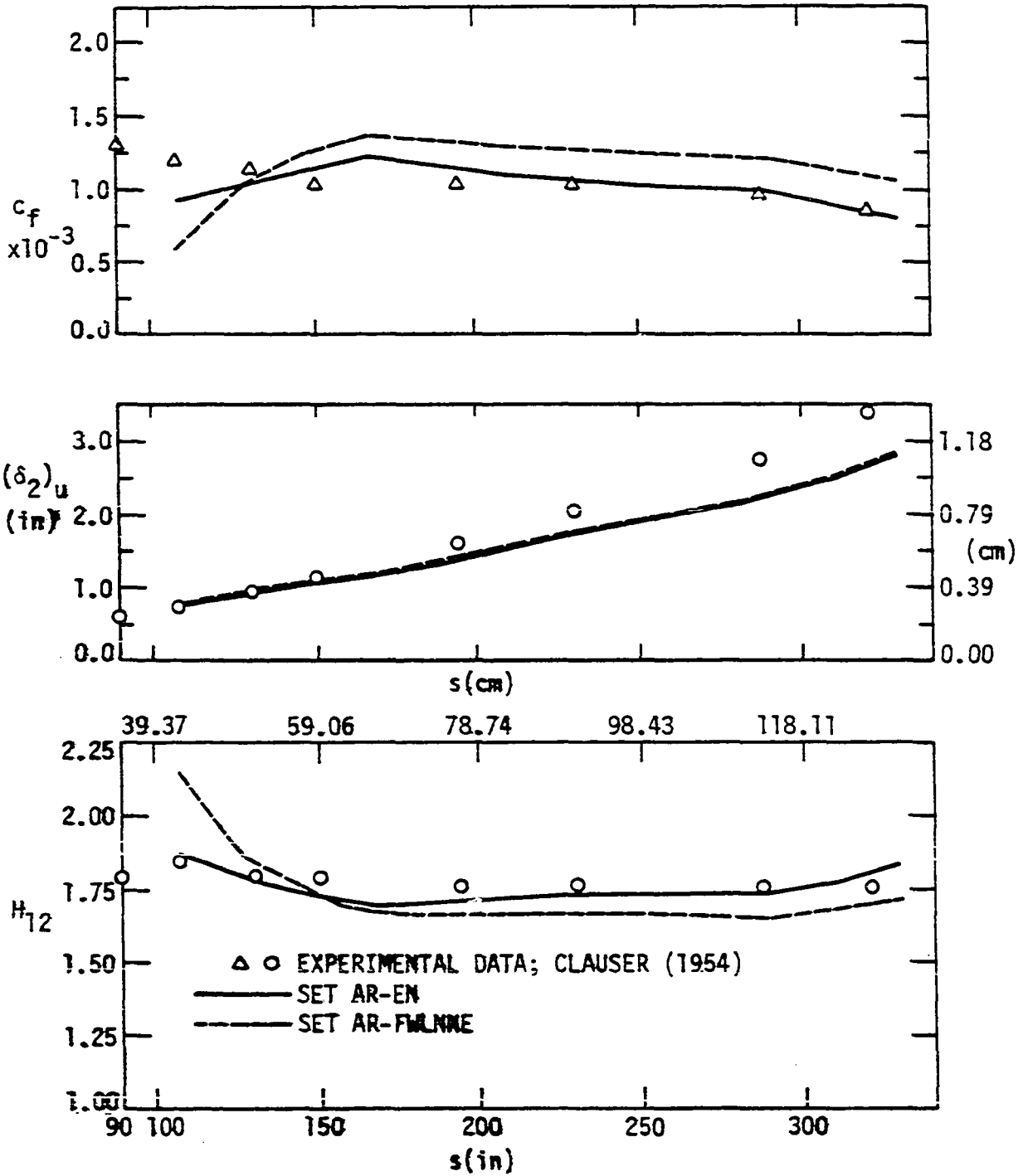


Figure 5.1. Comparison of calculated and experimental results for Clauser (1954) flow. Calculations based on auxiliary relation sets AR-EN and AR-FWLNNE.

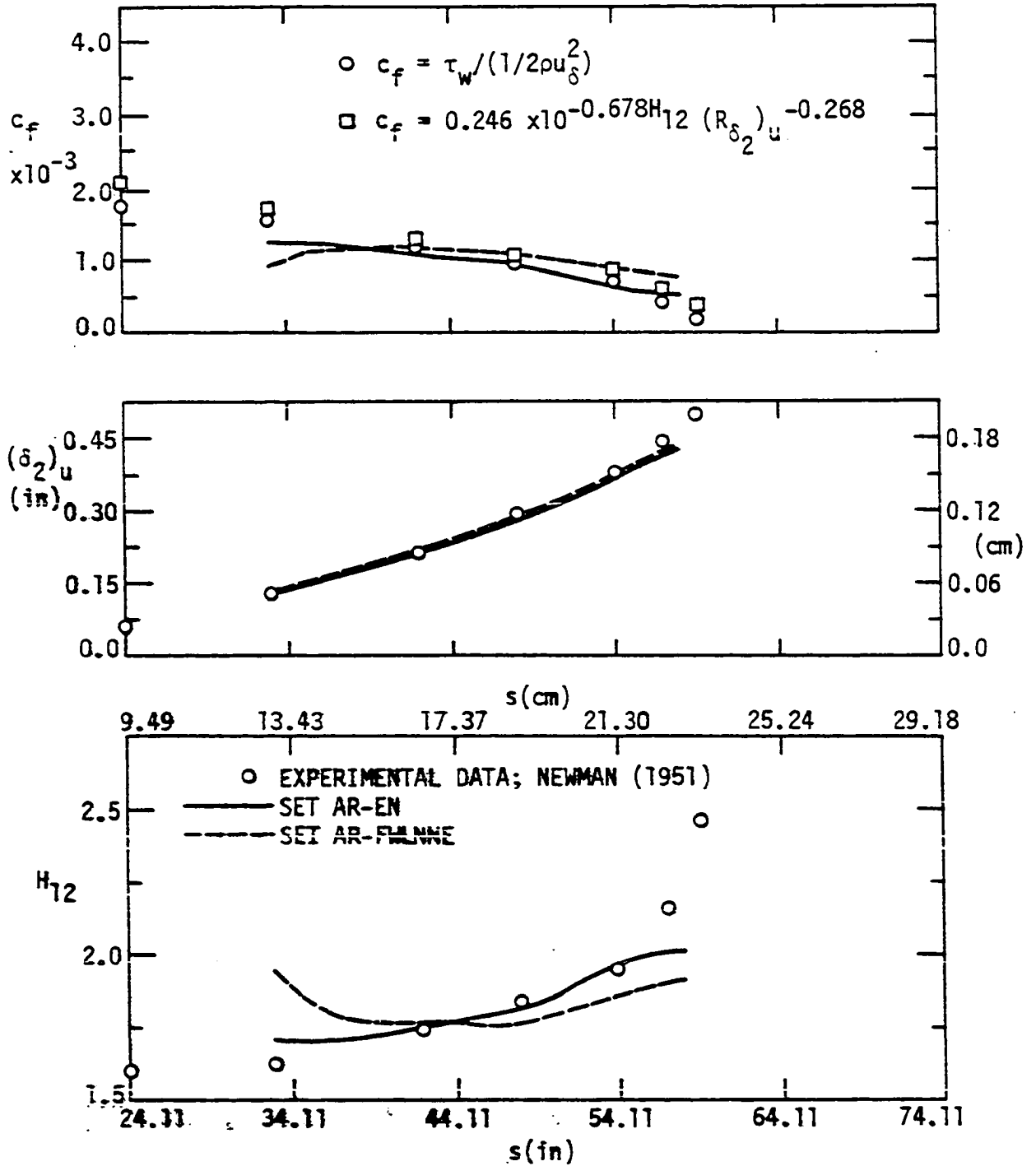


Figure 5.2. Comparison of calculated and experimental results for Newman (1951) flow. Calculations based on auxiliary relation sets AR-EN and AR-FWLNE.

at the Stanford Conference. The calculation was started at the second experimental profile, following the same procedure as with the other two cases. The comparison of results in Fig. 5.3 shows that both sets of auxiliary relations perform well in this flow.

Based on the comparisons in the test cases just discussed, the set of experimental auxiliary relations developed by Escudier and Nicoll (1968), i.e., set AR-EN, was adopted in this investigation. It should be pointed out that the dependence of this set of auxiliary relations on local R_{δ_2} is thought to be an improvement over alternative correlations lacking this dependence.

5.3. Laminar Starting Procedure

The laminar boundary layer calculation cannot be started at the stagnation point because the method exhibits a singularity at this point. The flat plate stagnation point similarity solution first given by Hiemenz and presented in Schlichting (1968, p. 87) was used to provide an initial boundary layer thickness in the neighborhood of the stagnation point.

Hiemenz used an inviscid outer flow described by

$$u = a x ; \quad v = - a y \quad (5.64)$$

where "a" is a constant. This is a plane potential flow impinging normally on a flat plate oriented along $y = 0$. McDonald (1978) related this flow to the more appropriate circular cylinder potential flow

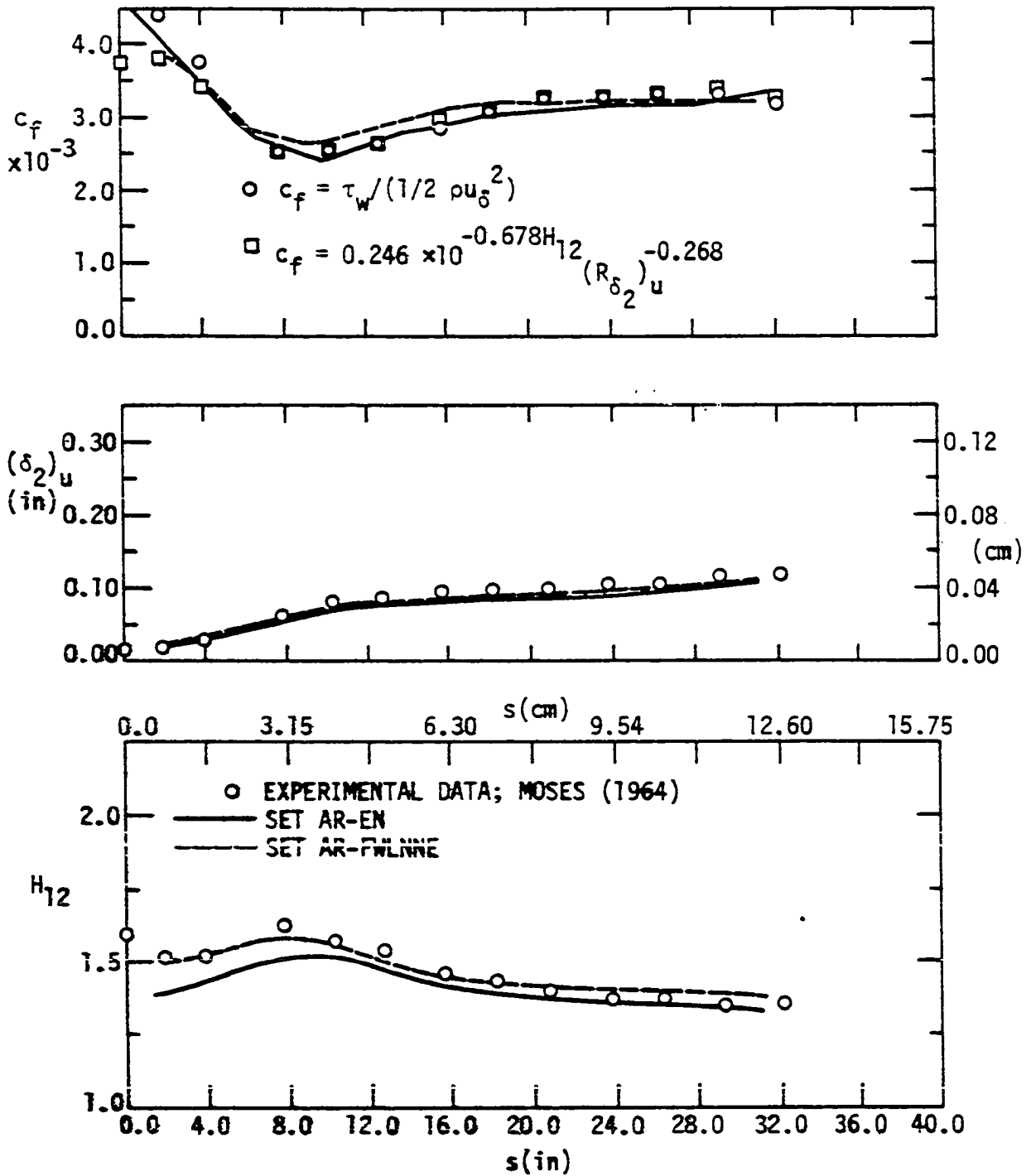


Figure 5.3. Comparison of calculated and experimental results for Moses (1964) flow. Calculations based on auxiliary relation sets AR-EN and AR-FWLNNE.

(in the neighborhood of the stagnation point) by letting

$$a = \frac{2V_1}{RLE} \quad (5.65)$$

in which RLE is the cylinder (or leading edge) radius and V_1 is the approaching stream velocity.

The functions occurring in the solution of the Hiemenz flow given by Schlichting (1968, p. 90) were numerically integrated to obtain the following expressions for $(\delta_2)_u$ and $(\delta_3)_u$

$$(\delta_2)_u = 0.28846 \sqrt{\frac{\nu}{a}} \quad (5.66)$$

and

$$(\delta_3)_u = 0.46880 \sqrt{\frac{\nu}{a}} \quad (5.67)$$

In the procedure used, the stagnation point was determined from the leading edge reanalysis results and the boundary layer calculation started at the second closest mesh point on either side of the stagnation point. Initial data were obtained from Eqns. 5.66 and 5.67 with initial static pressure and density calculated from the local u_δ and upstream total conditions, and the viscosity from the equations in Appendix F.

5.4. Natural Transition Model

Transition of the profile laminar boundary layer into a turbulent one is known to play an important role in determining cascade losses. How closely transition starts to the leading edge of the blade bears

directly on the resulting thickness of the turbulent layer at the trailing edge; that is, the earlier transition occurs, the thicker the turbulent boundary layer, and the larger the attendant losses.

Theoretical prediction of natural transition is still an unresolved problem, due mainly to the large number of parameters that are known to affect the phenomenon. Such a list of factors for two-dimensional cascades is the following:

- Local surface pressure gradients
- Free-stream turbulence level
- Local Reynolds number
- Shock/boundary layer interaction
- Mach number
- Surface roughness
- Wall curvature
- Temperature gradients
- Inlet unsteadiness (passing blade wakes)
- Axial velocity density ratio

Without a clear theoretical approach to determine the exact location of onset of transition, the alternative is to use experimentally determined transition data correlated against the most important parameters.

Crimi and Reeves (1972) produced a semi-empirical model to take into account the important effects of pressure gradient and local free-stream turbulence level. The model, which is a modification of the

results presented by van Driest and Blumer (1963) to better account for pressure gradient effects on transition, is given by

$$3.6 \left(\frac{u'}{u_\delta}\right)^2 (R_\delta^2)_{tr} + f_p(\Lambda)(R_\delta)_{tr} - 9860 = 0. \quad (5.68)$$

In this relation, u' is the local root-mean-square fluctuation of the free stream velocity due to turbulence, Λ is the Karman-Pohlhausen pressure gradient parameter - $(\delta^2/\mu u_\delta) dp/ds$, and $(R_\delta)_{tr}$ is the maximum Reynolds number based on boundary layer thickness and local external flow for which the boundary layer flow remains laminar. The function f_p involved in Eqn. 5.60 is plotted in Fig. 5.4. Also plotted is a comparison between the model of Crimi and Reeves (Eqn. 5.68) and that of van Driest and Blumer (1963). The stabilizing effect of a negative pressure gradient (negative Λ) on transition is observed to be stronger in the model of Crimi and Reeves, especially at low Tu . Also, the destabilizing effect of a positive pressure gradient (positive Λ) is slightly stronger in the Crimi and Reeves model.

Dunham (1972) has presented a purely empirical correlation accounting for pressure gradient and free-stream turbulence effects. The experimental data included several cascade flows as well as flat plate data. The following equation is a reasonable representation of the compiled data:

$$(R_{\delta_2})_{tr} = [0.27 + 0.73 \exp(-80 \overline{Tu})] [550 + 680 (1 + 100 \overline{Tu} - 21\lambda)^{-1}]. \quad (5.69)$$

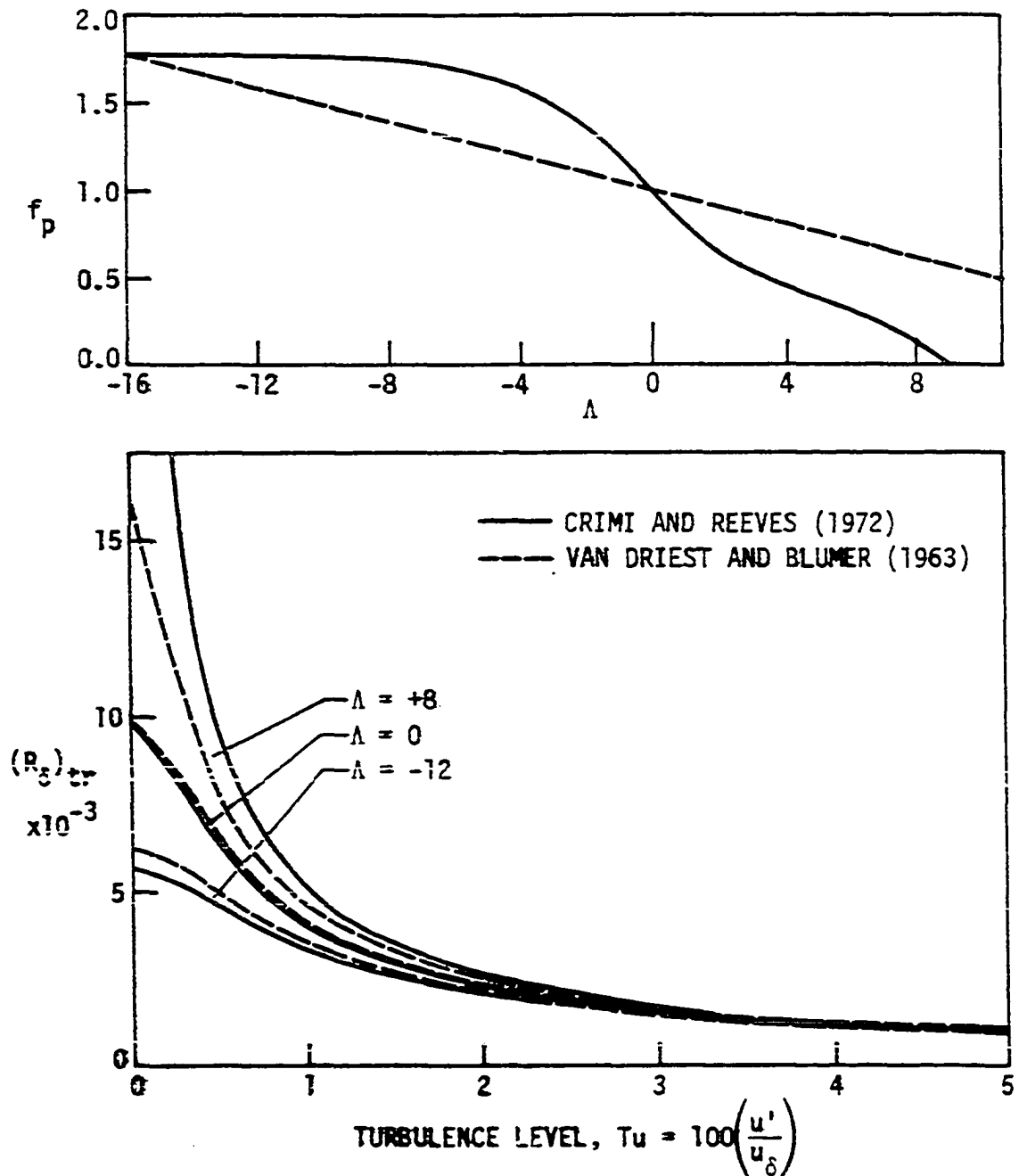


Figure 5.4. Comparison of natural transition models of Crimi and Reeves (1972) and van Driest and Blumer (1963).

Here, \overline{Tu} is a mean turbulence level characterizing the flow throughout the history of the boundary layer, λ is the pressure gradient parameter $(\delta_2^2/\nu) du/ds$, and $(R_{\delta_2})_{tr}$ is the maximum Reynolds number based on momentum thickness and local external flow for which the flow remains laminar. The parameter \overline{Tu} is the mean between the upstream turbulence level, Tu_1 , which is the value usually measured and reported in the literature, and a local turbulence level Tu normalized on u_δ .

The theoretical calculation of the decay or amplification of local turbulence level Tu ($Tu = u'/u_\delta$ for isotropic turbulence) from an upstream value Tu_1 is one of the most difficult problems in fluid dynamics. Based on Batchelor's (1953) linear analysis, however, an approximate expression of the local turbulence level can be proposed. The expression given by Batchelor for the case of a uniform stream passing through a symmetric change of section considered by him is

$$\frac{Tu}{Tu_1} = \sqrt{\frac{1}{2c} \left(1 + \frac{F}{c^3} \right)} \quad (5.70)$$

where

$$F = \frac{\tan^{-1} \sqrt{c^{-3} - 1}}{\sqrt{c^{-3} - 1}} \quad (\text{for } c < 1; \text{ diffusion}) \quad (5.71)$$

$$F = \frac{\ln [c^{1.5} (1 + \sqrt{1 - c^{-3}})]}{\sqrt{1 - c^{-3}}} \quad (\text{for } c > 1, \text{ acceleration}). \quad (5.72)$$

Here, c is taken as the ratio of local surface velocity to upstream velocity, i.e., $c = u_\delta/V_1$.

In the developed program for the profile boundary layer analysis, both the Crimi and Reeves and the Dunham models are available. However, the calculated cascade results presented in Chapter 6 were obtained with the Crimi and Reeves model only. This model was preferred over Dunham's because there was more theoretical consideration involved in its development. The local turbulence level was calculated with Eqns. 5.70, 5.71, and 5.72.

With the onset of natural transition determined, it remains to calculate transition length. The calculation of flow through the transition region can be made using an intermittency function γ first introduced by Emmons (1951) for which $\gamma = 0$ in fully laminar flow and $\gamma = 1$ in fully turbulent.

Dhawan and Narasimha (1958) obtained a correlation for γ using the source density function of Emmons (1951). According to these results, the intermittency function in the streamwise direction is

$$\gamma = 1 - \exp(-0.412 \xi^2) \quad (5.73)$$

where,

$$\xi = \frac{s - s_{tr}}{\Delta} \quad (s_{tr} \leq s \leq s_{tur}) \quad (5.74)$$

and where Δ is a measure of the extent of the transition region as given by

$$\Delta = s|_{\gamma=0.75} - s|_{\gamma=0.25} \quad (5.75)$$

The point s_{tur} at which the flow becomes fully turbulent is estimated

by a correlation between the transition Reynolds number $R_{s_{tr}}$, and the Reynolds number R_{Δ} based on the physical extent of the transition region. This correlation, due to Dhawan and Narasimha (1958) is

$$\Delta = \frac{5.0}{R^*} (R_{s_{tr}})^{0.8} \quad (5.76)$$

where R^* is the local unit Reynolds number, u_{∞}/ν .

The extent of the transition region is calculated, therefore, by using Eqn. 5.76 together with Eqn. 5.73 to solve for s_{tur} in the form:

$$s_{tur} = s_{tr} + \Delta \sqrt{-\frac{\ln(1 - \gamma)}{0.412}} \quad (5.77)$$

where s_{tur} is calculated for $\gamma = 0.95$ since γ presents an asymptotic behavior, as fully turbulent flow is approached.

The experimental data used by Dhawan and Narasimha to obtain Eqn. 5.76 were mostly flat plate data with a few airfoil data points. It should be noted that neither the effects of the pressure gradient parameter λ nor the effects of free stream turbulence Tu are included in the transition length correlation. Also, it should be pointed out that McDonald and Fish (1972) presented a field method using an integral form of the turbulent kinetic energy equation to predict transition location and extent, taking into account pressure gradient and free stream turbulence level.

Recent cascade data presented by Heilmann (1972) appear to indicate that Tu acts in reducing the extent of the transition region; however, no concluding data have been reported in the literature attempting to

correlate transition length against Tu . The length of the transition regions reported by Heilmann was on the order of 2 to 5 percent of chord.

Finally, the turbulent boundary layer calculation is started at s_{tur} following a suggestion of Seyb (1972) who has pointed out that, for well behaved boundary layers, it is usually adequate to assume the shape factor H_{12} equal to 1.4 at the start of the turbulent layer. In addition, Seyb suggests a constant momentum loss thickness across the transition region.

5.5. Laminar Separation Bubble Model

The transition from laminar to turbulent flow can also occur through laminar separation, transition to a turbulent state in the free layer, and reattachment as a fully turbulent boundary layer; created in the process is a so-called laminar separation bubble.

The onset of laminar separation is established in the boundary layer calculation when either the calculated H_{32} is less or equal to 1.515 or when the pressure gradient parameter λ is less or equal to -0.09.

With the onset of laminar separation established, the model of Roberts (1975) for laminar separated regions is used to calculate across the separation bubble. Roberts (1975) considered two regions in the bubble. A first region, characterized by a length l_1 and located immediately after the laminar separation point, is a free layer for which the thickness grows rapidly and the surface inviscid velocity is assumed to remain constant. The free layer is laminar in this region.

The second region, characterized by a length ℓ_2 , is where the free layer is considered as fully turbulent and thus able to do more diffusion; therefore, a reattaching process is initiated. The free shear layer is assumed to reattach at the end of this region with the surface inviscid velocity being modeled as a linear distribution between the transition and reattachment points. The transition from laminar to turbulent flow is assumed to occur instantaneously at the end of ℓ_1 and beginning of ℓ_2 . The equations presented by Roberts (1975) are given below.

For the laminar part, the transition length and the momentum thickness growth are given by

$$\ell_1 = (\delta_2)_{\text{sep}} (2.5 \times 10^4) \log_{10} (\coth(20Tu_1)) / (R_{\delta_2})_{\text{sep}} \quad (5.78)$$

$$\frac{d\delta_2}{ds} \approx 0. \quad (5.79)$$

For the turbulent part, the reattachment length and momentum thickness at reattachment are given by

$$\ell_2 = 85.227 (\delta_2)_{\text{sep}} (1 - (\bar{u}_\delta)_{\text{re}}) / ((\bar{u}_\delta)_{\text{re}}^4 - 0.497) \quad (5.80)$$

$$(\delta_2)_{\text{re}} = \frac{1}{(\bar{u}_\delta)_{\text{re}}^3} \left[(\delta_2)_{\text{sep}} + \frac{0.005833 (1 - (\bar{u}_\delta)_{\text{re}}^4) \ell_2}{(1 - (\bar{u}_\delta)_{\text{re}})} \right]. \quad (5.81)$$

The velocity $(\bar{u}_\delta)_{\text{re}}$ in Eqns. 5.80 and 5.81 is the reattachment velocity normalized with respect to the velocity at the separation point.

In the present application, the iteration procedure presented by

Hansen (1978) including the bursting bubble case, was used to solve Roberts' equations.

At separation, the needed data to calculate l_1 with Eqn. 5.78 are known. A first estimate of the reattachment position is made as $s_{re} = s_{sep} + l_1$. The velocity $(u_\delta)_{re}$ is found from the inviscid velocity distribution, and Eqn. 5.80 is used to calculate l_2 . A revised estimate for the reattachment position as $s_{re} = s_{sep} + l_1 + l_2$ gives a new estimate for $(u_\delta)_{re}$ and l_2 . The iteration is continued until l_2 is converged upon.

When $(\bar{u}_\delta)_{re}^4$ approaches 0.497 in Eqn. 5.80, l_2 goes to infinity, indicating a burst bubble. Following Hansen (1978), l_2 is limited in size to $0.7 l_1$, and $(\bar{u}_\delta)_{re}$ is required to be greater than 0.841 to keep l_2 positive.

Finally, the turbulent calculation is initiated at the reattachment point with $(\delta_2)_{re}$ and with $H_{32} = 1.501$, indicating just separated turbulent velocity profile.

5.6. Inclusion of Wall Curvature Effects on Development of Turbulent Boundary Layer

It is now well established that for the radii of curvature encountered in turbomachine airfoils, curvature effects are not felt by the profile laminar boundary layer. On the other hand, although its effect on the structure of the governing equations is secondary, wall curvature does play an important role in the development of the turbulent boundary layer through modification of the properties of turbulence.

The effects of curvature on turbulence start to be appreciable for ratios of boundary layer thickness to surface curvature greater than 1/300 (Papailiou et al. (1972)). This is in the range typical for turbomachinery airfoils.

The method developed by Papailiou et al. (1972), based on Bradshaw's analogy between buoyancy and centrifugal forces acting on the turbulent boundary layer and applicable to dissipation-integral methods, was used in this study to account for wall curvature effects. The resulting formula for the correction, \tilde{c}_{Di}' , to be added to the two-dimensional dissipation integral, \tilde{c}_{Di} , is

$$\tilde{c}_{Di}' = - \frac{\beta}{2Ru_{\delta}} S_1 [H_{12}, (R_{\delta_2})_u] + \frac{\beta^2}{2(Ru_{\delta})^2} S_2 [H_{12}, (R_{\delta_2})_u] \quad (5.82)$$

where β is a constant determined experimentally equal to 7 for a convex surface (suction side), and equal to 4 for a concave surface (pressure side). R is the radius of curvature of the flow boundary.

The functions S_1 and S_2 are

$$S_1 [H_{12}, (R_{\delta_2})_u] = -Z_1 \epsilon_1 (R_{\delta_2})_u \quad (5.83)$$

$$S_2 [H_{12}, (R_{\delta_2})_u] = Z_2 \epsilon_2 (R_{\delta_2})_u \quad (5.84)$$

where, in turn

$$\epsilon_1 = 1 + \frac{0.029}{(H_{12} - 1)^4} \frac{10.3 - \ln(R_{\delta_2})_u}{2 \ln(R_{\delta_2})_u} \quad (5.85)$$

$$\epsilon_2 = 1 + \frac{0.14 H_{12}}{(H_{12} - 1)^2} \frac{10.3 - \ln(R_{\delta_2})_u}{2 \ln(R_{\delta_2})_u} . \quad (5.86)$$

The functions Z_1 and Z_2 were presented in tabular form in Papailiou et al. (1972) as functions of H_{12} and $(R_{\delta_2})_u$. In the program developed in this study, a table look up procedure was implemented to determine Z_1 and Z_2 .

The correction procedure for \tilde{c}_{Di} was tested by calculating turbulent boundary layer data on a large airfoil reported by Schubauer and Klebanoff (1951) with and without wall curvature effects included. The pressure gradient was first mildly negative, then strongly positive, with eventual separation. The results in Fig. 5.5 show that the simple two-dimensional calculation was unable to follow the separation trend exhibited by the experimental data. The corrected results (radius of curvature of the suction side 30 ft.), on the other hand, agree well with the experimental data, with the turbulent separation point correctly predicted.

In summary, the general trends caused by wall curvature effects on the turbulent boundary layer development are:

- (i) Separation tendency on the suction side of the airfoil is enhanced.
- (ii) Separation tendency on the pressure side is suppressed.
- (iii) Losses are not substantially altered since momentum thickness is essentially unchanged.

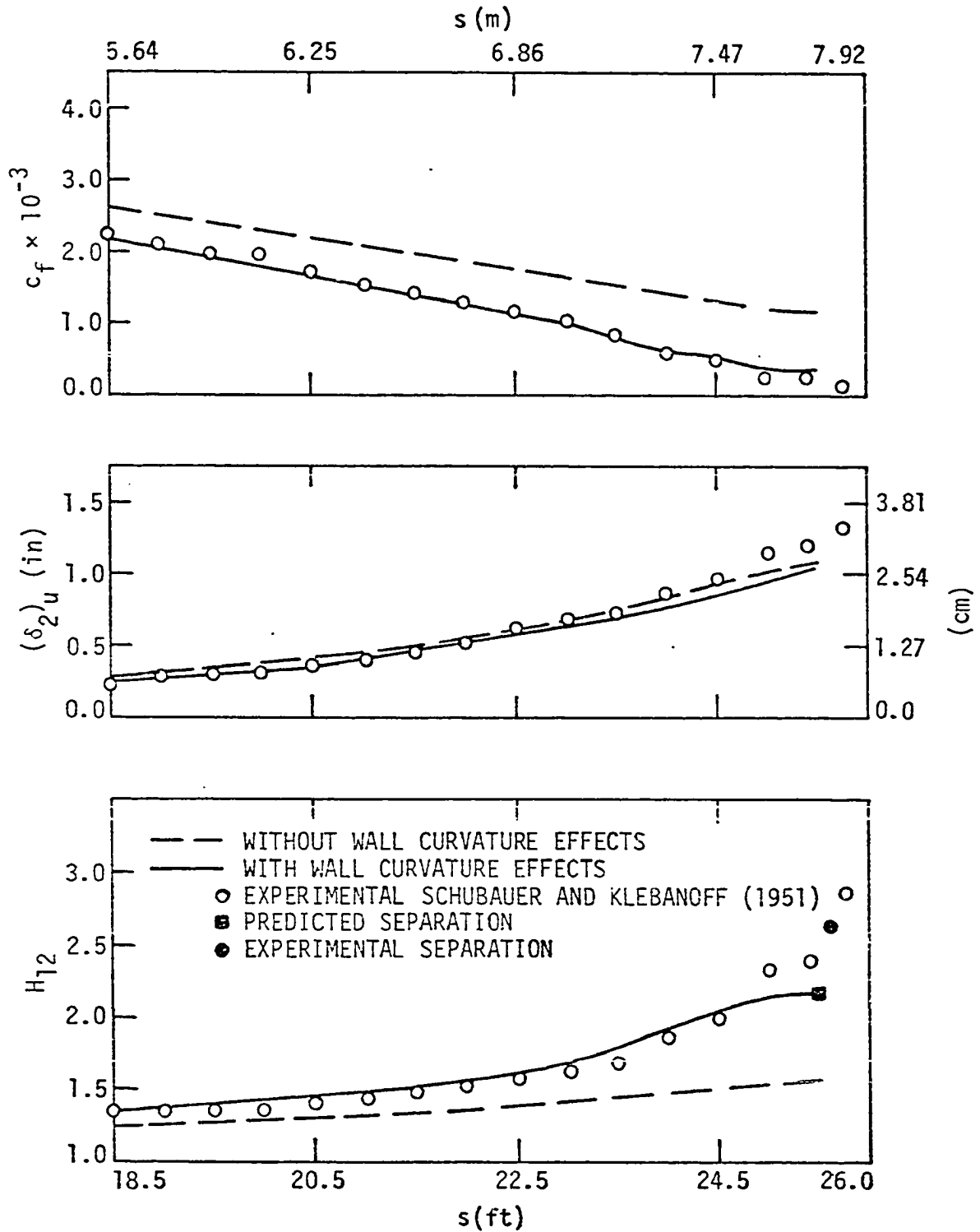


Figure 5.5. Comparison of calculated results and experimental airfoil data of Schubauer and Klebanoff (1951).

5.7. Inclusion of Free Stream Turbulence Effects on Development of Turbulent Boundary Layer

A simple empirical model was developed in this investigation to account for the effects of free stream turbulence on the development of an incompressible turbulent boundary layer. The method is based on two main considerations:

- (i) Following Evans and Horlock (1974), the skin friction term in the momentum integral equation is considered to be the net result of the wall shear stress minus the apparent Reynolds shear stress $-\overline{u'v'}$ at the edge of the boundary layer ($y = \delta$) where integration of the boundary layer integral parameters is terminated.
- (ii) The Reynolds normal stresses, $\overline{u'^2}$, $\overline{v'^2}$, and $\overline{w'^2}$ are retained in the integral equations since the data of Huffman et al. (1972) show a pronounced dependence of these terms on local free stream turbulence level.

The incompressible momentum integral equation, considering the Reynolds shear stress at the edge of the boundary layer, τ_δ , and retaining the normal Reynolds stresses, can be written as (see, for instance, Evans and Horlock (1974))

$$\frac{d(\delta_2)_u}{ds} + (\delta_2)_u \frac{du_\delta/ds}{u_\delta} \left[2 + \frac{(\delta_1)_u}{(\delta_2)_u} \right] = \frac{\tau_w - \tau_\delta}{\rho u_\delta^2} + \frac{1}{u_\delta^2} \frac{d}{ds} \int_0^\delta (\overline{u'^2} - \overline{v'^2}) dy. \quad (5.87)$$

Similarly, the incompressible energy integral equation (see, for instance, Assassa and Papailiou (1979)) can be written as

$$\frac{d(\delta_3)_u}{ds} + 3(\delta_3)_u \frac{du_\delta/ds}{u_\delta} = -2 \frac{\tau_\delta}{\rho u_\delta^2} + c_{Df} + \frac{2}{u_\delta^3} \frac{d}{ds} \int_0^\delta u \frac{\bar{u}'^2 + \bar{v}'^2 + \bar{w}'^2}{2} dy \quad (5.88)$$

in which the dissipation integral c_{Df} is defined as

$$c_{Df} = \frac{2}{\rho u_\delta^3} \int_0^\delta \tau(y) \frac{\partial u}{\partial y} dy - \frac{2}{u_\delta^3} \frac{d}{ds} \int_0^\delta u \frac{u'^2 + v'^2 + w'^2}{2} dy. \quad (5.89)$$

The following integral parameters are now defined (with "f" referring to fluctuating):

$$(\delta_1)_f = (\delta_1)_u \quad (5.90)$$

$$(\delta_2)_f = (\delta_2)_u - \int_0^\delta \frac{u'^2 - v'^2}{u_\delta^2} dy \quad (5.91)$$

$$(\delta_3)_f = (\delta_3)_u - \int_0^\delta \frac{u}{u_\delta} \left(\frac{u'^2 + v'^2 + w'^2}{u_\delta^2} \right) dy \quad (5.92)$$

$$(H_{12})_f = \frac{(\delta_1)_f}{(\delta_2)_f} \quad (H_{32})_f = \frac{(\delta_3)_f}{(\delta_2)_f}. \quad (5.93)$$

By defining also a length parameter,

$$Z_f = (\delta_2)_f (R_{\delta_2})_f^n \quad (5.94)$$

and

$$\tilde{c}_{ff} = \tilde{c}_f \left(1 - \frac{\tau_\delta}{\tau_w} \right) \quad (5.95)$$

$$\tilde{c}_{Df} = \frac{c_{Df}}{2} - \frac{\tau_{\delta}}{\rho u_{\delta}^2} \quad (5.96)$$

the system 5.87 and 5.88 can be written in the form of Eqns. 5.13 and 5.14 in terms of the dependent variables Z_f and $(H_{32})_f$. Obviously, then, the same solution procedure used with Eqns. 5.13 and 5.14 can be used with Eqns. 5.87 and 5.88. The auxiliary relations needed to close the system are:

$$\alpha_f = \alpha_f ((H_{32})_f, Tu) \quad (5.97)$$

$$\tilde{c}_{Df} = \tilde{c}_{Df} ((H_{32})_f, Tu) \quad (5.98)$$

$$(H_{12})_f = (H_{12})_f ((H_{32})_f, Tu). \quad (5.99)$$

The auxiliary relation 5.97 was not obtained explicitly; equivalently, \tilde{c}_{ff} was set as a function of Tu in the calculation procedure via the ratio τ_{δ}/τ_w shown correlated in Fig. 5.6 against local $(R_{\delta_2})_u$ and Tu . The data points used in the correlation (solid points in Fig. 5.6) were those presented by Huffman et al. (1972) and Evans (1974). Charnay et al. (1971) did not report the local $(R_{\delta_2})_u$ and therefore their data could not be used in the present correlation.

The fluctuating dissipation integral, \tilde{c}_{Df} , in Eqn. 5.98 was assumed to be independent of Tu since the effects of τ_{δ} and the Reynolds normal stresses on c_{Df} in Eqn. 5.89 are opposed. Therefore, \tilde{c}_{Df} may be assumed unchanged from its \tilde{c}_{Di} value.

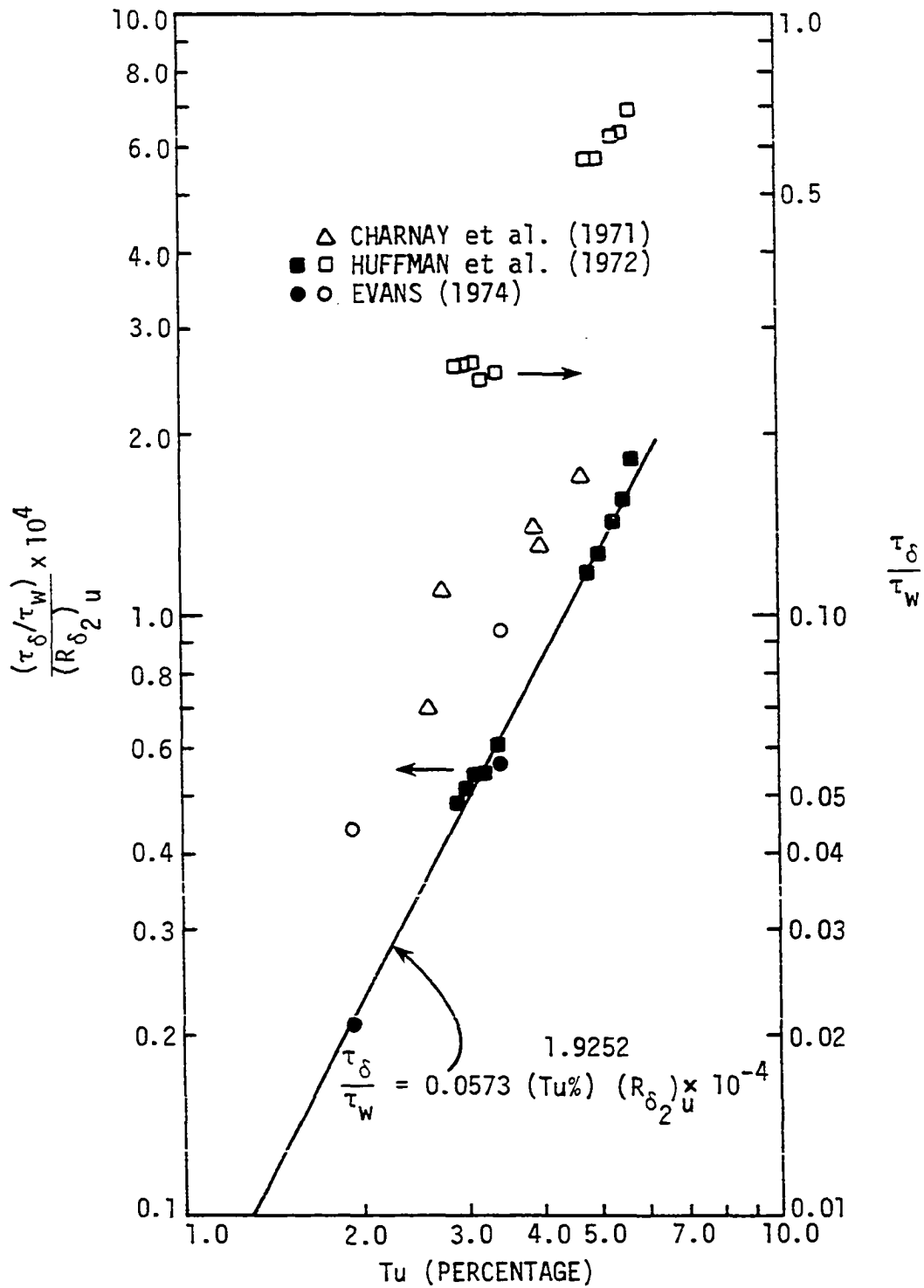


Figure 5.6. Influence of local free stream turbulence level on apparent Reynolds shear stress τ_δ at the edge of the boundary layer.

The auxiliary relation 5.99 was derived by first assuming $(H_{32})_f = H_{32}$ as in Assassa and Papailiou (1979). $(H_{12})_f$ was then correlated against H_{12} and Tu as presented in Fig. 5.7. The single solid data point shown in Fig. 5.7 was obtained from the measurements of Schubauer and Klebanoff (1951), supposedly carried out at low free stream turbulence level. The normal Reynolds stresses measured by Schubauer and Klebanoff (1951), however, are now recognized to be about 30% too high explaining why this point did not correlate with the present correlation. Huffman et al. (1972) did not measure the terms \bar{u}'^2 , \bar{v}'^2 , and \bar{w}'^2 separately, but only the turbulent kinetic energy $0.5 (\bar{u}'^2 + \bar{v}'^2 + \bar{w}'^2)$ across the boundary layer. Therefore, the following assumptions were made to obtain $(\delta_2)_f$ from integration of the kinetic energy data:

- (i) $\bar{w}'^2 \approx 1.2 \bar{v}'^2$, which was also assumed by Huffman et al. (1972).
- (ii) $\bar{v}'^2 \approx 0.5 \bar{u}'^2$, which is a reasonable assumption from the data of Evans (1974).

The experimental data of Huffman et al. (1972) are compared in Fig. 5.8 with the results obtained with the present calculation method incorporating the correlations in Figs. 5.6 and 5.7. Corresponding results obtained by McDonald and Kreskovsky (1974) with a field method are also shown. The present method is observed to predict the development of the shape factor H_{12} and momentum thickness $(\delta_2)_u$ well, and to slightly over predict the skin friction c_f .

In summary, the general trends caused by the free stream turbulence level on the turbulent boundary layer development are:

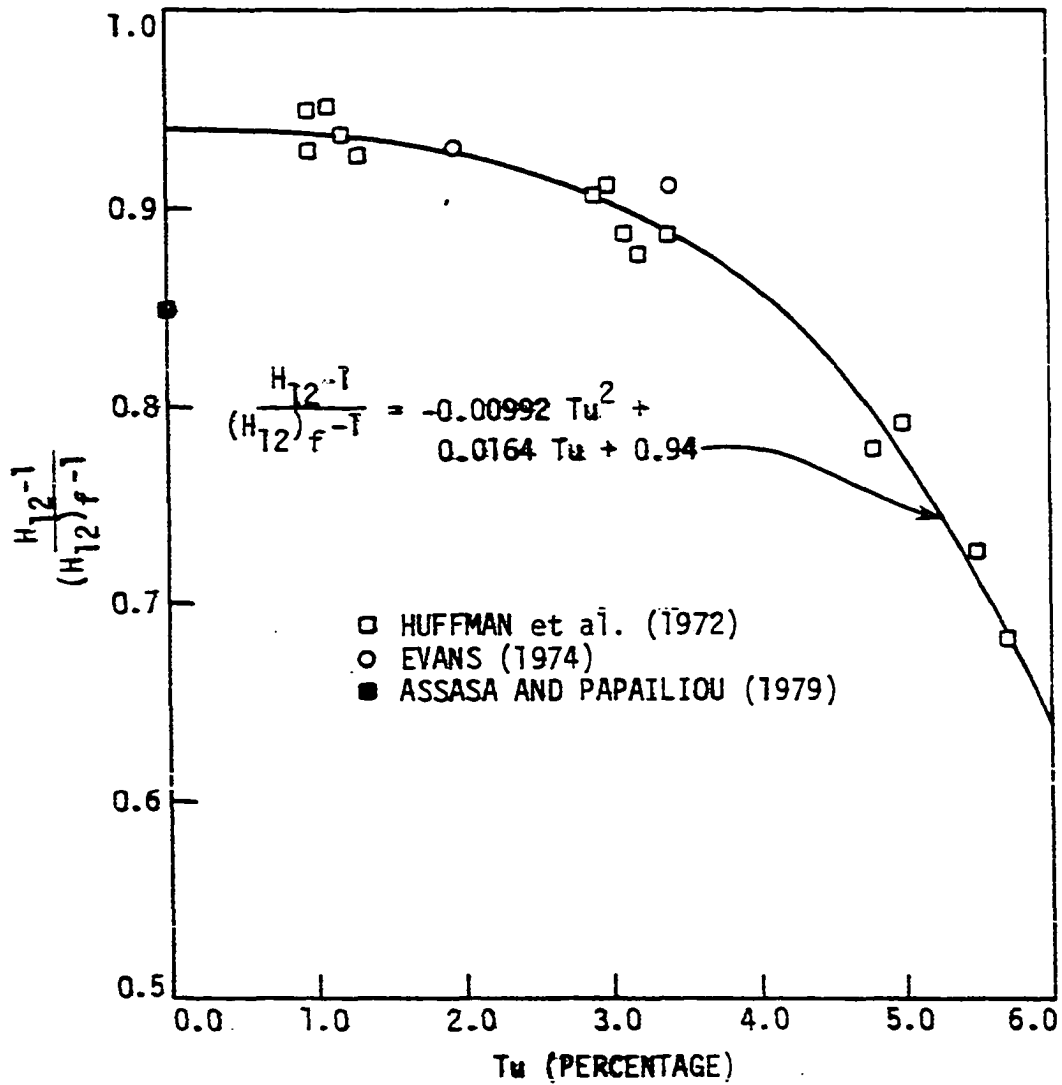


Figure 5.7. Influence of local free stream turbulence level on shape factor $(H_{12})_f$ obtained by retaining the normal Reynolds stresses in $(\delta_2)_f$

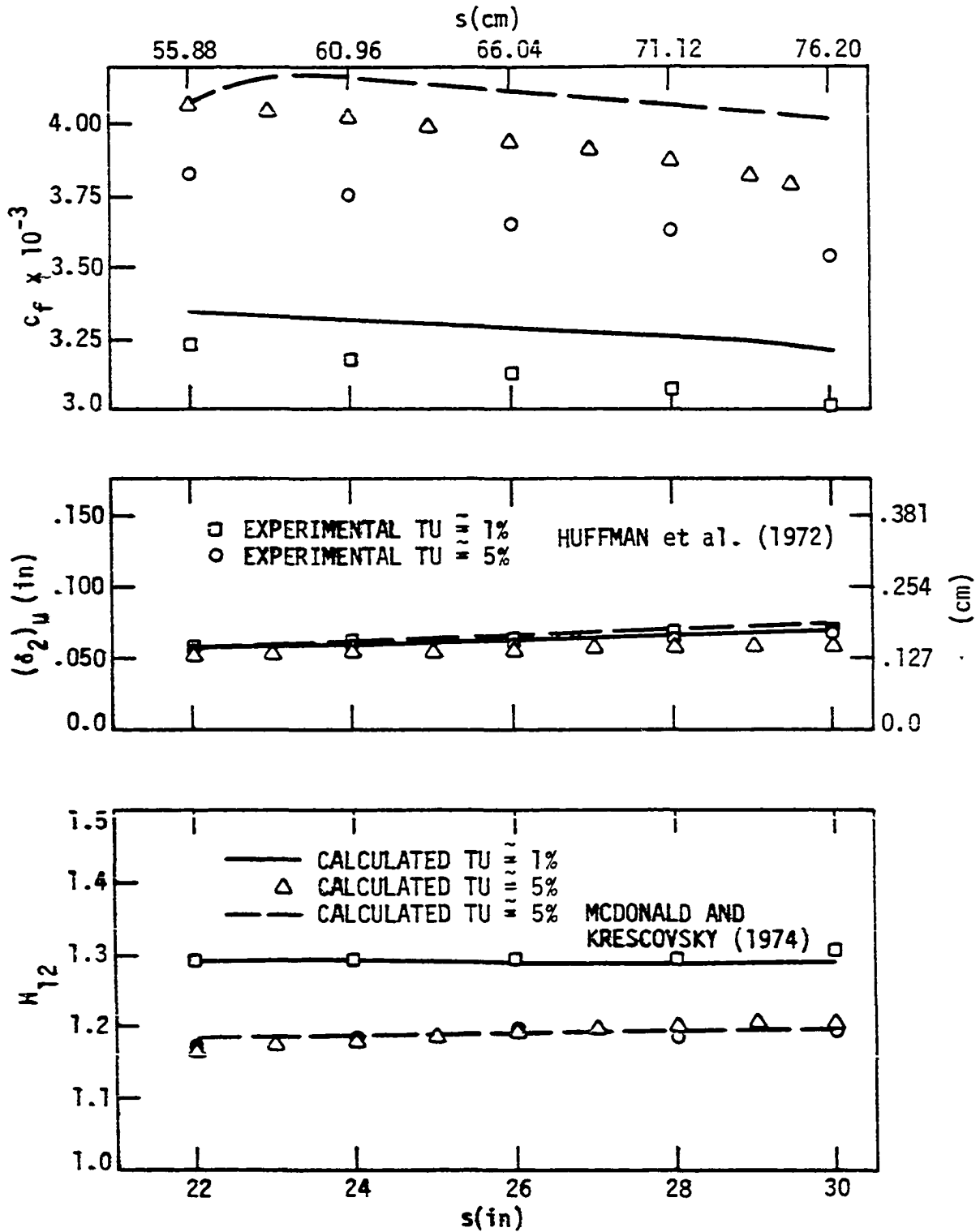


Figure 5.8. Comparison of predicted and experimental turbulent boundary layer development under the influence of different free stream turbulence levels for Huffman et al. (1972).

- (i) Separation tendency on both surfaces of the airfoil is suppressed.
- (ii) The skin friction is slightly increased.
- (iii) Losses are not substantially altered since momentum thickness is essentially unchanged in cases short of turbulent separation. Losses could be reduced if the turbulent separated region is reduced by the free stream turbulence level.

In the programmed calculation method, the free stream turbulence effects on the development of the turbulent boundary layer have been included in such a way that the user can easily leave them out if the case being treated is a compressible one. Batchelor's linear analysis is used to estimate the local free stream turbulence level.

5.8. Empirical Model for Proceeding After Turbulent Separation

The onset of turbulent separation is established in the boundary layer calculation by the condition $\tilde{c}_f = 0$. This condition and the auxiliary relations 5.45, 5.46, 5.47, 5.48, and 5.52 yield the values of 1.5008 and 2.7078 for H_{32} and H_{12} at separation. Therefore, turbulent separation is predicted when either the calculated H_{32} is less than 1.5 or when the calculated H_{12} is greater than 2.7. In some cases, however, the value of H_{12} increases rapidly near separation, and begins to decrease without reaching the critical value of 2.7. In that case, the point corresponding to the maximum value of H_{12} is taken as the separation point (see Cebeci et al. (1972)).

The method of Föttner (1972), applicable to either the suction or pressure side of the airfoil, was implemented in this study to proceed with the boundary layer calculation after the occurrence of turbulent separation. This method is based on the idea that momentum loss thickness $(\delta_2)_{TE}$ at the trailing edge of the airfoil with the boundary layer separated is always greater than the momentum loss thickness $(\delta_2)_{TE,req}$ obtained at the trailing edge as if the boundary layer had not separated at a point upstream. In the limiting case of no separation, both momentum loss thicknesses are of course the same.

Föttner obtained his relationship between $(\delta_2)_{TE}$ and $(\delta_2)_{TE,req}$ by a reverse wake mixing loss calculation carried out between the trailing edge plane and the downstream plane where homogeneous outlet flow exists. Using a large number of total pressure loss data for cascades measured for different extents of the separated region on the airfoil, Föttner made the reverse wake mixing calculation to obtain $(\delta_2)_{TE}$ needed to reproduce the measured total pressure loss. On the other hand, $(\delta_2)_{TE,req}$ was obtained by continuing the boundary layer calculation from the separation point under the conditions of inviscid velocity distribution and non-separated flow, and with the assumption that the shape factor H_{32} remains constant and equal to the separation value.

The results for the ratio $(\delta_2)_{TE}/(\delta_2)_{TE,req}$ are plotted in Fig. 5.9 as a function of separation point c_s along the airfoil chord. Also, $(H_{12})_{TE}$ is plotted in Fig. 5.9 against separation point s_s measured along the profile of the airfoil from the leading edge stagnation point.

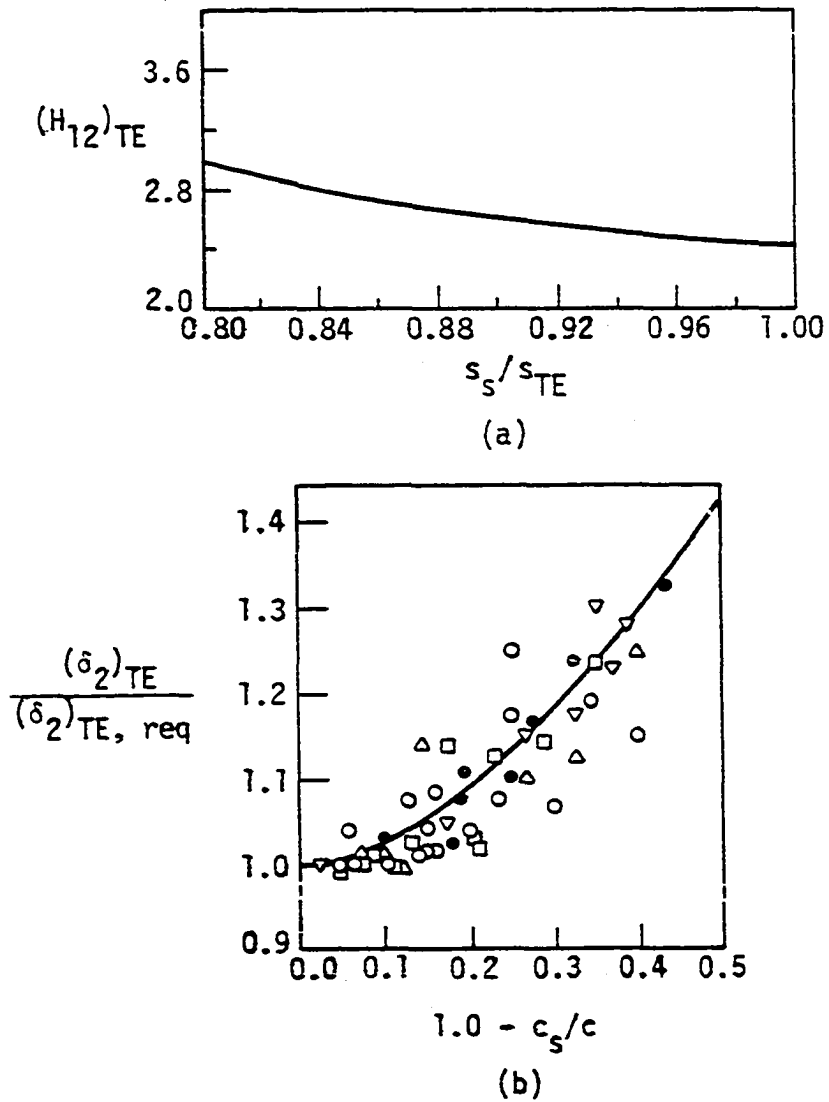


Figure 5.9. Turbulent separation model due to Föttner (1972).
 (a) Shape factor $(H_{12})_{TE}$ correction for separation.
 (b) Momentum loss thickness $(\delta_2)_{TE}$ correction for separation.

Even though not explicitly said by Föttner, it is conjectured that not only the losses but also the exit gas angle were matched in the reverse calculation in order to obtain $(H_{12})_{TE}$.

In this application, the inviscid flow solution was not corrected for the effects of boundary layer displacement thickness.

5.9. Wake Mixing Loss Calculations

The method used for the wake mixing loss calculation in the incompressible case was that due to Speidel (1954). This choice is consistent with Föttner's (1972) choice of wake mixing loss model in the turbulent separation model. Speidel modified the camber line and the inviscid turning of the cascade by the difference in the suction and pressure surface displacement thickness and calculated again the potential flow through the cascade before applying the wake mixing analysis. In this application, the cascade was not modified by the boundary layer displacement thickness, and the wake mixing loss calculation was carried out with the first boundary layer results. Speidel's analysis is presented in Appendix G neglecting the inviscid-viscous interaction.

For the compressible case, Föttner used the analysis of Stewart (1955) which was also used here.

6. VALIDATION OF THE INVISCID-VISCOUS BLADE-TO-BLADE FLOW ANALYSIS

6.1. Introduction

This chapter is devoted to validating the combined inviscid-viscous blade-to-blade flow calculation procedures developed in Chapters 3, 4, and 5. The accuracy in predicting airfoil pressure distributions, cascade total pressure losses and exit gas angles is tested by comparing calculated results for two different turbine cascades with available experimental data.

The input variables needed for the blade-to-blade analysis programs, along with the input format, are explained in Appendix H.

6.2. Experimental Cascade Data as Test Cases

Numerous cases of turbine cascade experimental tests have been reported in the literature. Experimental data prior to that of Ainley and Mathieson (1955) have generally omitted reference to Reynolds number or to cascade pitch-to-chord ratio as important parameters. As a result, such data are usually difficult to compare with more recent and comprehensive test results.

Table 6.1 contains a listing of reference sources plus a brief summary of turbine cascade experimental data useful in large part for validation of blade-to-blade calculation procedures. This listing is by no means an exhaustive compilation, consisting of the most well-

Table 6.1. Summary of Experimental Turbine Cascade Data .

Cascade Reference	Cascade Geometry	Contraction Ratio, CR	Turning Angle, θ , deg	Pitch/Chord, τ/c	Inlet Conditions
Ainley and Mathieson (1955)	•	1.00 - 5.76	40-140	0.3-1.0	—
Dunavant and Erwin (1956)	•	1.00 - 3.86	60-120	0.56, 0.67	•
Wilson and Pope (1954) Bridle (1949)	•	1.30 - 2.00	60-110	0.57	•
Forster (1964)	—	—	—	—	—
Turner (1971) Hodge (1960) Andrews and Schofield (1950)	•	1.64 - 2.00	25-95	0.65	•
Huffman et al. (1971) Delaney (1979)	•	1.92 - 2.42	51-72	0.75	•
VKI Lecture Series Nos 59,84 (1973, 1976)	•	—	—	—	•

A dot means the information is given in the reference.

Exit Reynolds No., $R_c \times 10^{-5}$	Axial Velocity Density Ratio, AVDR	Losses	Exit Mach No., M_2	Exit Gas Angle, β_2 , deg	Remarks
0.7 - 2.0	—	•	$\approx 0.0-0.6$	•	
3.2 - 5.0 12.0 - 15.0	—	•	$\approx 0.0-0.97$	•	Surface pressure distributions given. R_c based on average con conditions.
1.8 - 7.0	—	•	—	•	Surface pressure distributions given. Tu_1 studied but not reported.
1.0 - 4.0	—	•	0.4-1.34	•	R_c based on axial chord.
2.6 - 10.5	—	•	0.3-0.9	•	Surface pressure distributions given. Tu_1 ranged from 0.45 to 5.0 percent.
4.6 - 5.6	•	•	0.55-1.30	•	Surface pressure distributions given. Low turbulence level.
2.0 - 14.0	—	•	0.5-1.9	—	Surface pressure distributions given. Tu_1 reported in some cases.

known published data sets only. The data references in Table 6.1 generally contain test information on gas properties, inlet stagnation conditions, Mach number and flow angle, inlet turbulence level, chord Reynolds number (based on exit conditions), exit stagnation pressure, Mach number, and gas angle. In addition, in some cases, airfoil pressure distributions and axial velocity density ratio, AVDR, are known. If AVDR is different from unity, its distribution in the axial direction between the upstream and downstream measuring stations is of paramount importance. However, this type of data have not yet been published to this author's knowledge. Also, the experimental data on the aerodynamic parameters described above are of little use for validation of blade-to-blade flow calculation methods if a detailed description of the cascade geometry on which the experiments were performed is not given.

6.3. Test Cases and Results

Calculations for the Test Cases No. 1 and No. 2 presented here were carried out on the VAX PDP-11 computer. Typical computing times to perform the complete blade-to-blade flow analysis for these cases including the global inviscid analysis, leading edge reanalysis, boundary layer, and wake-mixing analysis ranged from 3 to 5 CPU minutes. For all three cases, the streamline curvature calculations in the global analysis (SCA) were made using the calculated β_2 option for the exit flow, and the natural transition model due to Crimi and Reeves (1972)

was used in the boundary layer analysis. Complete listings of actual program input data for some of the test cases are given in Appendix H, along with definitions or descriptions of the program input parameters. Additional user information for the programs comprising the overall turbine cascade design system, covering input data preparation, program output description, and sample cases is given by Alarcon (1980). For Test Case No. 1, a comparison analysis was carried out for one of the Dunavant and Erwin (1956) blade cascades listed in Table 6.1. The airfoil, identified as a NACA primary blade section with $\theta_c = 80^\circ$ and $t/c = 0.10$, is shown in Fig. 6.1. Additional cascade geometry data are $\tau/c = 0.56$ and $c = 6.00$ in (15.24 cm). The cascade analysis was made over a range of inlet angle, α_1 , (see Fig. 6.1) covering positive and negative incidences while keeping the inlet gas angle, β_1 , and the inlet gas velocity, V_1 , constant at 75° and 100 ft/sec, respectively. Dunavant and Erwin obtained their experimental results over a range of flow incidence by holding β_1 constant and restaggering the cascade to produce different α_1 angle values. This means of varying incidence of the inlet flow proved to be difficult to simulate, since the airfoil coordinates for each cascade stagger had to be calculated and readjusted in a trial and error procedure to obtain smooth curvature distributions for the spline-fitted profiles. Adequacy of the fit around the leading edge was found to reflect directly on the smoothness of the velocity distribution calculated in the leading edge reanalysis (REA).

The flow at five values of α_1 (39, 45, 48, 54, and 60 degrees) was calculated. The turning angle, θ , and drag coefficient, C_{d_1} ,

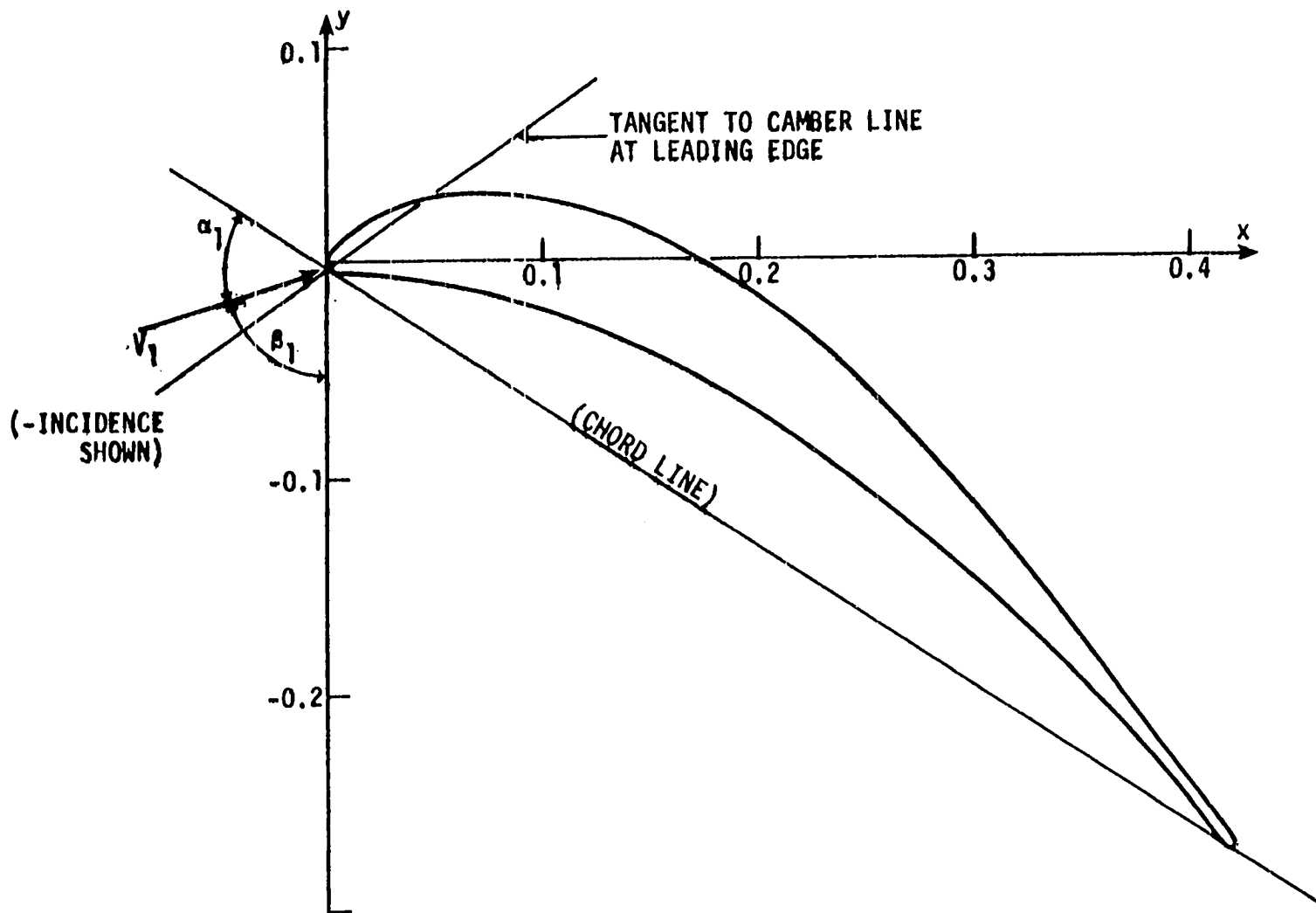


Figure 6.1. Turbine cascade airfoil for Test Case No. 1. $\beta_1 = 75^\circ$, $\tau/c = 0.556$, $\alpha_1 = 48^\circ$ for setting shown. Dunavant and Erwin (1956).

plotted against α_1 are shown in Fig. 6.2. These results were obtained by adjusting Tu_1 , and therefore the location of natural transition, in order to match the loss level at the value of α_1 giving minimum loss, i.e., $\alpha_1 = 48^\circ$. This gave a Tu_1 value of 2.75% which was then used with the other four values of α_1 . The calculated drag coefficient (see Appendix G for C_{d_1} equation) agrees well with the data at high values of α_1 , but is somewhat low at low values of α_1 . The increase in C_{d_1} with α_1 is to be expected, since, as α_1 increases, the velocity peak on the suction side of the airfoil increases and the transition point moves forward, with laminar separation eventually occurring. This same phenomenon occurs at low α_1 , but on the pressure side. The calculated turning angle is observed to agree with the experimental data to within 0.5 degrees throughout the range of α_1 . The location of the laminar turbulent transition for each computed test point is summarized in Table 6.2.

Table 6.2. Laminar-turbulent transition locations for Test Case No. 1. N.T. (Natural transition), F.T. (Fully turbulent), L.S. (Laminar separation), T.R. (Turbulent reattachment) are noted

α_1 (deg)	R_c $\times 10^{-5}$	B_x (ft)	Suction Side, x/B_x				Pressure Side, x/B_x			
			N.T.	F.T.	L.S.	T.R.	N.T.	F.T.	L.S.	T.R.
39.0	3.78	0.4584	0.241	0.435	-----	-----	-----	-----	0.023	0.059
45.0	4.01	0.4346	0.249	0.436	-----	-----	0.270	0.453	-----	-----
48.0	4.53	0.4209	0.251	0.437	-----	-----	0.280	0.457	-----	-----
54.0	5.19	0.3901	-----	-----	0.008	0.021	0.748	-----	-----	-----
60.0	6.27	0.3552	-----	-----	0.011	0.026	0.757	-----	-----	-----

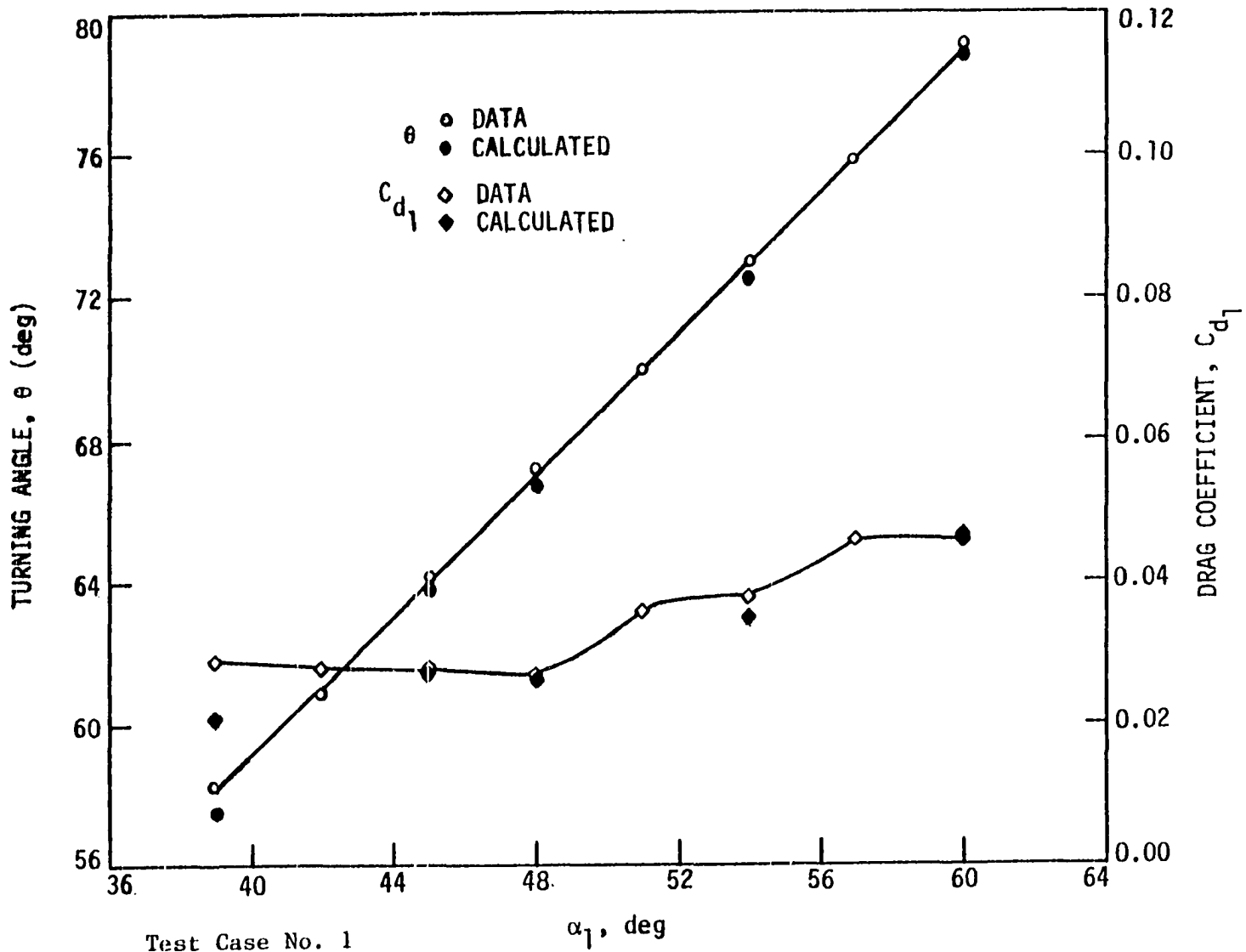


Figure 6.2. Calculated turning angle and drag coefficient compared with experimental data. $Tu_1 = 2.75\%$, $M_1 = 0.088$, $\tau/c = 0.56$, $c = 6$ in (15.24 cm). Data from Dunavant and Erwin (1956).

Figures 6.3, 6.4, and 6.5 show the airfoil pressure distribution and the AVDR distribution through and downstream of the cascade for three of the α_1 test points computed. The results shown are for the α_1 giving the minimum experimental loss and for α_1 at either end of the range calculated. For $\alpha_1 = 48^\circ$, and with AVDR = 1 through the cascade, as shown in Fig. 6.3, the airfoil pressure distribution matches well with the experimental data. However, as shown in Fig. 6.4 and 6.5, values of AVDR ≤ 1 inside and downstream of the cascade (indicating an increase in stream sheet thickness inside and downstream of the cascade) were needed in order to match the experimental and calculated pressure distributions when α_1 was increased or decreased from minimum loss incidence.

By comparing mass flow rates, measured by Dunavant and Erwin, upstream and downstream of the cascade, values of AVDR ranging from 0.97 to 1.05 were determined. The AVDR values used in Fig. 6.4 and 6.5 are within this range. As already stated in the discussion of example E3 in Chapter 3, AVDR < 1 might be explained in terms of three-dimensional endwall flow effects affecting the midspan two-dimensionality in cascades at moderate to low aspect ratios (the aspect ratio for this cascade was not reported).

The results shown in Figs. 6.3, 6.4, and 6.5 demonstrate well the ability of the leading reanalysis to determine the velocity distribution and local overspeeding around the leading edge over a range of flow incidence. Figure 6.4 shows that for the case of high positive incidence

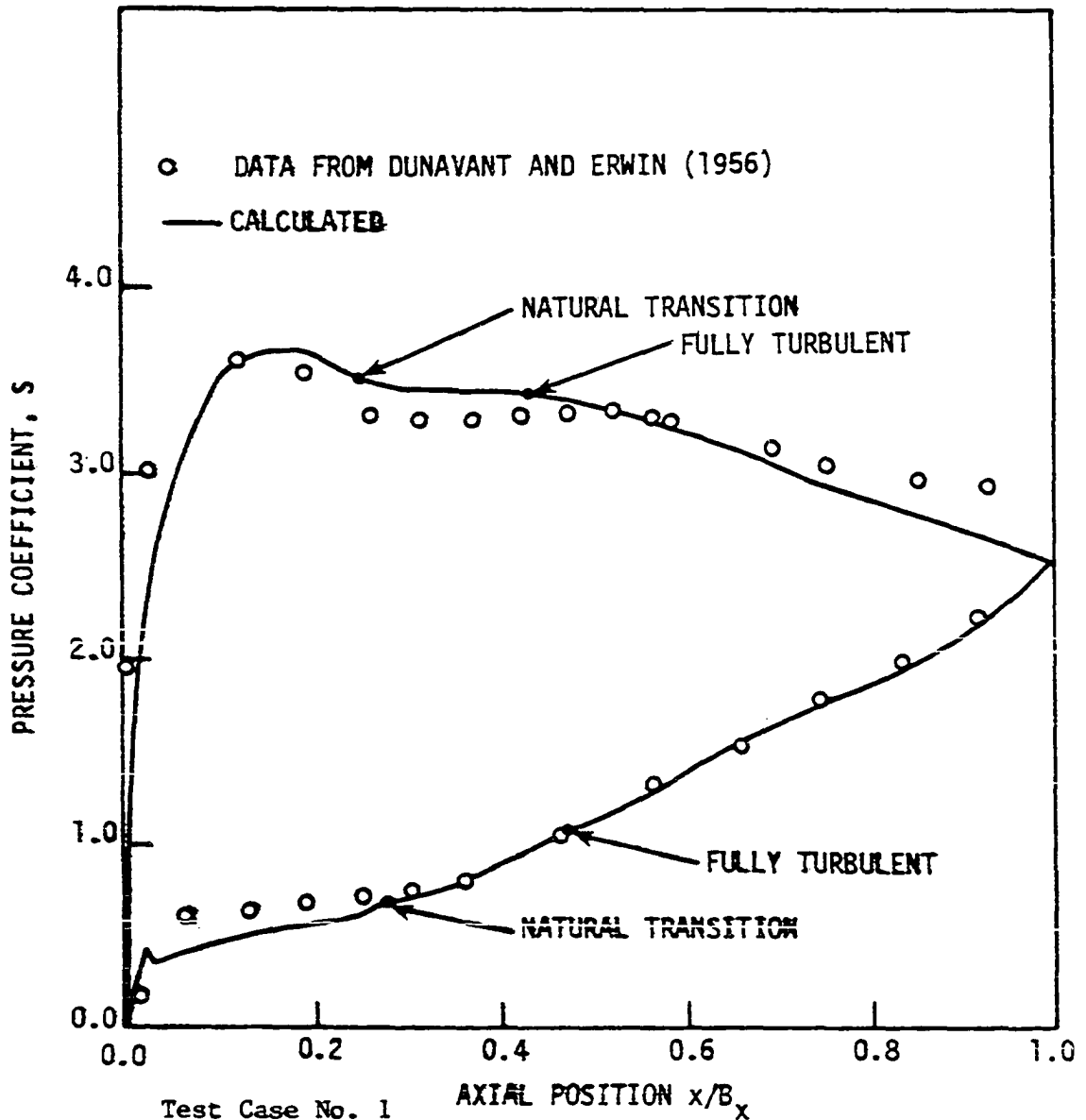
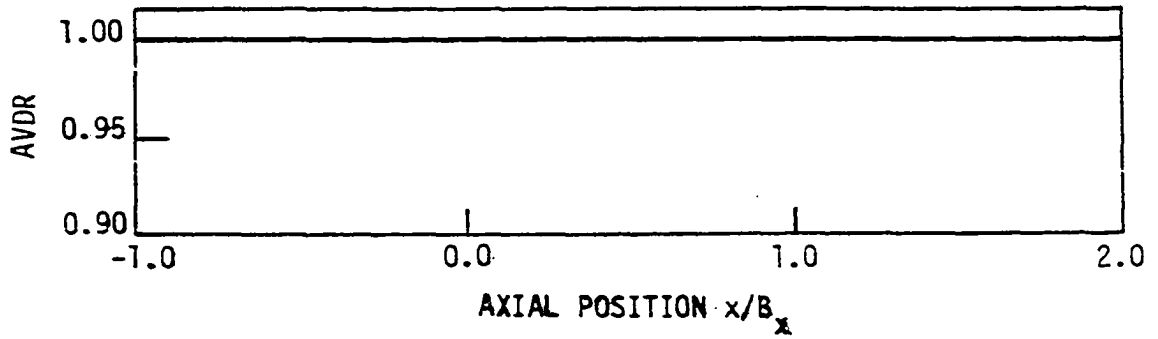
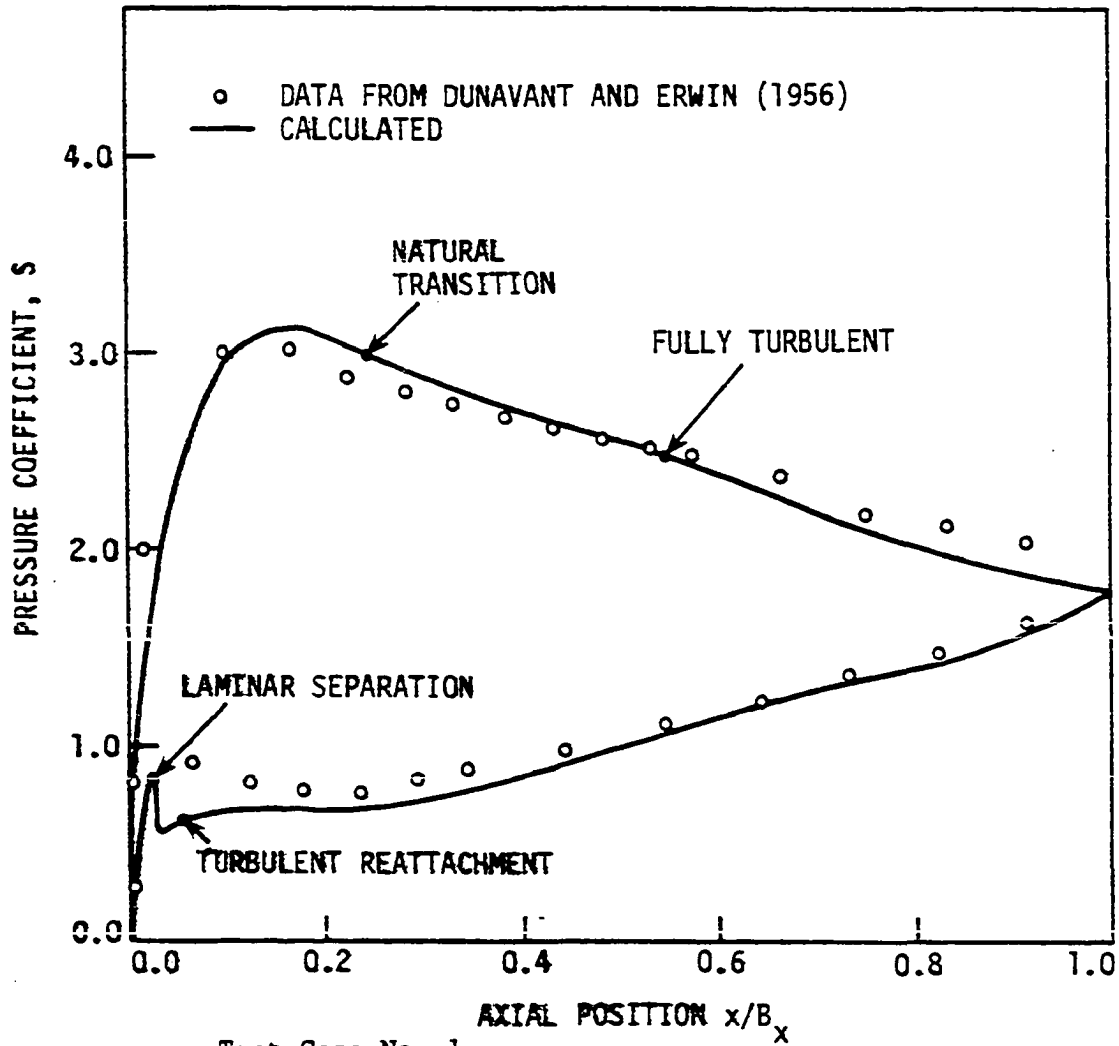
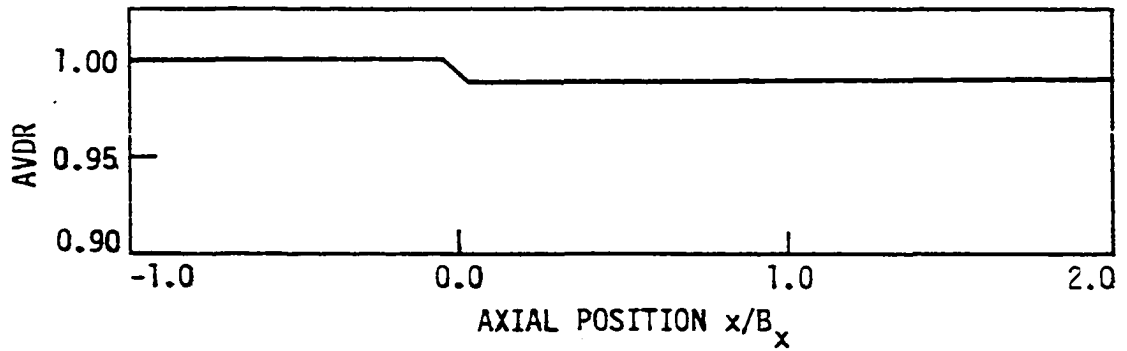


Figure 6.3. Calculated airfoil pressure distribution compared with experimental data. $Tu_1 = 2.75\%$, $\alpha_1 = 48^\circ$.



Test Case No. 1

Figure 6.5. Calculated airfoil pressure distribution compared with experimental data. $Tu_1 = 2.75\%$, $\alpha_1 = 39^\circ$.

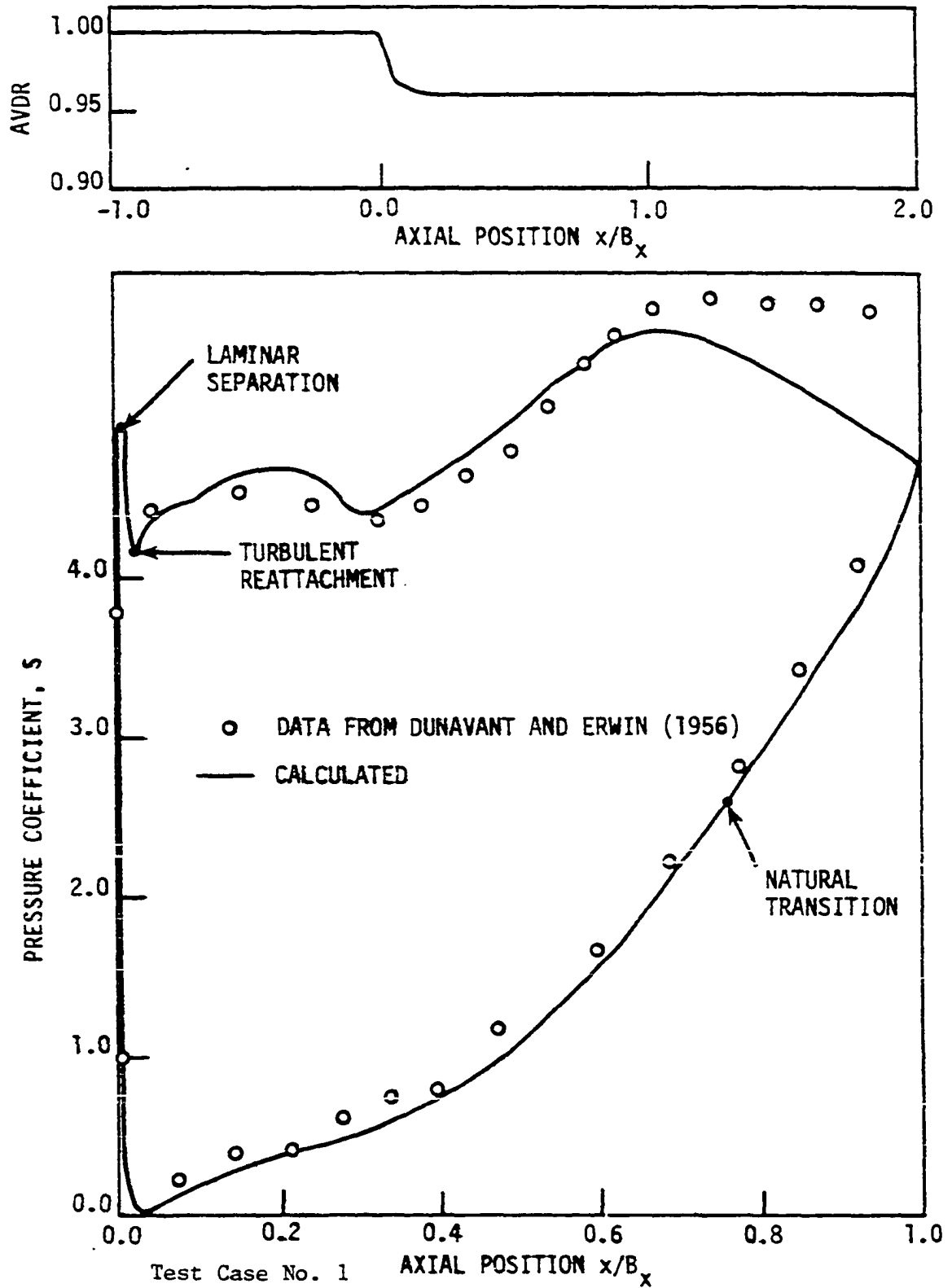


Figure 6.4. Calculated airfoil pressure distribution compared with experimental data. $Tu_1 = 2.75\%$, $\alpha_1 = 60^\circ$.

($\alpha_1 = 60^\circ$) the laminar boundary layer separated on the suction side forming a separation bubble. Also, the strong acceleration on the pressure side resulted in late natural transition, with the boundary layer reaching the trailing edge in a transitional state. Figure 6.5, which is for the case of high negative incidence, shows, on the other hand, laminar separation on the pressure side with formation of a separation bubble; fully turbulent flow occurs on both the suction and pressure sides of the airfoil.

Test Case No. 2 comprised a comparison analysis for the Huffman et al. (1971) vane cascade listed in Table 6.1. The airfoil in cascade has already been shown in Fig. 3.16. The following cascade geometry data apply: $\tau/c = 0.75$, $c = 1.80$ in (4.75 cm) and $B_x = 1.20$ in (3.051 cm). In contrast to the Dunavant and Erwin data cited in Test Case No. 1, the Huffman data were obtained for varying inlet flow incidence, as well as varying Mach number, at constant setting of cascade stagger. However, in the theoretical analysis for Test Case No. 2 it was decided to maintain constant (zero) incidence while varying the Mach number level of the flow.

Test points at four different inlet Mach numbers were calculated. These points are listed in Table 6.3, along with the experimentally determined exit Mach number and exit chord Reynolds number. Also shown in Table 6.3 is a breakdown of computing times required in various parts of the analysis.

Table 6.3. Test Case No. 2. Test point conditions and computing times required on the VAX-PDP 11.

Inlet Mach No., M_1	Exit Chord Reynolds No. $R_c \times 10^{-5}$	Exit Mach No., M_2	CPU Minutes		
			Streamline Curvature	Reanalysis	Boundary Layer
0.201	4.57	0.553	1.27	0.73	1.30
0.223	4.98	0.653	1.03	0.79	1.15
0.238	5.34	0.756	1.92	0.90	1.26
0.245	5.60	0.855	3.23	1.09	1.02

In the global inviscid analysis (streamline curvature calculations) for each test point, M_2 and β_2 were determined using the calculated β_2 option for the exit gas angle, and by taking the total pressure losses as zero. Also, adjustments were made to the stream sheet thickness Δz through the cascade to satisfy AVDR requirements for the flow cases. These calculations, therefore, produced inviscid answers for M_2 and β_2 . In addition, the boundary layer and mixing loss calculations produced viscous answers for β_2 along with predicted total pressure loss coefficients, $\bar{\omega}_2$. For the boundary layer analysis, Tu_1 was set at 1% for all the test points (the inlet turbulence level was known to be low for the experimental cascade data).

The various calculated β_2 and $\bar{\omega}_2$ results are shown plotted compared with experimental values in Fig. 6.6. The calculated M_2 is the abscissa in each graph. The loss coefficient $\bar{\omega}_2$ is seen to agree well with the experimental points over the range of M_2 tested. Furthermore, the calculated $\bar{\omega}_2$ (at 1.0 times axial chord downstream of the cascade) lie

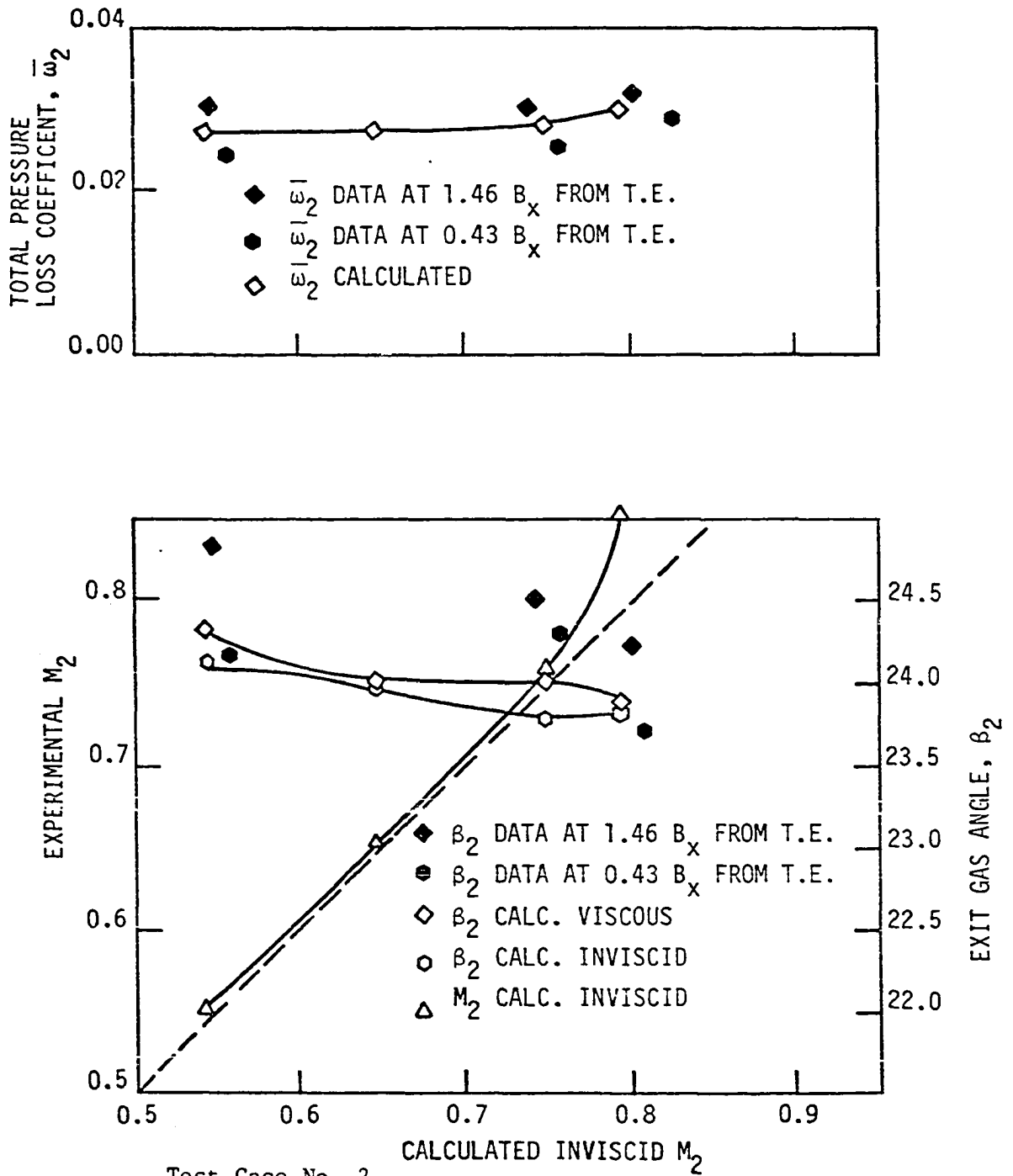


Figure 6.6. Calculated exit gas angle, losses and exit Mach number compared with experimental data from Huffman et al. (1971). $Tu_1 = 1\%$.

in between the values measured at 0.43 times axial chord, and at 1.46 times axial chord downstream of the cascade. It is implied in these results that a distance downstream of this cascade greater than one axial chord is required for mixing out of the flow to be computed. Also, as seen in Fig. 6.6, the viscous β_2 and the experimental β_2 agree to within 1.0 degree, and the calculated and experimental M_2 agree closely, except at the high end of the range where a difference of approximately 0.06 is noted. The general agreement between calculated and experimental M_2 tends to confirm the values of AVDR used in the calculations.

Figures 6.7 and 6.8 compare the predicted velocity distribution on the airfoils with the experimental distributions for two of the test points corresponding to the lowest and highest M_1 calculated. The distribution of AVDR shown in the top graph of each Figure was obtained after several tries in which Δz was adjusted so that calculated and experimental surface velocity distributions matched reasonably well. The determined distribution also matched the two experimental AVDR points measured downstream of the cascade. Experimental AVDR data points shown in Fig. 6.9 are lumped values accounting for the ratio \dot{m}_2/\dot{m}_1 and the contraction coefficient measured by Huffman et al. (1971). Upstream of the leading edge, the endwall boundary layer was assumed to be negligible giving, therefore, AVDR = 1.0 in this region. Inside and downstream of the cascade, AVDR < 1.0 was required. As already explained in Example E3 in Chapter 3 and in Test Case No. 1, this

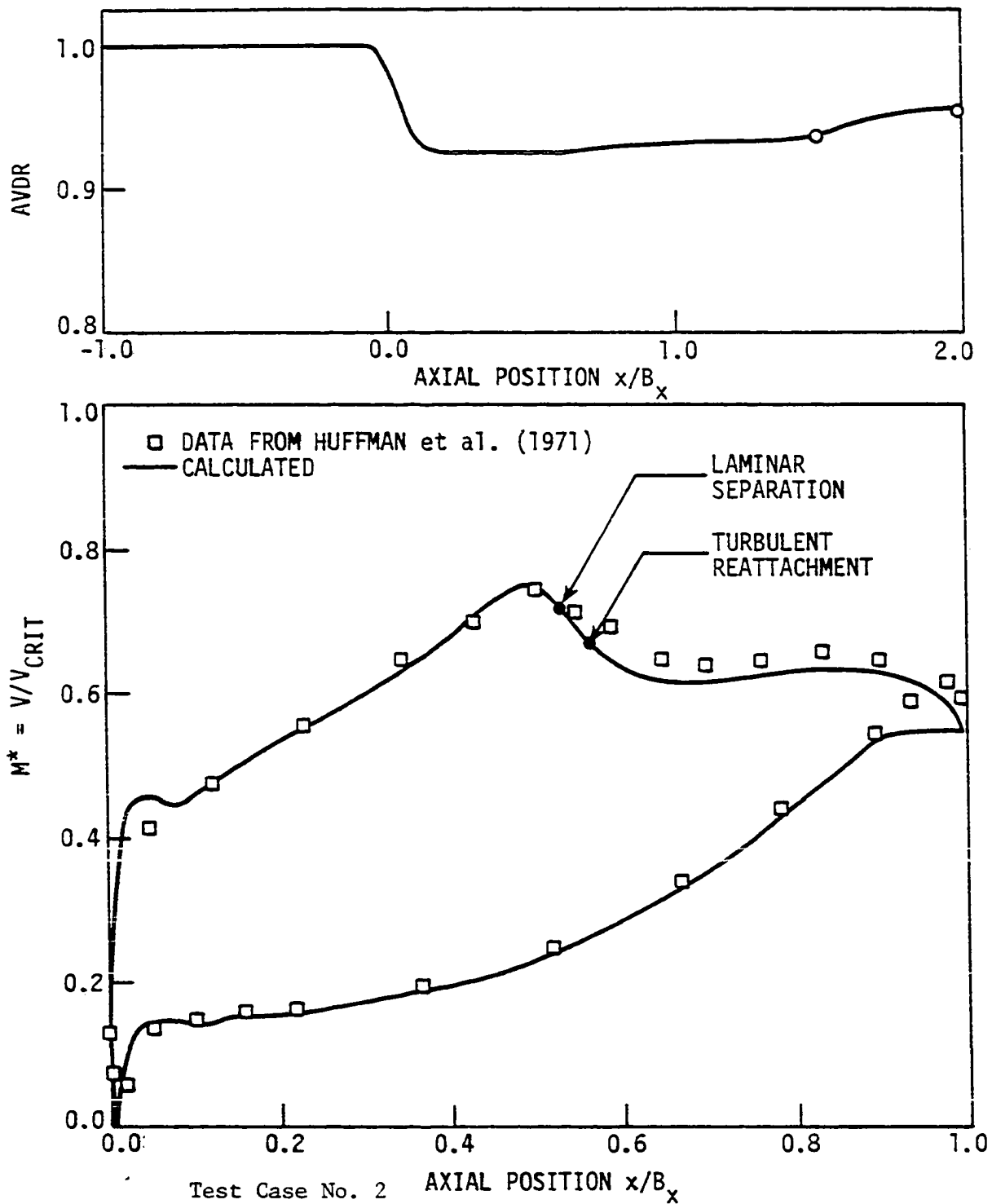


Figure 6.7. Comparison of predicted profile velocities and AVDR distribution with experimental data. $Tu_1 = 1\%$, $M_1 = .201$.

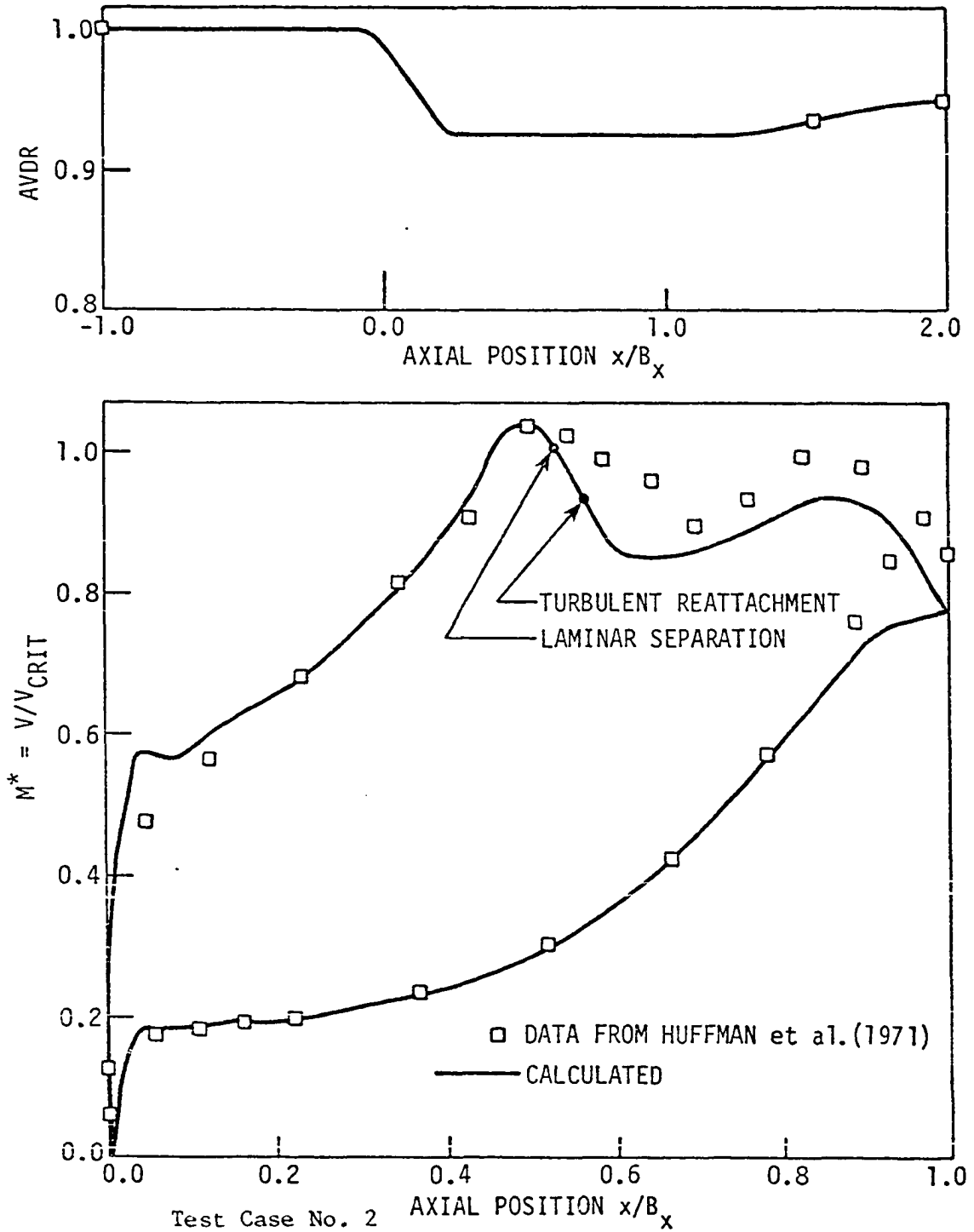
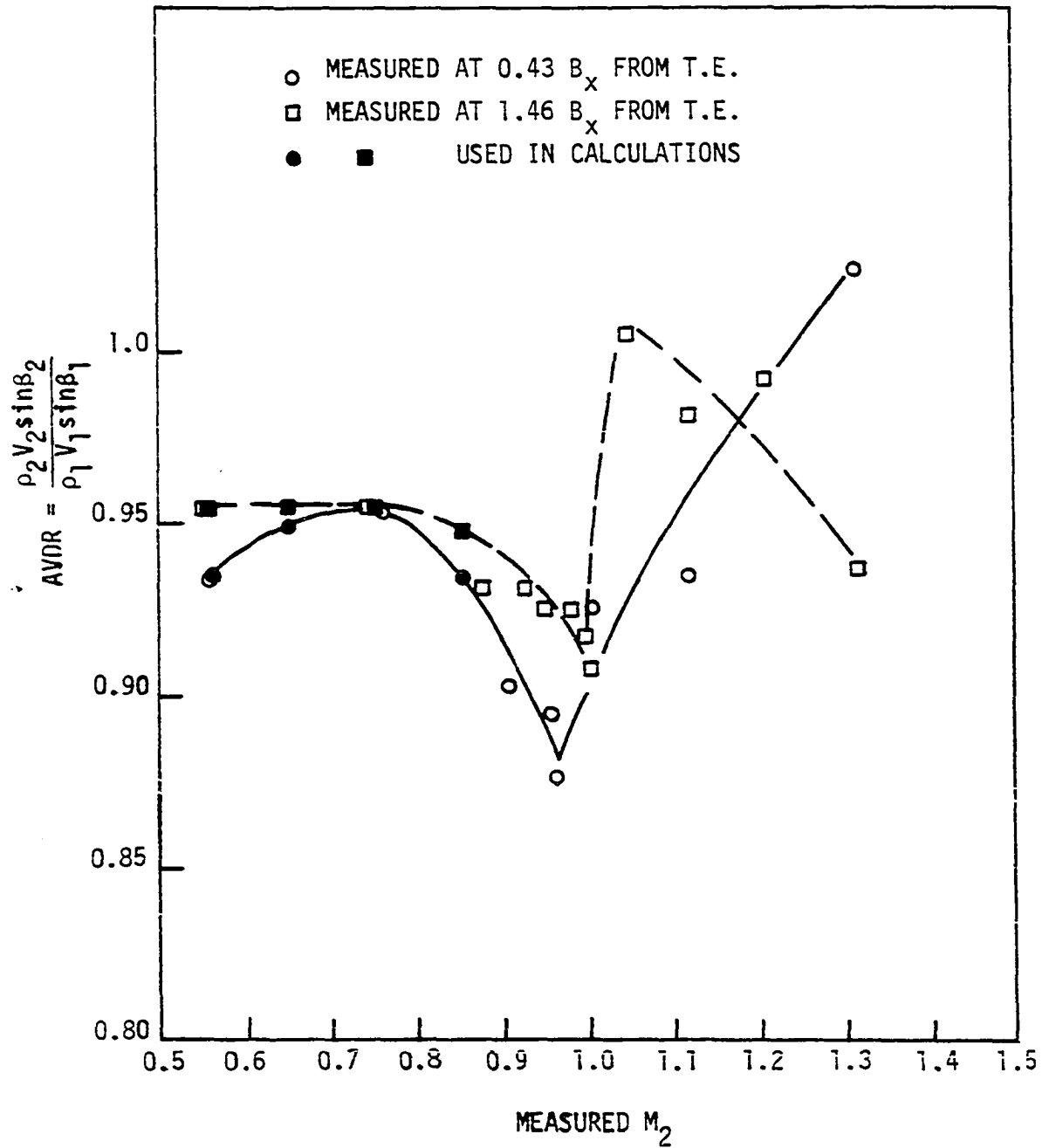


Figure 6.8. Comparison of predicted profile velocities and AVDR distribution with experimental data. $Tu_1 = 1\%$, $M_1 = .245$.



Test Case No. 2

Figure 6.9. Experimental values of axial velocity density ratio measured by Huffman et al. (1971).

seemingly unusual behavior might be explained in terms of three-dimensional endwall flow effects.

For each of the four test points, a separation bubble was predicted on the suction side of the airfoil at about 52.7% of axial chord with turbulent reattachment occurring at about 56.1% of axial chord. Figures 6.7 and 6.8 display these locations for the test points corresponding to the lowest and highest M_1 calculated. These results indicate that there is little influence of Mach number level on the location of laminar separation. The results also indicated a slight reduction of the separation bubble extent as the Mach number level increased. The boundary layer remained laminar on the pressure side for the four test points due to the strong flow acceleration. The locations of laminar separation in Fig. 6.7 and 6.8 are probably right since the experimental data appear to show a constant velocity region following the laminar separation points. Also, a linear drop in velocity at the end of the constant velocity region, as would be expected for reattachment to occur, appears to be indicated by the data. It should be noted that a small supersonic pocket was calculated for the test point with $M_1 = 0.245$, as shown in Fig. 6.8.

Figures 6.7 and 6.8 also provide a validation of the leading edge reanalysis in compressible flow cases.

7. CONCLUSIONS

The present study considered the development of a computerized "direct" design system for two-dimensional turbine cascades. The conclusions drawn from the study are as follows:

1. A fast computer code was developed to accomplish the geometric design of arbitrary turbine cascades from given velocity triangle requirements.

2. The developed streamline curvature for global inviscid analysis was found to be accurate, fast, and flexible, accounting for important flow effects such as total pressure loss, stream sheet thickness variation, flow periodicity and stagnation streamline shaping, and compressibility through slight transonic conditions. Exit gas angle may be predicted in the analysis or supplied as input through empirical correlations.

3. The developed reanalysis procedure for the airfoil leading edge provides fast and detailed results of the flow characteristics in this region. Rapid changes in velocities and accurate location of the stagnation point are determined.

4. The developed transitional boundary layer calculation procedure provides fast calculations of the profile boundary layer accounting for the laminar region and laminar separation bubble, transitional, turbulent and turbulent separated regions. Important effects accounted for are wall curvature and influence of turbulence level on turbulent boundary layer development.

5. Application of the inviscid and profile boundary layer analyses yielded results for exit gas angle and total pressure loss which were in good agreement with experimental turbine cascade data. This suggests that although inviscid-viscous interaction is important in compressor cascades, it may be unnecessary in turbine cascades.

6. The developed overall "direct" design system can be used rapidly and effectively in an automated, interactive mode for design of turbine cascades. The procedure is widely applicable, accurate and economical.

8. SUGGESTIONS FOR FURTHER RESEARCH

The different calculation procedures incorporated in the present "direct" design system have more potential than has been stated or demonstrated so far. Here, a few suggestions are made for future work which would further improve the capabilities of the procedures and extend their applications.

1. The geometry design program can be easily extended to design exit guide vane (diffusing) cascades by taking the exit plane in the accelerating cascade as being the inlet plane in the diffusing cascade.

2. The streamline curvature analysis should be extended to handle stream sheet radius change through annular cascades and to incorporate uneven spacing of the quasi-orthogonals. Application of the analysis to transonic flow with supersonic exit Mach number should also be investigated where the stagnation streamline shaping becomes extremely difficult.

3. The reanalysis finite area technique can be used in the solution of potential problems such as the two-dimensional heat conduction problem with the advantage of the body-fitted computational mesh.

4. Additional testing of the procedure developed to account for the effects of free stream turbulence level on the development of incompressible turbulent boundary layers should be carried out. In particular, testing against experimental data obtained in a pressure gradient would be important.

5. The capabilities of the complete procedure in predicting turning

angle and losses in compressor cascades with and without turbulent separated regions should be explored.

6. The "direct" design system should be further exercised in the design of turbine cascades and linked with experimental verification programs. Also, the design system should be used in checking experimental correlation methods based on basic cascade geometric parameters.

9. REFERENCES

- Ainley, D. G. 1948. The performance of axial-flow turbines. Proceedings Institution of Mechanical Engineers 159:230-244.
- Ainley, D. G. and G. C. R. Mathieson. 1955. An examination of the flow and pressure losses in blade rows of axial flow turbines. Aero. Res. Council Reports & Memoranda No. 2891.
- Alarcon, G. A. 1980. Turbine cascade design program; User's manual. Iowa State University. Engineering Research Institute. ISU-ERI-Ames-81020; TCRL-16.
- Alarcon, G. A. and P. Kavanagh. 1980. Streamline curvature method for cascade flow analysis. Iowa State University. Engineering Research Institute. ISU-ERI-Ames-80218; TCRL-15.
- Andrews, S. J. and N. W. Schofield. 1950. An experimental investigation of a thick airfoil nozzle cascade. Aero. Res. Council Reports & Memoranda No. 2883.
- Assassa, G. M. and K. D. Papailiou. 1979. An integral method for calculating turbulent boundary layer with separation. Journal of Fluids Engineering 101:110-116.
- Baljí, O. E. 1968. Axial cascade technology and application to flow path designs. Journal of Engineering for Power 90:309-340.
- Baljí, O. E. and R. L. Binsley. 1968. Axial turbine performance evaluation. Part A - Loss-geometry relationships. Journal of Engineering for Power 90:341-348.
- Batchelor, G. K. 1953. The theory of homogeneous turbulence. Cambridge University Press, Cambridge, Massachusetts.
- Bindon, J. P. and A. D. Carmichel. 1971. Streamline curvature analysis of compressible and high Mach number cascade flows. Journal of Mechanical Engineering Science 13:344-357.
- Boiko, A. V. and S. N. Kozhevnikov. 1978. Designing subsonic turbine profiles of optimal aerodynamic shape. Teploenergetika 25:55-57.
- Bridle, E. A. 1949. Some high-speed tests on turbine cascades. National Gas Turbine Establishment, Report No. R.48.
- Calvert, W. J. and D. J. L. Smith. 1976. A digital computer program for the subsonic flow past turbomachine blades using a matrix method. Aero. Res. Council Reports & Memoranda No. 3838.

- Caspar, J. R., D. E. Hobbs, and R. L. Davis. 1979. The calculation of two-dimensional compressible potential flow in cascades using finite area techniques. *AIAA Journal* 18:103-109.
- Cebeci, T., G. J. Mosinskis, and A. M. O. Smith. 1972. Calculation of separation points in incompressible turbulent flows. *Journal of Aircraft* 9:618-624.
- Charnay, G., G. Compte-Bellot, and J. Mathieu. 1971. Development of a turbulent boundary layer on a flat plate in an external turbulent flow. AGARD CP93, paper No. 27.
- Clauser, F. H. 1954. Turbulent boundary layers in adverse pressure gradients. *Journal of Aeronautical Sciences* 21:91-108.
- Coles, D. 1968. The young person's guide to the data. In *Proceedings of the Computation of Turbulent Boundary Layers - 1968 AFOSR-IFP Stanford Conference*. pp. 1-45, Vol. 2.
- Collyer, M. R. 1977. An extension to the method of Garabedian and Korn for the calculation of transonic flow past an aerofoil to include the effects of a boundary layer and wake. *Aero. Res. Council Reports & Memoranda No. 3828*.
- Cox, H. J. 1976. Through flow calculation procedure for application to high speed large turbines. AGARD Conference Proceedings 195.
- Crimi, P. and B. L. Reeves. 1972. A method for analyzing dynamic stall of helicopter rotor blades. NASA CR 2009.
- Davis, W. R. 1971. A matrix method applied to the analysis of the flow past turbomachinery blades. Carleton University, Rept. No. ME/A 72-7.
- Delaney, R. A. 1979. Private communication. Detroit Diesel Allison Co., Indianapolis, Indiana.
- Delaney, R. A. and P. Kavanagh. 1976. Transonic flow analysis in axial-flow turbomachinery cascades by a time-dependent method of characteristics. *Journal of Engineering for Power* 98:356-364.
- Denton, J. D. 1975. A time-marching method for two- and three-dimensional blade-to-blade flows. *Aero. Res. Council Reports & Memoranda No. 3775*.
- Dhawan, S. and R. Narasimha. 1958. Some properties of boundary layer flows during the transition from laminar to turbulent motion. *Journal of Fluid Mechanics* 3:418-436.

- Dodge, P. R. 1976. A non-orthogonal numerical method for solving transonic cascade flows. American Society of Mechanical Engineers Paper 76-GT-63.
- Dongarra, J. J., C. B. Moler, J. R. Bunch, and G. W. Stewart. 1979. LINPACK User's Guide. SIAM, Philadelphia.
- Dorman, T. E., H. Welna, and R. W. Lindlauf. 1968. The application of controlled vortex aerodynamics to advanced axial flow turbines. Journal of Engineering for Power 90:245-250.
- Dring, R. P. and W. G. Heiser. 1978. Turbine aerodynamics. Chapter 18 in Gordon C. Oates, ed. The aerothermodynamics of aircraft gas turbine engines. Report No. AFAPL-TR-78-52. Air Force Wright Aeronautical Laboratories, Air Force Systems Command, Wright-Patterson Air Force Base, Ohio.
- Dunavant, J. C. and J. R. Erwin. 1956. Investigation of a related series of turbine-blade profiles in cascade. NACA TN-3802.
- Duncombe, E. 1964. Aerodynamic design of axial flow turbines. In W. R. Hawthorne, ed. Aerodynamics of turbines and compressors. Princeton University Press, Princeton, New Jersey.
- Dunham, J. and P. M. Came. 1970. Improvements to the Ainley-Mathieson method of turbine performance prediction. Journal of Engineering for Power 92:252-256.
- Dunham, J. 1972. Predictions of boundary layer transition on turbomachinery blades. AGARDograph 164:57-71.
- Emmons, H. W. 1951. The laminar turbulent transition in a boundary layer - Part I. Journal of Aerospace Sciences 18:235-246.
- Engeli, M., H. J. Follinger, and J. C. Allemann. 1978. A computer program for the design of turbomachinery blades. American Society of Mechanical Engineers. Paper 78-GT-36.
- Escudier, M. P. and W. B. Nicoll. 1968. A shear-work-integral method for the calculation of turbulent boundary layer development. In Proceedings of the Computation of Turbulent Boundary Layers - 1968 AFOSR-IFP Stanford Conference. pp. 136-146, Vol. 1.
- Evans, R. L. 1974. Free-stream turbulence effects on the turbulent boundary layer. Aero. Res. Council C.P.No. 1282.
- Evans, R. L. and J. H. Horlock. 1974. Calculation of the development of turbulent boundary layers with a turbulent free stream. Journal of Fluids Engineering 96:348-352.

- Farn, C. L. S. and D. K. Whirlow. 1975. Design estimate of cascade performance. *Computer & Fluids* 3:225-233.
- Felsh, K. O., D. Geropp, and A. Walz. 1968. Method for turbulent boundary prediction. In *Proceedings of the Computation of Turbulent Boundary Layers - 1968 AFOSR-IFP Stanford Conference*. pp. 170-176, Vol. 1.
- Forster, V. T. 1964. Turbine-blading development using a transonic variable density cascade wind tunnel. *Proceedings Institution of Mechanical Engineers* 179 (Part I):155-195.
- Föttner, L. 1972. Analytical approach for the loss and deflection behavior of cascades in transonic flow including axial mass flow variation. *AGARDograph* 164:119-140.
- Fox, R. W. and A. T. McDonald. 1973. Introduction to fluid mechanics. John Wiley & Sons, Inc., New York.
- Frost, D. H. 1970. A streamline curvature through-flow computer program for analyzing the flow through axial-flow turbomachines. *Aero. Res. Council Reports & Memoranda No. 3687*.
- Garabedian, P. R. and D. G. Korn. 1971. Analysis of transonic aerofoils. *Comm. Pure and Appl. Math* 24:841-851.
- Gopalakrishnan, S. and R. Bozzola. 1971. A numerical technique for the calculation of transonic flow in turbomachinery cascades. *American Society of Mechanical Engineers Paper No. 71-GT-42*.
- Gostelow, J. P. 1965. Potential flow through cascades - a comparison between exact and approximate solutions. *Aero. Res. Council C.P. No. 807*.
- Gostelow, J. P. 1973. Review of compressible flow theories for airfoil cascades. *Journal of Engineering for Power* 95:281-292.
- Hamm, B. 1980. Private communication. The Trane Co., LaCrosse, WI.
- Hansen, E. C. 1976. A study of the methods for analysis of the flow field in cascades. NASA Grant NSG 3033-Blade surface boundary layer and wake computation. Iowa State University. Engineering Research Institute. ISU-ERI-Ames-77065; TCRL-6.
- Hansen, E. C. 1978. Blade surface boundary layer and wake computation models for estimation of axial flow compressor and fan blade-row deviation angles and losses. Unpublished Ph.D. dissertation. Iowa State University, Ames, Iowa.

- Heilmann, W. 1972. The influence of axial velocity density ratio on compressor cascade performance in compressible flow. AGARDograph 164:225-240.
- Henderson, M. L. 1978. Inverse boundary-layer technique for airfoil design. NASA conference publication No. 2045, Part 1, Vol. 1.
- Hobson, D. 1974. Shock-free transonic flow in turbomachinery cascades. Ph.D. thesis, Cambridge University.
- Hodge, R. I. 1960. A turbine nozzle cascade for cooling studies, Parts I and II. Aero. Res. Council C.P. Nos. 492 and 493.
- Horlock, J. H. 1973. Axial flow turbines. Robert E. Krieger Publishing Company, New York.
- Huffman, D. G., R. B. McClure, R. L. Haltman, and G. T. Sinnet. 1971. Results of a two-dimensional turbine cascade (ACEII) test. Detroit Diesel Allison Division, General Motors Corporation, Indianapolis, Indiana. Research Note 71-47.
- Huffman, G. D., D. R. Zimmerman, and W. A. Bennett. 1972. The effect of free stream turbulence level on turbulent boundary layer behavior. AGARDograph 164:91-115.
- Huo, S. 1972. Blade optimization based on boundary layer concepts. AGARDograph 164:141-170.
- Ives, D. C. and J. F. Liutermoza. 1977. Analysis of transonic cascade flow using conformal mapping and relaxation techniques. AIAA Journal 15:647-652.
- Katsanis, T. 1965. Use of arbitrary quasi-orthogonals for calculating flow distribution on a blade-to-blade surface in a turbomachine. NASA TN D-2809.
- Katsanis, T. 1969. FORTRAN program for calculating transonic velocities on a blade-to-blade stream surface of a turbomachine. NASA TN D-5427.
- Katsanis, T. and W. D. McNally. 1969. FORTRAN program for calculating velocities in a magnified region on a blade-to-blade stream surface of a turbomachine. NASA TN D-5091.
- Keenan, J. H. and F. G. Keyes. 1969. Steam Tables. John Wiley & Sons, Inc., New York.

- Kline, S. J., M. V. Morkovin, G. Sorvan, and D. J. Cockrell (eds.). 1968. Computation of Turbulent Boundary Layers. Proceedings - 1968 AFOSR-IFP-Stanford Conference.
- Kurzrock, J. W. and A. S. Novick. 1975. Transonic flow around rotor blade elements. *Journal of Fluids Engineering* 97:598-607.
- Langston, L. S., M. L. Nice, and R. M. Hooper. 1977. Three-dimensional flow within a turbine cascade passage. *Journal of Engineering for Power* 99:21-28.
- Le Foll, J. 1965. A theory of the representation of the properties of boundary layers on a plane. In Cassady K. and J. Chauvin, eds. *Proceedings of the Seminar on Advanced Problems in Turbomachinery Part I held at the von Karman Institute, Belgium.*
- Marsh, H. 1968. A digital computer program for the through-flow field mechanics in an arbitrary turbomachine using a matrix method. *Aero. Res. Council Reports & Memoranda No. 3509.*
- Martelli, F. 1979. Prediction of subsonic flow angle in turbine blades. In *Proceedings of the Fifth World Congress on Theory of Machines and Mechanisms held in Montreal, Canada.* American Society of Mechanical Engineers.
- McDonald, P. W. 1971. The computation of transonic flow through two-dimensional gas turbine cascades. *American Society of Mechanical Engineers Paper No. 71-GT-89.*
- McDonald, H. 1978. Boundary layers in turbomachines. Lecture 17, ASME Turbomachinery Institute course on Fluid Dynamics of Turbomachinery, Iowa State University.
- McDonald, H. and R. W. Fish. 1972. Practical calculations of transitional boundary layers. *AGARDograph* 164:29-54.
- McDonald, H. and J. P. Kreskovsky. 1974. Effect of free stream turbulence on the turbulent boundary layer. *International Journal of Heat and Mass Transfer* 17:705-716.
- Miller, M. J. 1973. Some aspects of deviation angle estimation for axial-flow compressors. Ph.D. thesis. Iowa State University.
- Monello, J. A., W. S. Mitchell, and W. A. Tall. 1979. Application of nonseries airfoil design technology to highly loaded turbine exit guide vanes. *Journal of Engineering for Power* 101:202-211.
- Moses, H. L. 1964. The behavior of turbulent boundary layers in adverse pressure gradients. MIT Gas Turbine Laboratory Report 73, Cambridge, Massachusetts.

- Nash, J. F. 1965. Turbulent boundary layer behavior and the auxiliary equation. AGARDograph 97:245-279.
- Newman, B. G. 1951. Some contributions to the study of the turbulent boundary layer near separation. Department of Supply ACA-53, Australia.
- Nicoll, W.V. and M. P. Escudier. 1966. Empirical relationships between the shape factors H and H^* for uniform density turbulent boundary layers and wall jets. AIAA Journal 4:940-942.
- Novak, R. A. 1978. Some blade-to-blade solution techniques for turbomachinery. Lecture 12, ASME Turbomachinery Institute course on Fluid Dynamics of Turbomachinery, Iowa State University.
- Papailiou, K. 1970. Boundary layer optimization for the design of high turning axial flow compressor blades. Journal of Engineering for Power 93:147-155.
- Papailiou, K. D., A. Satta, and F. Nurzia. 1972. On the two-dimensional boundary layers as they appear on turbomachine blades. AGARDograph 164:1-28.
- Pratap, V. S. and D. B. Spalding. 1976. Fluid flow and heat transfer in three-dimensional duct flows. International Journal of Heat and Mass Transfer 19:1183-1188.
- Roberts, W. B. 1975. Effect of Reynolds number and laminar separation on axial cascade performance. Journal of Engineering for Power 97:261-273.
- Scholz, N. 1965. Aerodynamics of cascades. Translated from the original German by Armin Klein. NTIS AD-A051233.
- Schmidt, E. 1980. Computation of supercritical compressor and turbine cascades with a design method for transonic flows. Journal of Engineering for Power 102:68-74.
- Schubauer, G. and Klebanoff, P. 1951. Investigation of separation of the turbulent boundary layer. NACA TR 1030.
- Schlichting, H. 1968. Boundary Layer Theory. 6th Edition. McGraw-Hill, New York.
- Schlichting, H. and A. Das. 1966. Recent research on cascade-flow problems. Journal of Basic Engineering 88:221-228.

- Seyb, N. J. 1972. The role of boundary layers in axial flow turbo-machines and the prediction of their effects. AGARDograph 164:241-259.
- Silvester, M. E. and C. M. Fitch. 1974. Matrix methods for the design of cascades to prescribed surface velocity distributions and for fully compressible flow. Pgs. 75-100 in Lakshminarayana, B., W. R. Britsch, and W. S. Gearhart, eds. Fluid mechanics acoustics and design of turbomachinery. Part I. NASA SP-304.
- Singhal, A. D. and D. B. Spalding. 1976. A 2-D partially-parabolic procedure for axial-flow turbomachinery cascades. Aero. Res. Council Report & Memoranda No. 3775.
- Smith, D. L. and D. H. Frost. 1970. Calculation of the flow past turbo-machine blades. Proceedings The Institution of Mechanical Engineers 184 (Part 3G-II):72-85.
- Speidel, L. 1954. Berechnung der Strömungsverluste von ungestaffelten ebenen Schaufelgittern. Dissertation, T. H. Braunschweig, 1953. Ingenieur Archiv 22:295-322.
- Stewart, W. L. and A. J. Glassman. 1973. Blade design. Chapter 4 in Arthur J. Glassman, ed. Turbine design and application. Volume 2. NASA SP-290.
- Stewart, W. 1955. Analysis of two-dimensional compressible-flow loss characteristics downstream of turbomachinery blade rows in terms of basic boundary-layer characteristics. U.S. NACA TN 3515.
- Streeter, V. L. 1961. Handbook of fluid dynamics. McGraw-Hill Co., New York.
- Talbert, J. E. and J. C. Smith. 1948. Aerothermodynamic design of turbines for aircraft power plants. Journal of Aeronautical Sciences 15:556-564.
- Thomas, K. M. and J. J. Piendel. 1974. An automated interactive design system for advanced gas turbines. American Society of Mechanical Engineers Paper No. 74-GT-82.
- Thompson, J. F., F. C. Thames, and C. W. Mastin. 1974. Automatic numerical generation of body-fitted curvilinear coordinate system for field containing any number of arbitrary two-dimensional bodies. Journal of Computational Physics 15:299-319.

- Turner, A. B. 1971. Local heat transfer measurements on a gas turbine blade. *Journal Mechanical Engineering Science* 13:1-12.
- van Driest, E. F. and C. B. Blumer. 1963. Boundary layer transition: free-stream turbulence and pressure gradient effects. *AIAA Journal* 1:1303-1306.
- VKI Lecture Series 59. 1973. Transonic flows in axial turbomachinery. Von Karman Institute for Fluid Dynamics, Belgium.
- VKI Lecture Series 84. 1976. Transonic flows in axial turbomachinery. Von Karman Institute for Fluid Dynamics, Belgium.
- Walz, A. 1969. Boundary layers of flow and temperature. The M.I.T. Press, Cambridge, Massachusetts.
- Webster, D. F. 1976. Design of a 4 1/2 stage turbine with a stage loading factor of 4.66 and high specific work output. NASA CR-2659.
- Whitney, W. J. and W. L. Stewart. 1973. Velocity diagrams. Chapter 3 in Arthur J. Glassman, ed. *Turbine design and application*. Volume 1. NASA SP-290.
- Wilkinson, D. H. 1970. Stability, convergence and accuracy of two-dimensional streamline curvature methods using quasi-orthogonals. *Proceedings The Institution of Mechanical Engineers* 184 (Part 3G-I):108-119.
- Wilkinson, D. H. 1972. Calculation of blade-to-blade flow in a turbomachine by streamline curvature. *Aero. Res. Council Reports & Memoranda No. 3704*.
- Wilson, D. G. and J. A. Pope. 1954. Convective heat transfer to gas turbine blade surfaces. *Proceedings The Institution of Mechanical Engineers* 168:861-874.
- Wright, L. C. 1974. Blade selection for a modern axial-flow compressor. Pgs. 603-626 in Lakshminarayana, B., W. R. Britsch, and W. S. Gearhart, eds. *Fluid mechanics, acoustics, and design of turbomachinery*. Part II. NASA SP-304.
- Wu, C. H. 1952. A general theory of three-dimensional flow in subsonic and supersonic turbomachines of axial, radial and mixed-flow types. NACA TN 2604.
- Zweifel, O. 1945. The spacing of turbomachine blading, especially with large angular deflection. *The Brown Boveri Review*, Dec. 1945: 436-444.

10. ACKNOWLEDGMENTS

The author wishes to express his deepest gratitude to Dr. Patrick Kavanagh for consenting to serve as his major professor and for his continuous assistance, invaluable advice, and encouragement throughout the course of this study.

The author also wishes to thank Dr. Theodore H. Okiishi, Dr. George K. Serovy, Dr. Donald F. Young, and Dr. Harry J. Weiss, the members of his dissertation committee, for their teaching and assistance throughout his Ph.D. program.

The program "Gran Mariscal de Ayacucho" of the Government of Venezuela and the "Universidad de Los Andes" are acknowledged for the sponsorship. The author also acknowledges the computing funds he received from the TRANE Co. and from the Department of Mechanical Engineering. The Detroit Diesel Allison Co. cooperation in making available cascade data is appreciated.

Obviously, the author is appreciative to his wife, Alexia, for creating a motivating atmosphere at home. Last, but not the least, the author appreciates the emotional back up provided by his children Annie, Gonzalo and Alexia who constituted the main motivation of this effort.

11. APPENDIX A.

CALCULATION OF FLOW PASSAGE CROSS SECTIONAL AREA

The cascade flow passage cross-sectional area is calculated by constructing normals to a mid-streamline at the intersection of pitch-wise lines (q-os) with the mid-streamline. Intersections of the normals are then found with the pressure and suction sides of the passage (p and s, respectively).

The y coordinate of the mid-streamline is found for each q-o from

$$y_{\text{mid}} = (y_p - y_s)/2 . \quad (11.1)$$

The resultant function is then differentiated to give $(dy/dx)_{\text{mid}}$. The equation of the normal through the point (x, y_{mid}) is, therefore,

$$y = ax + b \quad (11.2)$$

where $a = -1/(dy/dx)_{\text{mid}}$ and $b = y_{\text{mid}} + x_{\text{mid}}/(dy/dx)_{\text{mid}}$.

A first approximation to the intersection of a normal with the suction side (s) is

$$x'_s = x_{\text{mid}} + \frac{(y_p - y_s)}{4} \sin^2 \beta_{\text{mid}} \quad (11.3)$$

where β_{mid} is the angle the mid-streamline makes with the x axis. The four neighbor points describing the suction side nearest to x'_s (two either side of x'_s) are located and the coefficients found for a cubic through the four points of the form

$$y = C_1 + C_2x + C_3x^2 + C_4x^3. \quad (11.4)$$

For equal y , then, determined by the normal and cubic (at their intersection)

$$f(x) = (C_1 - b) + (C_2 - a)x + C_3x^2 + C_4x^3 = 0. \quad (11.5)$$

This equation is solved for x'_s by Newton's method, starting from the approximate x'_s .

A similar procedure is followed to find the intersection of the normal with the pressure side, p . The cross-sectional area is then the length of the normal times a unit depth.

In the programmed method, the q -os used to calculate the cross-sectional area variation correspond to the q -os used for the streamline curvature calculation. However, any number of q -os can be used. For normals outside the covered channel of the cascade, the intercepts with the extended camber lines are found.

12. APPENDIX B.

PRESSURE--MOMENTUM BALANCE IN TANGENTIAL DIRECTION

Let D be the cascade flow domain in the x - y plane indicated in Fig. 3.1 and D^* the three-dimensional domain obtained by extending D at each point upward and downward a distance $\Delta z/2$ in the out-of-plane direction. Newton's second law of motion requires

$$\sum \vec{F} = \int_S \rho \vec{V} (\vec{V} \cdot d\vec{A}) \quad (12.1)$$

where $\sum \vec{F}$ is the sum of the forces exerted on D^* , $\vec{V} = u\vec{i} + v\vec{j} + w\vec{k}$ is the velocity vector, and S is the surface of D^* . Since the flow is assumed two-dimensional, all quantities are functions of x and y alone. Furthermore, the boundaries of D^* parallel to the x - y plane are stream surfaces on which $\vec{V} \cdot d\vec{A} = 0$. The only forces present are pressure forces, and these cancel on the upper and lower stream surface boundaries (since P depends only on x and y). Thus, Eqn. 12.1 can be expressed in the x - y plane by

$$- \int_{\partial D} p \Delta z \vec{n} ds = \int_{\partial D} \rho \vec{V} (\vec{V} \cdot \vec{n}) \Delta z ds \quad (12.2)$$

where \vec{n} is the unit outward normal, and the integrals are taken counterclockwise around ∂D , the boundary of D .

The integrals on the periodic boundaries cancel, and $\vec{V} \cdot \vec{n} = 0$ on the airfoils. Thus Eqn. 12.2 becomes

$$-(p_1 \Delta z_1 \bar{n}_1 + p_2 \Delta z_2 \bar{n}_2) \tau - \int_{\partial A} p \Delta z \bar{n} ds =$$

$$\rho_1 \bar{V}_1 (\bar{V}_1 \cdot \bar{n}_1) \Delta z_1 \tau + \rho_2 \bar{V}_2 (\bar{V}_2 \cdot \bar{n}_2) \Delta z_2 \tau \quad (12.3)$$

where the integral is taken counterclockwise around the airfoil. Now

$$\bar{n}_1 = -\bar{i}, \quad \bar{n}_2 = \bar{i}, \quad \bar{V}_1 \cdot \bar{n}_1 = -u_1, \quad \bar{V}_2 \cdot \bar{n}_2 = u_2, \quad \text{and } \bar{n} ds = -dy \bar{i} + dx \bar{j}.$$

So Eqn. 12.3, expressed componentwise, becomes

$$(-\rho_1 u_1^2 \Delta z_1 + \rho_2 u_2^2 \Delta z_2) \tau + (-p_1 \Delta z_1 + p_2 \Delta z_2) \tau = \int_{\partial A} p \Delta z dy \quad (12.4)$$

$$(-\rho_1 u_1 v_1 \Delta z_1 + \rho_2 u_2 v_2 \Delta z_2) \tau = - \int_{\partial A} p \Delta z dx \quad (12.5)$$

The mass flow across the upstream vertical boundary into D^* must equal the mass flow across the downstream vertical boundary out of D^* . Thus,

$$\rho_1 u_1 \Delta z_1 \tau = \rho_2 u_2 \Delta z_2 \tau. \quad (12.6)$$

Substituting Eqn. 12.6 into Eqns. 12.4 and 12.5, we obtain

$$F_{AM} \equiv \rho_1 u_1 \Delta z_1 \tau (u_1 - u_2) - (-p_1 \Delta z_1 + p_2 \Delta z_2) \tau =$$

$$- \int_{\partial A} p \Delta z dy \equiv F_{AP} \quad (12.7)$$

$$F_{TM} \equiv \rho_1 u_1 \Delta z_1 \tau (v_1 - v_2) = \int_{\partial A} p \Delta z dx \equiv F_{TP} \quad (12.8)$$

F_{AM} , F_{AP} , F_{TM} , and F_{TP} are referred to as the axial momentum force, axial pressure force, tangential momentum force, and tangential

pressure force, respectively. The requirements that $F_{AM} = F_{AP}$ and $F_{TM} = F_{TP}$ are referred to as the "axial pressure-momentum balance" and the "tangential pressure-momentum balance," respectively. Taken together, these balances express the fact that the changes in momentum of the fluid as it passes through the cascade passage must be accounted for by the pressure forces on the airfoil.

In the streamline curvature calculation, only the tangential momentum balance is calculated since it is the most significant force balance in cascade calculations. This calculation then provides a check between calculated pressure distribution and velocity triangles.

13. APPENDIX C.

SYSTEMS OF EQUATIONS FOR PERIODICITY CONDITIONS
IN STREAMLINE CURVATURE ANALYSIS

The systems of equations leading to stagnation streamline shifts (δ_j) upstream and downstream of a cascade in the global inviscid analysis are presented. The three systems of equations which apply are shown in Fig. 13.1 through 13.3.

The constants a_i and b_i shown in the equations come from the nine point differentiation formulae given in Eqns. 3.58 and 3.59. Similarly, constants c_i and d_i are from the five point differentiation formulae given in Eqns. 3.60 and 3.61. The factors A contained in the coefficients for each equation of the systems are calculated with Eqn. 3.40. Likewise the factors B forming the right hand side of the equations are calculated with Eqn. 3.41 (except for B_1 and B_M as noted below).

Figure 13.1 shows the system of equations which applies upstream of the cascade. In this case, B_1 is calculated as

$$B_1 = h \tan(90^\circ - \beta_1) - h (dy/dx)_{1,NM} . \quad (13.1)$$

Figure 13.2 shows the system of equations which applies downstream of the cascade when the calculated β_2 option is used. Figure 13.3 shows the system of equations which also applies downstream of the cascade, but when the input β_2 option is used. Here, B_M is calculated by

$$B_M = h \tan(\beta_2 - 90^\circ) - h (dy/dx)_{M,NM} . \quad (13.2)$$

-1.5	2	-0.5								δ_1	B_1	
-0.60417A ₂	0.33333A ₂	0.125A ₂	0.16667A ₂	-0.02083A ₂						δ_2	B_2	
+0.72917	-1.16667	+0.125	+0.33333	-0.02083						δ_3	B_3	
$c_{-2}A_3 + d_{-2}$	$c_{-1}A_3 + d_{-1}$	$c_0A_0 + d_0$	$c_1A_3 + d_1$	$c_2A_3 + d_2$						δ_4	B_4	
	$c_{-2}A_4 + d_{-2}$	$c_{-1}A_4 + d_{-1}$	$c_0A_4 + d_0$	$c_1A_4 + d_1$	$c_2A_4 + d_2$					δ_5	B_5	
$a_{-4}A_5 + b_{-4}$	$a_{-3}A_5 + b_{-3}$	$a_{-2}A_5 + b_{-2}$	$a_{-1}A_5 + b_{-1}$	$a_0A_5 + b_0$	$a_1A_5 + b_1$	$a_2A_5 + b_2$	$a_3A_5 + b_3$	$a_4A_5 + b_4$		
	
		$a_{-4}A_{nL-4} + b_{-4}$	$a_{-3}A_{nL-4} + b_{-3}$	$a_{-2}A_{nL-4} + b_{-2}$	$a_{-1}A_{nL-4} + b_{-1}$	$a_0A_{nL-4} + b_0$	$a_1A_{nL-4} + b_1$	$a_2A_{nL-4} + b_2$	$a_3A_{nL-4} + b_3$	$a_4A_{nL-4} + b_4$	δ_{nL-4}	B_{nL-4}
			$a_{-4}A_{nL-3} + b_{-4}$	$a_{-3}A_{nL-3} + b_{-3}$	$a_{-2}A_{nL-3} + b_{-2}$	$a_{-1}A_{nL-3} + b_{-1}$	$a_0A_{nL-3} + b_0$	$a_1A_{nL-3} + b_1$	$a_2A_{nL-3} + b_2$	$a_3A_{nL-3} + b_3$	δ_{nL-3}	B_{nL-3}
				$a_{-4}A_{nL-2} + b_{-4}$	$a_{-3}A_{nL-2} + b_{-3}$	$a_{-2}A_{nL-2} + b_{-2}$	$a_{-1}A_{nL-2} + b_{-1}$	$a_0A_{nL-2} + b_0$	$a_1A_{nL-2} + b_1$	$a_2A_{nL-2} + b_2$	δ_{nL-2}	B_{nL-2}
					$a_{-4}A_{nL-1} + b_{-4}$	$a_{-3}A_{nL-1} + b_{-3}$	$a_{-2}A_{nL-1} + b_{-2}$	$a_{-1}A_{nL-1} + b_{-1}$	$a_0A_{nL-1} + b_0$	$a_1A_{nL-1} + b_1$	δ_{nL-1}	B_{nL-1}
						$a_{-4}A_{nL} + b_{-4}$	$a_{-3}A_{nL} + b_{-3}$	$a_{-2}A_{nL} + b_{-2}$	$a_{-1}A_{nL} + b_{-1}$	$a_0A_{nL} + b_0$	δ_{nL}	B_{nL}

Figure 13.1. System of equations for streamline shifts upstream of the cascade.

$a_0^{\Delta_{HT+1}} + b_0$	$a_1^{\Delta_{HT+1}} + b_1$	$a_2^{\Delta_{HT+1}} + b_2$	$a_3^{\Delta_{HT+1}} + b_3$	$a_4^{\Delta_{HT+1}} + b_4$							δ_{HT+1}	B_{HT+1}
$a_{-1}^{\Delta_{HT+2}} + b_{-1}$	$a_0^{\Delta_{HT+2}} + b_0$	$a_1^{\Delta_{HT+2}} + b_1$	$a_2^{\Delta_{HT+2}} + b_2$	$a_3^{\Delta_{HT+2}} + b_3$	$a_4^{\Delta_{HT+2}} + b_4$						δ_{HT+2}	B_{HT+2}
$a_{-2}^{\Delta_{HT+3}} + b_{-2}$	$a_{-1}^{\Delta_{HT+3}} + b_{-1}$	$a_0^{\Delta_{HT+3}} + b_0$	$a_1^{\Delta_{HT+3}} + b_1$	$a_2^{\Delta_{HT+3}} + b_2$	$a_3^{\Delta_{HT+3}} + b_3$	$a_4^{\Delta_{HT+3}} + b_4$					δ_{HT+3}	B_{HT+3}
$a_{-3}^{\Delta_{HT+4}} + b_{-3}$	$a_{-2}^{\Delta_{HT+4}} + b_{-2}$	$a_{-1}^{\Delta_{HT+4}} + b_{-1}$	$a_0^{\Delta_{HT+4}} + b_0$	$a_1^{\Delta_{HT+4}} + b_1$	$a_2^{\Delta_{HT+4}} + b_2$	$a_3^{\Delta_{HT+4}} + b_3$	$a_4^{\Delta_{HT+4}} + b_4$				δ_{HT+4}	B_{HT+4}
$a_{-4}^{\Delta_{HT+5}} + b_{-4}$	$a_{-3}^{\Delta_{HT+5}} + b_{-3}$	$a_{-2}^{\Delta_{HT+5}} + b_{-2}$	$a_{-1}^{\Delta_{HT+5}} + b_{-1}$	$a_0^{\Delta_{HT+5}} + b_0$	$a_1^{\Delta_{HT+5}} + b_1$	$a_2^{\Delta_{HT+5}} + b_2$	$a_3^{\Delta_{HT+5}} + b_3$	$a_4^{\Delta_{HT+5}} + b_4$			δ_{HT+5}	B_{HT+5}
...
		$a_{-4}^{\Delta_{H-4}} + b_{-4}$	$a_{-3}^{\Delta_{H-4}} + b_{-3}$	$a_{-2}^{\Delta_{H-4}} + b_{-2}$	$a_{-1}^{\Delta_{H-4}} + b_{-1}$	$a_0^{\Delta_{H-4}} + b_0$	$a_1^{\Delta_{H-4}} + b_1$	$a_2^{\Delta_{H-4}} + b_2$	$a_3^{\Delta_{H-4}} + b_3$	$a_4^{\Delta_{H-4}} + b_4$	δ_{H-4}	B_{H-4}
						$c_{-2}^{\Delta_{H-3}} + d_{-2}$	$c_{-1}^{\Delta_{H-3}} + d_{-1}$	$c_0^{\Delta_{H-3}} + d_0$	$c_1^{\Delta_{H-3}} + d_1$	$c_2^{\Delta_{H-3}} + d_2$	δ_{H-3}	B_{H-3}
						$c_{-2}^{\Delta_{H-2}} + d_{-2}$	$c_{-1}^{\Delta_{H-2}} + d_{-1}$	$c_0^{\Delta_{H-2}} + d_0$	$c_1^{\Delta_{H-2}} + d_1$	$c_2^{\Delta_{H-2}} + d_2$	δ_{H-2}	B_{H-2}
						$0.02083A_{H-1}$	$-0.16667A_{H-1}$	$-0.125A_{H-1}$	$-0.33333A_{H-1}$	$0.060417A_{H-1}$	δ_{H-1}	B_{H-1}
						-0.02083	$+0.33333$	$+0.125$	-1.46667	$+0.72917$	δ_H	B_H
								0.5	$-2.$	1.5		

Figure 13.3. System of equations for streamline shifts downstream of the cascade. Input β_2 option.

14. APPENDIX D.

DERIVATION OF K IN REANALYSIS EQUATIONS

The total differential of the stream function ψ can be written as

$$d\psi = \frac{\partial\psi}{\partial x} dx + \frac{\partial\psi}{\partial y} dy \quad (14.1)$$

or

$$d\psi = \frac{1}{K \rho_{01} \Delta z_1} (u\Delta z dy - v\Delta z dx) \quad (14.2)$$

when the definitions in Eqn. 4.2 are used.

The bracketed part of Eqn. 14.2 is equal to \dot{dm} , the differential mass flow rate shown in Fig. 14.1. Therefore,

$$d\psi = \frac{\dot{dm}}{K \rho_{01} \Delta z_1} \quad (14.3)$$

which can be integrated to give

$$\psi_B - \psi_A = \dot{m}_{AB} / (K \rho_{01} \Delta z_1) \quad (14.4)$$

where \dot{m}_{AB} is the mass flow rate across the line AB in Fig. 14.1.

If it is now assumed that points A and B lay on a line of constant x and are separated by the pitch τ , the following is true:

$$\psi_B - \psi_A = \psi(x, y + \tau) - \psi(x, y). \quad (14.5)$$

Therefore, from Eqn. 14.4, and assuming the stream function difference in Eqn. 14.5 is unity

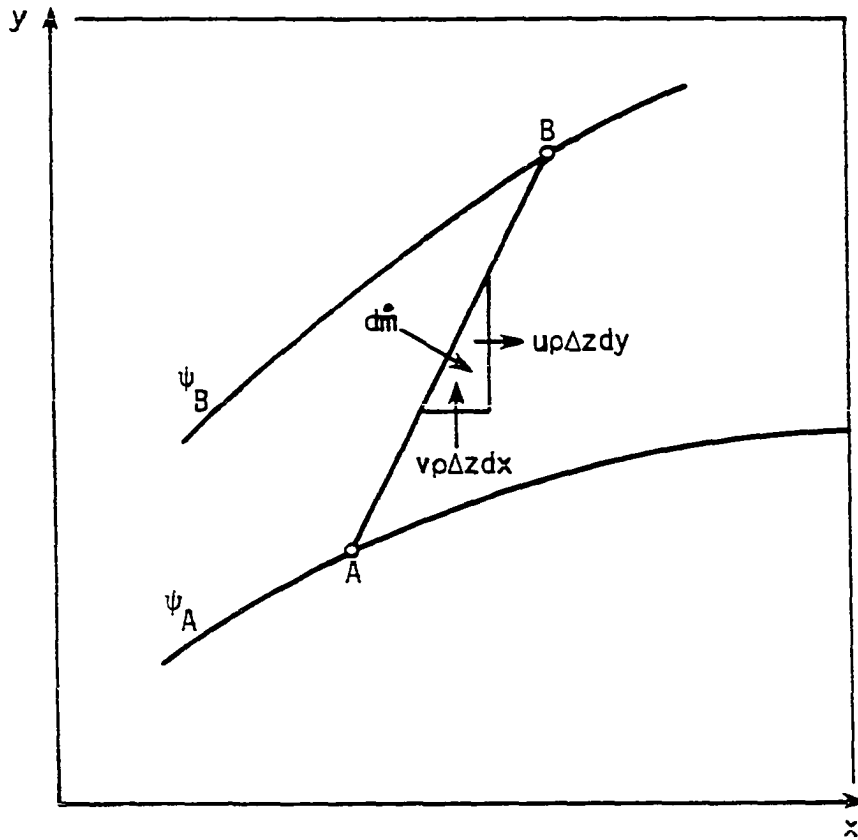


Figure 14.1. Mass flow rate-stream function relationship.

$$\frac{\dot{m}}{K \rho_{01} \Delta z_1} = 1 \quad (14.6)$$

where \dot{m} is the total mass flow rate through the cascade passage.

If \dot{m} is calculated at the upstream station where uniform flow exists, then

$$K = \frac{u_1 \rho_1 \tau}{\rho_{01}} \quad (14.7)$$

15. APPENDIX E.

LEAST SQUARES QUADRATIC POLYNOMIAL

The quadratic polynomial for the stream function ψ is of the form

$$\psi = a_1 + a_2x + a_3y + a_4xy + a_5x^2 + a_6y^2. \quad (15.1)$$

Let the known values of ψ at the cell points whose coordinates are x_i , y_i ($i = 1, 2, \dots, 9$) be designated by ψ_i ($i = 1, 2, \dots, 9$).

The values of the dependent variable calculated from the quadratic polynomial at the cell points are ψ'_i , i.e.,

$$\psi'_i = a_1 + a_2x_i + a_3y_i + a_4x_iy_i + a_5x_i^2 + a_6y_i^2. \quad (15.2)$$

The sum of the squares of the differences between the known values and the values obtained from the interpolating polynomial are given by

$$s = \sum_{i=1}^9 (\psi_i - \psi'_i)^2 \quad (15.3)$$

or

$$s = \sum_{i=1}^9 (\psi_i - a_1 - a_2x_i - a_3y_i - a_4x_iy_i - a_5x_i^2 - a_6y_i^2)^2. \quad (15.4)$$

In Eqn. 15.4, "s" is a measure of the error in the interpolating polynomial and is minimized by varying a_μ ($\mu = 1, 2, \dots, 6$) such that

$$\frac{\partial s}{\partial a_1} = \frac{\partial s}{\partial a_2} = \frac{\partial s}{\partial a_3} = \frac{\partial s}{\partial a_4} = \frac{\partial s}{\partial a_5} = \frac{\partial s}{\partial a_6} = 0. \quad (15.5)$$

Equation 15.5 provides six conditions for the coefficients a_μ ($\mu = 1, 2, \dots, 6$). With the indicated differentiations in Eqn. 15.5 performed,

these 6 conditions give rise to the following linear system of equations:

$$S \bar{a} = \bar{f} \quad (15.6)$$

where

$$S = \begin{bmatrix} 9 & \sum x_i & \sum y_i & \sum x_i y_i & \sum x_i^2 & \sum y_i^2 \\ \sum x_i & \sum x_i^2 & \sum x_i y_i & \sum x_i^2 y_i & \sum x_i^3 & \sum x_i y_i^2 \\ \sum y_i & \sum x_i y_i & \sum y_i^2 & \sum x_i y_i^2 & \sum x_i^2 y_i & \sum y_i^3 \\ \sum x_i y_i & \sum x_i^2 y_i & \sum x_i y_i^2 & \sum x_i^2 y_i^2 & \sum x_i^3 y_i & \sum x_i y_i^3 \\ \sum x_i^2 & \sum x_i^3 & \sum x_i^2 y_i & \sum x_i^3 y_i & \sum x_i^4 & \sum x_i^2 y_i^2 \\ \sum y_i^2 & \sum x_i y_i^2 & \sum y_i^3 & \sum x_i y_i^3 & \sum x_i^2 y_i^2 & \sum y_i^4 \end{bmatrix}$$

$$\bar{a} = \begin{bmatrix} a_1 \\ a_2 \\ a_3 \\ a_4 \\ a_5 \\ a_6 \end{bmatrix}, \quad \bar{f} = \begin{bmatrix} \sum \psi_i \\ \sum \psi_i x_i \\ \sum \psi_i y_i \\ \sum \psi_i x_i y_i \\ \sum \psi_i x_i^2 \\ \sum \psi_i y_i^2 \end{bmatrix}$$

The system 15.6 can be solved by matrix inversion in the form:

$$\bar{a} = S^{-1} \bar{f}. \quad (15.7)$$

16. APPENDIX F.

VISCOSITY-TEMPERATURE RELATIONSHIPS

The experimental correlations used in the program to calculate the dynamic viscosity, μ , wherever necessary, are presented here. For air, Sutherland's relation (Fox and McDonald (1973)) was used. For superheated steam, the constants in the air relationship were adjusted to fit viscosity data obtained from the steam tables of Keenan and Keyes (1969). Figure 16.1 shows the fit of the experimental data and the relationships used.

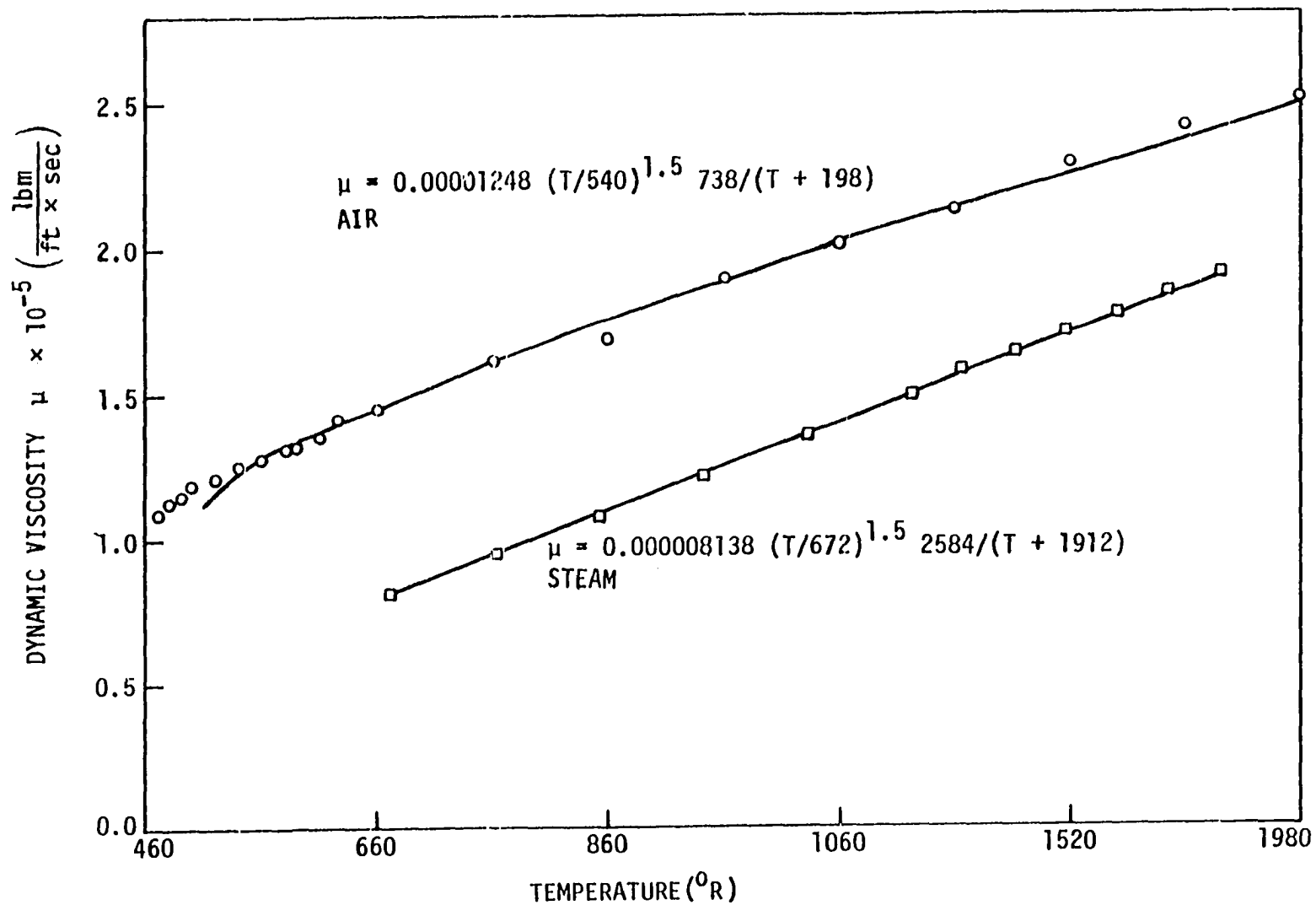


Figure 16.1. Viscosity-temperature relationships.
 Experimental data shown obtained from Streeter (1961) for air and from Keenan and Keyes (1969) for steam.

17. APPENDIX G.

SPEIDEL WAKE MIXING CALCULATION

The incompressible wake mixing calculation presented by Speidel (1954) is developed here. However, modifications of the camber line and inviscid turning due to boundary layer displacement thickness which Speidel incorporated before applying the wake mixing analysis are neglected.

Consider the plane cascade flow pictured in Fig. 17.1 with a control surface bounded by streamlines a2 and d2, station 2 "far downstream," and by incoming inviscid flow and airfoil wakes at stations bc, ab, and cd. The continuity equation between stations t and 2 is

$$\rho V_{x2} \tau = \rho \int_{-\tau/2}^{\tau/2} V_t \cos\beta_t dy \quad (17.1)$$

or

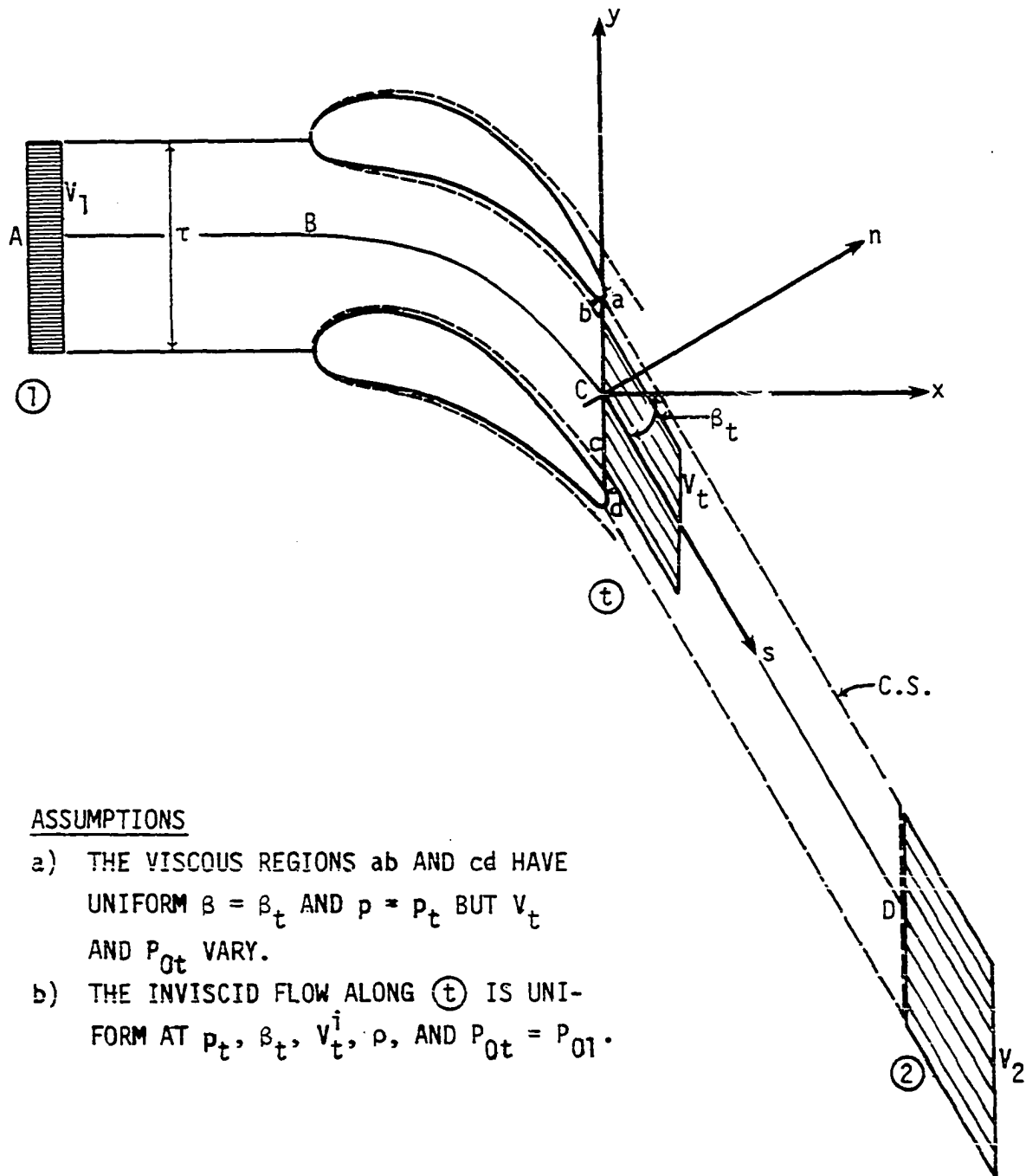
$$\rho V_{x2} \tau = \rho V_t^i \cos\beta_t (\tau - (\delta_{1p} + \delta_{1s})/\cos\beta_t) \quad (17.2)$$

where V_t^i is the inviscid velocity at the trailing edge with which the boundary layer calculation has been carried out, and δ_{1p} and δ_{1s} are the trailing edge displacement thicknesses on the pressure and suction sides of the airfoil, respectively. Writing

$$\theta_1 = \frac{(\delta_{1p} + \delta_{1s})}{\tau \cos\beta_t} \quad (17.3)$$

then

$$V_{x2} = V_t^i \cos\beta_t (1 - \theta_1). \quad (17.4)$$



ASSUMPTIONS

- a) THE VISCOUS REGIONS ab AND cd HAVE UNIFORM $\beta = \beta_t$ AND $p = p_t$ BUT V_t AND P_{0t} VARY.
- b) THE INVISCID FLOW ALONG (t) IS UNIFORM AT p_t , β_t , V_t^i , ρ , AND $P_{0t} = P_{01}$.

Figure 17.1. Schematic of the wake flow behind the cascade.

The y pressure-momentum balance between stations t and 2 is

$$\rho \int_{-\tau/2}^{\tau/2} v_{yt} v_t \cos\beta_t dy = \rho v_{x2} \tau v_{y2} \quad (17.5)$$

or

$$\cos\beta_t \sin\beta_t \int_{-\tau/2}^{\tau/2} v_t^2 dy = \tau v_{x2} v_{y2}. \quad (17.6)$$

The integral in the left hand side of Eqn. 17.6 is now transformed to make use of the trailing edge boundary layer thicknesses in the following way:

$$\int_{-\tau/2}^{\tau/2} v_t^2 dy = \frac{(v_t^i)^2}{\cos\beta_t} \int_{-\tau_n/2}^{\tau_n/2} \left[1 - \frac{v_t}{v_t^i} \left(1 - \frac{v_t}{v_t^i}\right) - \left(1 - \frac{v_t}{v_t^i}\right)\right] dn. \quad (17.7)$$

Outside of the boundary layer the velocity v_t equals v_t^i , and, therefore

$$\int_{-\tau/2}^{\tau/2} v_t^2 dy = (v_t^i)^2 \tau \left[1 - \frac{(\delta_{2s} + \delta_{2p}) + (\delta_{1s} + \delta_{1p})}{\tau \cos\beta_t}\right]. \quad (17.8)$$

Writing

$$\theta_2 = (\delta_{2s} + \delta_{2p}) / \tau \cos\beta_t \quad (17.9)$$

then

$$\int_{-\tau/2}^{\tau/2} v_t^2 dy = (v_t^i)^2 \tau (1 - \theta_2 - \theta_1) \quad (17.10)$$

and Eqn. 17.6 becomes

$$\cos\beta_t \sin\beta_t (v_t^i)^2 \tau (1 - \theta_2 - \theta_1) = \tau v_{x2} v_{y2}. \quad (17.11)$$

Substituting Eqn. 17.4 into Eqn. 17.11, we obtain the relationship

$$V_t^i \sin \beta_t = V_{y2} \frac{(1 - \theta_1)}{(1 - \theta_2 - \theta_1)} . \quad (17.12)$$

The x pressure-momentum balance between stations t and 2 is

$$\rho \int_{-\tau/2}^{\tau/2} V_{xt} V_t \cos \beta_t dy = \int_{-\tau/2}^{\tau/2} p_t dy = \rho V_{x2}^2 + p_2 \tau \quad (17.13)$$

or

$$\frac{\cos^2 \beta_t}{\tau} \int_{-\tau/2}^{\tau/2} V_t^2 dy - V_{x2}^2 = \frac{p_2 - p_t}{\rho} . \quad (17.14)$$

Using Eqns. 17.10 and 17.4, we can write Eqn. 17.14 as

$$\frac{p_2 - p_t}{\rho} = V_{x2}^2 \left(\frac{(1 - \theta_2 - \theta_1)}{1 - \theta_1} - 1 \right) . \quad (17.15)$$

In addition, the following relation between flow angles can be obtained from Eqns. 17.4 and 17.12:

$$\tan \beta_t = \tan \beta_2 \frac{(1 - \theta_1)^2}{(1 - \theta_2 - \theta_1)} . \quad (17.16)$$

Referring to Fig. 17.1, the total pressure loss along the streamline ABCD is $p_{01} - p_{02}$. The total pressure loss coefficient normalized with respect to the axial velocity V_x is expressed as

$$\xi = \frac{p_{0t} - p_{02}}{\frac{1}{2} \rho V_{x2}^2} = \frac{p_t - p_2}{\frac{1}{2} \rho V_{x2}^2} + \frac{V_t^2 - V_2^2}{V_{x2}^2} . \quad (17.17)$$

Substitution for $(p_t - p_2)$ and V_t^2 from Eqns. 17.4, 17.15, and 17.16 gives the expression

$$\xi = \frac{2\theta_2 + \theta_1^2}{(1 - \theta_1)^2} + \tan^2 \beta_2 \frac{(1 - \theta_1)^2}{(1 - \theta_2 - \theta_1)^2} - 1 \quad (17.18)$$

where β_2 is obtained from Eqn. 17.16 after a mass averaged β_t is calculated with the inviscid solution.

This loss coefficient as expressed in Eqn. 17.18 includes both the flow loss (profile loss) between stations 1 and t and the wake mixing loss between stations t and 2; however, the total pressure loss due to the sudden expansion at the trailing edge is not accounted for.

Scholz (1965) gives the following formula to calculate the attendant losses due to the trailing edge thickness:

$$\xi_t = \frac{P_{0t} - P_{02}}{\frac{1}{2}\rho V_x^2} = (1 + \tan^2 \beta_2) \left(\frac{2RTE}{\tau - 2RTE} \right)^2 \quad (17.19)$$

Finally, the drag coefficient, C_{d1} , defined as the drag force parallel to the mean velocity vector \bar{V}_m normalized with respect to chord and upstream dynamic pressure is calculated using the expression

$$C_{d1} = \xi \frac{\tau}{c} \cos^2 \beta_1 \cos \beta_m \quad (17.20)$$

18. APPENDIX H.

DESCRIPTION OF INPUT TO CASCADE FLOW ANALYSIS PROGRAM

The input variables needed for the cascade flow analysis program are described below. Two options are available in the program based on how the airfoil profile data are presented, i.e., by spline fitting (INCONT=0) or by polynomial fitting (INCONT=1).

Figures 18.1 and 18.2 show the input variables for the two options as they are punched on the data cards. Field column widths as shown are 5 and 10 for integer and real variables, respectively, with integer variables right justified and real variables entered with a decimal point.

Special comment is in order here concerning additional input factors required for the calculations in some cases and which are under control of the program user. The damping factors ODAMP and DVDAMP may be required for convergence of the streamline curvature calculation in high subsonic or transonic flow cases, or in cases of especially high pitch to chord ratios. With these damping factors applied, extensive calculations may be required for convergence. Recommended damping values are noted in the description of the damping factors in the list below. Also, the factors FLAMS, FTURBS, FLAMP, and FTURBP may be required in the boundary layer calculations on the suction or pressure surfaces of the airfoil with difficult regions being the start of the leading edge laminar calculation, and the start of the turbulent calculation after laminar separation. The start of the leading edge laminar calculation needs strong favorable velocity gradients for convergence

1	6	11	16	21	26	31	36	41	46	51	56	61	66	71	76
INCONT IREA IBDYLR															
TITLE															
RLE	RTE	BX	HTLRT	B1STAR	BWED1	B2STAR	BWED2								
X6	Y6	X7	Y7	PITCH	GAGANG	UNCTUR									
VX1NM	VY1NM	BETA2													
GAM	AR	TØ1	PØ1	AM1	ALOSSC										
ODAMP	DVDAMP														
DELTAZ ARRAY															
PERBX	PERTHR	NLE													
TU	ITU	ITR	ITRLG	RLAM	RTURB	CP	IFLUID								
FLAMS	FTURBS	FLAMP	FTURBP												

Figure 18.1. Input card format for cascade flow analysis program using polynomial fitted airfoil.

1	6	11	16	21	26	31	36	41	46	51	56	61	66	71	76
INCONT IREA IBOYLR															
TITLE															
PITCH				STGRF			CHORDF								
VX1NM		VY1NM		BETA2		AINC									
GAM		AR		TØ1		PØ1		AM1		ALOSSC					
ODAMP		DYDAMP													
NS	XLE		XTE		XLEC		XTEC		RI1		RØ1				
NP	YLE		YTE		YLEC		YTEC		RI2		RØ2				
XS ARRAY															
YS ARRAY															
XP ARRAY															
YP ARRAY															
DELTAZ ARRAY															
PERBX			PERTHR			NLE									
NLERI1															
TU		ITU	ITR	ITRLG		RLAM		RTURB		CP		IFLUID			
FLAMS		FTURBS		FLAMP		FTURBP									

Figure 18.2. Input card format for cascade flow analysis program using spline fitted airfoil.

with the normal calculated optimum number of stations on the profile; otherwise, the number of stations should be increased by increasing FLAMS or FLAMP without overflowing the allocated array storage. Similarly, the number of stations should be increased, by adjusting FTURBS and FTURBP, if convergence of the turbulent boundary layer calculation is not achieved after laminar separation. The first try should be made with FLAMS, FTURBS, FLAMP and FTURBP equal to 1.0. The program then prints messages telling the user why the boundary layer calculation stopped and gives guidelines on how to adjust the particular factor in case convergence was not achieved.

INCONT	Type of airfoil description
	0; airfoil is spline fitted
	1; airfoil is polynomial fitted
IREA	Leading edge reanalysis option
	0; reanalysis is not performed
	1; reanalysis is performed
IBDYLR	Boundary layer analysis option
	0; boundary layer analysis is not performed
	1; boundary layer analysis is performed
RLE, RTE	Radii of leading- and trailing-edge circles, ft, see Fig. 18.3
BX	Axial chord, ft, see Fig. 18.3
HTLRT	H/L ratio, see Fig. 18.3

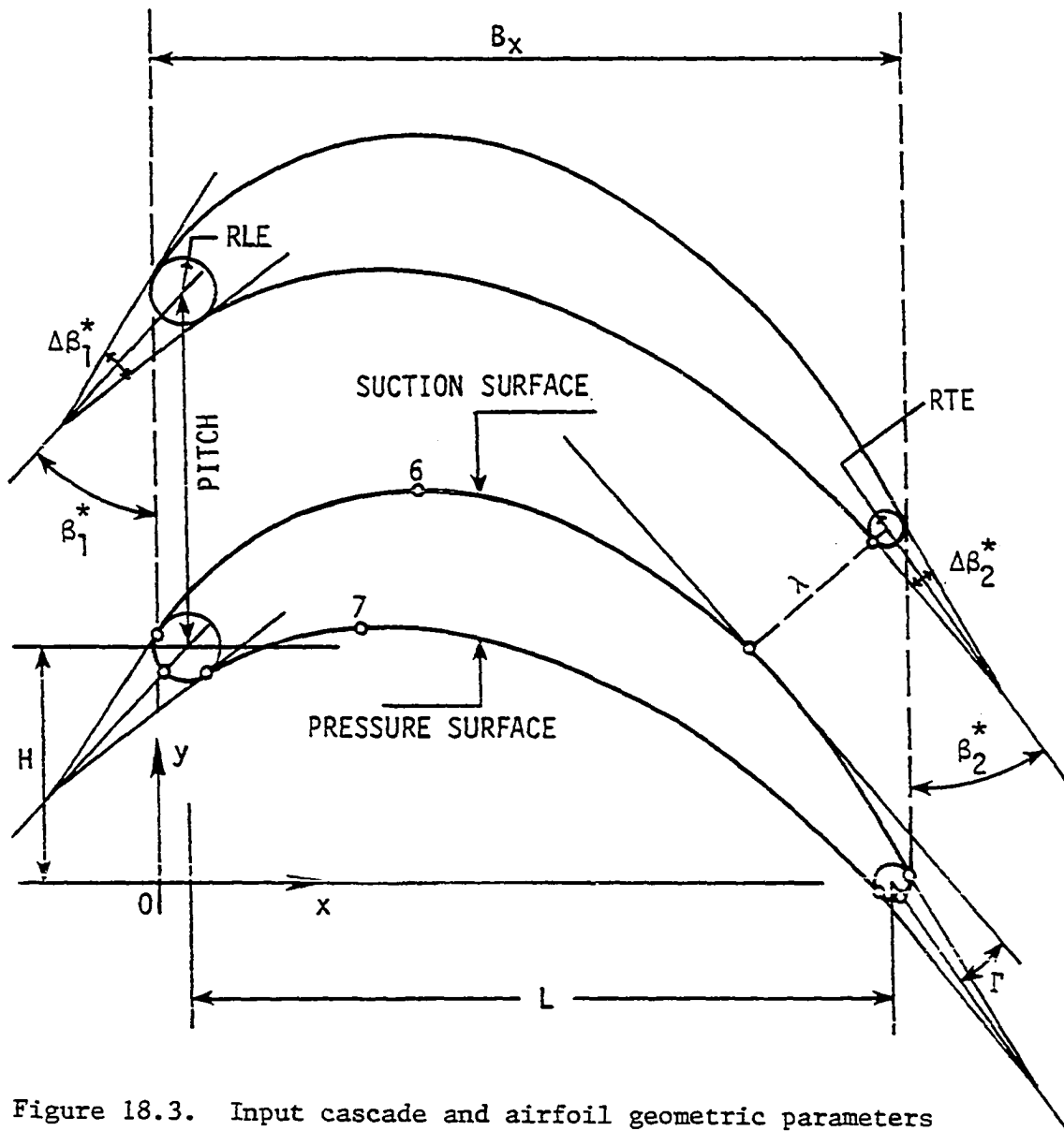


Figure 18.3. Input cascade and airfoil geometric parameters for polynomial fitted airfoil.

B1STAR, B2STAR	Metal angles β_1^* and β_2^* (measured from downward pointing vertical), deg, see Fig. 18.3
BWED1, BWED2	Wedge angles $\Delta\beta_1^*$ and $\Delta\beta_2^*$, deg, see Fig. 18.3
X6, Y6	Coordinates of auxiliary point 6, ft, see Fig. 18.3
X7, Y7	Coordinates of auxiliary point 7, ft, see Fig. 18.3
PITCH	Cascade spacing, ft, see Figs. 18.3 or 18.4
GAGANG	Gaging angle, $\sin^{-1}(\lambda/\text{PITCH})$, deg, see Fig. 18.3
UNCTUR	Uncovered turn, Γ , deg, see Fig. 18.3
STGRF	Vertical distance between centers of leading- and trailing-edge circles, ft, see Fig. 18.4
CHORDF	Axial chord, ft, see Fig. 18.4
NS, NP	Number of spline points given for suction and pressure surfaces, maximum of 50 points each; NS is equal to NP, see Fig. 18.4
XLE, YLE	Coordinates of leading edge, ft. Intersection of camber line with leading-edge circle
XTE, YTE	Coordinates of trailing edge, ft. Intersection of camber line with trailing edge circle
XLEC, YLEC	Coordinates of center of leading edge circle, ft
XTEC, YTEC	Coordinates of center of trailing edge circle, ft
RI1, RI2	Leading edge radii, ft, see Fig. 18.4
RO1, RO2	Trailing edge radii, ft, see Fig. 18.4
XS, XP	Arrays of X coordinates of spline points on the suction and pressure surfaces, ft, see Fig. 18.4

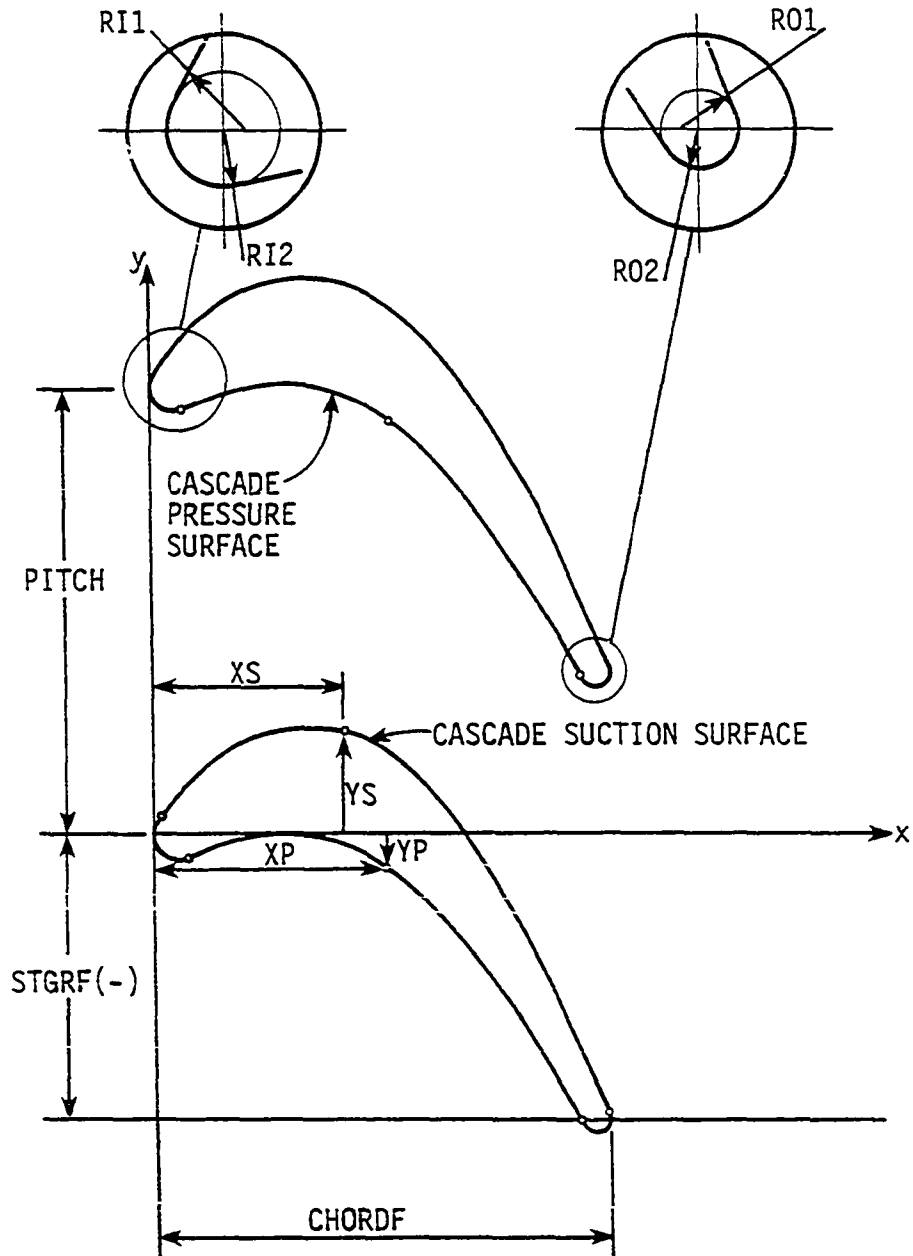


Figure 18.4. Input cascade and airfoil geometric parameters for spline fitted airfoil.

YS, YP	Arrays of Y coordinates of spline points on the cascade suction and pressure surfaces, ft, see Fig. 18.4
VX1NM	Upstream axial velocity, ft/sec, see Fig. 18.5
VY1NM	Upstream tangential velocity, ft/sec, see Fig. 18.5
	VX1NM and VY1NM are used to input the upstream flow angle, β_1 , and to initiate the streamline curvature calculation. The upstream velocity need not match the mass flow rate
BETA2	Final downstream flow angle, β_2 , deg, see Fig. 18.5 If entered as zero, the streamline curvature calculation solves for this angle
AINC	Incidence angle, deg, see Fig. 18.5 Included for information only, not required for calculation
GAM	Specific heat ratio
AR	Gas constant, (lbf)(ft)/(lbm)(°R)
T01	Inlet stagnation temperature, °R
P01	Inlet stagnation pressure, lbf/ft ²
AM1	Inlet Mach number
ALOSSC	Relative total pressure loss $(p_{01} - p_{02})/p_{01}$
ODAMP	Over-damping factor. Value by which changes in velocity gradient are multiplied after regular damping factor is applied. Values less than 1.0 are used if convergence of streamline curvature

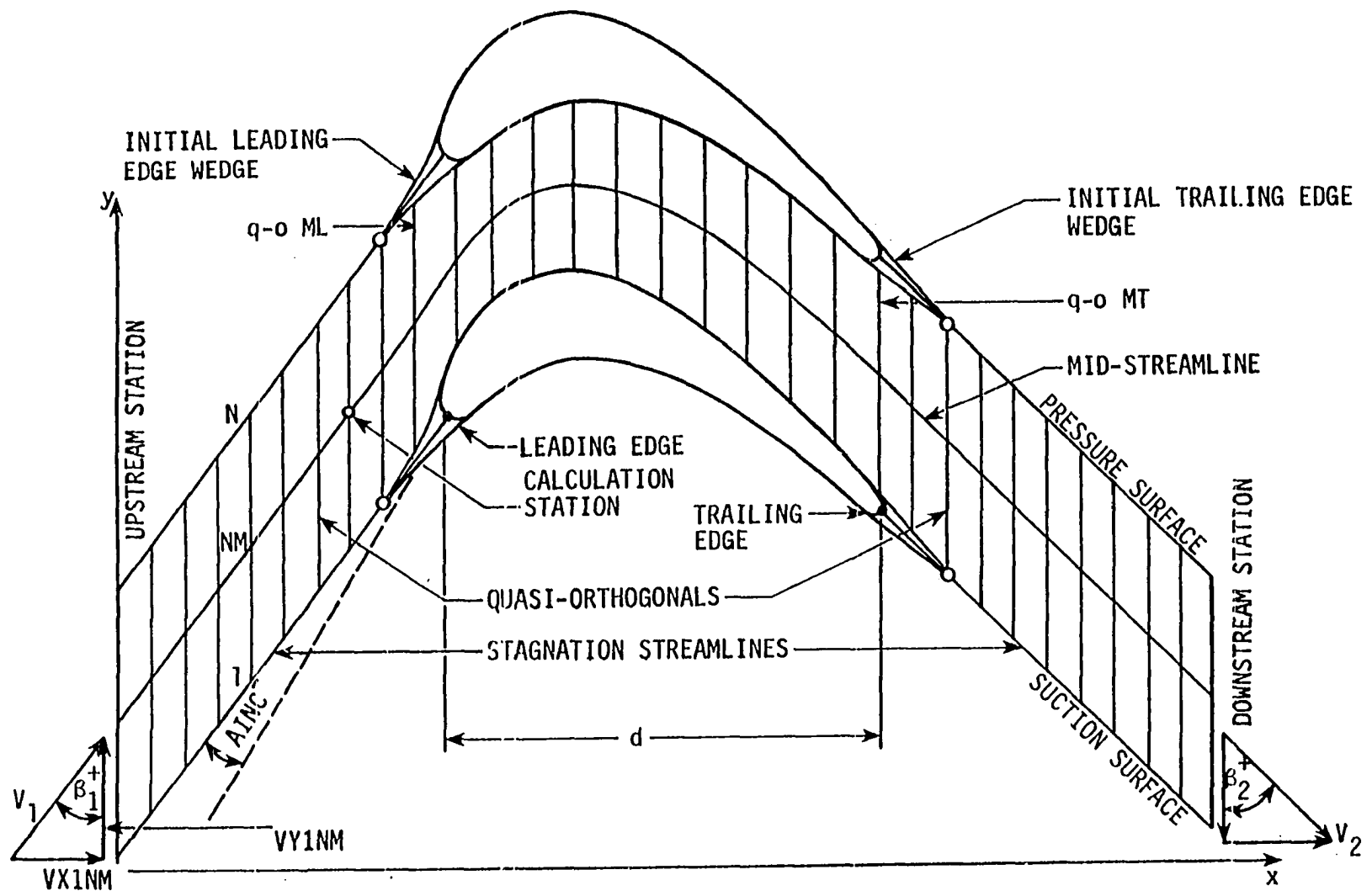


Figure 18.5. Input cascade flow field parameters.

calculations is not achieved with regular damping factor. Values of 0.75 and 0.5 should be tried first

DVDAMP Damping factor for change in slope, dy/dx , between streamline curvature iterations. Values less than 1.0 are used if convergence is not achieved with regular damping factor. Values of 0.75 and 0.5 should be tried first.

DELTAZ Array of ratios of upstream stream sheet thickness to that at $q-os$. See Fig. 18.5; 39 values are required which are defaulted to 1 if $DELTAZ(1) = 0$.

PERBX Extent of reanalysis mesh in the axial (x) direction from the leading edge as a fraction of axial chord. A value of 0.2 has been found reasonable.

PERTHR Extent of reanalysis mesh normal to the airfoil surface as given as a fraction of cascade throat. A value of 0.6 has been found reasonable. When $INCONT=0$, then PERTHR is entered as the actual mesh extent, ft

NLE Number of reanalysis mesh points on the leading edge circle, usually less than 21

NLERI1 Number of reanalysis mesh points on the suction side of the leading edge circle; less than NL

TU Upstream turbulence intensity, percent

ITU Control variable on free stream turbulence level

effects on development of turbulent boundary layer

0; effects are not accounted for

1; effects are accounted for

ITR Natural transition model option

1; Crimi and Reeves (1972) model

2; Dunham (1972) model

ITRLG Natural transition length model option

1; Dhawan and Narasimha (1958) model

2; model based on fully turbulent Reynolds number being twice the transition Reynolds number

RLAM, RTURB Laminar and turbulent recovery factors for

temperature. The following values have been used

	RLAM	RTURB
air	0.86	0.88
steam	0.97	0.99

CP Specific heat at constant pressure,

(lbf)(ft)/(lbm)(°R). The following values have been used

	CP
air	186
steam	389

IFLUID Control variable on type of fluid for viscosity calculation purposes

0; air

1; superheated steam

FLAMS Factor by which the optimum number of suction
 surface laminar boundary calculations is
 multiplied. For instance:
 FLAMS=2; the optimum number is doubled
 FLAMS=0.5; the optimum number is halved

FTURBS Factor similar to FLAMS applied to suction surface

FLAMP, FTURBP Factors similar to FLAMS and FTURBS for the
 pressure surface

Figure 18.6 shows an input data set example for the spline fit option. The data set corresponds to Test Case No. 1 presented in Chapter 6 for $\alpha_1 = 48^\circ$ (see Fig. 6.3).

```

1      6      1      1      2      2      3      3      4      4      5      5      6      6      7      7      8
0      1      1
NACA PRIMARY TURBINE SERIES;B1=75,A1=48,C/T=1.8,THC=80
0.2777801 -0.272501 0.4208871
9.65926   2.58819   0.0       0.0
1.4       53.35      540.0     2040.0    0.0878    0.0
1.0       1.0
140.0005   0.4198354 0.0051756 0.4183871 0.0051756 0.0025
14-.0017353 -.2745391 0.0       -.2725009 0.0051756 0.0025
0.0010972 0.0084597 0.0176567 0.0355728 0.0691620 0.0997384 0.127628 0.1533418
0.177239 0.220457 0.276925 0.310873 0.374823 0.420413
0.0031864 0.0112122 0.0178529 0.0258224 0.0312277 0.0285554 0.0210354 0.0105591
-.0021725 -.0325601 -.0864774 -.1258882 -.2086681 -.2710360
0.0062074 0.0142804 0.0235369 0.0391226 0.0653740 0.0889561 0.1113473 0.1330338
0.1541531 0.2156311 0.2748398 0.3130043 0.3677651 0.416361
-.0050721 -.0051269 -.0063020 -.0085850 -.0136480 -.0193820 -.0262399 -.0345776
-.0443306 -.0806200 -.1254835 -.1592352 -.2144910 -.2739668
0.0
0.25      0.055      9
6
2.75      0      1      1      0.86      0.88      186.      0
1.0       1.0       1.0       1.0

```

Figure 18.6. Example input data set for spline fit option. Data set is for Test Case No. 1, $\alpha_1 = 48^\circ$.